The University Of Sheffield

The Study of Combustion and Emission Characteristics of Partially Cracked Ammonia and Chemiluminescent Emission for Hydrocarbon Fuel Based on the Chemical Kinetic Mechanisms

Miss Jing Zhang

Combustion and Flow Diagnostics Research Group

Department of Mechanical Engineering

2021

This thesis is submitted to the University of Sheffield for the degree of Doctor of Philosophy in the faculty of Engineering.

Declaration

The work presented in this thesis is that of the Author and has not been submitted for any other award or degree at the University of Sheffield or any other university or institution.

Acknowledgements

Three years already passed, the working time in our combustion group was really happy. My supervisor is knowledgeable and has wide-ranging academic interests. He is always curious about everything and shared his knowledge, experience and wisdom with me. Also, my colleagues are very nice, the time working with them is part of my precious memory.

First of all, during my PhD study, I would like to express my sincere gratitude to my supervisor, Professor Yang Zhang, for his invaluable guidance, encouragement and support. More importantly, I am really appreciated that my supervisor and the University of Sheffield offers me a great opportunity and financial support to pursue my PhD degree.

Second, I would also express my gratitude to my family members, who always offer me support and encouragement throughout the PhD studies. They have also provided the freedom for me to pursue my dream. The most important thing in the world is family and love, they help me get through the hard time.

Finally, I would like to thank my colleagues. Particularly, to Miss Muyi Pan, who has accompanied and helped me a lot during my PhD studies, our friendship will not fade away; to Dr Yufeng Lai for his great help of sharing his experimental experience and for the wonderful time we spend together in the combustion lab; and to Mr Ahmed Albadi for his useful suggestions and recommendations. I would also be thankful to all my colleagues in Combustion and Flow Diagnostics Research Group, Dr Lukai Zheng, Dr Ahmad Fuad, Dr Hang Xu Zhou, Dr Houshi Jiang, Dr Xiao Wang, Mr Yuchen Zhang, Dr Xu Wang, Mr Haibo Zhou, Mr Xuanqi Liu and Mr Huarong Lei. It is a memorable and enjoyable time to work with them.

Publications

[1] **J, Zhang**. and Y, Zhang., 2019. Reduced mechanism generation for methanol-based toluene reference fuel with combined reduction methods. Fuel, 247, pp.135-147.

[2] **J, Zhang**. and Y, Zhang., Numerical Study of OH*, CH* and C_2* Radicals in a New Reduced Ethanol Kinetics, 27th ICDERS, Beijing, China, 2019.

Abstract

It is notable that investigation of detailed kinetic mechanisms is beneficial to understanding of the combustion process and exhaust gases formation. Therefore, the aim of this thesis is to numerically study the combustion and emission characteristics of partially cracked ammonia ($NH_3/H_2/N_2$/air mixtures) and chemiluminescent emission for hydrocarbon fuel based on the chemical kinetic mechanism.

In this study, the potential of partially cracked ammonia in controlling NO_X emission and widening operation range in a single and staged combustion system is discussed for the first time. As well, the effect of cracking ratio and other influential factors on the NO_X emissions is numerically demonstrated. Besides, in order to further study the flame characteristics, the ability of flame chemiluminescence as a sensor of heat release rate at various equivalence ratios is discussed. Consequently, total chemiluminescence is more acceptable as a reliable signal to character the heat release rate.

Usually, development of an accurate and relatively compact reduced mechanisms is required to save computation time of numerical study. The direct relationship graph with error propagation (DRGEP) and the generalized entropy production analysis (GEPA) methods are integrated to establish the ethanol reduced kinetic mechanism. In addition, a two-stage reduction process combining the improved path flux analysis (IPFA) and the generalized entropy production analysis (GEPA) method is performed for the first time to develop the reduced ammonia/hydrogen/methane mechanism. The results show generally good agreements between reduced mechanism and extensive experimental measurements.

Table of Contents

List of Figures

List of Tables

Nomenclature

Symbol	Definition
A	Pre-exponential factor ($cm^3/(mol \cdot s)$)
A_k	Einstein coefficient for spontaneous emission of the kth species (s^{-1})
Ar	Argon
BSF	Burner stabilized flames
c_p	Molar heat capacity of the mixture at constant pressure (cal/(mol·K))
$\overline{c_v}$	mean molar heat capacity at constant volume (cal/(mol·K))
C	Carbon atom
C_2*	C_2 radical chemiluminescence
C_A	Consumption flux of species A ($(cm^3)/(mol \cdot s)$)
C_{AB}	Consumption flux of species A related to B ($(cm^3)/(mol \cdot s)$)
CFD	Computational fluid dynamics
CH_4	Methane
C_2H_2	Acetylene
CH*	CH radical chemiluminescence
C_3H_8	Propane
CH_3CHO	Acetaldehyde
CH_2O	Formaldehyde
CH_3OH	Methanol
C2H5OH	Ethanol
CIT	Combustor inlet temperature (K)
CM	Connectivity method
CO	Carbon monoxide
CO_2	Carbon dioxide
CR	Compression ratio
CRN	Chemical reactor network
CRZ	Central recirculation zone
CSP	Computational singular perturbation
CURV	Curvature
$\frac{dS}{dt}$	Variation of entropy production with time (cal/(mol·K·s))
DIC	Direct interaction coefficient
DRGASA	DRG aided sensitivity analysis
DRG	Directed relation graph
DRGEP	Direct relationship graph with error

	propagation
DRGEPSA	DRGEP with sensitivity analysis
Ea	Apparent activation energy (cal/mol)
EPA	Entropy production analysis
FPCA	functional PCA
FR	Flow reactor
GEPA	Generalized entropy production analysis
GHG	Greenhouse gas
GRAD	Gradient
h_j^0	Standard state enthalpy of the *j*th species (cal/mol)
h_k	specific enthalpy of the *k*th species (cal/mol)
H	Hydrogen atom
H_2	Hydrogen
H_2O	Water
HPST	High-pressure shock tube
i_k	Chemiluminescent emission intensity of the *k*th excited species (mol·photons/($cm^3 \cdot s^{-1}$))
I	Total number of elementary reactions
IC	Internal combustion
IDT	Ignition delay time (s)
I_k	total chemiluminescence of the *k*th excited species (mol·photons/($cm^3 \cdot s^{-1}$))
ILDM	Intrinsic low dimensional manifold
IPFA	Improved path flux analysis
ISAT	*In situ* adaptive tabulation
JSR	Jet-stirred reactor
k_f	Forward reaction rate constant ((cm^3)/(mol·s))
k_r	Reverse reaction rate constant ((cm^3)/(mol·s))
K	Total number of species
L	Integration length (m)
LBV	Laminar flame velocity
LHV	Lower heating value
LIF	Laser induced fluorescence
$\dot{M}$	Mass flow rate (kg/s)
M_i	Third reactant
MOF	Metal-organic frameworks
N	Nitrogen atom
N_2	Nitrogen
NA	Necessity analysis

NH_3	Ammonia
NO	Nitric oxide
N_2O	Nitrous oxide
NOx	Nitrogen oxide
O	Oxygen atom
O_2	Oxygen
OH*	OH radical chemiluminescence
OIC	Overall interaction coefficient
pw	Pathway
P	Pressure (atm)
P^0	Standard state pressures (atm)
P_A	Production flux of species A ($(cm^3)/(mol \cdot s)$)
P_{AB}	Production flux of species A related to B ($(cm^3)/(mol \cdot s)$)
PCA	Principal component analysis
PEA	Partial equilibrium assumption
PFA	Path flux analysis
PFR	Plug flow reactor
PIC	Path interaction coefficient
PLIF	Plane laser induced fluorescence
PSR	Perfectly stirred reactor
q_k^f	Forward reaction rate of the *k*th reaction ($mol/cm^3 \cdot s$)
q_k^b	Backward reaction rate of the *k*th reaction ($mol/cm^3 \cdot s$)
Q_{loss}	Net heat flux directed out of the reactor (cal)
$\dot{Q}_{rad}$	radiation heat release (cal)
Q_{source}	Source of heat release in reactor (cal)
QSSA	Quasi steady state approximation
$r_{\mathrm{AB}}^{\mathrm{DRGEP}}$	Numerator of coefficient between species A and B in the DRGEP method
$r_{AB,IPFA}^{con-1st}$	Interaction coefficient for consumption of species A via species B of first generation in the IPFA method
$r_{AB,IPFA}^{con-2nd}$	Interaction coefficient for consumption of species A via species B of second generation in the IPFA method
$r_{AB,IPFA}^{pro-1st}$	Interaction coefficient for production of species A via species B of first generation in the IPFA method
$r_{AB,IPFA}^{pro-2nd}$	Interaction coefficient for production of species A via species B of second

	generation in the IPFA method
r_{AB}^{IPFA}	Numerator of coefficient between species A and B in the IPFA method
$r_k(t)$	Relative contribution of *k*th reaction to the total entropy production at time *t*
$R_{\mathrm{AB}}^{\mathrm{DRGEP}}$	Overall interaction coefficient between species A and B in the DRGEP method
R	gas constant (cal/(mol·K))
RCM	Rapid compressor machine
ROP	Rate of production
s_j^0	Standard state entropy of the *j*th species (cal/(mol·K))
S	Intermediate species between species A and B
SA	Sensitivity analysis
SEM	Simulation error minimization
SF	Spherical flame
SI	Spark internal
S_L	Laminar flame speed (m/s)
SP	Species profile
ST	Shock tube
t	Time (s)
T	Temperature (K)
T_{B}	Temperature of burned gas (K)
T_{U}	Temperature of unburned gas (K)
u	Axial speed of the fluids (cm/s)
UHC	Unburned hydrocarbon
U_{sys}	Total internal energy (cal)
V_k	Ordinary diffusion velocity of the *k*th species (cm/s)
$\overline{W}$	Mean molecular weight (g/mol)
W_k	Molecular weight of the *k*th species (g/mol)
x	Spatial coordinate (cm)
X_j	Mole fraction of the *j*th species
$[X_k]$	Mole concentration of the *k*th species (mol/cm^3)
Y_k	Mass fraction of the *k*th species
α_k	Chemical affinity of the *k*th reaction (cal/mol)
δ_{B}^i	Parameter of judgement on whether species B is involved in the *i*th reaction or not
ε	User-specified threshold

γ	Cracking ratio
λ	Thermal conductivity of the gas mixture (cal/cm·s·K)
$\nu_{A,i}$	Stoichiometric coefficient of species A in the *i*th reaction
μ_j	Chemical potential of the *j*th species (cal/mol)
$\dot{\omega}$	Reaction rate (mol/cm^3·s)
$\omega_{f,i}$	Forward reaction rate of the *i*th reaction (mol/cm^3·s)
$\omega_{b,i}$	Backward reaction rate of the *i*th reaction (mol/cm^3·s)
ω_i	Net reaction rate of the *i*th reaction (mol/cm^3·s)
ρ	Mass density (g/cm^3)
Φ	Equivalence ratio
$\Phi_{overall}$	Overall equivalence ratio in rich-lean burn combustor
$\Phi_{primary}$	Equivalence ratio of primary stage in rich-lean burn combustor
τ_{PFR}	Residence time in PFR (ms)
τ_{PSR}	Residence time in PSR (ms)
τ_{total}	Total residence time (ms)

1. Introduction

1.1. Motivation

Combustion, as one of the common ways of energy conversion, plays a key role in varied important fields such as energy, electricity, transportation. It promotes rapid industrial and economic development while also contributing to significant consumption of fossil fuels, leading to large number of emissions of pollutants and many environmental problems.

In order to achieve the target of reduction in greenhouse gas (GHG) emissions, it is important to explore renewable energy sources for human and industrial activities. Hydrogen, natural gas, alcohols and ammonia, as low or zero carbon fuels were proposed to alleviate the energy shortage crisis [1]. As a promising carbon free fuel, the possibility of using ammonia as a surrogate of hydrocarbon fuels in engines was discussed in previous experimental works [2-5]. However, due to its noticeably low laminar burning speed, narrow flammability limits and high ignition energy, ammonia-fuelled combustors are prone to low combustion stability and combustion efficiency [6-9]. To solve this problem, one of the effective enhancement strategies is to mix ammonia with other reactive fuels, such as oxidizer, hydrocarbons and hydrogen [10,11]. It is important to note that the production of H_2 from cracked ammonia is straightforward, there is no need to add new components when using H_2 as an addictive [12,13]. Thereby directly using partially cracking ammonia instead of hydrogen enables to enhance combustion performance and effectively avoid the safety problem of H_2 in transportation. Therefore, the present work considers using cracking ammonia for keeping high combustion efficiency and low NO_X emissions in gas turbines, based on its capability of thermally cracking to nitrogen, hydrogen, and unburned ammonia radicals.

Another great challenge of ammonia combustion is high NO_X emissions that hinders NH_3 utilization in gas turbines [14]. Consistent results were reported by a number of researchers [15-18] that NO_X emission is able to be remarkably reduced under slightly rich equivalence ratios (1.05-1.2) compared to stoichiometric or slightly fuel-lean conditions. However, these studies also implied excessive emissions of unburnt NH_3 and H_2 and efficiency issues under the rich burning condition. Therefore, rich-lean combustion is considered since it can take advantage of suppressing NO_X production, as well as burning off the remaining ammonia and hydrogen in the lean-burn stage [12,17,19].

In order to explore the potential of partially cracked ammonia ($NH_3/H_2/N_2$/air mixtures) in controlling NO_X emission and widening operation range in single and two-staged combustors, a numerical study on the combustion and emission characteristics for partially cracked ammonia ($NH_3/H_2/N_2$/air mixtures) in gas turbines is performed for the first time.

It is known that investigation of detailed kinetic mechanisms is beneficial to deeply understand the combustion process and exhaust gases formation. Most combustion reaction kinetics models consist of more than hundreds of elementary chemical reaction steps that have a profound impact on the combustion phenomena [20]. Usually, it is necessary to reduce the extremely rigid problems of complex detailed mechanisms encountered in the numerical simulation of flow and combustion coupling. Meanwhile the reduced model should maintain the physicochemical properties of the fuel within wide operating conditions. To further study of the ammonia combustion process and NO_X emissions, development of an accurate and relatively compact reduced mechanism for the ammonia oxidation is required. Therefore, in order to retain the essential dynamic features of the reaction system and reduce stiffness

induced by the highly reactive radicals, a reduced kinetics mechanism for $NH_3/H_2/CH_4$ mixtures is developed and well validated.

In addition, application of renewable and clean energy, alcohols, especially ethanol that are applied as fossil fuel substitute fuels have attracted more attention as well [21,22]. To reduce computation time of simulation, a new reduced ethanol mechanism including excited radicals (OH*, CH* and C_2*) is developed and successfully validated with extensive experimental results.

With the aim of better studying the complex phenomena in the combustion process, the optical diagnostic technology has been widely concerned, as it has no interference to the combustion field during the diagnosis process. Chemiluminescence is regarded as a promising low-cost optical diagnostic tool [23,24]. At present, the applications of chemiluminescence are performed to understand the ignition and flame development characteristics more intuitively [25,26,27,28]. It has long been known that kinetic modelling is a very effective tool for combustion investigations. Therefore, numerical analysis of ethanol flame structure based on chemiluminescence from the flame is motivated and conducted by using the reduced ethanol mechanism. Also, the peak chemiluminescence intensity of C_2*/CH* as an indicator of local equivalence ratio is illustrated in hydrocarbon fuel flames from the aspect of the chemical mechanism.

1.2. Aim and Objective

Based on the motivation of the present thesis, the main objective includes three aspects: firstly, develop a compact reduced kinetics mechanism of ethanol for further investigation of

flame chemiluminescence, and establish an accurate reduced mechanism for $NH_3/H_2/CH_4$ mixtures to understand the $NH_3/H_2/CH_4$ combustion process and exhaust gases generation. Secondly, explore the potential of partially cracked ammonia ($NH_3/H_2/N_2$/air mixtures) in controlling NO_X emission and widening operation range in a single and two-staged combustion system. Moreover, provide a deep insight in improving combustion and controlling emission characteristics of partially cracked ammonia in both single and 2-stage rich-lean gas turbine combustors. Finally, analyse the equivalence ratio and heat release rate determination by using excited state species (OH*, CH* and C_2*) chemiluminescence profiles. In detail, the objectives are listed as follows:

- **For establishing the reduced kinetic mechanism**

- The direct relationship graph with error propagation (DRGEP) and the generalized entropy production analysis (GEPA) methods are integrated to establish the ethanol reduced kinetic mechanism.
- The reduced ethanol mechanism is validated by available experimental data including ignition delay time, species mole fraction in jet stirred reactor and laminar burning velocity over numerous operating conditions.
- A two-stage reduction process combining the improved path flux analysis (IPFA) and the generalized entropy production analysis (GEPA) methods is performed for the first time to develop the reduced ammonia/hydrogen/methane mechanism.
- Extensive validations of the proposed reduced model are conducted by comparing with the detailed mechanism as well as available experimental data of ignition delay time in shock tube, species profiles and laminar flame speed over a broad range of

equivalence ratios, temperatures, and pressures.

- The NO_X emission characteristics of $NH_3/H_2/CH_4$ mixtures in a gas turbine are numerically investigated through a chemical reactor network (CRN) model based on the proposed ammonia reduced mechanism.

➢ **For studying combustion and NO_X emission characteristics for partially cracked ammonia**

- The laminar burning velocity of partially cracked ammonia flame is predicted with a one-dimensional freely propagating laminar flame calculation model of CHEMKIN-PRO [29].
- The chemical reactor network (CRN) model is constructed to characterize the NO_X emission of partially cracked ammonia combustion in a single stage and 2-stage gas turbine combustor.
- A reaction pathways flux method is used to represent NO reaction pathways at various operating factors and cracking ratios.
- The potential of controlling the important intermediate species and reactions on NO formation/reduction is demonstrated by identifying the major NO_X reaction pathways and analysing the NO rate of production (ROP).

➢ **For studying the ability of flame chemiluminescence as a sensor of heat release rate at various equivalence ratio**

- The ability of flame chemiluminescence as a sensor of heat release rate at various

equivalence ratio is discussed by combining rate of production analysis and sensitivity analysis.

- Reaction paths analysis is conducted for better understanding ethanol oxidation process and the formation and consumption reactions of the excited state species.
- The correlations between the chemiluminescence intensity ratio of C_2*/CH* and the equivalence ratio are investigated in hydrocarbon premixed flames based on chemical reaction kinetics mechanisms.
- The phenomenon, where the peak chemiluminescence intensity ratio of C_2*/CH* increases almost linearly following by a descending trend when the local equivalence ratio increases, is demonstrated from chemical mechanisms' aspect for the first time.

1.3. Outline of the thesis

In this thesis, the combustion and emission characteristics of partially cracked ammonia (NH_3/H_2/N_2/air mixtures) and chemiluminescent emission for hydrocarbon fuel based on the chemical kinetic mechanism are mainly studied. Firstly, to save computation time of numerical study, the direct relationship graph with error propagation (DRGEP) and the generalized entropy production analysis (GEPA) methods are integrated to establish the ethanol reduced kinetic mechanism. In addition, a two-stage reduction process combining the improved path flux analysis (IPFA) and the generalized entropy production analysis (GEPA) method is performed. Secondly, the potential of partially cracked ammonia in controlling NO_X emission and widening operation range in a single and staged combustion system is discussed for the first time. As well, the effect of cracking ratio and other influential factors on the NO_X

emissions is numerically demonstrated. Last but not least, in order to further study the flame characteristics, the ability of flame chemiluminescence as a sensor of heat release rate at various equivalence ratios is discussed. Consequently, total chemiluminescence is more acceptable as a reliable signal to character the heat release rate.

In detail, the present thesis consists seven chapters, which are the introduction, the basic background knowledge, the numerical methods, the numerical results as well as the conclusions. The contents are listed in detail as follows:

In Chapter 1, the motivation of the present study is provided, the aim and objectives of this work, and the outline of the thesis are presented.

In Chapter 2, the background knowledge associated with the present thesis has been given. The literature review includes four primary aspects, consisting of the fundamental knowledge of chemical kinetics mechanism, the introduction of mechanism reduction methods and the methods of reduced mechanism validation; the background of ammonia as a fuel, including the review for the application of ammonia in engines, the introduction of the ammonia combustion in gas turbines and the ammonia cracking, and the review of ammonia chemical kinetics mechanism development; the introduction of the general optical diagnostic, and flame chemiluminescence; the general concept of hydrocarbon combustion, the brief definition of premixed flame, equivalence ratio and the laminar flame speed. This chapter concentrates on the elementary knowledge of the present thesis, more details will be given in the introduction part of corresponding chapters.

In Chapter 3, the basic numerical methods are developed and presented as results. The theories of DRGEP, IPFA and GEPA methods are introduced in the first section. As well, the

validation model for reduced mechanism is discussed in the second section. The third section introduces the CRN model including the fundamentals, the components of CRN models in singe and two staged gas turbine combustion, and the validation of the CRN model. At the end of this Chapter, for simulating the flame chemiluminescence, the chemiluminescence reaction mechanism of OH*, CH* and C_2* and the theory of chemiluminescent intensity calculation are introduced. And the validation of the chemiluminescent intensity modelling of excited state species is provided.

In Chapter 4, reduced reaction mechanisms for ethanol and $NH_3/H_2/CH_4$ mixtures are developed. In detail, the DRGEP combined with GEPA method and an integrating method of IPFA and GEPA are employed to reduce ethanol and $NH_3/H_2/CH_4$ mechanisms respectively, including the error analysis and the reduction process for both methods. Besides, the validations of ignition delay time, species profiles and laminar flame speed for the reduced mechanisms of ethanol and $NH_3/H_2/CH_4$ mechanisms are performed separately under numerous conditions.

In Chapter 5, it is mainly to investigate the combustion and NO_X emission characteristics of partially cracked ammonia in gas turbines. The effect of cracking ratio, equivalence ratio and initial pressure on the NOX emissions and laminar flame velocity (LBV) are numerically discussed separately from the aspect of kinetics mechanism. Moreover, a reaction pathways flux method is performed to present NO reaction pathways of practically cracked ammonia at virous operating parameters. In addition, important species and reactions of NO formation/reduction are analysed for getting low levels of NO_X emissions.

In Chapter 6, numerically analysing on the equivalence ratio and heat release rate

determination by using common excited state species (OH*, CH* and C_2*) chemiluminescence profiles is investigated in one-dimensional laminar premixed ethanol flame. The ability of flame chemiluminescence as a sensor of heat release rate at various equivalence ratio is discussed by combining rate of production analysis and sensitivity analysis. Moreover, the correlations between the ratio of C_2*/CH* and the equivalence ratio are investigated in hydrocarbon premixed flames based on chemical reaction kinetics mechanisms. At the end of the chapter, the phenomenon where the peak chemiluminescence intensity ratio of C_2*/CH* increases almost linearly following by a descending trend when the local equivalence ratio rises is demonstrated from the chemical mechanisms' aspect for the first time.

In Chapter 7, the main conclusions and contributions of the present thesis are listed. At the end of this chapter, some suggestions of future works are presented.

2. Basic Background Knowledge

2.1. Introduction

The basic background knowledge of the present thesis is introduced in this chapter which contains four main parts. The first section provides the background knowledge of chemical kinetics mechanism, the methods of mechanism reduction and validation, including the definition of ignition delay time as well as laminar burning velocity. The second part is the background of ammonia combustion. The properties and the applications of ammonia in engines and gas turbines are introduced. Then, studies related with ammonia cracking are reviewed. Moreover, the development of ammonia chemical kinetics mechanism is concluded for further study. The third section introduced the background of optical diagnostic methods that consists of laser diagnostic and chemiluminescence. In addition, the application and mechanism of excited state species for flame chemiluminescence are reviewed separately. The last part of this chapter is general concept of hydrocarbon combustion including of premixed flame and laminar flame speed. Literature review in this chapter covers basic background knowledge of this study, more details of this filed will be discussed in its relative chapter.

2.2. Chemical Kinetics Mechanism Reduction

2.2.1. Introduction

Chemical kinetic mechanisms for combustion area have been developed rapidly in recent years [30-36]. It is notable that chemical kinetic mechanisms can be applied for descriptions of combustion processes at the level of elementary chemical steps occurring, based on their

individual rate parameters. Various specific applications are targeted by different mechanisms. For chemical kinetic mechanisms establishment, they have common in the principle, in which the elementary rate parameters are consistent with fundamental rate computations and measurements.

A chemical kinetic mechanism consists of two parts: (i) species with related transport and thermodynamic properties; (ii) elementary chemical reactions with related rate constants [37]. For example, the hydrogen oxidation is described applying the global reaction $2H_2+O_2=2H_2O$. However, this reaction does not occur as above in reality. The description of hydrogen oxidation over a broad range of pressures and temperatures requires eight species and around 30 elementary reactions [38,39], which are more complicated. In an elementary reaction, the reactant and product species as well as the related rate constant are specified. Here, the elementary (reversible or irreversible) reactions as follows are taken as an example:

$$\mathrm{A} \leftrightarrow \mathrm{B}. \tag{2.1}$$

If the reaction goes forward (i.e., from left to right), the species A is reactant, the species B represents product. Otherwise, species B is reactant, and species A is product. Accordingly, the forward and reverse rates can be written as k_f[A] and k_r[B], where [A] and [B] are the molar concentration of species A and B, k_f and k_r are the forward and backward rate constants, respectively. The expressions for k_f and k_r are given in the modified Arrhenius form [40,41]:

$$k = AT^n e^{-Ea/RT}, \tag{2.2}$$

where *A* represents the pre-exponential factor, *n* is the exponent of the absolute temperature *T*(K), *Ea* is the apparent activation energy (cal/mol), *R* is the gas constant (cal/(mol K)). When at the equilibrium state, both forward and backward rates are equal. Hence, based on the

known forward rate constant as well as the thermochemical parameters of the reactant and product species, the reverse rate constant can be possibly obtained under the thermodynamic equilibrium condition [42].

2.2.2. Background knowledge of mechanism reduction

Due to the great importance of different elementary steps in various applications, the wider the scope of applications is addressed, the larger size are displayed for chemical kinetic mechanisms. Therefore, some detailed chemical kinetic mechanisms include thousands of elementary reactions and hundreds of chemical species, seen in Figure 2.1, which present strong challenges to researchers in combustion area.

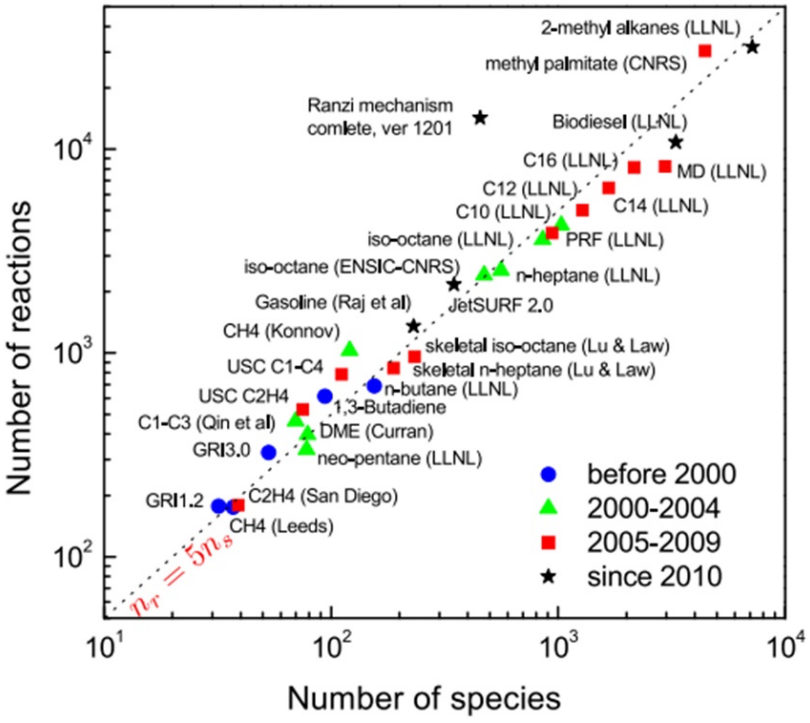

Figure 2.1 Size of detailed chemical kinetics for various fuel [43].

Reduced kinetic mechanisms, which contain much fewer numbers of species and elementary reactions compared with the detailed mechanisms, can reproduce the associated physical phenomena satisfactorily under a wide range of targeted situations [44,45,46]. Besides, three-

dimensional and large-scale combustion modelling with detailed kinetic mechanisms needs comparatively huge calculational costs in terms of computation time and memory [47]. Furthermore, the application of detailed kinetic mechanisms is limited since large inconsistencies in timescale for variation of different species leading to the problem of stiffness [43]. Therefore, considering the disadvantages of using the detailed mechanisms for numerical simulations, there is an imperious demand of reduced kinetic mechanisms. The reduced models should be accurate, relatively compact and robust. More importantly, it needs to be beneficial for decreasing computational time for CFD simulation.

2.2.3. Mechanism reduction methods

In recent days, the research topics of chemical mechanism reduction have attracted more attention. As a result, various methods have been proposed to generate reduced chemical kinetic mechanisms, which can generally be categorised into four aspects: (i) solution mapping methods; (ii) timescale analysis methods; (iii) lumping methods; (iv) species and reaction removement methods [48]. These methods are elaborated in the following paragraphs.

(i) Solution mapping methods employ stored solutions to replace the differential equations embedding mass-action kinetics [49]. Therefore, the mechanistic details are totally lost. The solution mapping methods include (a) parameterization based on orthonormal polynomials [50], (b) piecewise reusable implementation of solution mapping [51], and (c) *in situ* adaptive tabulation (ISAT) [52,53]. In the ISAT, when the simulation is performed *in situ*, the chemical source term is integrated, and the essential information is stored using binary tree data structures [52,53]. However, the disadvantages of these methods are unavoidable, since for a combustion including large mechanisms covering a broad range of temperature and

concentration gradient distributions, the difficulties in data retrieval and large time consumption need to be considered carefully [54].

(ii) Timescale analysis methods are applied to reduce detailed mechanisms, which are based on the decomposition of movement into slow and fast in the phase space [55]. In this type of approach, the concentrations related with species with fast timescales are expressed as functions of those associated with slow subsystems. Two typical approaches employing this view are partial equilibrium assumption (PEA) [56] and quasi steady state approximation (QSSA) [57,58]. The PEA can eliminate fast timescales from the problem and leads to a reduction in the number of independent thermodynamic variables [56]. The QSSA is based on recognizing species reacting on comparably fast timescales and thus equilibrate in comparison with slower species locally [57,58]. Besides, from the point view of the dynamical systems and according to Jacobian analysis, the intrinsic low dimensional manifold (ILDM) [59] and computational singular perturbation (CSP) [60-63] methods are proposed for mechanisms reduction. In the ILDM method, the local timescales in the composition space are recognized by the eigenvector analysis of the governing equations in a homogeneous system. The state properties are determined automatically as functions of coordinates related to the freedom degrees [59]. In the CSP method, the time dependency of the Jacobian matrix is fully considered. Meanwhile, the fast modes can be identified accurately [60-63]. However, the disadvantages of above methods are obvious, i.e., the refinement procedure for conducting time-dependent Jacobian analysis requires a large amount of calculation time.

(iii) As the name suggests, lumping methods use lumped species and reactions to replace species and reactions which have similarities in chemical or physical properties [58,64,65]. In

this category, constrained nonlinear lumping [66], unconstrained nonlinear lumping [65] as well as reaction lumping applying QSSA methods [58] are proposed. In the constrained and unconstrained nonlinear lumping methods, reduced differential equation systems with higher dimensional constrained and unconstrained nonlinear lumping schemes, respectively, are given to describe new variables, that are nonlinearly associated with the original ones [65,66]. In the reaction lumping applying QSSA method, reaction lumping with QSSA is employed to obtain a reduced mechanism in standard kinetic form involving new lumping reaction rate coefficients but results in elimination of QSS species increasing computational overhead [58]. The shortcomings of the lumping methods are that low-order approximation is introduced to develop the reduced mechanisms, which leads to uncertainties relevant to kinetic data [67].

(iv) Generally, the detailed mechanisms need to be made as robust and accurate as possible. Therefore, detailed mechanisms probably contain all the elementary reactions, which are significant under a wide range of conditions, but may not be necessary in certain specific conditions. As a result, a great number of unimportant species and redundant elementary reactions can be removed, when detailed mechanisms are applied in some specific problems. This is the basic idea behind the species and reaction elimination methods. The insignificant species can be eliminated by, for instance, (a) necessity analysis (NA) [68], (b) the connectivity method (CM) [69], and simulation error minimization CM (SEM-CM) [70], (c) directed relation graph (DRG) [7175], DRG aided sensitivity analysis (DRGASA) [76], DRG with error propagation (DRGEP) [77,78], and DRGEP with sensitivity analysis (DRGEPSA) [79], (d) path flux analysis (PFA) [80], and improved path flux analysis (IPFA) [81]. In the NA, each species is given a necessity value corresponding to the combination of atoms flow between species, which is

used for identification of important species [68]. In the CM, strongly connected sets of species, identified based on normalization, are added into the reduced mechanisms [69,70].

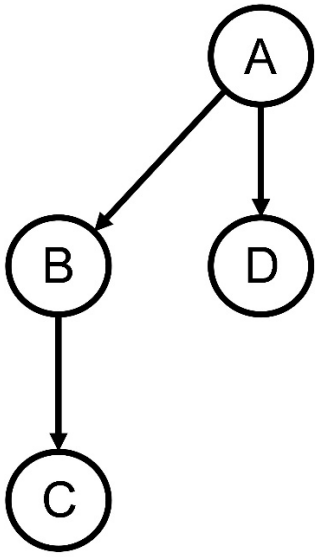

Figure 2.2 A directed relation graph presenting relations of each species.

As for the DRG and its derived methods, the net reaction flux across multi generations is used to generate a directed relation graph whose nodes are the species (as shown in Figure 2.2). The strength of the directed edge linking one species to another species is defined as the direct interaction coefficient (DIC) and used to identify the important species. The link with lower strength (i.e., smaller DIC) will not be considered (i.e., the unimportant species is removed) [71,76,77,79]. In the PFA and its improved version, instead of employing net reaction fluxes, the production and consumption fluxes are used separately to seek significant reaction pathways. According to this type of operation, the drawbacks of the DRG methods can be overcome [80,81]. As for elimination of reactions having minimal effects on mechanisms, the following methods can be employed: (a) principal component analysis (PCA) [82,83], the functional PCA method (FPCA) [84], and PCA of rate-sensitivity matrix [85], (b) sensitivity analysis (SA) [69,86,87,88], (c) species production and heat rate analysis [89], (d)

entropy production analysis (EPA) [42], and generalized entropy production analysis (GEPA) [90]. In the PCA and its extended methods, the eigenvalue-eigenvector analysis is conducted to reveal the parts of the detailed mechanism containing strongly interacting reactions [82,84,85]. In the SA, the reactions with those parameters which can lead to large uncertainties need to be retained. The parameters include activation energies, rate constants, transport coefficients and thermodynamic constants. The SA, which can give aid to further mechanism reduction, is normally combined with other elimination methods [69,86,87,88]. In the species production and heat rate analysis, the reduction is on the basis of testing the production rate of the reactions and contributions of the reactions to the heat release [89]. Compared to the methods introduced to eliminate redundant reactions, the EPA and its general version are much easier to implement and have attracted more attention. The contribution of the reactions to the total entropy production is identified as an index to eliminate unimportant reactions. The calculation of the local contribution of the reactions is based on the reaction rates and thermodynamic properties of species [42].

2.2.4. Mechanism validation methods

A large number of fundamental studies have been performed to have better understandings of the combustion characteristics of fuels. The investigations involve the ignition delay [2,36,91-107], speciation [35,42,80,108-121], and flame propagation [44,45,122-130]. Those data can serve as validation targets for the reduced kinetic mechanisms. In detail, the validation for the ignition delay time, mole fraction of species as well as laminar burning velocity which are the three most significant combustion characteristics, are reviewed in the following paragraphs.

(i) Ignition delay time.

Validation using Ignition delay time of fuels can be traced back to the 1960s [96,98]. Since then, a couple of studies have been conducted in shock tubes at different temperatures and pressures to validate chemical kinetic mechanisms of fuel oxidation [93,94,95,97]. Among these studies, Drummond et al. employed ignition delay times measurement to validate their proposed mechanisms at higher pressures [93]. The high-pressure results of their work results in troubles for the model validation. Therefore, a great many new experimental work for ignition delay times have been reported in recent years [2,36,91,99-102,104,106]. Mathieu et al. validated their reduced mechanisms of fuel mixtures applying measured ignition delay times in a shock-tube experiment, covering temperatures of 1560-2455 K and pressures (1.4, 11, 30 atm). The fuel mixtures were highly diluted by Ar with different equivalence ratios [102]. Considering operating conditions of modern transport systems, Shu et al. broadened the range of measured ignition delay times to pressures of 20 and 40 atm and validated their reduced kinetic mechanisms, employing undiluted fuel/air mixtures at different equivalence ratios in a shock tube [101]. Pochet et al. performed validation of their proposed reduced model with measured ignition delay times of lean fuel mixtures, which are at low temperature of 1000-1100 K and high pressures of 43 and 65 atm in a rapid compression machine [100]. Further, He et al. validated their reduced kinetic mechanism with extension of the ignition delay times measurement at low temperatures of 950-1150 K, pressures of 20, 40, 60 atm, applying diluted fuel/oxygen mixtures in a rapid compression machine [36]. Most recently, Dai et al. conducted ignition delay times measurement for diluted fuel/oxygen mixtures in a rapid compression machine. In their work, they further extended the pressure range, i.e., 20-70 atm

[104,105] and validated their models.

(ii) Mole fraction of species.

Validating the reduced kinetic mechanism with the mole fraction of species started in the 1960s [108,114]. Later, Dean et al. measured the mole fraction of species at different distances from the burner and performed validations on their reduced models, however in their studies, the temperatures and the pressures were not given in detail [117,118,119]. To cover a broad range of operating operations, a few studies have been conducted. Sun and Gou's group reduced the chemical kinetic mechanisms of the fuel/air mixtures, the mole fractions of species were measured at the temperatures of 400-2400 K and the pressures of 1-20atm in a flow reactor [80,81,131]. Perini et al. validated their reduced mechanism of fuel mixtures using the measurement of mole fractions of species in a flow reactor. The parameters are the temperatures ranging 750-1500 K and the pressures ranging 2-20 atm [132]. Kooshkbaghi et al. performed reduction for detailed kinetic mechanisms of fuel mixtures and validated their model on the experimental data of mole fractions of species in a jet-stirred reactor. The perfectly stirred reactor (PSR) module in the CHEMKIN-PRO package is used to simulate the JSR. The model predictions may be considered accurately in the following two cases:

(a) the model curve fits with the experimental data very well;

(b) the predicted maximum species mole fraction is within a factor of 2-3 of the experimental data.

The ranges of temperatures and pressures are 600-2400 K and 1-20 atm, respectively [42]. Duynslaegher et al. proposed an improved ammonia mechanism and validated the mole fractions of species measured in jet-stirred reactor experiment. The operating conditions

cover the low pressures of 0.06-0.12 atm [120]. Xiao et al. [121] conducted validation for their reduced model with measured mole fractions of species in the jet-stirred reactor experiment of Tian et al., where the temperatures range from 1250-2100 K and the pressure is low at 0.04 atm [113].

(iii) Laminar burning velocity.

Validation based on laminar burning velocity (flame speed) of fuel mixtures began in the 1950s, where the measurements were performed in combustors and the laminar burning velocities were calculated by the Bunsen flame area approach [122-125]. In the 1970s to 1990s, Zakaznov's and Ronney's groups validated their reduced models with measured laminar burning velocities in lean and rich fuel mixtures at pressures of 0.6-2 atm [126,127]. Nowadays, the validation using laminar burning velocity measurement and modelling has attracted more attention. Okafor et al. developed a reduced mechanism for fuel/air mixtures at pressures ranging from 1 to 5 atm. In their work, their also optimized their reduced model against the measurements and data of laminar burning velocities in their experiments [44]. Cazeres et al. validated their developed reduced mechanisms of fuel mixtures based on the laminar burning velocity measurement. In their study, the measurement is conducted under the atmosphere condition [45]. Xi et al. validated their proposed reduce model with the experimental data of laminar burning velocities at the temperatures of 360-470 K and the atmospheric pressure [130]. Luo et al. proposed a reduced mechanism for fuel mixtures and then optimized it based on the validation of the experimental laminar burning velocity. The measurement is performed at the temperatures higher than 1000 K and the pressures of 1-10 atm [129]. Considering the extension of measurement range, Li et al. developed a reduced chemical

model for comprehensive prediction of fuel mixtures combustion, with the validations of laminar burning velocity measurement in the experiments. The operating conditions cover the temperatures of 1000-2000 K and pressures of 1-50 atm [128].

2.3. Background of Ammonia Combustion

2.3.1. Introduction

Owing to the great contribution to global warming, carbon dioxide emissions from fossil fuels have been regarded as a major threat to climate change. In order to achieve the target of reduction in greenhouse gas (GHG) emissions, it is significant to explore renewable energy sources for human and industrial activities. Renewable energy sources, for example, wind, solar and tidal power, are performing an increasingly important role in reducing CO_2. However, the increasing penetration of intermittent renewable energy leads to fluctuations in energy production, which brings new challenges of the development of energy storage technology. Also, high cost is required for obtaining energy from these stationary facilities. In order to mitigate their fluctuating nature in energy production, electrical, mechanical, chemical and thermal methods have been proposed to store electrical energy. However, storage solutions such as lithium batteries cannot supply energy storage with required capacity on the scale of the grid [133,134]. Pumped storage and compressed air storage methods are subject to the geological constraints. Only chemical storage methods can allow the storage of grid-scale energy anywhere for a long time [135,136,137]. Therefore, the advantage of chemical storage for allowing long-term storage anywhere makes it as an effective option for low-carbon storage.

Hydrogen, natural gas, alcohols and ammonia, as low or zero carbon fuels were proposed to alleviate the energy shortage crisis [1]. Considering high carbon content of part alternatives, such as biomass, natural gas, alcohols, etc., hydrogen energy as an efficient and clean energy carrier has received extensive attention and in-depth research in the past few decades. Hydrogen has many merits as a fuel, such as wide flammability limits, minimum ignition energy, and the high heating value [138].

However, utilization of hydrogen fuel brings a series of safety, storage and transportation problems due to its physical and chemical properties [139-143]:

(1) Hydrogen has the smallest molecular size; thus it is difficult to seal in storage.

(2) Hydrogen has an extremely wide flammability limits and high laminar flame velocity, which is very easy to explode during storage and transportation.

(3) The flame of hydrogen is difficult to detect and control due to its weak flame radiation [144].

(4) High costs are required to compress hydrogen in liquid.

(5) Hydrogen is colourless and its diffusion rate is extremely fast. Once a leak occurs, it is difficult to detect and is prone to spontaneous combustion in the environment.

Considering the challenges mentioned above, ammonia as one of a new zero-carbon hydrogen storage alternatives has emerged [33]. In 1996, Lovegrove et al. carried out experimental research of ammonia dissociation for solar energy storage and transport. The experiment was operated using an open-loop configuration with a high-pressure ammonia dissociation [145]. Hereafter, their group performed experiment for solar-driven ammonia-based loop closing thermochemical energy storage system [146]. In addition, ammonia dissociation experiments

have been conducted successfully by other groups [147]. Accordingly, ammonia is widely used to offer energy storage and transport to solar thermal power generation.

Same as synthesised hydrogen, NH_3 can be obtained from organic wastes, traditionary fossil fuels or other renewable sources including photovoltaics and wind. Ammonia (NH_3) has more obvious advantages as an energy carrier medium especially compared with hydrogen [148,149,150,151]:

(1) Ammonia is carbon-free, and it only produce water and nitrogen when completely burned.

(2) Ammonia can easily be liquefied under low pressure and the liquefaction temperature of ammonia is -33 ℃, which is easy to store and transport.

(3) Large-scale industrial production of ammonia is relatively mature, such as making synthetic ammonia by coal gasification, or making ammonia by methane by Haber-Bosch method [152], because it only contains N and H elements, it is highly possible for ammonia to be made directly by synthesizing air and water with solar energy in the future.

(4) Laminar flame velocity of ammonia combustion is low [8] and combustion range is narrow [6], so it is not easy explode compared to hydrogen.

(5) The energy density per unit volume of liquid ammonia is more than 1.5 times that of liquid hydrogen, which is equivalent to that of gasoline. Therefore, ammonia gas has the potential to be used as a fuel needed for transportation.

2.3.2. Ammonia as a fuel

Ammonia is known as a promising carbon free fuel with a compound of nitrogen and hydrogen.

Only water (H_2O) and nitrogen gas (N_2) are released when ammonia is completely oxidized according to the reaction (2.3). The enthalpy of NH_3 combustion is 317 kJ/mol at standard conditions (25 ℃, 1 atm) [153]. Therefore, ammonia can be considered as an environmentally friendly and clean fuel when properly treated.

$$4NH_3 + 3O_2 \rightarrow 2N_2 + 6H_2O \qquad (1270\ kJ/mol). \qquad (2.3)$$

In early years, most of the ammonia produced has widely been applied into the agriculture systems as a fertilizer and refrigeration systems as a refrigerant [149]. Only a small portion of ammonia is directly used in industrial applications as a chemical. Recently, energy shortage and environmental concerns stimulate ammonia utilization in the energy sector. Many attempts are devoted into using ammonia for power generation and internal combustion engines, etc.

(i) Properties of Ammonia.

Ammonia can be synthesized directly from nitrogen and hydrogen through a spontaneous exothermic reaction. There are no precursors and by-products in this progress. Noted that N_2 is non-activated owing to its strong triple bond, non-polarity and low proton affinity. In nature, enzymes and abiotics in soil and sand produce a small amount of NH_3 through fixing nitrogen. However, naturally produced NH_3 is far from sufficient to meet current and future NH_3 needs (such as fertilizer and fuel) [27]. NH_3 is mainly produced in industrial processes based on the ancient Haber-Bosch process. Optimized for more than 100 years, the Haber-Bosch process enables NH_3 production efficiencies of more than 95% (achieved through multiple cycles of unreacted gas). The nitrogen used in the current Haber-Bosch process is derived from separation of air, while the hydrogen is derived from a typical steam methane reforming

process. During the reforming process to produce hydrogen, a large amount of carbon dioxide as a by-product also can be produced, which is estimated to result in 289.8 million tons of CO_2 emissions worldwide from ammonia production. Moreover, Haber-Bosch is an energy-intensive process requiring high temperature and pressure to separate impurities such as CO_2 from natural gas reforming and prevent poisoning of part catalysts. As the low-carbon economy becomes more popular in the world, alternatives and modifications to the Haber-Bosch process are worth exploring to reduce energy costs and greenhouse gas emissions.

Ammonia as a fuel, its physical and chemical properties also have a good performance.

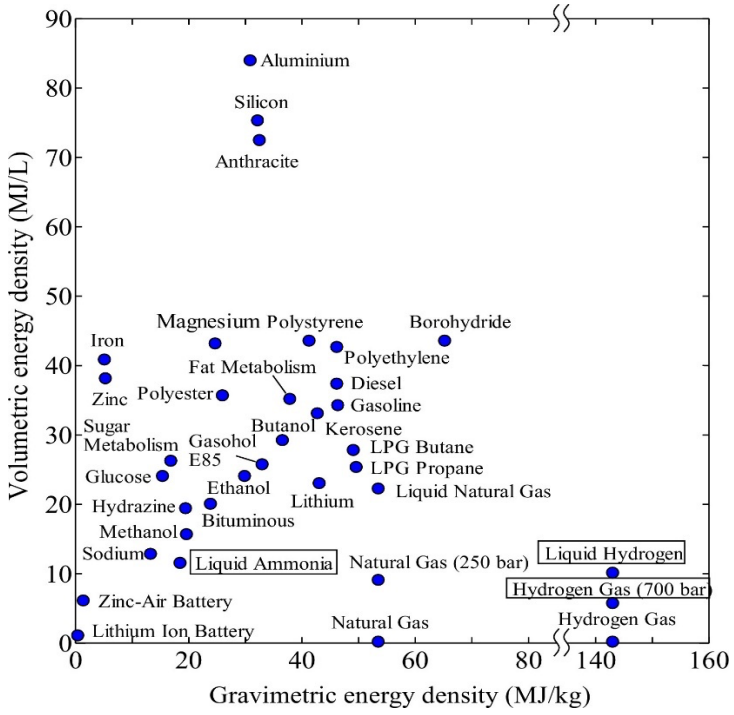

Figure 2.3 Volumetric and gravimetric energy density of a variety of combustible batteries and materials from [12].

As shown in Figure 2.3, the volumetric energy density of liquid ammonia (20℃, 0.7MPa) is between gas fuel and solid-liquid fuel. Also, high H content property enables its gravimetric energy density to show a good performance. The energy density of liquid ammonia is similar to that of lignite, and its gravimetric and volume energy density are about 1/3 of that of

gasoline. At the same time, the energy density of NH_3 is almost 3 times higher than that of hydrogen stored at similar pressures. The quality of higher volumetric energy density of liquid ammonia makes it more attractive than liquid hydrogen and batteries in the aspect of energy storage and transport.

Table 2.1 Fundamental combustion characteristic of hydrocarbon and ammonia fuels [12].

Properties	NH_3	H_2	CH_4	C_3H_8
Boiling temperature at 1atm (°C)	−33.4	-253	-161	-42.1
Condensation pressure at 25°C (atm)	9.90	N/A	N/A	9.40
Lower heating value, LHV (MJ/kg)	18.6	120	50.0	46.4
Flammability limit (Equivalence ratio)	0.63-1.40	0.10-7.1	0.50-1.7	0.51-2.5
Adiabatic flame temperature (°C)	1800	2110	1950	2000
Maximum laminar burning velocity (m/s)	0.07	2.91	0.37	0.43
Minimum auto ignition temperature (°C)	650	520	630	450

In addition, liquid ammonia has a high-octane number (around 130) and can be used in high pressure internal combustion engines with a high combustion quality. Table 2.1 shows fundamental combustion characteristics of hydrocarbon and ammonia fuels [12]. It is shown that ammonia requires very low temperature, the liquefaction temperature of ammonia is 33.4 ℃ at 1 atm [12]. Moreover, the condensation pressure and boiling temperature of ammonia are nearly identical to that of propane.

However, the application of ammonia as a fuel has its disadvantages compared with traditional hydrocarbon fuels. In general, there are some problems in the combustion of

ammonia as an energy storage material. One is the low laminar burning velocity caused by the poor reactivity of ammonia, which makes it more difficult to design and manufacture ammonia utilization equipment. Furthermore, part of nitrogen oxides and unburned ammonia will be produced in the process of ammonia oxidation, which will affect the atmospheric environment and biological safety respectively. Besides, high ignition temperature and narrow flammability range for NH_3/air mixture are accounting for low flammability of ammonia.

(ii) Ammonia as an effective hydrogen storage.

Hydrogen is one of the most widely concerned energy storage carriers because it does not generate greenhouse gases during utilization. Hydrogen has the higher mass energy density (120 MJ/kg) than other traditional fuels such as gasoline (44 MJ/kg), shown in Figure 2.3. The production of H_2 can be conducted by a variety of techniques, including thermochemical route (gasification, modification), biochemical route (fermentation) and electrolysis [16]. Hydrogen can also be used in a variety of ways, including battery packs and direct combustion. However, the volume energy density of H_2 is only 0.01 MJ/L at room temperature and pressure, making it difficult to store. To effectively store hydrogen, various hydrogen storage technologies have been proposed, including high-pressure gaseous hydrogen storage, liquid hydrogen storage, organic liquid hydrogen storage [17], metal hydrogen storage [18], synthetic methanol (CH_3OH), ammonia (NH_3) and other chemical hydrogen storage.

Using high-pressure storage is the simplest method for hydrogen storage. Due to the low hydrogen density, this method requires a high pressure (density of 42.2 kg /m^3 at 69 MPa). For hydrogen vehicles, a high-pressure container of about 70 MPa is currently required to store hydrogen. In addition, as hydrogen is a very small and light element, the possibility

leakage at high pressures should be considered during storage and transportation.

Liquid hydrogen storage is also considered as an efficient and promising hydrogen storage option. It has a high density about 800 times that of hydrogen under uncompressed standard conditions. However, to introduce hydrogen into the liquid phase, hydrogen needs to be refrigerated to a low temperature (-252.8 ℃). Besides, liquid hydrogen is also not conducive to long-term storage or transportation over long distances because of cooling requirements.

Solid state hydrogen storage is mainly though physical adsorption or chemical adsorption [20]. Physical adsorption technologies use a range of materials including activated carbon, carbon nanotubes, zeolite, and metal-organic frameworks (MOF), which have low hydrogen storage efficiency (less than 5wt% at room temperature) and greater demand for low temperatures [21]. In chemisorption, hydrogen reacts with solids to produce hydrides. Many complicated hydrides have been developed, such as $NaAlH_4$, $Mg(NH_3)_2$-LiH, etc. Although these materials have a high hydrogen density (up to 10 wt%), their dehydrogenation and hydrogenation are very complicated and relatively reversible [22]. The process of dehydrogenation is usually an endothermic process, leading to a reduction in energy efficiency.

Therefore, it is concluded that conventional hydrogen storage has technical difficulties such as low volume energy density, difficult storage and processing. Another non-trivial issue is that hydrogen can permeate many materials due to its high diffusivity, and the risk of leakage for hydrogen is high. Long-term storage of hydrogen using traditional methods is more expensive than employing other alternative fuels. A more popular option is to store hydrogen in more stable compounds.

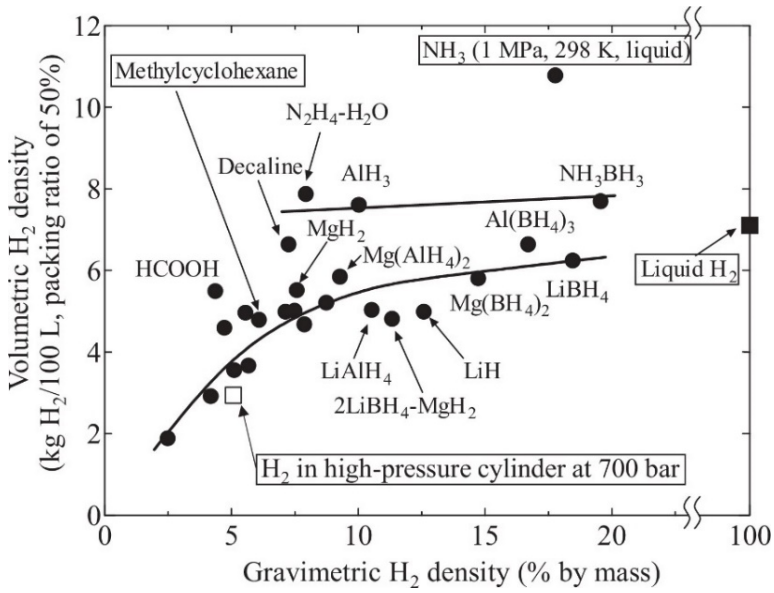

Figure 2.4 Volumetric and gravimetric H_2 density of hydrogen carriers from [154].

Figure 2.4 presents the volumetric and gravimetric hydrogen densities for various hydrogen carriers [154]. It shows that ammonia is more advantageous in storing hydrogen for all candidates, due to its high hydrogen density (17.8wt %). Nitrogen in atmospheric can be separated at a lower price than CO_2. So, it is economical to combine with renewable hydrogen to produce ammonia. Unlike hydrogen, ammonia is more easily stored and transported. Ammonia is now widely employed as agricultural fertilizer and refrigerant gas, and a large amount of ammonia gas is also used as raw material for the manufacture of explosives, pesticides and other chemicals. Infrastructure for the production, storage, transport and utilization of ammonia has been established globally. Due to its long-term stability in transportation and storage, ammonia can also meet the demand for real-time storage of energy and energy import and export [26]. Therefore, ammonia is a kind of high-quality hydrogen storage carrier, showing great potential as a fuel in combustion system.

2.3.3. Application of ammonia for engines

The ammonia for engines applications goes back as far as the times of World War two. During

this period, it is widely looking for alternative fuels for public transport drown by the shortage of fossil fuels in some areas. Ammonia with high octane (around 130) was used in engines, this enables engine to have efficient operation under condition of higher compression ratio (CR) [155]. Ammonia has relatively lower energy density compared with diesel and gasoline, but its energy density is larger than that of liquid hydrogen and compressed natural gas. Basic characteristics of ammonia and traditional fuels are shown in Table 2.2 [5].

Table 2.2 Comparations of the fuel properties for ammonia against hydrocarbon fuels [5].

Properties	Units	Ammonia	Natural gas	Gasoline	Diesel
Storage method		Compressed Liquid	Compressed Liquid	Liquid	Liquid
Storage temperature	K	298	298	298	298
Storage pressure	kPa	1030	24,821	101.3	101.3
Autoignition temperature	K	924	723	573	503
Flammability limits (gas in air)	Vol.%	16–25	5–15	1.4–7.6	0.6–7.5
Absolute minimum ignition energy	MJ	8	–	0.14	–
Fuel density	kg/m^3	602.8	187.2	698.3	838.8
Energy density	MJ/m^3	11,333	7132	31,074	36,403
Octane rating	RON	110	107	90–98	–

Despite this early start, research into ammonia-fuelled IC engines and spark-ignition engines was limited until recent decades. Johnsson et al. [156] reported that narrow flammability limits and low flame speed properties is likely to limit ammonia combustion in spark internal (SI) engines. In 1968, Starkman et al. [157] studied application of ammonia in spark ignition engines and found that it was successful in the case ammonia was regarded as vapour and first decomposed into hydrogen and nitrogen. Since then, studies on ammonia application in internal combustion engines have been reported in literature [158,159,160,161].

In the past decades, ammonia has enjoyed renewed interest because of the urgent for decarbonizing the global economy. Due to its carbon-free property and simplicity to be stored and transported, ammonia was paid more attention to decrease fossil fuel consumption as well as greenhouse gas emissions. Stefano Frigo et al. [162] carried out an experiment to analyse the performance of a 4-stroke SI engine which uses ammonia and hydrogen as burning substance. The results show that ammonia is directly used as a fuel for an internal combustion engine, but an accelerant is required to accelerate combustion. Also, hydrogen is a good promoter to speed up the ammonia flame velocity. Considering ammonia high latent of heat, direct injection was proposed to reduce in-cylinder temperature [163]. It is noticed that ammonia is better operated under lower engine speeds because of its low flame velocity in internal combustion engines [164]. Koike et al. [165] pointed out that an auto-thermal-cracker helps the engine fuelled with ammonia to run stably. In addition, large number of studies were reported the combustion of ammonia in compression ignition engines [166,167], which gives insight of ammonia application for marine and power generation [151,168,169].

2.3.4. Ammonia combustion in gas turbines

Because of the low flame velocity of NH_3 flame, the combustion stability and efficiency are obvious lower than that of methane. One possible way to promote ammonia combustion is to generate turbulence in the combustion chamber, which is helpful to accelerate mixtures mixing. It has been shown that strong swirling currents using CH_4/NH_3 and H_2/NH_3 mixtures can stabilize the flame with low emissions. However, proper swirl number has great effect on combustion performance. Since when swirl number is too high, it can affect combustion negatively by blowing the flame out. Because of the higher minimum ignition energy and slower flame speed of ammonia than that of conventional hydrocarbon fuels, more results reported that it is potential to enhance ammonia combustion with cofiring with more reactive fuels [33,170]. Xiao et al. [171] established an ammonia/hydrogen combustion model of gas turbine combustor by employing large eddy simulation. Iowa State University [172] have developed a system with a flame holder that enable to produce stable swirl flame and improve the combustion process. Usually, the Perfectly Stirred Reactor (PSR) is adopted to simulate a swirling flame including the premixing, circulation and flame zone, followed by a Plug Flow Reactor (PFR) that represents a post-flame zone. In a PSR, reactants as well as products are assumed to be instantly mixed and there exist no variation of temperature or composition in the reactor.

The other main challenge of ammonia combustion in gas turbines is high NO_X emission. Experimental studies show that rich fuel condition is beneficial to reduce NO_X emissions in laminar premixed ammonia flame [15,16,173]. Iki et al. [174] studied the NO_X emissions in microturbines, results shown that the NO_X can be reduced by 50% in rich-lean combustor

when ammonia cofiring with methane. Li et al. [175] numerically demonstrated that NO_X emissions can reach to 30 ppm when ammonia cofiring with 60% CH_4 volumetric ratio in 2 stage combustor. A number of research also confirmed that NO_X production is significantly influenced by rich/lean conditions in turbulent NH_3/air swirling flames [12,19,176].

2.3.5. Ammonia cracking

Other effective methods were proposed to enhance ammonia combustion flame, in which ammonia cracking should be noticed. Since hydrogen can be directly cracked from ammonia, which is an energy carrier and has the potential to be applied as a fuel.

Gill et al. [177] initially evaluated the carbon-based emissions in a dual-fuel diesel engine that is fuelled with cracked ammonia (a mixture of a tiny amount of NH_3, H_2, and N_2). Result shows that disassociated ammonia provides better performance with lower brake thermal efficiency than ammonia under condition of higher loads. Frigo and Gentili [178,179] analysed the performance of a hybrid electric vehicle using ammonia/hydrogen as fuel. The hydrogen was produced by ammonia thermal cracking. In addition, research by Pratt [180] and Verkamp et al. [181] presented that ammonia partially cracking into H_2 as well as NH radical is beneficial for flame stability and low NO_X emission. However, as highlighted by Comotti and Frigo [159], the higher overall NO_X emission is displayed in a dissociated ammonia flame for a four-stroke twin-cylinder spark. This is mainly caused by high pressure and temperature in cylinder due to faster flame speed in engine.

Usually, ammonia cracking is performed at elevated temperatures, pressures, and catalyst addition conditions to reach high NH_3 conversion efficiency [27]. At temperatures lower than 698K, catalytic cracking of ammonia into H_2 and N_2 can reach 98–99% efficiency. When the

temperature is above 773K, NH_3 decomposition can be conveniently reached without catalysts by thermal cracking [182,183]. Besides, as similar molecular sizes and quadrupole moments of H_2 and N_2 and relatively low Knudsen selectivity of H_2 and N_2, separating H_2 from cracked nitrogen is technically difficult [184]. This is also the reason that direct usage of NH_3 as a fuel rather than a hydrogen carrier should become the more attractive choice.

Limited publications have been reported to discuss ammonia cracking combustion characteristics in gas turbines. Mei et al. [184] focused on laminar flame propagation of partially cracked NH_3/air mixtures. Also, they clarified that NO formation shows a dramatic non-monotonic behaviour with increasing of cracking ratio. Alboshmina et al. [185] developed a novel cracker system that is expectable to mitigate NO_X emissions for using ammonia as a fuel.

2.3.6. Chemical kinetics mechanism of ammonia

To better understand the ammonia combustion process in engines by numerical simulation, detailed kinetic mechanisms for ammonia oxidation are required. A great many previous investigations have focused on the development of NH_3 detailed chemical mechanisms. Mathieu and Petersen [102] performed a Shock Tube (ST) experiment and developed an ammonia oxidation mechanism. Hayakawa et al. [8] compared the predictions of several detailed mechanisms of ammonia oxidation that were proposed previously according to the experimental data of laminar burning speed they measured. They found that most mechanisms failed to represent experimental data. Kumar and Meyer [186] studied the performance of the mechanisms established by Konnov [187] and Tian et al. [113] in laminar premixed jet flames. It is shown that these two mechanisms perform better only in limited

ranges of NH_3 content. Mendiara and Glarborg [188] built a new mechanism on the basis of the NH_3 sub-mechanism given by Tian et al. [113]. It displayed better predictions than the mechanisms proposed by Klippenstein et al. [189], Shmakov et al. [190], and Duynslaegher et al. [120] by comparing the predictions with the measured flame temperatures and flame front position. Pochet et al. [100] and He et al. [36] conducted experiments to research the autoignition of ammonia and ammonia blending with hydrogen mixtures in a rapid compressor (RCM). Both studies evaluated the performance of various NH_3 kinetic models and concluded that neither mechanism can reproduce the experiment satisfactorily.

Among NH_3/H_2 mechanisms, mechanisms proposed by Mathieu and Petersen [102] as well as Tian et al. [113] are promising for studying ammonia combustion characteristics in practical industrial applications, especially under elevated pressure conditions [36]. In addition, Xiao and Valera-Medina [31] compared performance of 12 mechanisms on predicting laminar flame speed, NO_X emissions and ignition delay times for NH_3/H_2 mixtures. Discrepancies between predictions of majority of kinetic models were demonstrated, and further supplement of the experimental database of ammonia oxidation was required. Furthermore, as methane is one of main fuels of gas turbines, the detailed kinetic mechanisms of NH_3/CH_4 were investigated to better analyse and design ammonia combustion systems for power generation. Xiao et al. [191] appraised five different NH_3/CH_4 mechanisms, mechanisms proposed by Tian [113] and Teresa [188] show the best prediction of ignition delay time.

As is known to us all, most of combustion reaction kinetics models include more than hundreds of elementary chemical reaction steps that have a profound impact on the combustion phenomena [20]. Usually, a detailed reaction kinetic mechanism is very

complicated, it is essential to reduce the extremely rigid problems of ammonia model encountered in the numerical simulation of flow and combustion coupling. Meanwhile the reduced model should maintain the physicochemical properties of the fuel under numerous operating conditions. As for ammonia kinetic model reduction, Duynslaegher et al. [120] reduced the Konnov mechanism [187] based on a contribution rates calculation of the Cosilab software [192]. The reduced mechanism of ammonia combustion includes 19 species and 80 reactions. After that Nozari et al. [193] also established reduced mechanisms applying a renewed version of the Konnov's mechanism. Currently, Li et al. [128] proposed an integrated mechanism of $NH_3/H_2/CH_4$, then reduced the model using directed relation graph with error propagation (DRGEP) as well as DRGEP with sensitivity analysis (DRGEPSA) methods. However, laminar burning velocities were over-predicted for both detail reduced mechanisms of pure NH_3, mixtures of NH_3/H_2 as well as NH_3/CH_4. Therefore, more accurate ammonia reaction kinetic model and extensive experimental database are required for further studying ammonia combustion characteristics.

Recently, Okafor et al. [11] combining GRI Mech 3.0 mechanism [194] as well as mechanism proposed by Tian et al. [113], developed a mechanism for laminar flame velocity study. Otomo et al. [44] established NH_3/air as well as NH_3/H_2/air combustion mechanisms according to Song et al. [195], in which the reactions of NH_2, HNO and N_2H_2 are improved. Later, Shrestha et al. [196] improved their previous ammonia oxidation model [34] and extended experimental database, including ignition delay times (IDT), speciation in jet-stirred reactors (JSR), and burner stabilized flames (BSF).

Table 2.3 Overview of ammonia chemical kinetic mechanisms (IDT: ignition delay time, SP: species profile, LBV: laminar burning velocity. ST: shock tube, JSR: jet-stirred reactor, SF: spherical flame, FR: flow reactor, RPM: rapid compression machine).

Authors/year	Species	Reactions	*T*/K	*P*/atm	Φ	Validation
Mendiara et al., 2009 [188]	97	779	973-1773	1	0.13-1.55	SP(FR)
Tian et al., 2009 [113]	84	703	1250-2100	0.04	1	SP
Duynslaegher et al., 2012 [120]	31	241	400-2000	0.06-0.12	0.9-1.1	SP
Hayakawa et al., 2015 [8]	42	130	298	1-5	0.7-1.3	LBV(SF)
Song et al., 2016 [195]	32	204	450-925	30-100	1	SP(FR)
Shrestha et al., 2018 [34]	125	1090	298-2000	1-33	0.5-1.8	IDT(ST), SP(JSR,FR), LBV
Okafor et al., 2018 [11]	59	356	298	1	0.8-1.3	SP, LBV(SF)
Otomo et al., 2018 [32]	33	222	1500-2500	1.4-30	0.5-2	IDT(ST), LBV(SF)
Glarborg et al., 2018 [197]	151	1397	760-2500	1-1.4	0.7-1.6	IDT(ST), SP(FR)
Mei et al., 2019 [7]	38	265	1500-2500	1-30	0.6-2	IDT(ST), LBV(SF)
Li et al., 2019 [128]	128	957	1000-2000	1-50	0.5-2	IDT(ST), LBV(SF)
Shrestha et al., 2020 [196]	125	1099	298-2500	1-40	0.5-2	IDT(ST,RCM), SP(JSR), LBV(SF)
Stagni et al., 2020 [112]	31	203	500-2000	1.4-60	0.01-0.375	IDT(ST,RCM), SP(JSR,FR), LBV(SF)

2.4. Background of Optical Diagnostics

2.4.1. Introduction

It is known that factors affecting the formation of pollutants, for example, nitrogen oxides, are

very complicated, and are closely associated with the type of fuels, the combustion mode, and the equivalence ratio of the combustion region. To further reduce pollution emissions, the proportion of air in the combustion zone can be increased. However, it could not only reduce the temperature in the combustion process but also increase CO and UHC emissions [198]. Furthermore, this circumstance of combustion may result in an unstable combustion regime, thermoacoustic instability, and severe pressure oscillations in the combustion chamber [199]. Consequently, to explore the feasibility of combustion technology and to understand the complex phenomena in engines, it is crucial to explore the essence of combustion. Thus, an important means is to study the evolution of the flame composition and transformation of the combustion model by measuring the concentration profiles of combustion intermediates. The measurement of combustion intermediates concentration is mainly achieved by using combustion diagnostic technology.

2.4.2. General methods of optical diagnostics

The combustion process in traditional engine is very complicated, because of the limited combustion space, high flow velocity, high mixing intensity, high combustion intensity, wide working ranges and sudden changes in parameters [200,201]. The main factors affecting engine combustion include combustion chemical reactions, combustion-flow interactions, and extreme operation conditions. Due to the high complexity of turbulent combustion, the flow and the many parameters of combustion are intertwined, and it is quite hard to quantitatively conduct measurements for temperature field, velocity field, flame surface structure and main component concentration. In modern combustion systems with high temperature, high pressure and other harsh environments, laser-based measurement

technology is a good method to do basic research on combustion, as well as achieving high combustion efficiency and less pollution in actual combustion devices.

Optical diagnostics are a non-intrusive measurement method that has good spatial and temporal resolution of the test region without any interference, so that it can precisely monitor burning process in combustion chamber. The existing optical testing technology can quantitatively measure the temperature field, concentration field, flame propagation process and the composition of each component of the combustion products, which can more intuitively understand the ignition and the flame development characteristics and deepen the cognition of the combustion process.

At present, with the development of laser and optical technology, the application of current optical testing technologies can directly measure the temperature field, self-luminous flame transition process in the cylinder, which can be more intuitively understood the ignition of flame and flame development characteristics. On the other hand, it can also provide real-time and high-resolution measurements. More specifically, with the rapid development of laser technology [202], laser Rayleigh scattering method [203 , 204], plane laser induced fluorescence method (PLIF) [205,206] and plane laser induced glazing method (PLII) [207,208] and other approaches have been utilized to perform temperature measurement in cylinder, mixture conditions and combustion intermediates [209 , 210 , 211]. Nevertheless, laser diagnostic techniques are quite unsuitable for practice especially in harsh environments because it requires an external source and optical port to link the laser beam with the combustion chamber. Moreover, additional technical modifications are more likely to affect the combustion process. Therefore, laser optical diagnostics are very expensive and

complicated for practical applications. These shortcomings of traditional laser-based diagnostic methods promote the further investigation of lower cost and more directly optical technologies.

(i) Laser diagnostics.

Usually, combustion optical diagnosis includes high-speed imaging, spectral analysis and laser diagnosis. Traditional two-dimensional optical diagnosis methods without laser, such as schlieren method [212,213] and shadow method [214,215], obtain the cumulative value of optical signal along the depth of the line of sight, so it is impossible to measure the signal value in a certain plane of space independently, which is that the measurement based on spatial resolution cannot be realized. In recent years, laser diagnosis technology has developed rapidly. Laser induced fluorescence (LIF) spectroscopy technique is regarded as a common tool for measuring free radicals. When the laser wavelength is tuned to a certain two specific energy levels of a molecule, the molecule resonation would happen, absorbing photon energy and exciting to a high level of energy state. It is known that molecules are unstable at high energy state, which is more possible to back to the ground state through emitting energy. The light emitted by molecules backing to the ground state by spontaneous emission is called laser-induced fluorescence. However, LIF measurements are also facing challenges in high-pressure flames due to the collision quenching of excited states and the high laser pulse energy required to generate detectable fluorescence signals. Additionally, the line light source is spread into a sheet light source to measure the stimulated emission of molecules on the basis of LIF, which is called PLIF. PLIF spectra can measure the information of two-dimensional spatial distribution and the concentration of combustion intermediate

radicals such as CH, OH, HCO in real time [216]. Complex laser-based diagnostics are employed to make the heat release distribution of flames visualized in laboratory. Heat emission imaging of formaldehyde (CH_2O) was diagnosed by LIF [217,218], which has been successfully used to characterize and quantify the spatial resolution of the concentration of CH_2O and OH, since the concentration of these intermediate radicals is related to the local exothermicity.

(ii) Chemiluminescence.

Chemiluminescence is regarded as a promising low-cost optical diagnostic tool. It is the spontaneous emission of electron-excited substances formed by chemical reactions in the combustion reaction zone, seen from Figure 2.5. The most common visible and ultraviolet light-emitting chemiluminescent radicals in a typical hydrocarbon flame are CH*, OH*, and C_2*, where the asterisk denotes electronic excitation. Figure 2.6 shows the flame spectrum of various excited species in a hydrocarbon flame at different wavelengths.

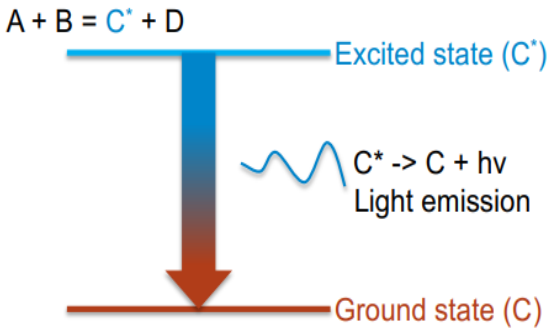

Figure 2.5 Chemiluminescence reaction mechanism [219].

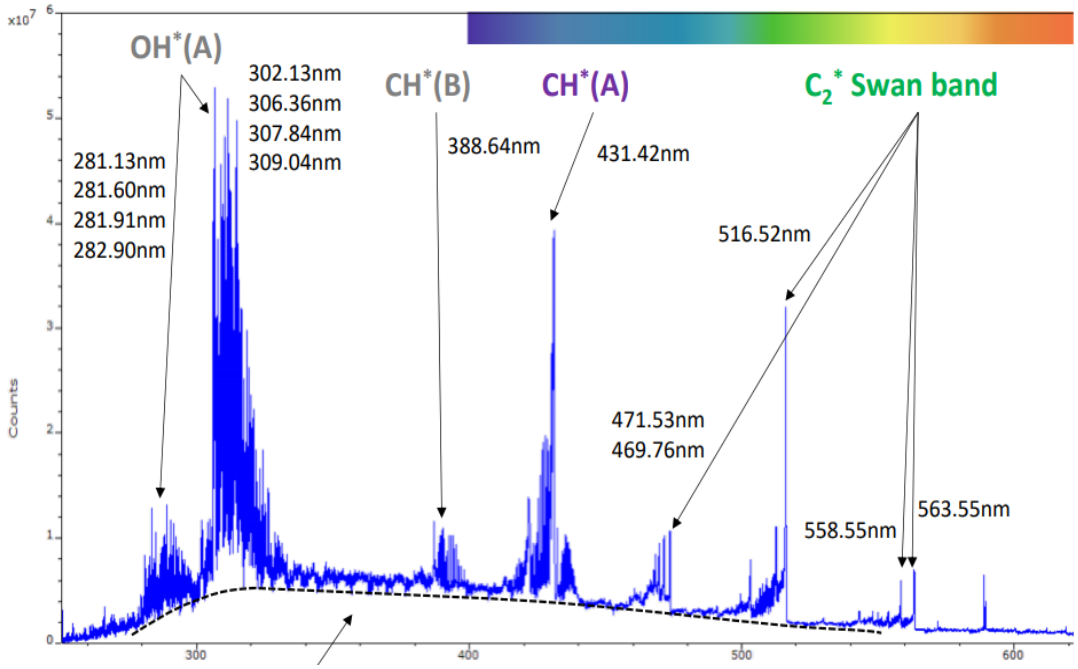

Figure 2.6 Flame spectrum of a hydrocarbon flame presenting the appearance of different excited species at different wavelengths [219].

Chemical reaction kinetics is very important in the study of pollutant formation process. CH has been considered as the key reactant for the formation of nitrogen oxides, so measuring the concentration and spatial distribution of CH is an important method to test the formation of pollutants. Since the short-lived chemical excited state CH* produces blue light in the low carbon smoke flame, it can provide an understanding of the C_2 reaction chain [220]. Therefore, predicting the concentration of excited state substances requires more effort to quantitative study through experiments or calculation methods.

The ability to simulate and predict chemiluminescence will provide an alternative and more flexible way to understand the effect of key combustion parameters on chemiluminescence signals. Such models will also be of practical value in the development of combustion diagnosis as well as interpretation of simulation and experiments results. Reliable chemiluminescence dynamic simulation requires accurate simulation of the formation rate of

excited state species. Therefore, it is necessary to know the chemiluminescence reaction steps and their rate constants. In addition, a standard fuel oxidant system that mimics the concentrations of precursor and quencher for chemiluminescence needs to be constructed with a reliable detailed chemical kinetic mechanism.

2.4.3. Flame chemiluminescence

Most studies focused on using optical techniques, such as laser induced fluorescence [221] or chemiluminescence [222] to research flame location, shape, and structure in combustors. Chemiluminescence is frequently applied to measure local distributions of heat release and investigate overall temporal fluctuations [223]. Tinaut et al. [224] concluded that the maximum OH* chemiluminescence was consistent with the highest rate of heat release.

(i) OH* chemiluminescence.

As an active radical that takes part in many crucial reactions, OH* (about 307nm) is especially important [225], due to the fact that it can be detected in the flame front [226], and it is used to mark ignition delay times in the oxidation of hydrogen flame systems [227] and diagnose equivalence ratio in methane air systems [228]. OH* emission reactions have been extensively studied [229,230,231,232]. Kaskan et al. [233] measured the OH* emission in a series of rich $H_2/O_2/N_2$ flames held on flat porous burners and found that the vibrational of OH* distributions are proportional to the fluctuation of flame gas temperature, which is attributed to the exothermicity of R1. Dandy et al [234] developed a model for use in predicting chemiluminescence and assumed that OH* radicals' products though the reaction (R2), which was firstly proposed by Krishnamachari et al. [235]. But this model only can be able to predict OH* radical chemiluminescence at one-dimensional and steady flame and in narrow

temperature scope. The shock-tube experimental results of Gutman et al. [236] showed that both of the chain reactions (R3) and (R4) are responsible for the OH* emission by monitoring OH* chemiluminescence in the induction process of the H_2-O_2 reaction. Later, Yoo et al. [237] also mentioned that the reaction of atomic H reacting with O and a three-body is likely a springhead of the OH* state in hydrogen/methane flames. The reaction (R3) as the source of OH* chemiluminescence at room temperature also was demonstrated by Spindler and his co-workers [238]. Moreover, the most popular reactions of OH* formation also include R2 [239,240]. Carl et al. [240] demonstrated conclusively that OH* emission intensities are consistent with concentrations of O_2 and CH in low pressure C_2H_2/O/H/O_2 atomic flames.

$$H + OH + OH \rightarrow H_2 + OH^* \text{ (R1)}, \tag{2.4}$$

$$CH + O_2 \leftrightarrow OH^* + CO \text{ (R2)}, \tag{2.5}$$

$$H + O + (M) \leftrightarrow OH^* + (M) \text{ (R3)}, \tag{2.6}$$

$$H + O_2 + (M) \leftrightarrow OH^* + (M) \text{ (R4)}. \tag{2.7}$$

In 2006, Hall et al. [241] assembled and optimized a kinetics model of OH* chemiluminescence to predict OH* formation as well as quenching at high temperature and atmospheric pressures. OH* quenching occurs generally by channel Q1. The partners that participate in the collisional quenching of OH* include H_2, H_2O, CO, CO_2, O_2, N_2 and Ar [242,243,244,245]. However, there are lots of controversies for the contribution rate among those partners on the collisional quenching of OH*. On top of that, the chemiluminescence emission from excited OH* is absorbed not only by self-absorption but also by other molecules, such as CO_2 and H_2O [246,247].

$$OH^* + M \leftrightarrow OH + M \text{ (Q1)}. \tag{2.8}$$

(ii) CH* chemiluminescence.

The spectrum of the CH* species (about 431nm and 390nm) are located in the visible region [239]. Because of the weak transitions of CH* (about 390nm) and lack of formation reaction rates, it is not studied in current study. Based on the sources of CH* that are proposed previously, research has mainly paid attention to the following reactions:

$$C_2H + O \leftrightarrow CH^* + CO \text{ (R1)}, \quad (2.9)$$

$$C_2H + O_2 \leftrightarrow CH^* + CO_2 \text{ (R2)}, \quad (2.10)$$

$$C_2 + OH \leftrightarrow CH^* + CO \text{ (R3)}. \quad (2.11)$$

R3 (Equation 2.11) was first showed in the study of hydrocarbon flame by Gaydon [248], and then Bowman [249] presented that it is a primary exothermic reaction to form CH* for methane in high temperature oxidation shock-tube experiments. However, it was agued by Brenig [250] and Smith [251]. Brenig's experiments found that the O atoms played a key role in the formation of CH*, which can react with ethynyl radicals (C_2H), also Glass et al. [252] and Grebe and Homann [253] regarded the R2 as the main channel. Smith suggested that reaction R3 has a minor contribution for CH* formation with less than 10 %. Later Hand [254] proposed reactions of equation 2.9 and 2.10 via shock tube experiments of acetylene-oxygen reactions, which also were supported by Hall [255] who suggested that R2 (Equation 2.10) is an important CH* formation pathway over the wide range of conditions. Devriendt et al. [256] measured CH* chemiluminescence by pulse laser photolysis at low pressure and indicted that the R1 (Equation 2.9) is the major of CH* production. On the other hand, Renlund et al. [257] depicted that O_2 is more advantaged than O atom for reacting with C_2H.

For the formation pathways of CH*, it is clear there is not good agreement. Also, the rate coefficient of the reactions leading to the generation of CH* are different by several orders of magnitude in the literature. Grebe and Homann [253] reported the rate data of R1 was k(R1) = 6.6×10^{11} $cm^3mol^{-1}s^{-1}$ at room temperature, which is one order of magnitude lower than that of Joklik et al. [258] who studied acetylene flame in low-pressure conditions. Devriendt [259] made estimation for the room temperature rate of this reaction R1 as k(R1) = 1.08×10^{13} $cm^3mol^{-1}s^{-1}$ by a sophisticated pulsed laser photolysis study over the temperature range (300-1000 K). Lens-based optical alignment may have influenced the conclusions of the measurements of chemiluminescence intensity. Smith et al. [251] suggested that the rate coefficient of R1 was k(R1) = 6.2×10^{12} $cm^3mol^{-1}s^{-1}$ by calibrating procedure of the optical detection system in low pressure premixed methane/air flame system. Afterwards, the authors recommend that k(R1) should be lower in CH_4/N_2O oxide flames. Among earlier studies on the R2, Hwang et al. [260] estimated a rate coefficient k(R1) = $4.10\times10^{13}\exp(Ea/RT)$ $cm^3mol^{-1}s^{-1}$ by means of a shock-tube investigation, which is three order magnificent higher than that of Devriendt [259]. Later on, Elsamra et al. [261] reported a temperature rate coefficient of R2 to be $6.0\times10^{-4}T^{4.4}\exp(Ea/RT)$ $cm^3mol^{-1}s^{-1}$ by comparing modelling values with different experiments data, but it was proved to be overpredicted the CH* concentration by Kathrotia et al. [262]. Smith et al. [251] proposed for k(R1) = 3.2×10^{11} $\exp(Ea/RT)$ $cm^3mol^{-1}s^{-1}$. So, it is ambiguity about the key reactions and its rate coefficient continuously. Further efforts should be paid on this area to make the contribution of CH* formation more clearly. Table 2.4 shows about all the important CH* formation and quenching reactions along with the irrespective rate parameters and sources.

Table 2.4 The rate parameters and sources of all the important formation and quenching reactions for CH*.

No.	Reaction	A(cm^3/(mole s))	b	E(cal/mol)	Reference
$R_{CH*}1$	$C_2H+O=CH^*+CO$	1.080×10^{13}	0.00	0	[259]
		6.023×10^{12}	0.00	457	[261]
		2.5×10^{12}	0.00	0	[253]
		6.2×10^{12}	0.00	0	[239]
$R_{CH*}2$	$C_2H+O2=CH^*+CO_2$	2.170×10^{10}	0.00	0	[259]
		6.023×10^{-4}	4.4	-2285.1	[261]
		4.470×10^{15}	0.00	25000	[263]
		3.2×10^{11}	0.00	805	[253]
		3.2×10^{11}	0.00	6.7	[262]
		4.1×10^{13}	0.00	4500	[239]
$R_{CH*}3$	C_2 +OH=CO+ CH*	1.1×10^{13}	0.00	0	[239]
$R_{CH*}4$	C+H+M=CH*+M	3.630×10^{13}	0.00	0	[264]
$Q_{CH*}1$	CH*=CH	1.850×10^{6}	0.00	0	[265]
		2.1×10^{6}	0.00	0	[266]
		2.08×10^{6}	0.00	0	[267]
		2.25×10^{6}	0.00	0	[268]
		2.17×10^{6}	0.00	0	[269]
		1.87×10^{6}	0.00	0	[270]
		1.97×10^{6}	0.00	0	[271]
		2.27×10^{6}	0.00	0	[272]
$Q_{CH*}2$	$CH^*+N_2=CH+N_2$	3.030×10^{2}	3.40	-381	[265]
$Q_{CH*}3$	CH*+AR=CH+AR	3.130×10^{11}	0.00	0	[264]
$Q_{CH*}4$	$CH^*+O_2=CH+O_2$	2.480×10^{6}	2.14	-1720	[265]
		2.480×10^{6}	2.14	-7.2	[264]
$Q_{CH*}5$	$CH^*+H_2O=CH+H_2O$	5.30×10^{13}	0.00	0	[265]
$Q_{CH*}6$	$CH^*+H_2=CH+H_2$	1.470×10^{14}	0.00	1361	[265]
$Q_{CH*}7$	$CH^*+CO_2=CH+CO_2$	2.400×10^{-1}	4.30	-1694	[265]
		2.480×10^{-1}	4.30	-7.1	[264]
$Q_{CH*}8$	CH*+CO=CH+CO	2.440×10^{12}	0.50	0	[265]
$Q_{CH*}9$	$CH^*+CH_4=CH+CH_4$	1.730×10^{13}	0.00	167	[265]
		1.730×10^{13}	0.00	0.7	[264]
$Q_{CH*}10$	CH*+M=CH+M	6.502×10^{12}	0.00	0	[273]
$Q_{CH*}11$	CH*+H=CH+H	2.010×10^{14}	0.00	5.7	[264]
$Q_{CH*}12$	CH*+OH=CH+OH	7.130×10^{13}	0.00	5.7	[264]

(iii) C_2* chemiluminescence.

The spectrum of the C_2* species is mainly found between 470-550nm. There is not enough data for C_2* formation, among which reactions $CH_2 + C = H_2 + C_2$*($R_{C2*}1$) and $C_2H + H = H_2 + C_2$*($R_{C2*}2$) were originally proposed by Gaydon [248], and Kathrotia [264] proposed $C_3 + O <=> CO + C_2$*($R_{C2*}3$). According to the study of the electronically excited C_2* radical in C_2H_2 flames [274], either $R_{C2*}2$ or $2CH = C_2$* + H ($R_{C2*}4$) do not show significantly influence on C_2* production that has been recognized by other studies [275,276,277]. The reaction of CH_2 with C is investigated in C_2H_2/O/H system by Grebe and Homann [275] who proposed reaction ($R_{C2*}1$) that is regarded as primary exothermic reaction for C_2* formation. Marques et al. [278] simulated the C_2* production rate that shows $R_{C2*}1$ is the main source of the C_2* excited radical, contributing to about 98% of the total amount, while $R_{C2*}2$ contributes only around of 2% to C_2* production in acetylene flames. In previous studies, Savadatti [279] suggested that the reaction of C_3 with atomic oxygen can be also regarded as a source of C_2*, and this reaction $R_{C2*}3$ is also studied by Kathrotia [264]. Most of the Kinetic parameters of C_2* reactions were applied according to similar reactions of C_2 in the ground electronic state, due to that fact that it is lack the data to investigate this. Grebe proposed the rate of the $R_{C2*}1$ to be 7.5×10^{13} $cm^3mol^{-1}s^{-1}$ at room temperature as well as 2.4×10^{12} $cm^3mol^{-1}s^{-1}$ at high temperatures from 1500 to 1950 K [253]. Table 2.5 lists the irrespective rate parameters and sources of all the important formation as well as quenching reactions for C_2*.

Table 2.5 The irrespective rate parameters and sources of all the important formation and quenching reactions for C_2*.

No.	Reaction	A(cm^3/(mole s))	b	E(cal/mol)	Reference
$R_{C2*}1$	$CH_2+C=H_2+C_2$*	7.500×10^{13}	0.00	0	[253]
		2.400×10^{12}	0.00	0	[264]
$R_{C2*}2$	$C_3+O=CO+C_2$*	4.200×10^{11}	0.00	0	[264]
$Q_{C2*}1$	C_2*=C_2	1.000×10^{7}	0.00	0	[264]
$Q_{C2*}2$	C_2*+M=C_2+M	3.630×10^{13}	0.00	0	[239]
$Q_{C2*}3$	C_2*+O_2=C_2+O_2	4.800×10^{13}	0.00	0	[264]
$Q_{C2*}4$	C_2*+CO_2=C_2+CO_2	4.800×10^{13}	0.00	0	[264]
$Q_{C2*}5$	C_2*+H_2O=C_2+H_2O	4.800×10^{13}	0.00	0	[264]
$Q_{C2*}6$	C_2*+CO=C_2+CO	4.800×10^{13}	0.00	0	[264]
$Q_{C2*}7$	C_2*+CH_4=C_2+CH_4	4.800×10^{13}	0.00	0	[264]
$Q_{C2*}8$	C_2*+H_2=C_2+H_2	4.800×10^{13}	0.00	0	[264]
$Q_{C2*}9$	C_2*+AR=C_2+AR	4.800×10^{13}	0.00	0	[264]

2.5. General Concept of Hydrocarbon Combustion

2.5.1. Premixed flame

According to the premixing status of mixtures, the flame can be categorized into a diffusion flame (non-premixed flame) and a premixed flame. As well, according to fluid flow type, the flame can be sub-categorized into two flames: a laminar flame and a turbulent flame [280]. Usually, a flame on Bunsen burner is a kind of premixed laminar flame, while the flame such as in a gasoline turbine commonly belongs to premixed turbulent flame [281]. In addition,

flames like candle and wood flame are usually laminar diffusion flame [282].

For premixed flame, fuel as well as oxidizer are mixed homogeneously at molecular level prior to combustion. The initial reaction mainly occurs at the interfacial layer due to high temperature, which can be obtained by absorbing heat energy from the ignition source. From the initial reaction, the heat released is applied for burning the premixed molecule. During the period of this time, the reaction goes very fast, so that there is a thin combustion zone to separate the unburnt gas and burnt gas.

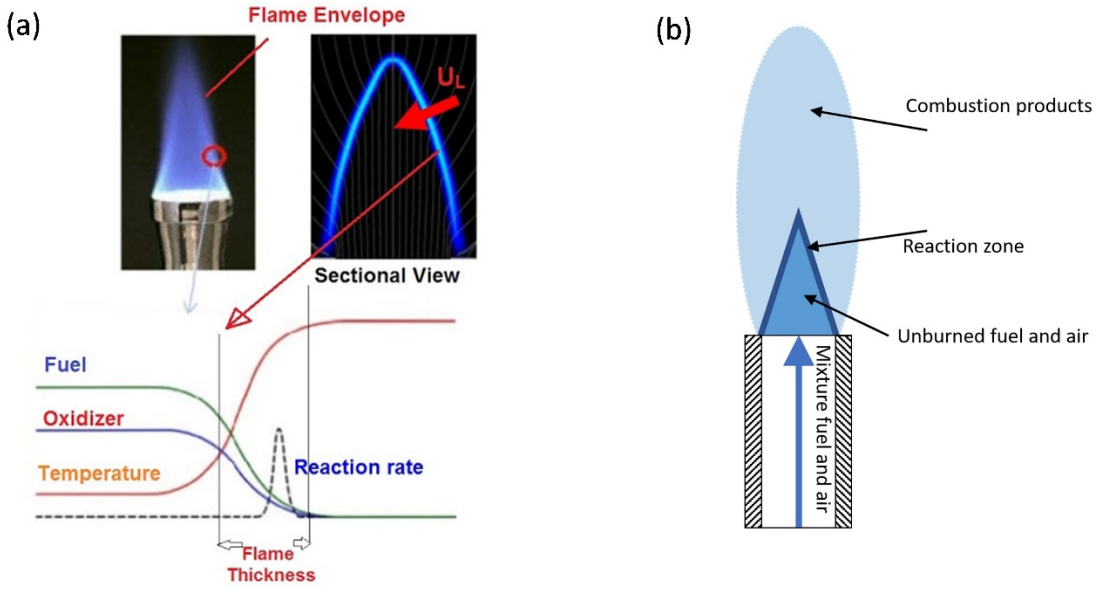

Figure 2.7 (a) The details of the chemical reaction structure and products [283]; (b) The schematic of the premixed flame.

The activation energy is provided in this area to decompose the fuel and oxidizer molecules, shown in Figure 2.7(a) [283]. When the temperature is beyond the critical point of the combustion, the heat is released mainly by a chain reaction. In Figure 2.7(b) presents the schematic of the premixed flame, and the inner luminous cone is defined by the laminar flame velocity ratio to the mixture velocity [284], where flame speed is roughly estimated as the premixed flame propagation speed. In premixed flame, chemical reaction has a dominant

effect on reaction rate. In luminous reaction zone, flame colour is produced by flame chemiluminescence.

2.5.2. Equivalence ratio

The equivalence ratio Φ indicates the fuel to air ratio under the combustion condition, which is defined as follows,

$$\Phi = \frac{(fuel\ to\ air\ molar\ ratio)_{\text{actual}}}{(fuel\ to\ air\ molar\ ratio)_{\text{stoichiometric condition}}}. \quad (2.12)$$

For Φ = 1, the fuel is theoretically consumed completely by the available oxidizer and no excess oxidizer or fuel is left after reaction at stoichiometric condition. Φ > 1 means the fuel is rich in mixture, while Φ < 1 means the fuel is lean in mixture.

The equivalence ratio is an important parameter in combustion. It has significant impact on numerous combustion characteristics, including laminar flame speed, exhaust emissions, temperature and even flammability. In practice, the operation condition of flame is hardly achieved under the stoichiometric condition due to the complex combustion progress. Therefore, analysis of fuel with various proportion in air is usually significant to fully study the combustion behaviour.

2.5.3. Laminar flame speed

Generally, laminar flame speed is one of fundamental properties of premixed combustible mixtures [285]. It is the homogeneous unburned reactants propagation speed that takes along the information on diffusivity, reactivity, and exothermicity of a given mixture [286]. Therefore, the laminar burning velocity is usually used to characterize flames.

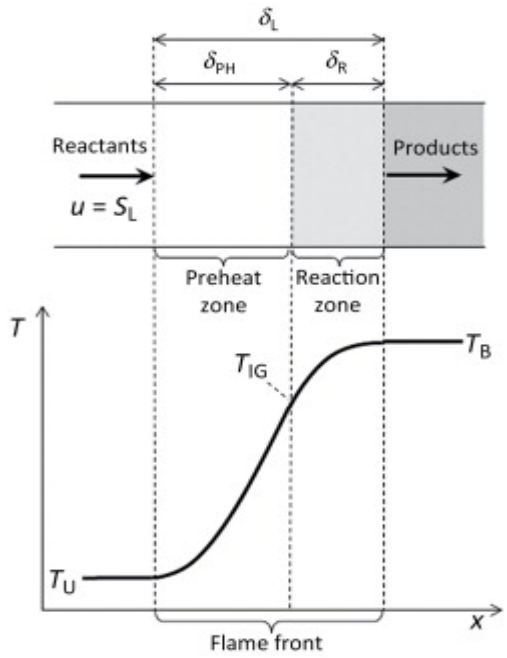

Figure 2.8 Schematic of a one-dimensional planar and unstretched flame front, from [287].

The initial theoretical analyses on the laminar flame speed were conducted by assuming that the combustion is sustained, and the temperature of the unburned mixture will increase to the ignition temperature by absorbing heat from upstream burned gas [281]. Therefore, the one-dimensional flame is split into two zones including of a preheat zone and a reaction zone, seen from Figure 2.8. According to postulation, although the laminar burning velocity strongly depends on the temperature of burned gas (T_B) and unburned gas (T_U), the heat diffusion in preheat zone as well as reaction zone should be also considered [288]. In the present work, the simulation of laminar premixed flame is conducted in CHEMKIN-PRO package, and the thermal diffusion is considered. Based on the energy balance and establishment of a proportionality between T_B, T_U and pressure *P*, the laminar flame speed S_L [289] is given as follows:

$$S_L \sim \left(\frac{T_U+T_B}{2}\right)^{0.375} \cdot T_U \cdot T_B^{-\left(\frac{n}{2}\right)} \cdot \exp\left(-\frac{E_A}{2RT_B}\right) \cdot p^{(n-2)/2}. \quad (2.13)$$

3. The Numerical Methods

3.1. Introduction

The main objective of the thesis is to develop a compact reduced kinetics mechanism of ethanol for further investigation of flame chemiluminescence and establish an accurate reduced mechanism for $NH_3/H_2/CH_4$ mixtures to better understand the $NH_3/H_2/CH_4$ combustion process as well as exhaust gases generation. In section 3.2, the theory of DRGEP and IPFA methods combined with GEPA are presented respectively to reduce the detailed mechanisms of ethanol and ammonia. As well, the validation model for reduced mechanism is shown in section 3.3. Furthermore, in section 3.4, the CRN models are demonstrated including the fundamentals, components of CRN models in singe and two staged gas turbine combustors, and the validation of the CRN model. At the end of this Chapter, the chemiluminescence reaction mechanism of OH*, CH* as well as C_2* and chemiluminescent intensity calculation theory are introduced. And the validation of the chemiluminescent intensity modelling of excited state species is provided.

3.2. The methods of mechanism reduction

3.2.1. DRGEP

The DRGEP method, a derived method from the DRG method, was proposed by Pepiot et al. [77,78]. In this approach, interaction coefficients of two species are defined and used for identification of the dependence of one species on the other species. The direct interaction coefficient (DIC), used for describing reliance of species A on species B, can be expressed as follows [77]:

$$r_{\mathrm{AB}}^{\mathrm{DRGEP}} = \frac{\left|\sum_{i=1,I} \nu_{\mathrm{A},i}\omega_i\delta_{\mathrm{B}}^{i}\right|}{max(P_{\mathrm{A}}, C_{\mathrm{A}})}, \tag{3.1}$$

$$\omega_i = \omega_{\mathrm{f},i} - \omega_{\mathrm{b},i}, \tag{3.2}$$

where *i* represents the whole number of elementary reactions, $\nu_{\mathrm{A},i}$ is stoichiometric coefficient of species A in the *i*th reaction, $\omega_{\mathrm{f},i}$, $\omega_{\mathrm{b},i}$, and ω_i are forward, backward, as well as net reaction rates of the *i*th reaction, P_{A} and C_{A} are production and consumption fluxes of species A, respectively, which are expressed with

$$P_{\mathrm{A}} = \sum_{i=1,I} max\left(\nu_{\mathrm{A},i}\omega_i, 0\right), \tag{3.3}$$

$$C_A = \sum_{i=1,I} max\left(-\nu_{A,i}\omega_i, 0\right). \tag{3.4}$$

In Equation 3.1, δ_{B}^{i} is given by

$$\delta_{\mathrm{B}}^{i} = \begin{cases} 1, & if\ the\ species\ B\ is\ involved\ in\ the\ ith\ elementary\ reaction \\ 0, & otherwise \end{cases} \tag{3.5}$$

The numerator of coefficient $r_{\mathrm{AB}}^{\mathrm{DRGEP}}$ can be easily demonstrated [77]:

$$\left|\sum_{i=1,I} \nu_{\mathrm{A},i}\omega_i\delta_{\mathrm{B}}^{i}\right| = \left|\sum_{i=1,I} max\left(\nu_{\mathrm{A},i}\omega_i\delta_{\mathrm{B}}^{i}, 0\right) - \sum_{i=1,I} max\left(-\nu_{\mathrm{A},i}\omega_i\delta_{\mathrm{B}}^{i}, 0\right)\right| = |P_{\mathrm{AB}} - C_{\mathrm{AB}}|, \tag{3.6}$$

where P_{AB} and C_{AB} represent production and consumption fluxes of species A related to species B, respectively. Substituting Equation (3.6) into Equation (3.1), the coefficient $r_{\mathrm{AB}}^{\mathrm{DRGEP}}$ is expressed by:

$$r_{\mathrm{AB}}^{\mathrm{DRGEP}} = \frac{|P_{\mathrm{AB}} - C_{\mathrm{AB}}|}{max(P_{\mathrm{A}}, C_{\mathrm{A}})}. \tag{3.7}$$

Based on the evaluated DIC for all species pairs, here, a DRG can be built. Strength of each edge linking one species A with another species B is indicated by $r_{\mathrm{AB}}^{\mathrm{DRGEP}}$. Suppose species A is the target species, intermediate species C is linked to target species A directly, and species B is linked to intermediate species C directly, i.e., indirectly linked to target species A (see the pathway 2 in Figure 3.1).

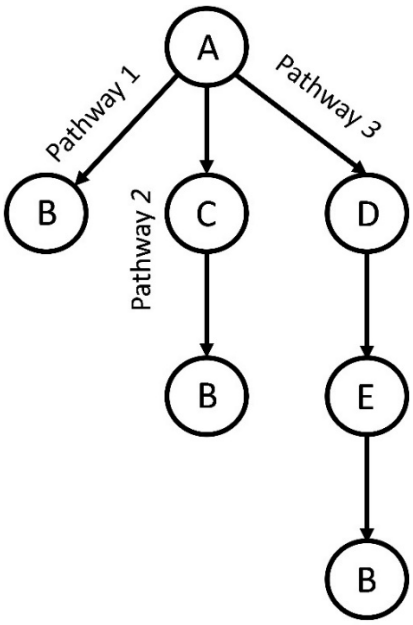

Figure 3.1 A relation graph involving species in the DRGEP method.

To consider this error propagation process due to the indirect links, a geometric damping is applied in the selection procedure. The path interaction coefficient (PIC), which represents product of intermediate DICs between target species A and species B via each pathway is given by

$$r_{\mathrm{AB},pw}^{\mathrm{DRGEP}} = \prod_{i=1}^{n-1} r_{S_i S_{i+1}}, \tag{3.8}$$

where *pw* is the certain pathway, *n* is number of species between species A and B in each pathway, *S* is intermediate species between species A and B, such as species C, D, E in Figure 3.1.

The maximum value of all PICs is expressed as overall interaction coefficient (OIC):

$$R_{\mathrm{AB}}^{\mathrm{DRGEP}} = \max_{\text{all } pw} r_{\mathrm{AB},pw}^{\mathrm{DRGEP}}. \tag{3.9}$$

If certain error is introduced into the prediction of species B, it has to propagate to longer way to reach the target species A, and typically, its effect is smaller. The DRGEP method is target oriented and used to provide a finer selection of the essential paths for accurately predicting

the targets set, by retaining species related to larger OIC and removing species with smaller OIC [77]. In the present thesis, the DRGEP method is applied to conduct reduction for detailed mechanism of ethanol, which contains 36 species and 252 reactions.

3.2.2. IPFA

The IPFA with multi generations method was proposed by Wang and Gou [81] based on the PFA method [80]. Compared to the DRGEP method, the IPFA method can obtain a more accurate and compact reduced mechanism from a larger-sized detailed mechanism containing hundreds of species as well as thousands of reactions [80,81]. Moreover, the IPFA method is an improved version of PFA method, capable of eliminating species with more caution, and avoid the phenomenon in which one species is removed since consumption or production rate is comparatively larger compared to the other [81].

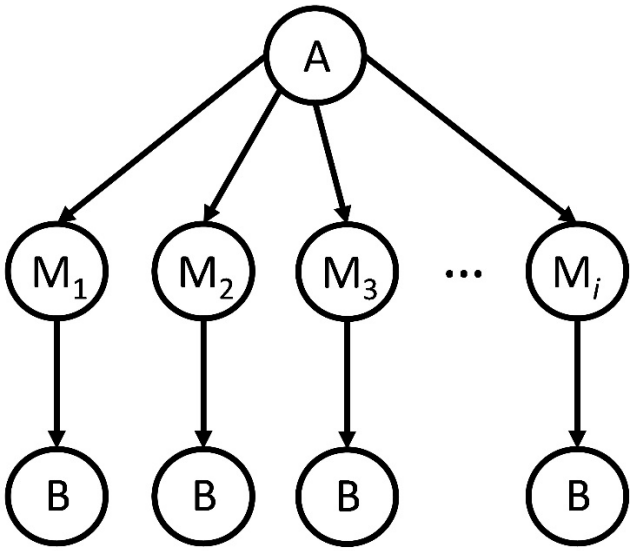

Figure 3.2 A relation graph involving species in the PFA and IPFA methods.

Considering the IPFA method with two generations, which was proved to be adequate for mechanism reduction in the previous studies [131,290], instead of employing net reaction rates to calculate DIC, the production as well as consumption fluxes are used separately to

seek significant reaction pathways. Therefore, interaction coefficients for production as well as consumption of species A via B of first generation, as well as those of second generation derived via a third reactant M_i (see Figure 3.2) are defined as follows [81]:

$$r_{AB,IPFA}^{pro-1st} = \frac{P_{AB}}{P_A}, \tag{3.10}$$

$$r_{AB,IPFA}^{con-1st} = \frac{C_{AB}}{C_A}, \tag{3.11}$$

$$r_{AB,IPFA}^{pro-2nd} = \sum_{M_i \neq A,B}\left(r_{AM_i}^{pro-1st} r_{M_iB}^{pro-1st}\right), \tag{3.12}$$

$$r_{AB,IPFA}^{con-2nd} = \sum_{M_i \neq A,B}\left(r_{AM_i}^{con-1st} r_{M_iB}^{con-1st}\right). \tag{3.13}$$

Theoretically speaking, for each interaction coefficient, one threshold value should be set. For simplicity, only one threshold value is set, and all the interaction coefficients are lumped together as follows [81]:

$$r_{AB}^{IPFA} = r_{AB,IPFA}^{pro-1st} + r_{AB,IPFA}^{con-1st} + r_{AB,IPFA}^{pro-2nd} + r_{AB,IPFA}^{con-2nd}. \tag{3.14}$$

The coefficient defined above, which evaluates dependence of species A on B, is applied to make decision whether species B is kept. The procedure for selecting significant species as well as their relevant reactions from detailed mechanisms are concluded: (i) one or more species including reactants, products or certain significant intermediate components are set as the initial target species; (ii) a user-specified threshold ε, larger or smaller than 1, is used to be standard to determine significance of other species to initial target species; (iii) computing the coefficient r_{AB}^{IPFA}; (iv) Updating the set of initial target species. If $r_{AB}^{IPFA} > \varepsilon$, the corresponding species are added into the updated initial target species set. If none of any species is appended, one can go directly to (v). Otherwise, the updated initial target species set is applied to be the initial one as well as (iii) needs to be repeated; (v) the skeletal mechanism, including the species as well as their relevant reactions selected from previous

steps, is generated.

In the present thesis, the IPFA method is applied to reduce detailed mechanism of ammonia/hydrogen/methane mixtures, which contains 125 species and 1099 reactions.

3.2.3. GEPA

The GEPA method is used to remove insignificant reactions with a proper threshold [90]. Here, the details are stated. Within the scope of chemical kinetics, the local entropy production is capable of characterizing crucial reactions in various regions of composition space [291]. An elaborate discussion of the concepts for entropy and entropy production was conducted by Gorban and Beretta [292,293]. According to these concepts, Kooshkbaghi et al. [42] proposed the EPA method to form the skeletal mechanism. For a homogeneous closed system, at time *t*, the total entropy production per unit volume due to chemical reactions can be expressed as [42]:

$$\frac{dS}{dt} = \frac{1}{T}\sum_{k=1,I} \alpha_k \left(q_k^f - q_k^b\right), \tag{3.15}$$

where *T* is the temperature, *I* is the whole number of reactions, q_k^f and q_k^b are forward as well as backward reaction rates of the *k*th reaction, respectively, α_k is the chemical affinity (or called as De Donder's affinity [294]) of the *k*th reaction, which is defined as [295]:

$$\alpha_k = \sum_{j=1,n_s} \nu_{jk}\, \mu_j, \tag{3.16}$$

where n_s is whole number of species, ν_{jk} is stoichiometric coefficient of the *j*th species of the *k*th reaction, μ_j is the chemical potential of the *j*th species.

At time *t*, relative contribution of the *k*th reaction to whole entropy production is expressed as:

$$r_k(t) = \frac{\left|\alpha_k\left(q_k^f - q_k^b\right)\right|}{\sum_{k=1,n_r}\left|\alpha_k\left(q_k^f - q_k^b\right)\right|}, \tag{3.17}$$

the absolute values are essential due to the fact that regardless of the sign of contribution of the *k*th reaction, the most significant reactions need to be identified.

In the EPA method, assuming that the deviations from the principle of detailed balance are absent [293], therefore, α_k becomes

$$\alpha_{k,EPA} = R_c T \ln\left(\frac{q_k^f}{q_k^b}\right), \tag{3.18}$$

where R_c is the ideal gas constant.

However, a great number of detailed reaction mechanisms, specifically those modelling complicated fuels including irreversible reactions, disobey detailed balance principle. In these cases, performance of the EPA approach is not satisfying, which can easily introduce arbitrariness.

The GEPA method is a more generalized form of EPA method, which can easily deal with those containing reversible reactions not satisfying the principle of microscopic reversibility or even irreversible reactions [90]. Considering ideal gas mixtures, the chemical potentials μ_j of *j*th species can be expressed as [296]:

$$\mu_j(T,P) = \left(\frac{h_j^0}{R_c T} - \frac{s_j^0}{R_c}\right) + R_c T ln\left(\frac{PX_j}{P^0}\right), \tag{3.19}$$

where P and P^0 are the current state and standard state pressures (usually 1atm), respectively. h_j^0 and s_j^0 are the standard state enthalpy and entropy of the *j*th species, which are calculated via thermodynamic data using NASA polynomials [297]. X_j is mole fraction of the *j*th species.

Substituting Equation (3.19) into (3.16), α_k is obtained as [90]:

$$\alpha_{k,GEPA} = \sum_{j=1,n_s} \nu_{jk} \left[\left(\frac{h_j^0}{R_c T} - \frac{s_j^0}{R_c} \right) + R_c T ln \left(\frac{P X_j}{P^0} \right) \right]. \quad (3.20)$$

Here, the relative contribution r_k of Eq. (3.17) is regarded as the standard of identifying unimportant reactions. The steps for reducing the mechanism are summarised: (i) a database of the thermochemical states (compositions, pressure, temperature) is constructed; (ii) a user-specified threshold ε is set as the standard to recognize significant reactions of the mechanism; (iii) calculating the relative contribution r_k of the equation (3.17); (iv) Selecting the significant reactions of the mechanism. If $r_k > \varepsilon$, the corresponding reactions are retained, otherwise, the reactions are eliminated; (v) The final reduced skeletal mechanism, containing the reactions retained from previous steps and the species participating in these reactions, can be generated.

In the present thesis, the GEPA approach is combined with DRGEP approach to reduce detailed mechanism of ethanol and is also combined with IPFA method to reduce detailed mechanism of ammonia/hydrogen/methane mixtures. The role of GEPA method in these combined approaches is to further eliminate redundant reactions from the skeletal mechanisms.

3.3. The validation model for reduced mechanism

3.3.1. Constant volume homogeneous reactor model

Validation of ignition delay times is completed by comparing the simulated values of reduced mechanisms with that of the detailed mechanism as well as the experimental measurements of shock tube. It is considered that the chemical reaction in the shock tube is in a homogeneous and constant volume adiabatic state [298]. Therefore, the constant volume homogeneous reactor model in the CHEMKIN-PRO package is employed for predicting ignition

delay time in a shock tube. Predicting ignition times is helpful to understand the underlying chemistry.

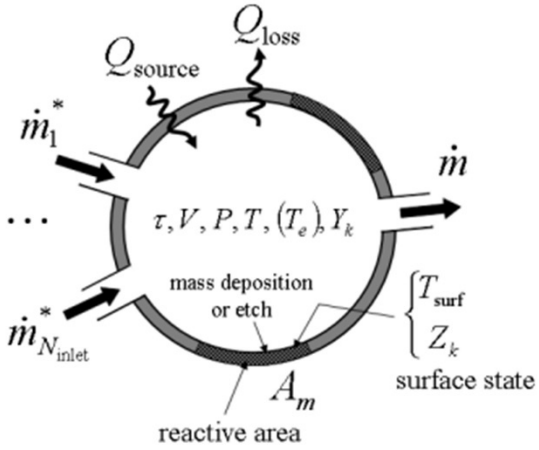

Figure 3.3 Schematic of a Well Mixed Reactor Module [299].

Figure 3.3 shows the schematic of a well-mixed reactor module. The gas reaction is conducted under constant volume and homogeneous adiabatic conditions, satisfying the conservation of mass, momentum and energy:

$$\frac{dT}{dt} = \frac{1}{\rho \overline{c_v}} \sum_{k=1}^{K} (h_k \dot{\omega} \times M_k) + \frac{T}{\overline{c_v}} \times \frac{dR}{dT}, \tag{3.21}$$

$$\frac{dP}{dt} = R \times T \times \frac{d\rho}{dt} + \rho \times R \times \frac{dT}{dt}, \tag{3.22}$$

$$\frac{dY_k}{dt} = \frac{\dot{\omega} \times M_k}{\rho}, \tag{3.23}$$

where *T*, *P*, and *R* are the temperature (K), pressure (atm) as well as gas constant. *k* and *K* are the serial number of species as well as total number of species. $\overline{c_v}$ represents mean molar heat capacity at constant volume (J/(mol·K)). h_k, M_k, and Y_k are specific enthalpy (J/mol), mole mass (g/mol), and mass fraction of the *k*th species, respectively. $\dot{\omega}$, is reaction rate (cm^2/s). ρ is the mass density of a gas mixture (g/cm^3). Conservation of energy equation [299] is:

$$\frac{dU_{sys}{}^{(j)}}{dt} = \sum_{i=1}^{N_{inlet}^{(j)}} \dot{m}^{*(j)} \sum_{k=1}^{K_g} (Y_{k,i}^* h_{k,i}^*)^{(j)} + \sum_{r=1}^{N_{PSR}} \dot{m}^{(r)} R_{rj} (Y_k h_k)^{(r)} - \left(\dot{m} \sum_{k=1}^{K_g} Y_k h_k\right)^{(j)} - Q_{loss}^{(j)} + Q_{source}^{(j)} - P^{(j)} \frac{dV^j}{dt} \qquad j=1, N_{PSR}, \tag{3.24}$$

where U_{sys} (J) is the whole internal energy, which contain internal energy of as, deposited phases, surface phases, and walls. $N_{inlet}^{(j)}$ is number of inlets for each reactor *j*. N_{PSR} is whole number of reactor modules in reactor network. $\dot{m}$ is outlet mas flow rate. K_g is the gas-phase species. Q_{loss} (J) is net heat flux directed out of the reactor. Q_{source} (J) is the source of heat release in reactor.

3.3.2. 1-D premixed laminar flames

The premixed laminar flame is simulated employing the PREMIX module in the CHEMKIN-PRO package. The model involves a freely propagating flame. The flame velocity of the gas mixture can be calculated at inlet temperature as well as specified pressure. The balance governing conservation equations for continuity, chemical species and energy are as follows [299]:

$$\dot{M} = \rho u A, \tag{3.25}$$

$$\dot{M}\frac{Y_k}{dx} + \frac{d}{dx}(\rho A Y_k V_k) - A\dot{\omega}_k W_k = 0 \quad (k = 1, \dots, K_g), \tag{3.26}$$

$$\dot{M}\frac{dT}{dx} - \frac{1}{c_P}\frac{d}{dx}\left(\lambda A\frac{dT}{dx}\right) + \frac{A}{c_P}\sum_{k=1}^{K}\rho Y_k V_k c_{Pk}\frac{dT}{dx} + \frac{A}{c_P}\sum_{k=1}^{K}\dot{\omega}_k h_k W_k + \frac{A}{c_P}\dot{Q}_{rad} = 0, \tag{3.27}$$

where x is coordinate in the space (cm); A is the area of the flame at the cross-sectional interface (cm^2); $\dot{M}$ denotes the mass flow rate (cm/s); Y_k is mass fraction of the kth species; *P* denotes the pressure (atm); $\dot{\omega}_k$ represents chemical production rate per unit volume of the *k*th species (mole/(cm^3s)); u is the axial speed of the fluids (cm/s); W_k is molecular weight of the kth species (g/mole); c_P is heat capacity of mixture at the constant pressure (J/(mole • K)); c_{Pk} is molar heat capacity of the kth species at the constant pressure(J/(mole • K)); h_k is the specific enthalpy of the kth species (J/g); λ is thermal conductivity of the gas mixture (J/cm • s • K); V_k is ordinary diffusion speed of the kth species

(cm/s); $\dot{Q}_{rad}$ is radiation heat release (J).

For calculation of the speed of laminar premixed flames, it is assumed that the mixtures are initialised with fully burnt composition at one side of an equilibrium composition, while the unburnt species on the other side.

3.4. CRN model construction for NO_X emission

Considering the requirement of 3D CFD simulation on high computational cost, a chemical reactor network (CRN) model is performed to study combustion in gas turbines [300-303]. Although the highly simplified CRN model is difficult to reflect the flow field structure and temperature field distribution in real combustors, it is regarded as an effective numerical method to predict NO_X emissions via calibrated and validated data in previously research [304-306]. Therefore, in the current study, the CRN model is employed to analyse NO_X emission characteristics of partially cracked ammonia combustion in single stage and 2-stage gas turbine combustor.

Two clusters are included in the chemical reactor network, seen in Figure 3.4. Different chemical reactors are used to accurately predict the combustion in each corresponding zone of the combustion chamber. The Perfectly Stirred Reactor (PSR) is adopted to simulate a swirling flame including the premixing, circulation and flame zone, followed by a Plug Flow Reactor (PFR) that represents a post-flame zone. In a PSR, reactants as well as products are assumed to be instantly mixed and there exist no variation of temperature or composition in the reactor. This is the reason that can be used to simulate combustion process in primary flame zone, where the reactants and temperatures are generally evenly distributed due to

intense recirculation. Three sub-zones are used to represent the swirling flame, i.e., PSR1 is the mixing zone near the inlet exit; PSR2 is the central recirculation zone (CRZ)with 20% recirculation rate; PSR3 is primary flame zone, as shown in Figure 3.4(b). The flame picture is provided by literature [307].

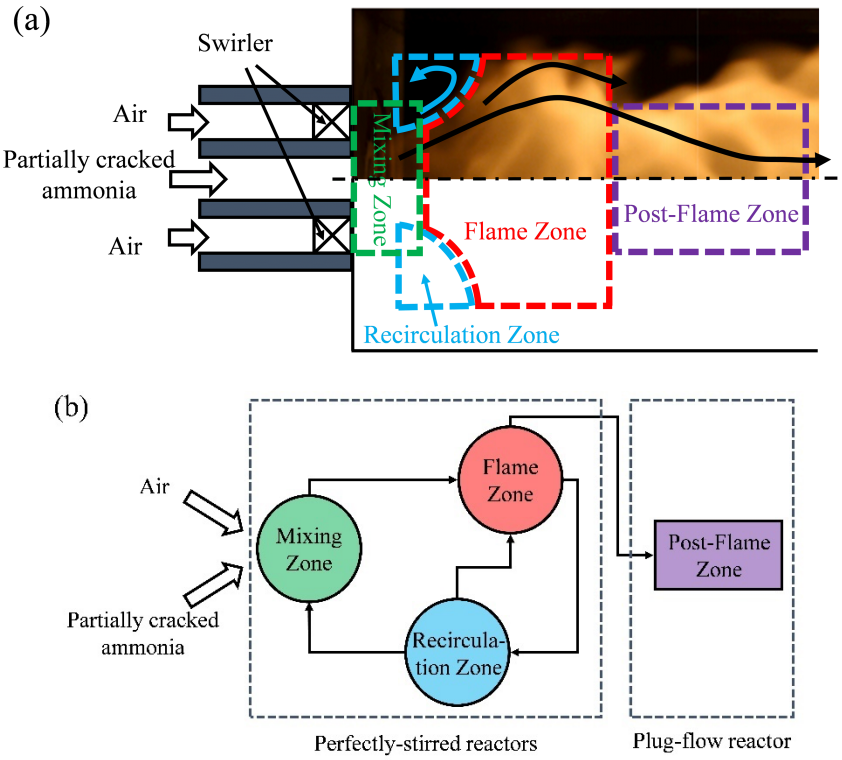

Figure 3.4 (a) The schematic of CRN model; (b) Single stage gas turbine network for 1-D modelling.

As for the 2-stage combustor, the schematic of the CRN model is depicted in Figure 3.5. Two network of combustion reactors, including a PSR followed by a PFR, are constructed for simulating rich-lean burn combustor.

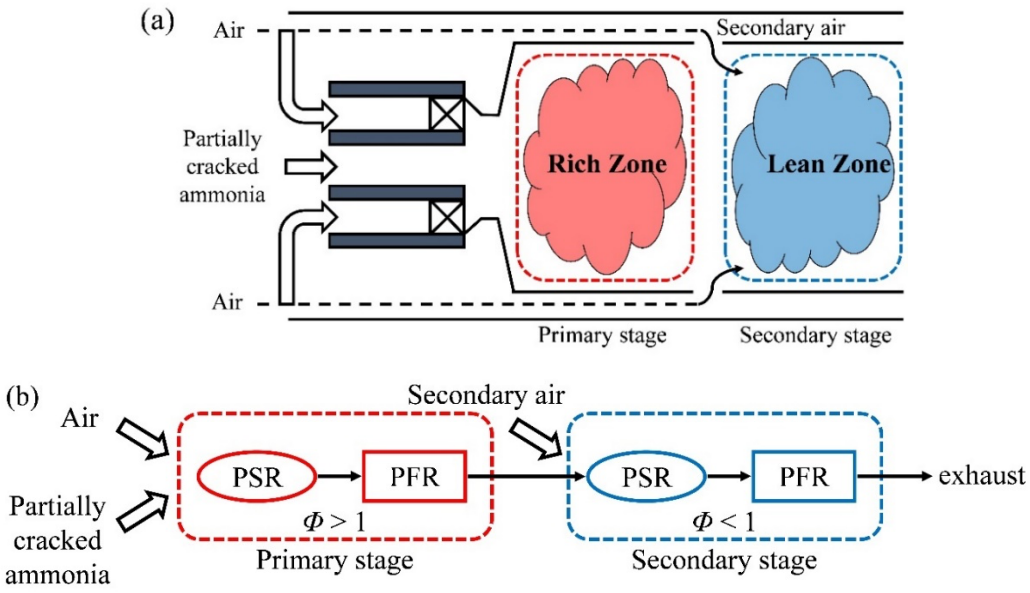

Figure 3.5 (a) The concept of rich-lean burn combustor; (b) CRN model of 2-stage gas turbine combustor.

Table 3.1 Specific pressure, temperature, and residence time parameters.

P (atm)	T_{unburn} (K)	T_{burn} (K)	single stage combustor (ms)		2- stage combustor (ms)			
20	600	1800	τ_{PSR}	τ_{PFR}	τ_{PSR1}	τ_{PSR2}	τ_{PFR1}	τ_{FPR2}
			5	20	3	2	18	2

The parameters for demonstrating NO_X emission characteristics in the CRN model are according to the state-of-the-art H/J class heavy duty gas turbines operating conditions [308]. The specific conditions are fixed and presented in Table 3.1 including the temperature at the outlet of the combustor and inlet air and fuel temperature, as well as total residence times of single stage and 2-staged combustors and PSRs. As inlet conditions, the inlet air and fuel temperature (CIT) is preheated to 600K and same total residence time (τ_{total}) for two combustors is set to 25ms according to the representative residence times in real combustion devices [175], in which the PSRs residence time (τ_{PSR}) is fixed at 5ms and PFR residence time (τ_{PFR}) is 20ms for single stage combustor. As for 2-staged combustor, the total residence time

of each two PSRs is 5ms. While, the factors, such as pressure, overall equivalence ratio, primary stage equivalence ratio for 2-staged combustor and cracking ratio of NH_3, are independently varied to explore the influence of NO_X emission characteristics.

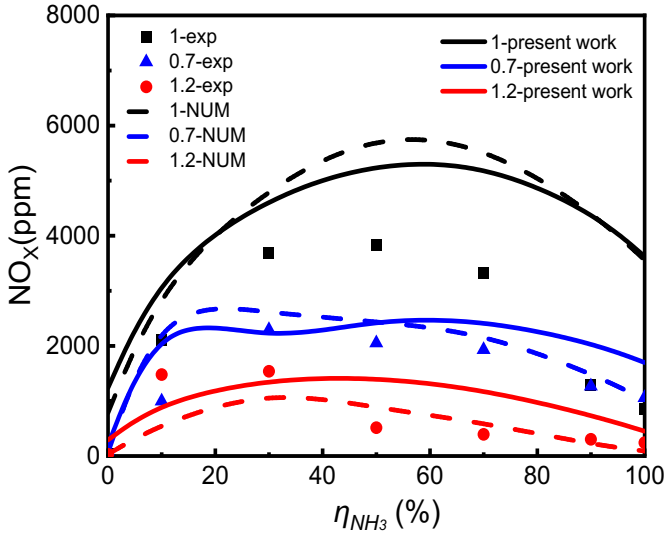

Figure 3.6 NO_X emission comparison of present simulations and experimental and numerical data reported by Zhang et al. [307] at various equivalence ratios. (Symbols: experimental data; Dash lines: simulation results; Solid lines, present work simulation results).

Further validation of the NO_X emissions was presented based on the CRN model established in this paper, shown in Figure 3.6. The parameters for running CRN model are provided from Zhang et al. [307]. They conducted experiments on a model swirl flame combustor for detecting the emission characteristics of CH_4/NH_3/air. In Figure 3.6, the dots and the dash lines are representing their experimental and numerical results separately, and the solid lines show the NO_X emissions calculations at various equivalence ratios in present work. Compared with reported experimental data and numerical results [307], good agreement on the trend of NO_X curves is captured. The differences between model and experimental results are regarded as predictable, since the flow parameters in real combustors are complex and independent with

chemical reaction and time, the limitation of CRN model on the conservation of momentum is not directly calculated. Therefore, the capability of the simplified model to conduct basic research on NO_X emissions is acceptable, instead of reproducing experimental measurements in real combustor.

3.5. Chemiluminescence modelling

In order to provide theoretical support to quantitatively simulate chemiluminescent emission intensity, the one-dimensional freely propagating laminar flame calculation model of CHEMKIN-PRO and PREMIX [309] are employed to perform detailed chemical kinetic calculations, without considering the influence of strain rate. Because the strain rate hardly affects premixed flame structure [310]. Sub-mechanisms of excited state radicals (OH*, CH* and C_2*) [311], which are listed in Table 3.2, are added into the fully developed ethanol model [312]. The effect of complementary sub-mechanisms on the overall combustion characteristics of ethanol can be neglected. Generally, the concentrations of the excited species are quite low due to their short lifetimes.

Seen from Figure 3.7, the radical CH and its excited state CH* are chosen as an example to investigate the relative order of magnitude for mole fraction profiles. The mole fraction profiles are calculated at constant temperature and atmospheric pressure under the stoichiometric ratio condition. It can be found that the peak ratio of CH*/CH is extremely small, around equal to 3.02×10^{-5}. Therefore, the sub-model of excited species is of interest in quasi-steady state assumption [240].

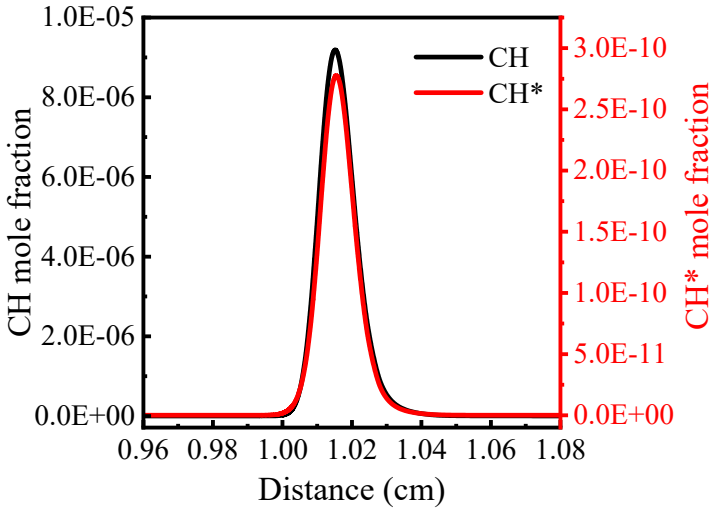

Figure 3.7 Simulation of mole fraction profiles of CH ground state and CH* excited state.

Emitting chemiluminescent light is result from the transition between excited-state radicals to the ground state. The chemiluminescent emission intensity (mol photons/($cm^3 \cdot s^{-1}$) of excited species (OH*, CH* and C_2*) is calculated by following equations [228]:

$$[X_k] = X_k \frac{\rho}{\overline{W}}, \tag{3.28}$$

$$i_k = A_k [X_k], \tag{3.29}$$

where $[X_k]$ is the concentration of the *k*th species (mol/cm^3), A_k is the Einstein coefficient for spontaneous emission (A(OH*)=1.40 × 106 s^{-1} [265], A(CH*)=1.85 × 106 s^{-1}[228], and A(C_2*)=1.0×106 s^{-1}[313]). There are no abundant literatures for C_2* studying, so the Einstein coefficient for C_2* was estimated according to [313]. ρ is mass density (g/cm^3), and $\overline{W}$ is the mean molecular weight (g/mol).

To reveal chemiluminescent emissions per unit flame area, the simulated photon emission intensity across the flame is integrated over the whole numerical length. So, total chemiluminescence emitted from flame is given by:

$$I_k = \int_0^L i_k d\,x, \tag{3.30}$$

where *L* is the integration length (m).

Table 3.2 Chemiluminescence reaction mechanism of OH*[311], CH* [311] and C_2* [314].

Number	Reaction	*A*	*B*	E_a
R106	$C_2H+O<=>CH^*+CO$	1.080×10^{13}	0.000	0.00
R107	$C_2H+O_2<=>CH^*+CO_2$	2.170×10^{10}	0.000	0.00
R108	$CH^*<=>CH$	1.850×10^{6}	0.000	0.00
R109	$CH^*+N_2<=>CH+N_2$	3.030×10^{2}	3.400	-381.00
R110	$CH^*+O_2<=>CH+O_2$	2.480×10^{6}	2.140	-1720.00
R111	$CH^*+H_2O<=>CH+H_2O$	5.300×10^{13}	0.000	0.00
R112	$CH^*+H_2<=>CH+H_2$	1.470×10^{14}	0.000	1361.00
R113	$CH^*+CO_2<=>CH+CO_2$	2.400×10^{-1}	4.300	-1694.00
R114	$CH^*+CO<=>CH+CO$	2.440×10^{12}	0.500	0.00
R115	$CH^*+CH_4<=>CH+CH_4$	1.730×10^{13}	0.000	167.00
R116	$CH+O_2<=>OH^*+CO$	6.00×10^{10}	0.000	0.00
R117	$OH^*<=>OH$	1.450×10^{6}	0.000	0.00
R118	$OH^*+N_2<=>OH+N_2$	1.080×10^{11}	0.500	-1238.00
R119	$OH^*+O_2<=>OH+O_2$	2.100×10^{12}	0.500	-482.00
R120	$OH^*+H_2O<=>OH+H_2O$	5.920×10^{12}	0.500	-861.00
R121	$OH^*+H_2<=>OH+H_2$	2.950×10^{12}	0.500	-444.00
R122	$OH^*+CO_2<=>OH+CO_2$	2.750×10^{12}	0.500	-968.00
R123	$OH^*+CO<=>OH+CO$	3.230×10^{12}	0.500	-787.00
R124	$OH^*+CH_4<=>OH+CH_4$	3.360×10^{12}	0.500	-635.00
R125	$CH_2+C<=>H_2+C_2^*$	7.500×10^{13}	0.000	0.00
R126	$C_2H+H<=>H_2+C_2^*$	1.000×10^{12}	0.000	0.00
R127	$C_2^*+M<=>C_2+M$	2.045×10^{12}	0.000	0.00
R128	$C_2^*<=>C_2$	1.000×10^{6}	0.000	0.00

Although sub-models of excited state species have been widely utilized, it is still required to examine the validity of this comprehensive model when sub-reaction mechanisms for excited state species are added into the ethanol mechanism. Bertran et al. [314] detected light emissions from ethanol flame under pressure of 35.5kPa and an equivalence ratio of 1.0. The experimental records are applied to compare with the kinetics simulation results of OH*, CH* and C_2* intensities that are evaluated by using post-possessing algorithms.

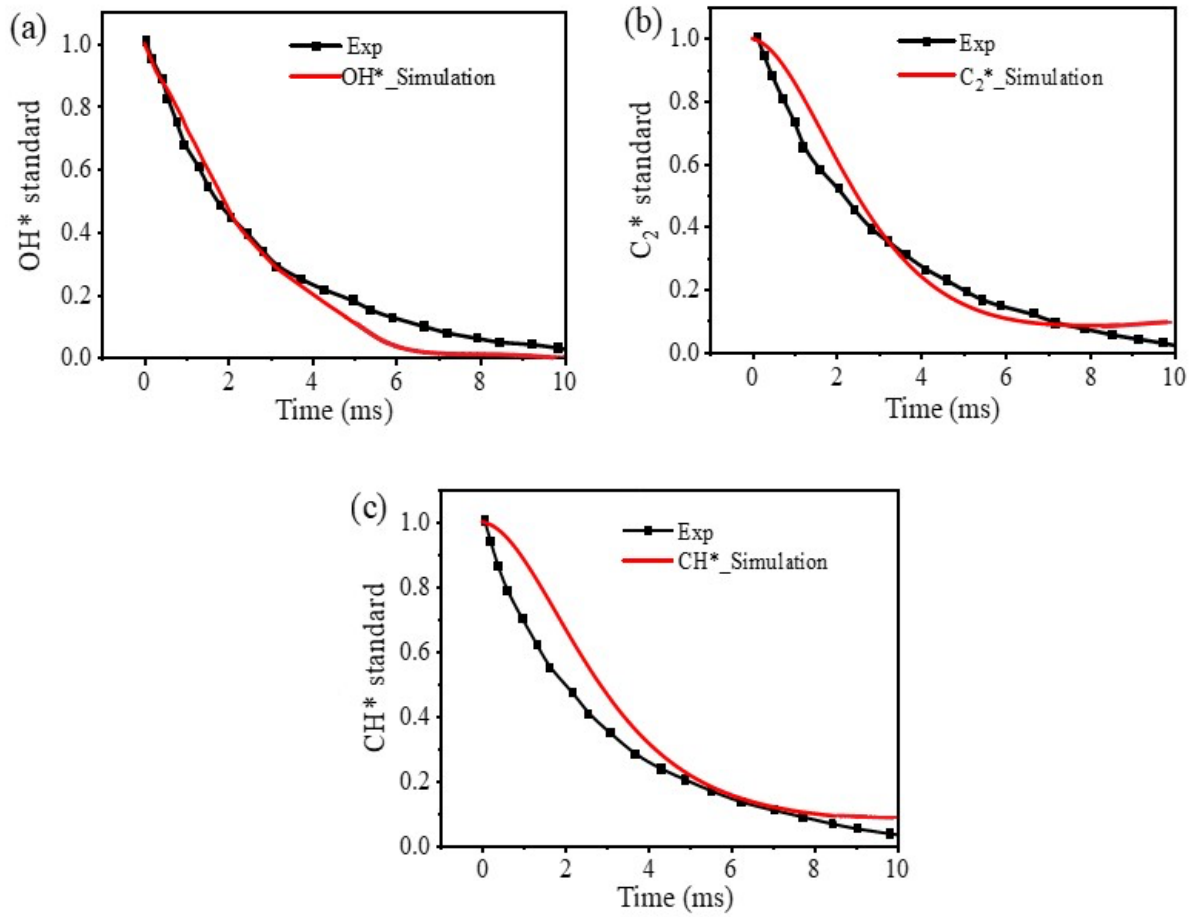

Figure 3.8 Comparison between experimental (black dot line) [314] and simulated (red line) chemiluminescence profiles with standard scale for excited radicals.

Considering that the excited reagents are mainly consumed after emission intensity reaching its peak value, and the reaction process is fairly homogeneous in the decreasing-intensity area that fits the condition of the experiment, so only the destruction rate curves for radiative decay reaction of every excited species are kept for comparison. As displayed in Figure 3.8, it presents the comparison between experimental results (black dot lines) [314] and simulated (red lines) chemiluminescence profiles with a standard scale for excited radicals. The consumption rate curves of radiative decay reaction of every excited species are normalized with its maximum value to compare with experimental data. The curves of chemiluminescent

profiles results do not show any deformation after normalizing. Basically, OH*, CH* and C_2* modelling curves agree well with its experimental chemiluminescent emission intensity. The simulated chemiluminescence results for excited species of the comprehensive model are significantly dependent on the specific reaction paths and intermediate species such as CH, CH_3 and C_2H_2, etc, which will be analysed in the following part. Therefore, the new proposed ethanol comprehensive reduced mechanism can be employed to study the ethanol flame structure and combustion characteristics.

4. Chemical Kinetics Mechanism Reduction

4.1. Introduction

In this chapter, reduced reaction mechanisms for ethanol and $NH_3/H_2/CH_4$ mixtures are developed respectively. In detail, in section 4.2, the DRGEP combined with the GEPA method are integrated to establish the ethanol reduced kinetic mechanism. The reduction methodology and error analysis, as well validations of ignition delay time, species mole fraction in a jet stirred reactor as well as laminar burning velocity over a broad range of conditions are presented in this section. In section 4.3, an integrating method of IPFA and GEPA are firstly employed to reduce $NH_3/H_2/CH_4$ mechanism, including a two-stage reduction process and error analysis. Besides, Extensive validations of the proposed reduced model are conducted by comparing with the detailed mechanism as well as available experimental measurements of ignition delay time in shock tube, species profiles, laminar flame speed over different equivalence ratios, temperatures, and pressures. Results of reduced chemical kinetics mechanism are concluded at the end of this chapter. It shows that the methods that are applied in this work can accurately reduce mechanisms, and the reduced ethanol mechanism and ammonia mechanism can be applied for further study.

4.2. Ethanol Mechanism Reduction and Validation

4.2.1. Reduction methodology and error analysis

Reduced mechanisms with smaller sizes are very promising in further numerical simulation for fuels combustion. They can be used in place of their corresponding comprehensive mechanisms under numerous conditions. In this section, the direct relationship graph with

error propagation (DRGEP) as well as the generalized entropy production analysis (GEPA) approaches are integrated to reduce the full mechanism of ethanol that was proposed and validated by N. Leplat et al. [312]. They investigated the combustion and oxidation of ethanol in both experimental and numerical studies, especially added investigation of JSR experiments on the basis of the work of Daguat et al. [315]. The ethanol mechanism includes 252 reversible reactions and 36 species, and its main feature was widely measured against experimental results. In the first stage of reduction process, unimportant species are supposed to be eliminated by DRGEP approach proposed by Pepiot-Desjardins and Pitsch et al. [77] based on the DRG approach.

Generally, the smaller tolerances are defined, the larger size of reduced mechanisms might be represented. However, it does not necessarily guarantee that larger size mechanisms have better performance than those of smaller size due to the complex nonlinear characteristics of comprehensive chemical mechanisms [316]. In Figure 4.1, number of species and reactions of different generation reduced mechanisms and average relative errors of ignition delay time are presented. The average relative errors are calculated by comparing the ignition delay time of reduced ethanol flame (2.5%C_2H_5OH/7.5%O_2/90%Ar) at different threshold values with experimental results under numerous conditions. The tolerance of average relative error for the reduced mechanism is defined around 10% comparing with experimental data, which is considered to be acceptable in this work.

During the reduction process, the DRGEP method is applied at the first time. The target species were defined as C_2H_5OH, O_2, H_2O and CO_2 under a broad range of test conditions, and different thresholds setting could generate various scale of semi-detailed mechanisms. Figure 4.1 shows

number of species and reactions of different generation reduced mechanisms and mean error of ignition delay time. In Figure 4.1(a), the skeleton mechanism that is produced by using DRGEP method at threshold ε_{DRGEP} = 0.4 has relatively small species and reactions (26 species and 188 reactions) while maintaining reasonable accuracy (uncertainty is approximately 9.08%). Therefore, it is better than other reduced mechanisms and are further reduced at the second stage. Afterwards, the final mechanism (26 species and 105 reactions) that has lower average error and smaller size is generated via the GEPA method based on the former skeleton mechanism, when the threshold α_{GEPA} is 0.003 and uncertainty is about 10.3%. Therefore, this final mechanism is validated and used for further chemiluminescence simulation, seen from Figure 4.1(b).

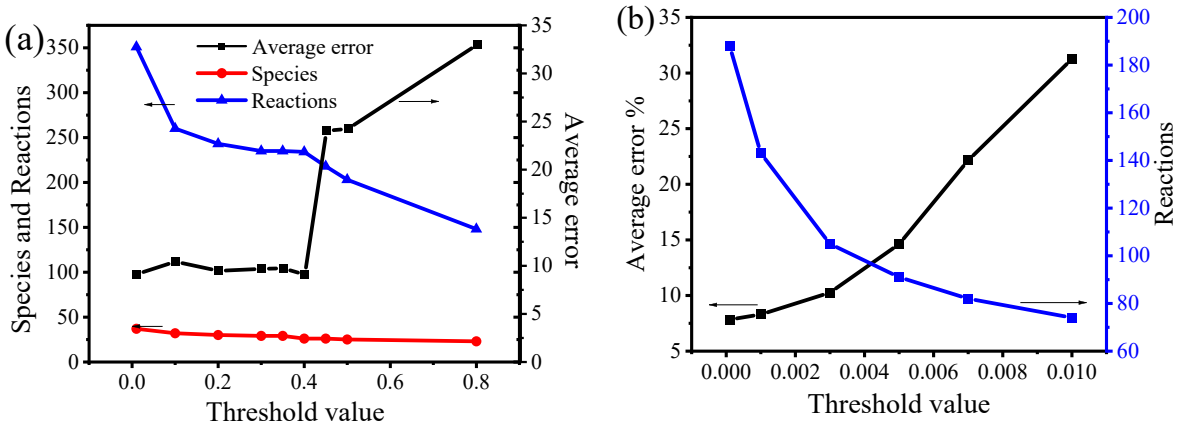

Figure 4.1 (a) Skeleton mechanisms by using DRGEP method; (b) Final reduced mechanisms by using GEPA method.

4.2.2. Validation for ignition delay time

The ignition delay time was identified as a significant parameter of combustion in previous study [312]. It was simulated in the constant volume homogeneous batch reactor in CHEMKIN-PRO package. Natarajan et al. [317] tested the ignition of ethanol oxygen under the condition

of P = 1.0, 2.0atm, T = 1300-1700K, and equivalence ratio which ranges from 0.5 to 2.0. Then, Dunphy et al. [318] also studied behind reflected shock waves but for different conditions. For the reason that the original detailed ethanol mechanism was validated based on the above experiments, these experimental results were also employed to check the accuracy of the ignition delay time for the reduced mechanism.

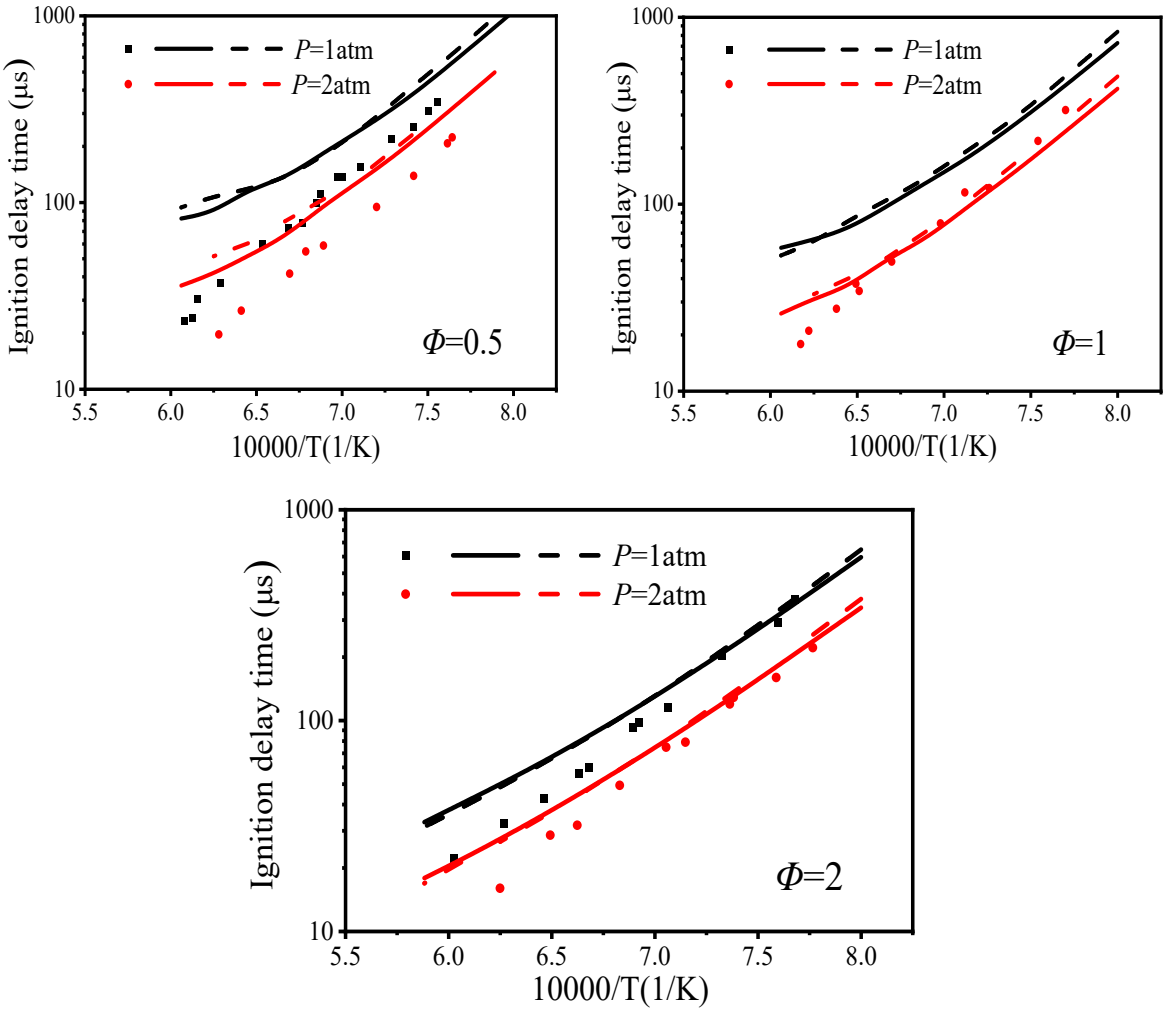

Figure 4.2 Ignition delay times at P = 1, 2atm, Φ = 0.5, 1 and 2 and 90% Ar dilution. Symbols are experimental results from Natarajan et al. [317]; Solid lines are modelling results of detailed mechanism; Dash lines are modelling results of reduced mechanism.

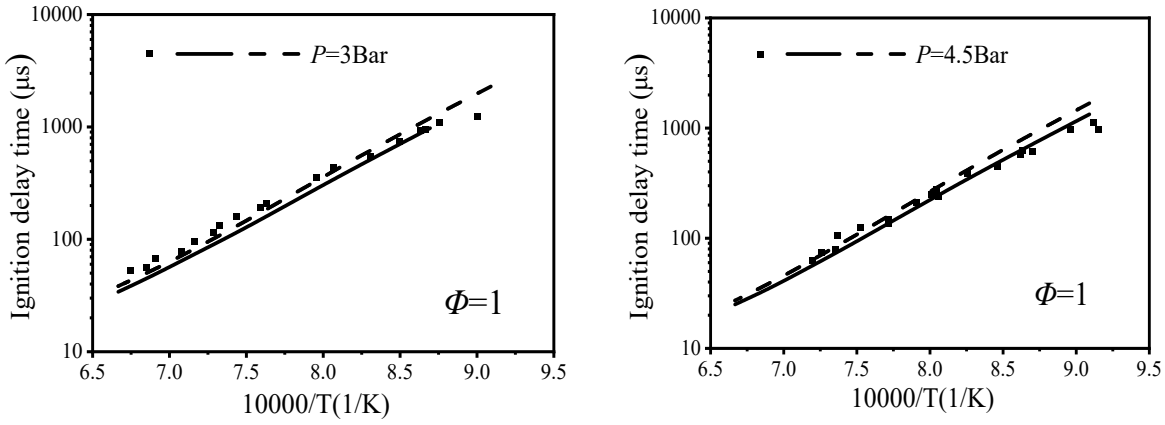

Figure 4.3 Ignition delay times at P = 3, 4.5bar, Φ = 1 and 90% Ar dilution. Symbols are experimental results from Dunphy et al. [318]; Solid lines are the modelling results of detailed mechanism; Dash lines are the modelling results of reduced mechanism.

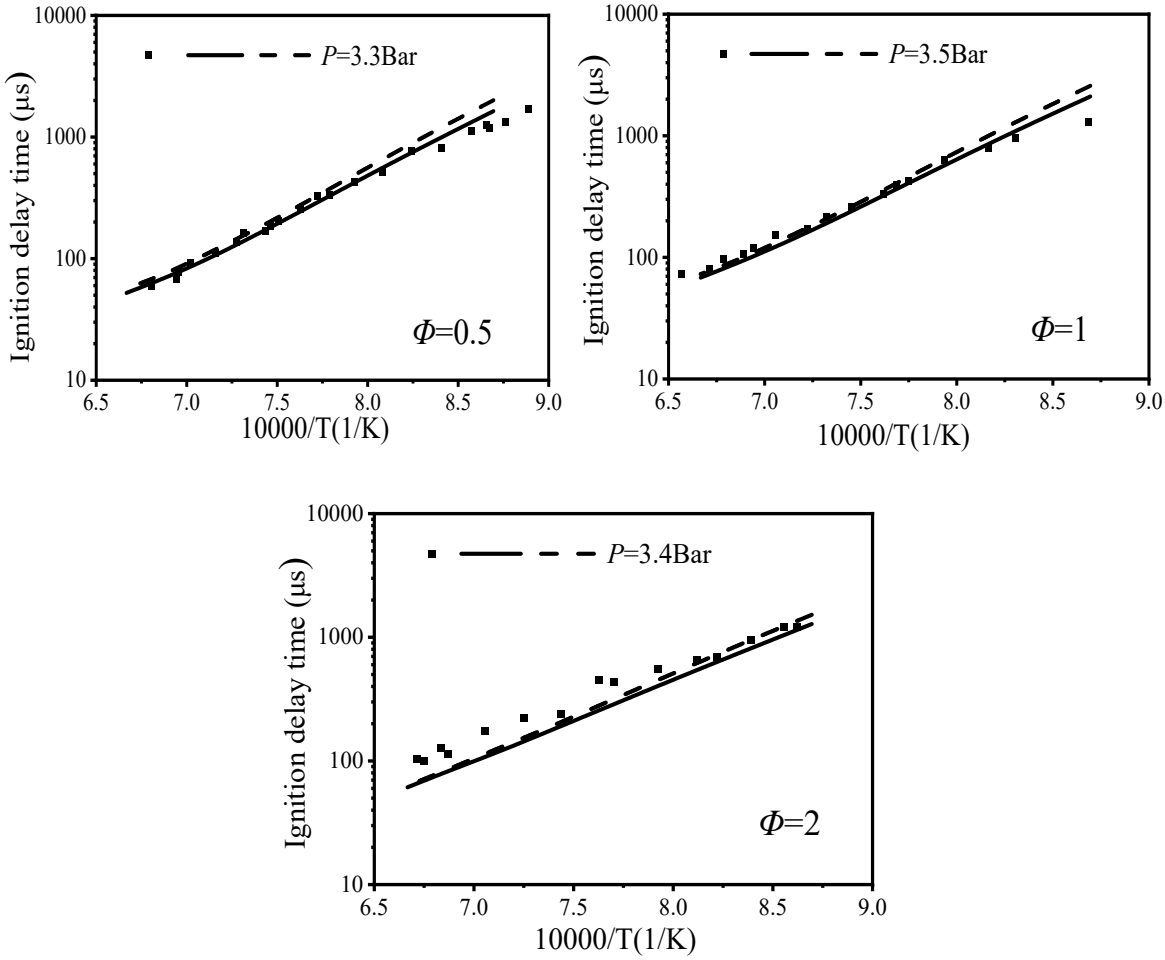

Figure 4.4 Ignition delay times at different pressures, equivalence ratios and 90% Ar dilution. Symbols are experimental results from Dunphy et al. [318]; Solid lines are the modelling results of detailed mechanism; Dash lines are the modelling results of reduced mechanism.

In Figure 4.2-4.4, the ignition delay time of reduced mechanism and detailed mechanism are compared with experimental measurements published by Natarajan et al. [317] (Figure 4.2) and by Dunphy et al. [318] (Figure 4.3, 4.4), where symbols indicate experimental data, solid and dash lines present full and reduced mechanism simulation results respectively. All these models agree with the experimental measurements quite well within uncertainties, and it can well reflect the reducing trend shown by the ignition delay time with the increase of temperature and pressure. Although both ethanol models slightly over-predicted the experimental value at Φ = 0.5, as shown in Figure 4.2, agreements remain generally good between reduced and detailed ethanol mechanism. Therefore, the reduced mechanism enables to well capture the ignition characteristics as the detailed one.

4.2.3. Validation for laminar flame species profile

Laminar flame species profiles were detected using the PREMIX module in the CHEMKIN-PRO software. Considering laminar premixed flame experiments that were performed on a cooled, brass, sintered plate burner with 8cm diameter at 50mbar, the simulation assumed mixture averaged transport, and around 200 grid points (GRAD 0.1, CURV 0.1) were used. The flame inlet parameters setting can be seen from reference [312].

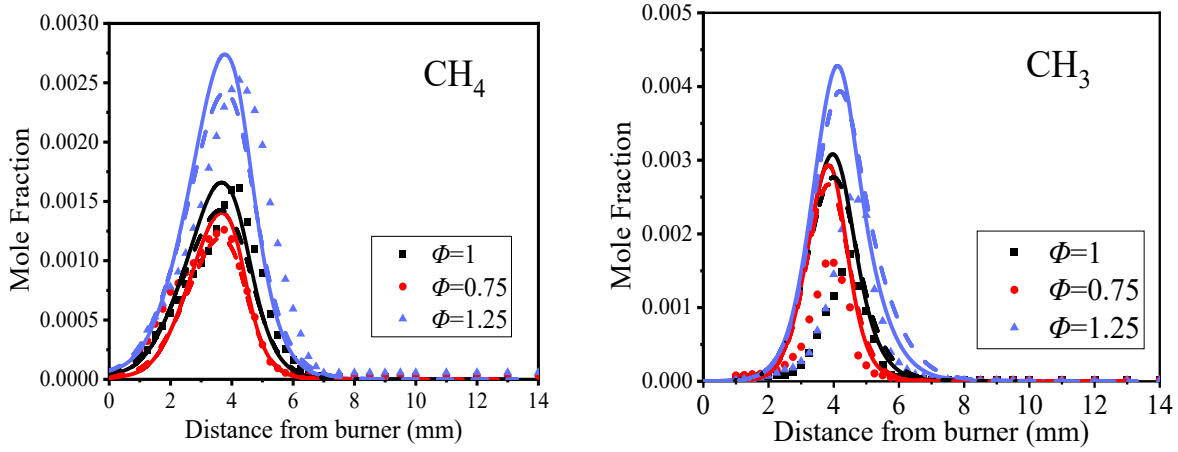

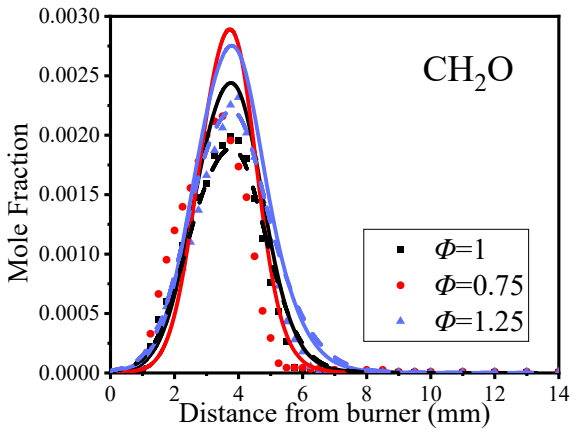
CH2O
Mole Fraction
Distance from burner (mm)
Φ=1
Φ=0.75
Φ=1.25

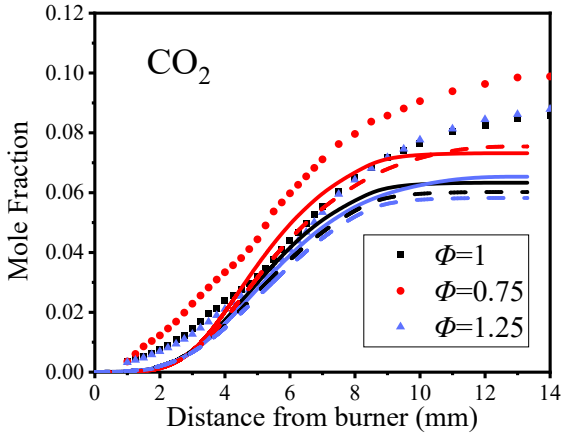
CO2
Mole Fraction
Distance from burner (mm)
Φ=1
Φ=0.75
Φ=1.25

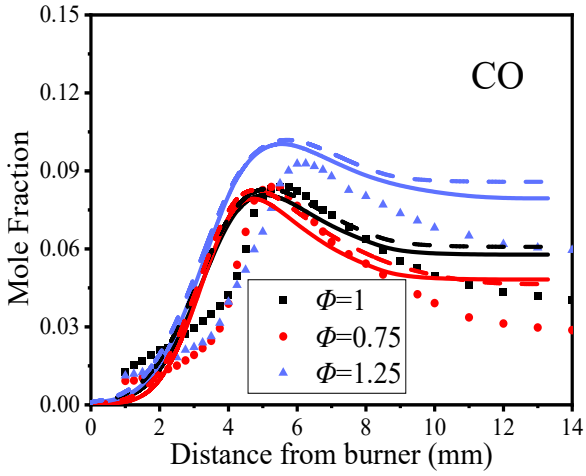
CO
Mole Fraction
Distance from burner (mm)
Φ=1
Φ=0.75
Φ=1.25

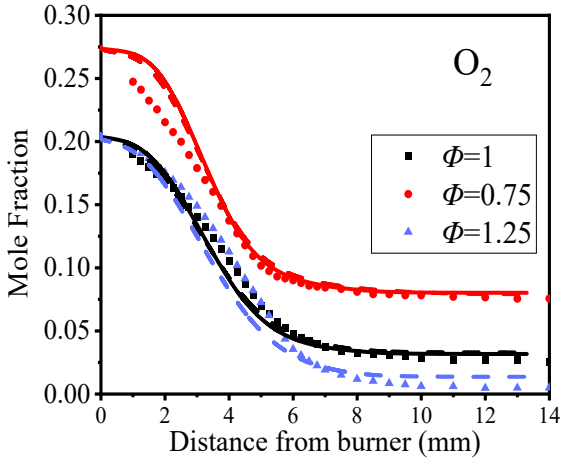
O2
Mole Fraction
Distance from burner (mm)
Φ=1
Φ=0.75
Φ=1.25

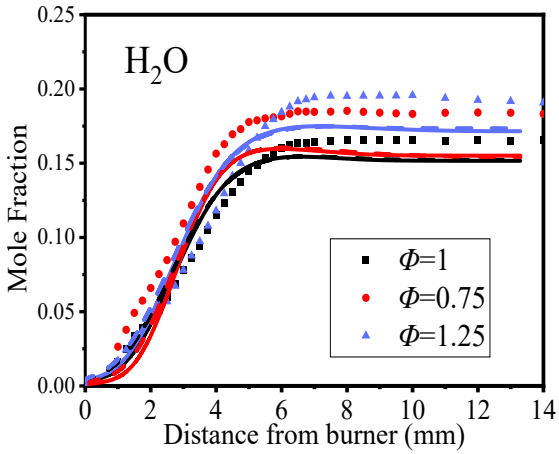
H2O
Mole Fraction
Distance from burner (mm)
Φ=1
Φ=0.75
Φ=1.25

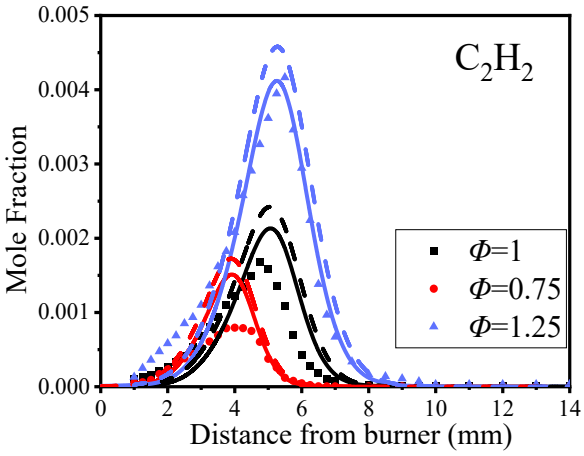
C2H2
Mole Fraction
Distance from burner (mm)
Φ=1
Φ=0.75
Φ=1.25

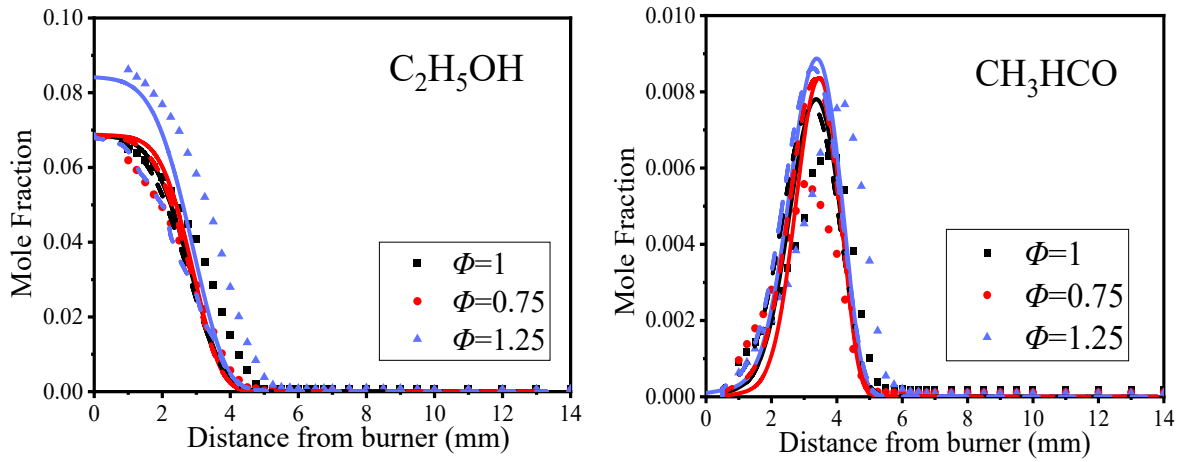

Figure 4.5 Experimental [312] and computed mole fraction profiles of species in ethanol/oxygen/argon flames.

Figure 4.5 shows the comparison of species profile (CH_3, CH_4, H_2O, C_2H_2, CO, CH_2O, O_2, CO_2, CH_3CHO, and C_2H_5OH) between simulation data and experimental value at various equivalence ratio conditions in ethanol laminar flame. Symbols indicate experimental data [312], solid and dash lines present detailed and reduced mechanism simulation results respectively. Generally, good agreements between experimental and modelling results can be observed on the perspective of the positions of concentration profile as well as their maximum values. Because most of CO, CO_2 and H_2O are generated along the flame front, and the mole fraction of these species can be more accurately predicted in both rich and lean ethanol flame. Despite that, the predicted mole fraction of C_2H_2 and CH_2O in lean flame are overestimated than that in rich fuel flame, and the reason could be due to uncomplete combustion with lower concentration of oxygen. In addition, although small discrepancies between simulations and experiments appear for CH_3HCO and CH_3, it notably appears that the difference between detailed and reduced model is not evident. Overall, seen from Figure 4.5, the above phenomenon is well predicted by the proposed reduced mechanism,

presenting great agreement with the detailed mechanism.

4.2.4. Validation for jet-stirred reactor species concentration

Oxidation of ethanol in a jet-stirred reactor (JSR) is simulated using the perfectly stirred reactor (PSR) module in the CHEMKIN-PRO package. Considering the experimental condition, a fixed mean residence time is set as 0.07s, and pressures are set as 1atm and 10atm at different equivalence ratio varying from 0.25 to 2. Mole fraction of main oxidation species is estimated, including H_2, CH_4, H_2O, C_2H_2, C_2H_4, C_2H_6, CO, CH_2O, O_2, CO_2, CH_3CHO, and C_2H_5OH, and compared with experimental data that reported in the reference [77] and [315] accordingly.

In Figure 4.6-4.7, the comparison of kinetic modeling results as well as JSR experimental data for species mole fraction of ethanol oxidation are presented. Symbols indicate experimental data, solid and dash line present detailed and reduced mechanism simulation results respectively. Seen from Figure 4.6-4.7, it is obviously that the simulated values of detailed and reduced model are extremely close excluding the predictions of CH_2O at Φ = 0.3, 0.6 and p = 10atm. However, the prediction of CH_2O mole fraction of reduced model shows more accuracy than that of detailed model, because the reaction rate constants are calculated during reduction process via DRGEP based on constant-volume homogeneous batch reactor that differ from jet-stirred reactor. In addition, discrepancy between to models are acceptable because its mean value is within a factor of two of the experimental data that can be regarded as reasonably accurate. Indeed, reduced mechanism model curve fits very well with the detailed model and have a similar trend as the experimental data at all of cases.

(a)

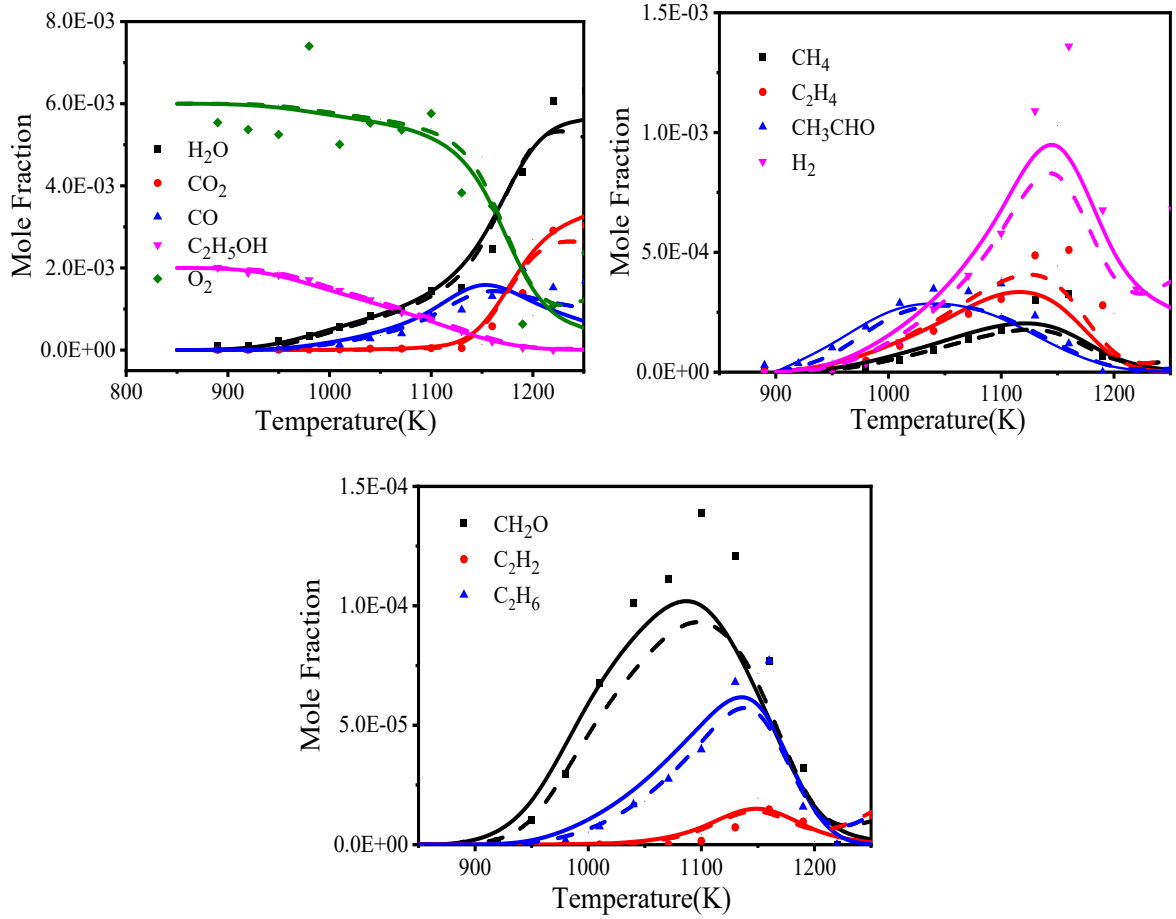
8.0E-03
6.0E-03
4.0E-03
2.0E-03
0.0E+00
Mole Fraction
800
900
1000
1100
1200
Temperature(K)
H2O
CO2
CO
C2H5OH
O2
1.5E-03
1.0E-03
5.0E-04
0.0E+00
CH4
C2H4
CH3CHO
H2
1.5E-04
1.0E-04
5.0E-05
CH2O
C2H2
C2H6

(b)

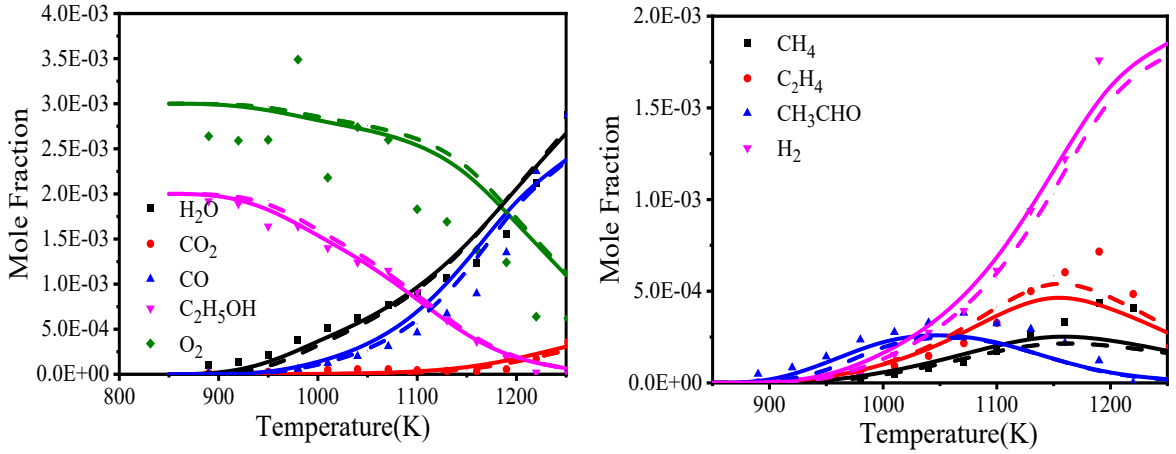
4.0E-03
3.5E-03
3.0E-03
2.5E-03
2.0E-03
1.5E-03
1.0E-03
5.0E-04
0.0E+00
Mole Fraction
800
900
1000
1100
1200
Temperature(K)
H2O
CO2
CO
C2H5OH
O2
CH4
C2H4
CH3CHO
H2

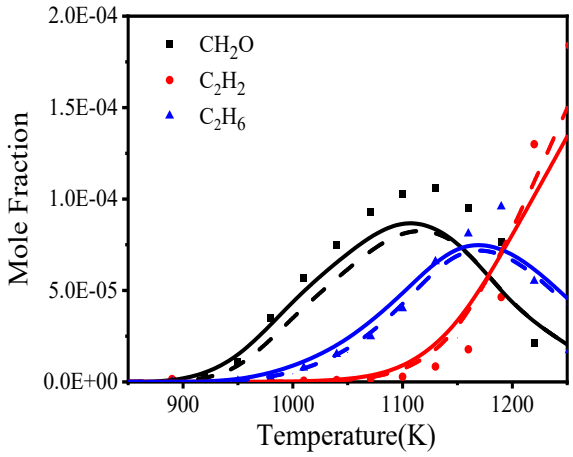
2.0E-04
1.5E-04
1.0E-04
5.0E-05
0.0E+00
Mole Fraction
CH2O
C2H2
C2H6
900
1000
1100
1200
Temperature(K)

(c)

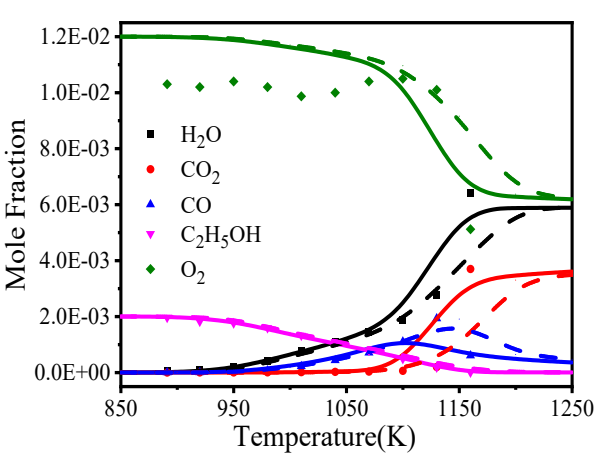
1.2E-02
1.0E-02
8.0E-03
6.0E-03
4.0E-03
2.0E-03
0.0E+00
Mole Fraction
H2O
CO2
CO
C2H5OH
O2
850
950
1050
1150
1250
Temperature(K)

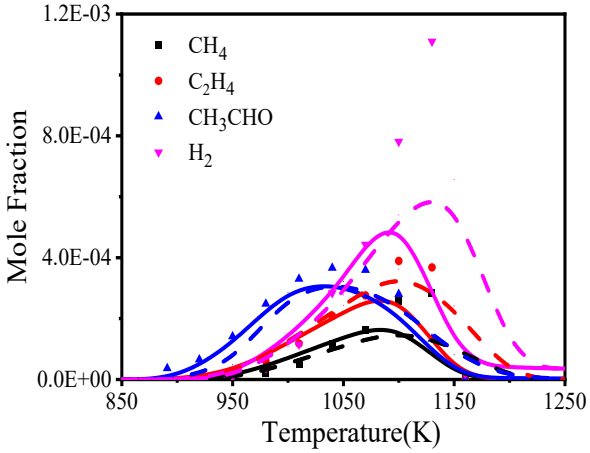
1.2E-03
8.0E-04
4.0E-04
0.0E+00
Mole Fraction
CH4
C2H4
CH3CHO
H2
850
950
1050
1150
1250
Temperature(K)

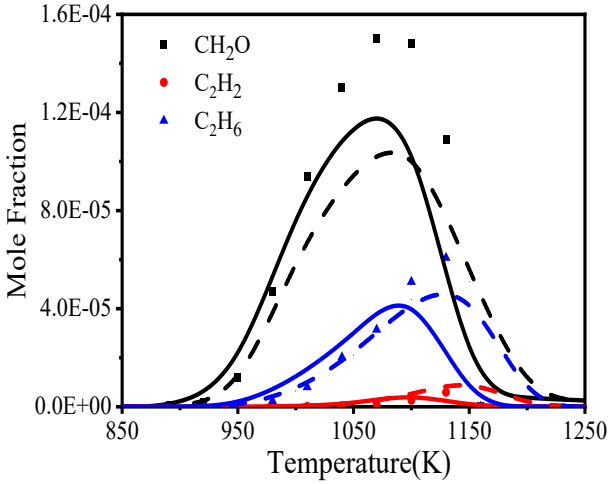
1.6E-04
1.2E-04
8.0E-05
4.0E-05
0.0E+00
Mole Fraction
CH2O
C2H2
C2H6
850
950
1050
1150
1250
Temperature(K)

(d)

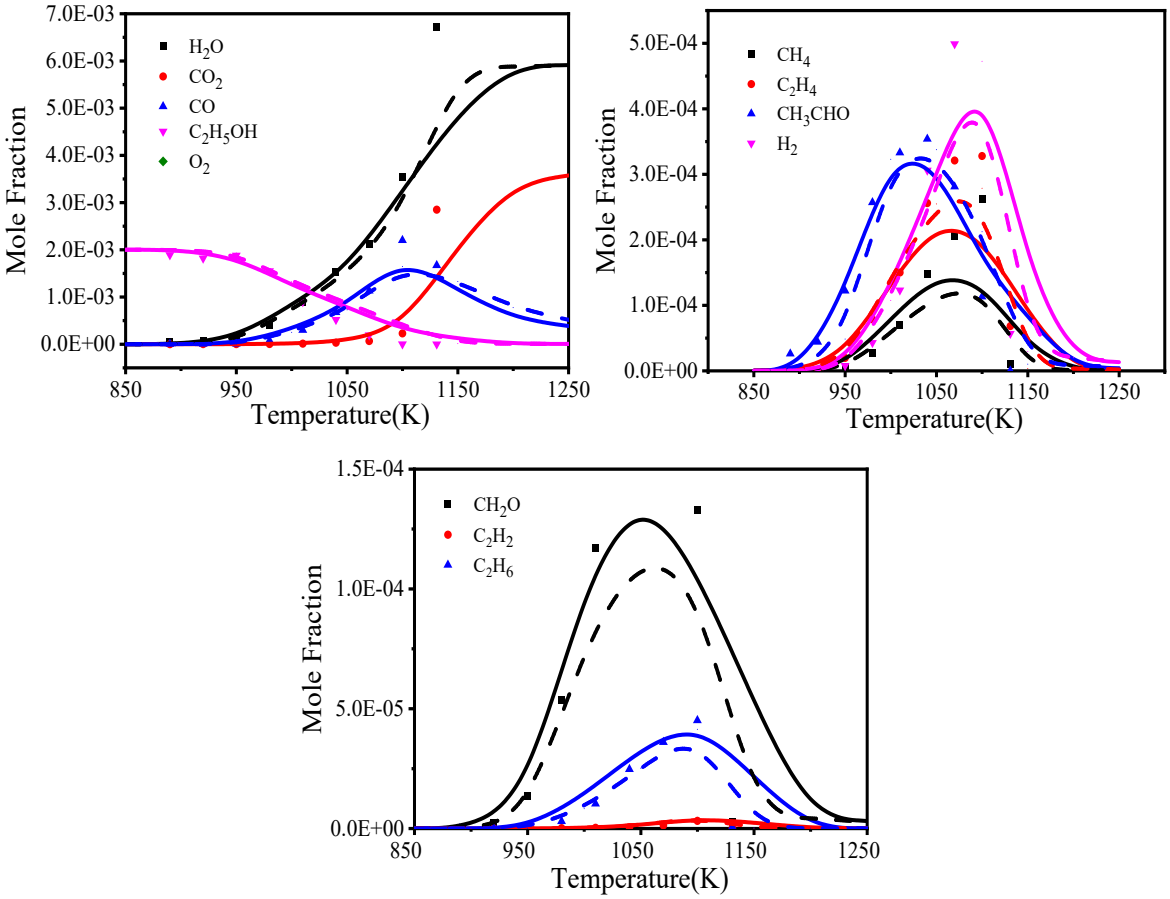

Figure 4.6 Oxidation of ethanol in a JSR at 1atm and (a) Φ = 1, (b) Φ = 2, (c) Φ = 0.5, (d) Φ = 0.25.

(a)

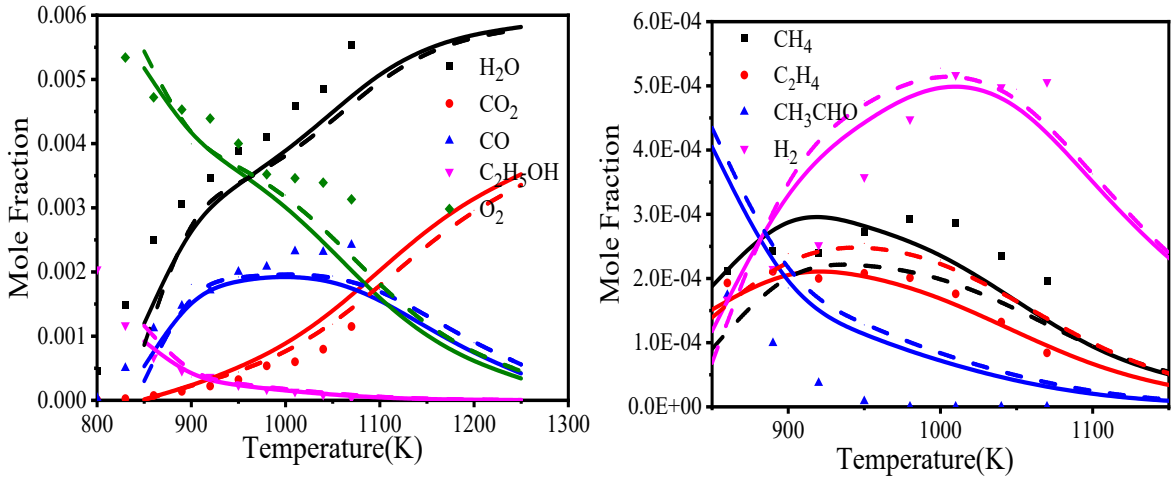

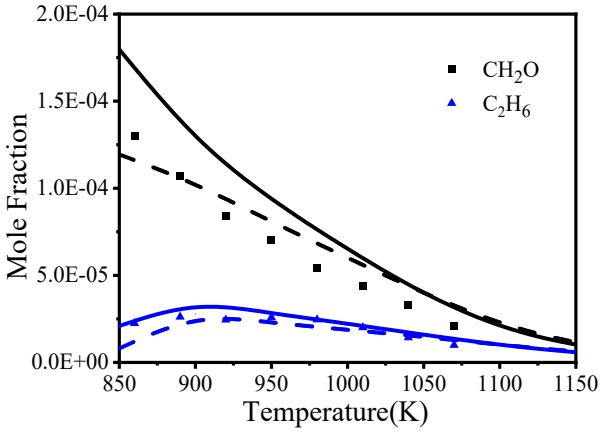
2.0E-04
1.5E-04
1.0E-04
5.0E-05
0.0E+00
Mole Fraction
850
900
950
1000
1050
1100
1150
Temperature(K)
CH2O
C2H6

(b)

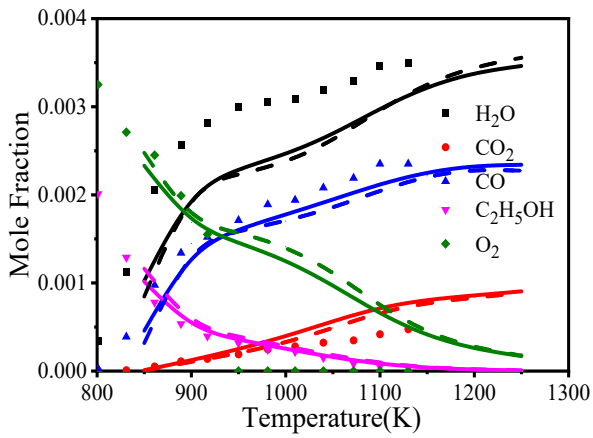
0.004
0.003
0.002
0.001
0.000
Mole Fraction
800
900
1000
1100
1200
1300
Temperature(K)
H2O
CO2
CO
C2H5OH
O2

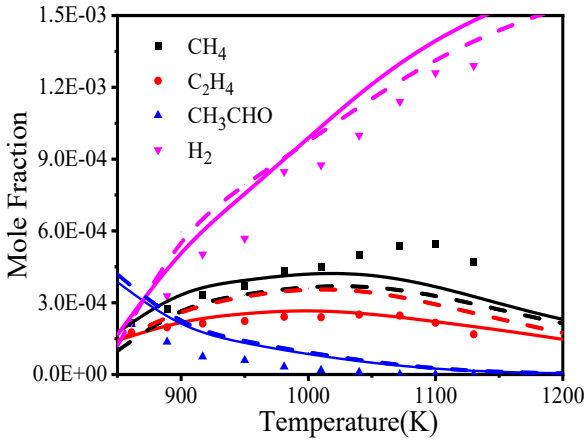
1.5E-03
1.2E-03
9.0E-04
6.0E-04
3.0E-04
0.0E+00
Mole Fraction
900
1000
1100
1200
Temperature(K)
CH4
C2H4
CH3CHO
H2

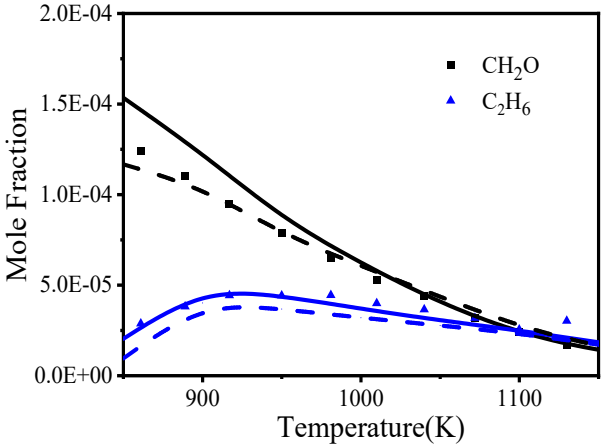
2.0E-04
1.5E-04
1.0E-04
5.0E-05
0.0E+00
Mole Fraction
900
1000
1100
Temperature(K)
CH2O
C2H6

(c)

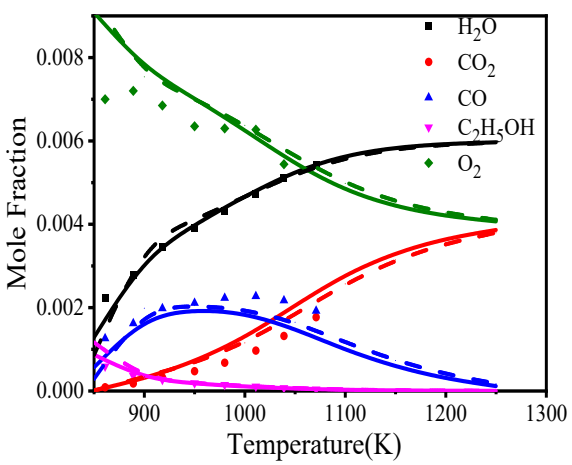
Mole Fraction
Temperature(K)
H2O
CO2
CO
C2H5OH
O2

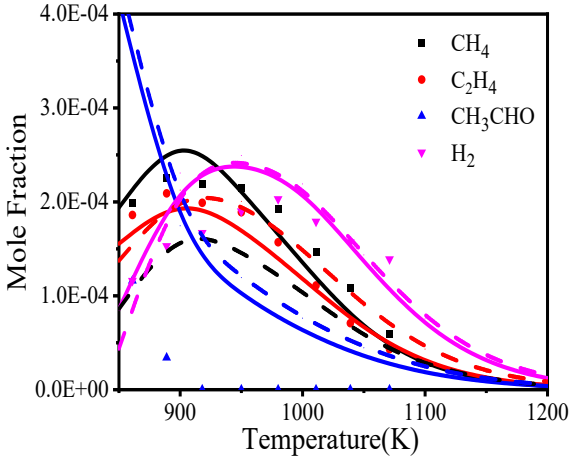
Mole Fraction
Temperature(K)
CH4
C2H4
CH3CHO
H2

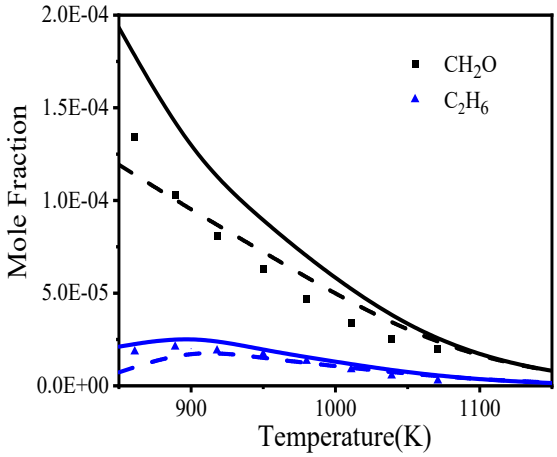
Mole Fraction
Temperature(K)
CH2O
C2H6

(d)

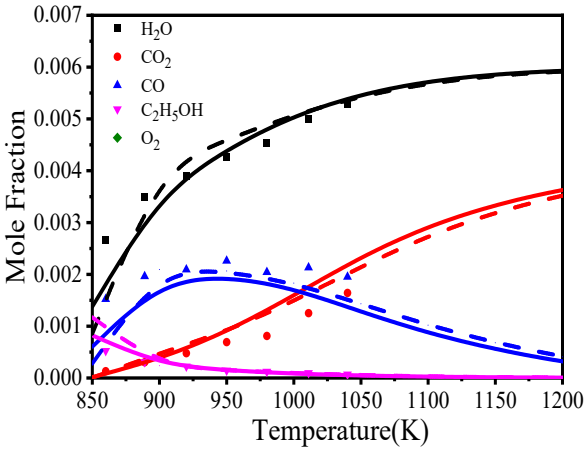
Mole Fraction
Temperature(K)
H2O
CO2
CO
C2H5OH
O2

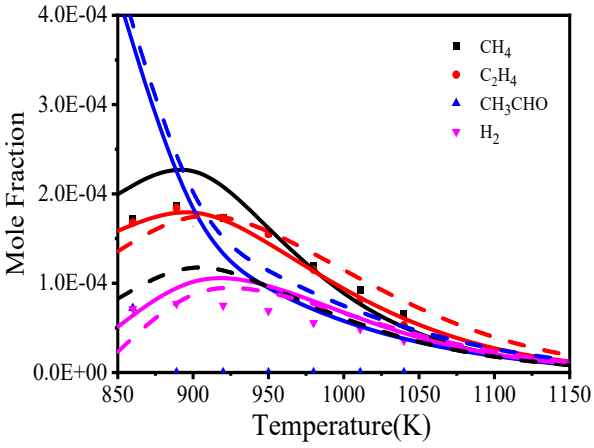
Mole Fraction
Temperature(K)
CH4
C2H4
CH3CHO
H2

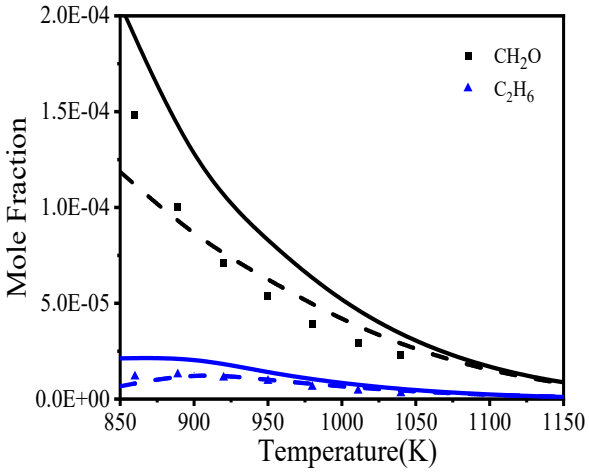

Figure 4.7 Oxidation of ethanol in a JSR at 10atm and (a) Φ = 1, (b) Φ = 2, (c) Φ = 0.6, (d) Φ = 0.3.

4.3. Ammonia Mechanism Reduction and Validation

Ammonia has been considered as a carbon-free fuel with great promise for power generation and marine sector in recent years. To have a better understanding of $NH_3/H_2/CH_4$ combustion process as well as exhaust gases formation, an accurate and relatively compact reduced kinetics mechanism for $NH_3/H_2/CH_4$ mixtures is developed. A two-stage reduction process combining IPFA and GEPAis performed for the first time to establish the reduced mechanism.

4.3.1. Reduction process and error analysis

The procedure of the two-stage mechanism reduction methodology is illustrated in Figure 4.8. Similarly, when applying the IPFA and GEPA methods, the size of the reduced skeletal mechanism depends non-linearly on the algorithm threshold, generally smaller algorithm thresholds lead to larger mechanism size. Therefore, an acceptable skeletal mechanism, which has a great compromise between compactness and accuracy, can be obtained through trial and error.

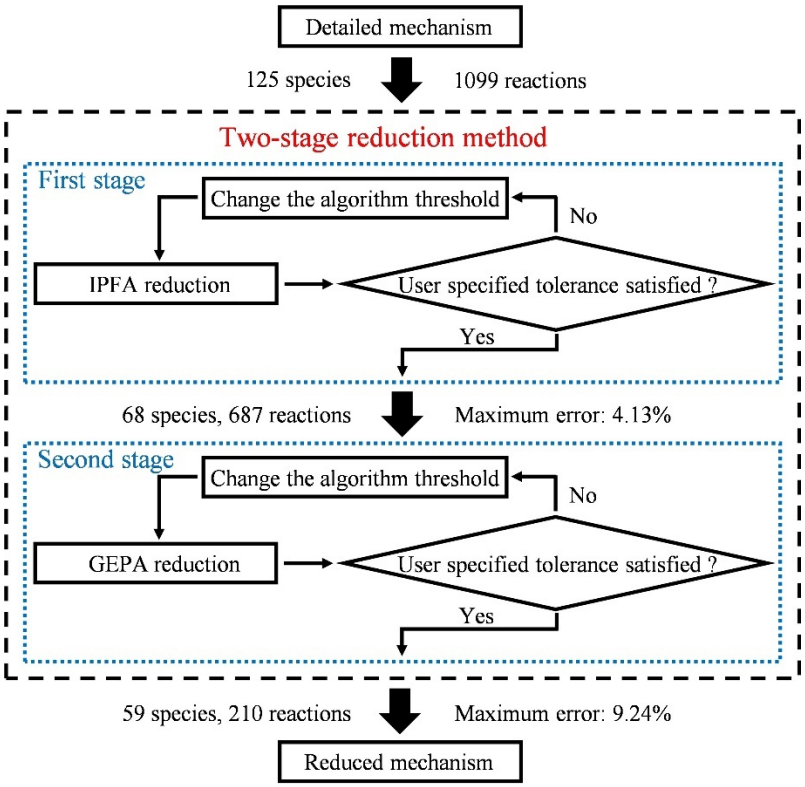

Figure 4.8 Mechanism reduction procedure.

(i) Skeletal reduction using IPFA.

The detailed mechanism of $NH_3/H_2/CH_4$ mixtures proposed by Shrestha et al. [196] is applied to be the original mechanism in this study, which involves 125 species and 1099 reactions. As reported in their work, validations have been conducted against numerous experimental data for ammonia and ammonia-hydrogen blends oxidation.

In order to generate an effective reduced mechanism for $NH_3/H_2/CH_4$ mixtures, reactants NH_3, H_2, CH_4, O_2 and the products N_2, H_2O, CO_2 are set to be the target species under various testing conditions, covering equivalence ratio of 0.5-2.0, pressure of 1-40atm, as well as initial temperature of 1300-2500K. The ignition delay time is selected to be the target parameter used for examination. The ignition delay time indicates the time required to obtain the maximum pressure rising rate in modelling.

Figure 4.9(a) presents the variation of maximum error and the number of remaining species as well as reactions with the threshold ε_{IPFA}. The maximum error is the maximum of relative errors between the reduced mechanism using the IPFA method and the detailed mechanism. As depicted in Figure 4.9(a), the error keeps constant at about 4% when ε_{IPFA} is below 1.15. However, when ε_{IPFA} exceeds this value, the error increases significantly. In this stage for reduction, the aim is to control the error at a quite small value, which is less than the specified tolerance (5% in this work), meanwhile keeping the skeletal mechanism as compact as possible. Therefore, according to the results shown in Figure 4.9(a), a skeletal mechanism including 68 species as well as 687 reactions is obtained (the error is 4.13%).

(ii) GEPA reduction.

Though the number of species in reduced mechanism using the IPFA approach has been reduced sharply, the skeletal mechanism size still quite large. In this stage, the GEPA method is employed to perform the further reduction by eliminating redundant reactions. Reduction of skeletal mechanism of the first stage is conducted using a sampling solution database for the ignition process covering equivalence ratio of 0.5-2.0, pressure of 1-40atm, as well as initial temperature of 1300-2500K. The ignition delay time is also chosen to be the target parameter.

Figure 4.9(b) presents the relation between the maximum error, the number of species as well as reactions and the threshold ε_{GEPA}. Here, the maximum error is the maximum of relative errors between the reduced mechanism applying the GEPA method and the detailed mechanism. The specified tolerance is set as 10%, which can allow the final reduced mechanism to be more compact under the condition of comparatively small error. It is seen

from Figure 4.9(b), the final reduced mechanism involving 59 species and 210 reactions is obtained (the error is 9.24%).

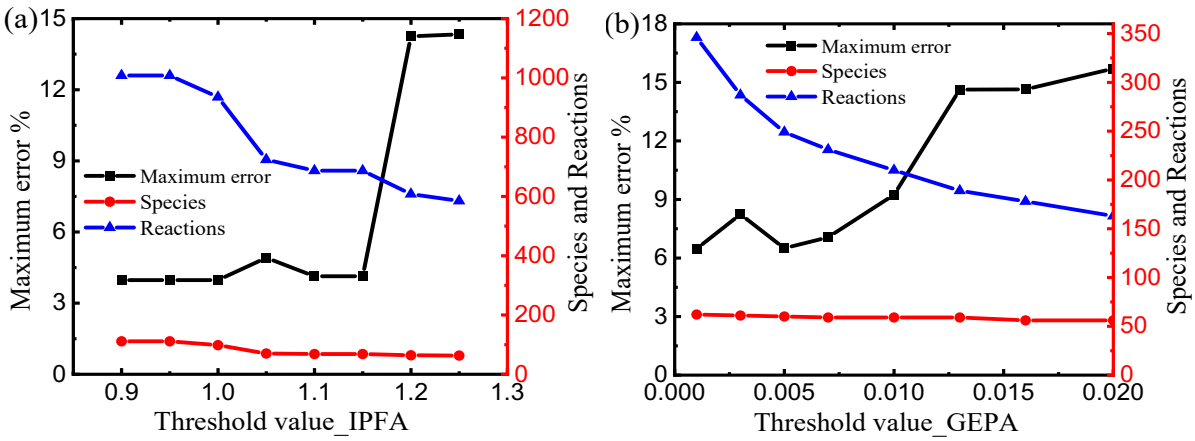

Figure 4.9 The variation of maximum error and the number of remaining species as well as reactions with the threshold in the reduction process using (a) IPFA, and (b) GEPA.

4.3.2. Validation for ignition delay time

Validation of ignition delay times is completed by comparing calculated values of detailed as well as reduced mechanisms with the experimental data of shock tube. Shu et al. [101] performed ignition delay experiments of ammonia/air mixture in a high-pressure shock tube (HPST) at near 20 and 40atm, high temperatures (1100 –1600K), as well as equivalence ratios of 0.5, 1.0, and 2.0. According to results of Shu et al. [101], the total uncertainty in the experiment is estimated to be less than 20%.

Table 4.1 shows the conditions for $NH_3/O_2/N_2$ mixture simulation according to the shock tube experiments conducted by Shu et al. [101]. In Figure 4.10, the predicted ignition delay times among detailed mechanism, reduced mechanism, as well as experimental data are compared at various equivalence ratios. Within the uncertainties, both models fit experiment equally well. It is particularly noted that there is quite small difference in predictions of ignition delay

time between detailed and reduced model. Additionally, the developed reduced mechanism well depicts that ignition delay time shows a reducing trend with increasing pressure.

Table 4.1 The parameters of $NH_3/O_2/N_2$ mixture in a shock tube [101].

Mixture	Φ	NH_3/%	O_2/%	N_2/%
1	0.5	12.3	18.4	69.3
2	1.0	21.9	16.4	61.7
3	2.0	35.9	13.5	50.6

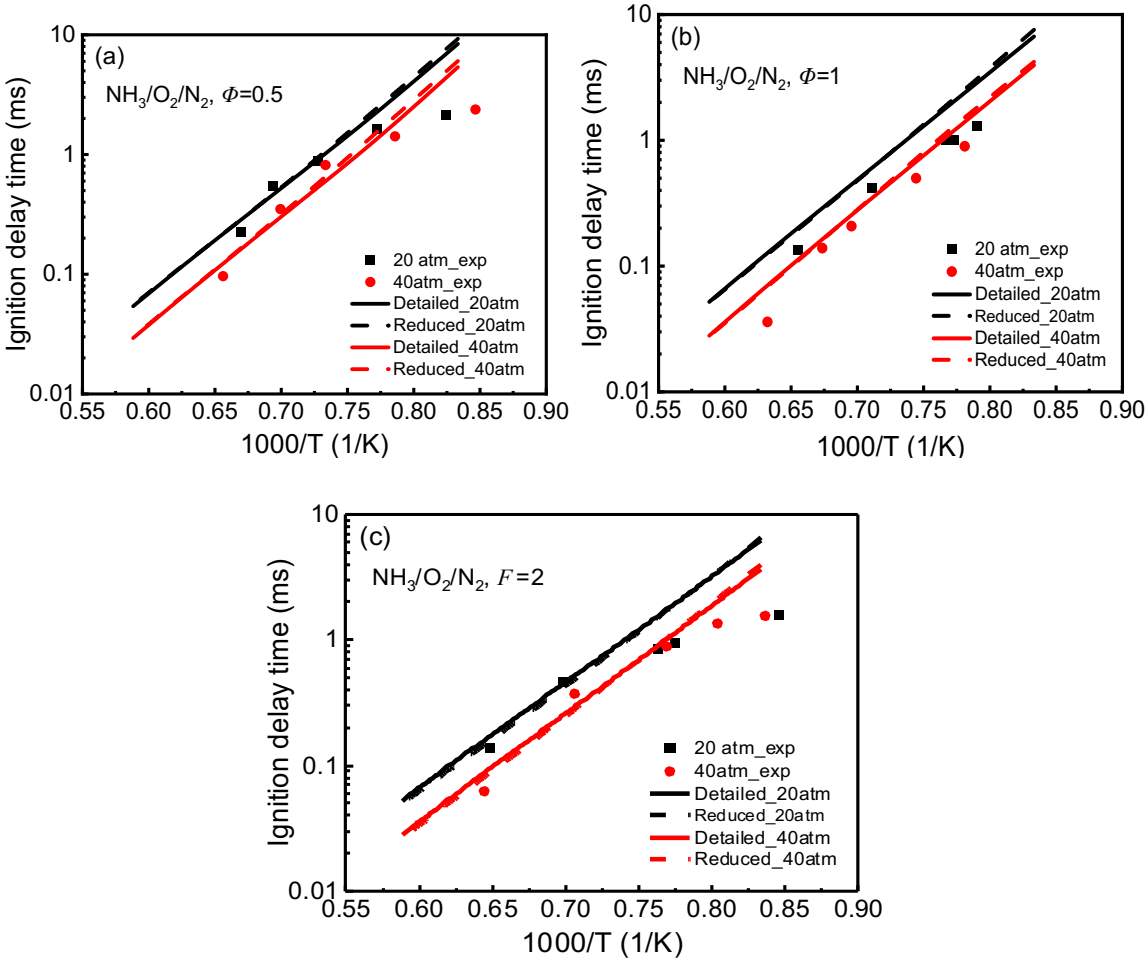

Figure 4.10 Comparison of the predicted ignition delay times of reduced and detailed mechanisms with experiments data for $NH_3/O_2/N_2$ mixture. Solid lines: detailed mechanism predictions [196], dash lines: reduced mechanism predictions (present work), symbols: experiment from [101].

Mathieu and co-workers [102] measured ignition delay times under condition of high temperatures (1560–2455K), three pressures (1.4, 11, and 30bar) as well as three equivalence ratios (0.5, 1.0, and 2.0) with highly diluted ammonia mixtures in Ar (98–99%). The simulation conditions of NH_3/O_2/Ar mixture are given in Table 4.2. Figure 4.11 shows the ignition delay times of NH_3/O_2/Ar mixture at various equivalence ratios and pressures. Same as Figure 4.10, the solid and dash lines represent simulated results of detailed and reduced mechanisms respectively, and the symbols are experimental data. Although both of these two mechanisms slightly under predict experimental data at 1.4 atm, it can be found that predictions by the reduced mechanism show considerably good agreement with results of the detailed model. The two lines in three mixtures can even be regarded as overlapped. The ignition characteristics are well captured by the reduced mechanism within the error tolerance.

Table 4.2 The compositions of NH_3/O_2/Ar mixture in a shock tube [102].

Mixture	Φ	NH_3/%	O_2/%	Ar/%
4	0.5	0.4	0.6	99
5	1.0	0.5715	0.4285	99
6	2.0	0.7273	0.2727	99

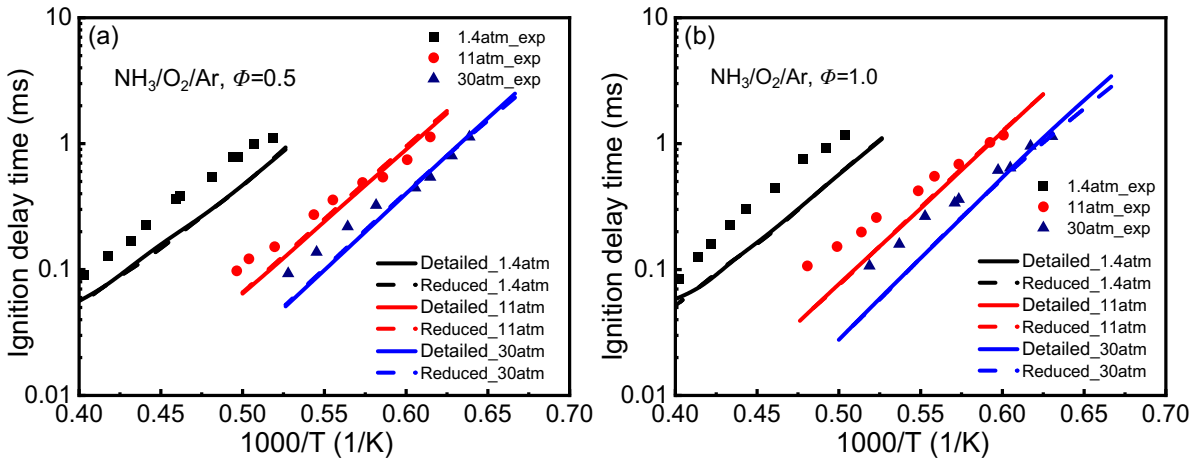

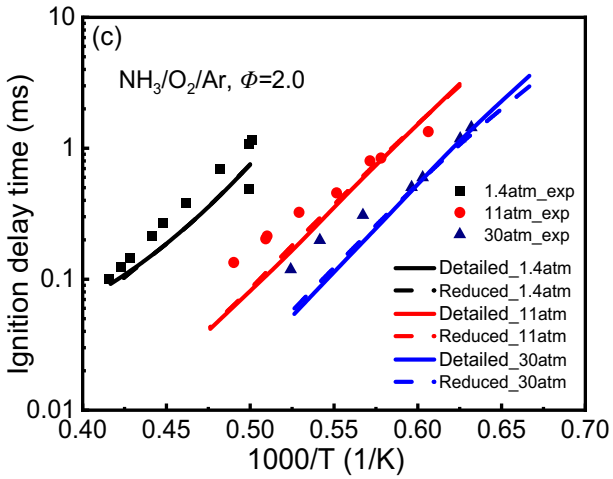

Figure 4.11 Comparison of the predicted ignition delay times of reduced and detailed mechanism with experiments data [102] for $NH_3/O_2/Ar$ mixture.

Xiao et al. [91] studied ignition characteristics for 60%NH_3/40%CH_4/air mixture with shock tube experiments. The measurements were performed behind reflected shock waves at pressure of 2-5atm, temperature of 1369-1804K and different equivalence ratios (0.5, 1, 2). Experimental results are compared with numerical predictions of detailed and reduced kinetic mechanism, presented in Figure 4.12. It can be seen that prediction results of reduced model show satisfactory agreement with experimental data and detailed mechanism simulations within the wide range of conditions. To sum up, a good agreement between predictions and measurements is captured, which indicates that the reduced kinetic mechanism is capable to reflect the ignition characteristics within the wide range of the equivalence ratios, temperatures, as well as pressures.

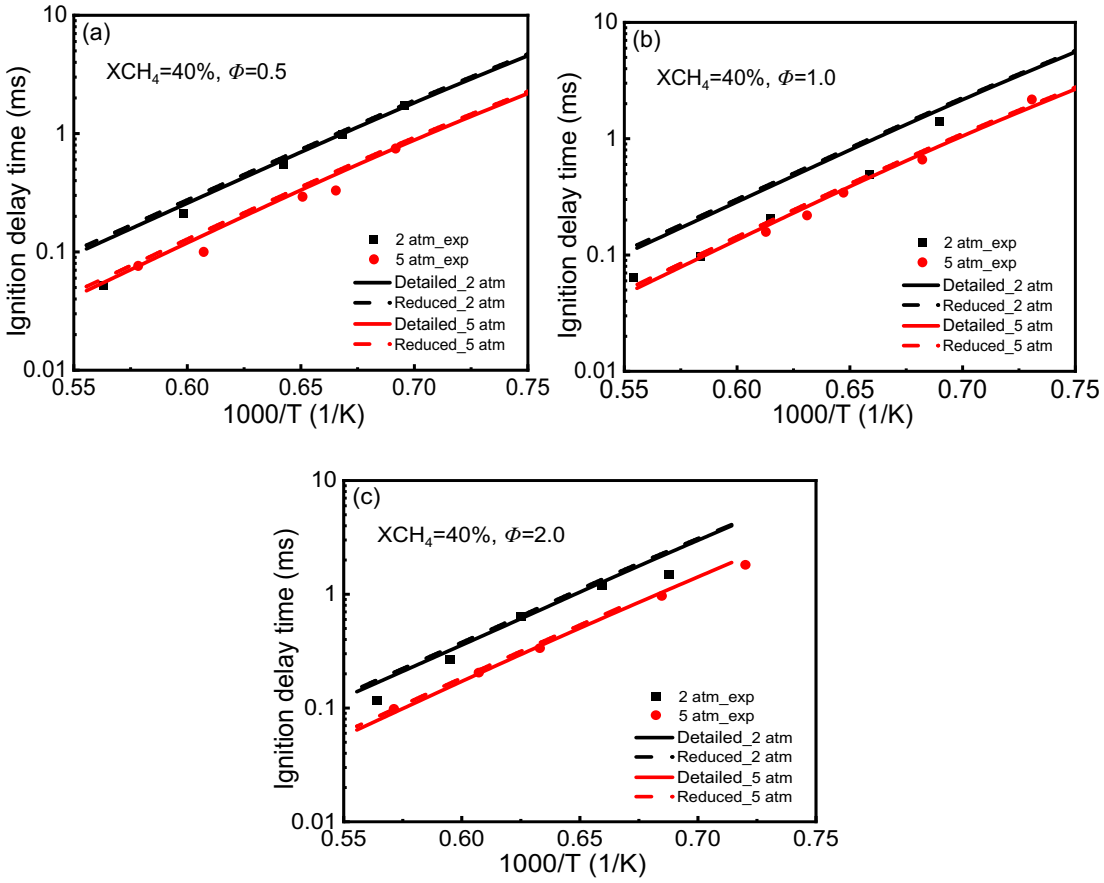

Figure 4.12 Comparison of the predicted ignition delay times of reduced and detailed mechanism with experiments data [91] for 60%NH_3/40%CH_4/air mixture.

4.3.3. Validation for jet-stirred reactor species concentration

Zhang et al. [319] investigated the oxidation of ammonia/hydrogen mixtures by implementing jet-stirred reactor (JSR) oxidation experiments at atmospheric pressure as well as intermediate temperatures (800-1280K). According to the experimental condition, the total initial mole fraction of NH_3/H_2 mixture is 2000ppm, in which the content of hydrogen ranges from zero to 70 vol% at equivalence ratio of 0.25 and 1.0. Mole fraction of intermediates for NH_3/H_2 mixture oxidation is simulated using the perfectly stirred reactor (PSR) module of the CHEMKIN-PRO package where mean residence time τ is fixed at 1s. The detailed operation parameters from literature [319] are displayed in Table 4.3.

Table 4.3 Detailed operation parameters for the oxidation of NH_3/H_2 mixture in JSR [319]

Φ	X_(H2)%	NH_3/ppm	H_2/ppm	O_2/%	N_2/%
0.25	0	2000	0	1	98.8
0.25	10	1800	200	0.94	98.86
0.25	30	1400	600	0.82	98.98
0.25	50	1000	1000	0.7	99.1
0.25	70	600	1400	0.58	99.22
1.0	0	2000	0	0.25	99.55
1.0	10	1800	200	0.235	99.565
1.0	30	1400	600	0.205	99.595
1.0	50	1000	1000	0.175	99.625
1.0	70	600	1400	0.145	99.655

In Figure 4.13 and 4.14, mole fraction of main oxidation species (NH_3, H_2O, NO, N_2O) is calculated and compared with experimental data reported by Zhang et al. [319] at the equivalence ratio of 0.25 and 1.0 respectively. The lines present the simulation results of reduced mechanism and symbols indicate experimental data. As seen from Figure 4.13, the predicted conversion of NH_3 and H_2O of reduced mechanism model fits very well with the experimental results under varying conditions at Φ = 0.25. Besides, the reduced model predicts the mole fraction of NO reasonably when H_2 content ranges from zero to 30 vol%. It is noted that the reduced model under-predicts the yields of NO when H_2 content are 50% and 70%. Moreover, the N_2O mole fractions are over-predicted generally, the peaks are twice higher than those of experimental data at lean-fuel conditions. This is mainly because the application range of equivalence ratio is 0.5-2 for Shrestha's detailed mechanism. Although the discrepancies of the simulated and experimental N_2O mole fraction are obvious, it is still able to capture the enhanced effects of H_2 blending.

At Φ= 1, shown in Figure 4.14, the results present similar trends with those at Φ= 0.25 under varying H_2 content. Furthermore, the predictions of the reduced mechanism are considerably consistent with experimental data under all the conditions investigated. In addition, the experimental data of NO and N_2O mole fraction is well predicted by the developed reduced model. The overall results show that blending hydrogen is able to improve the oxidation reactivity of NH_3 and increase the NO mole fraction. Therefore, the reduced kinetics mechanism basically captures the variation of species concentration in JSR, which is considered accurately in research conditions.

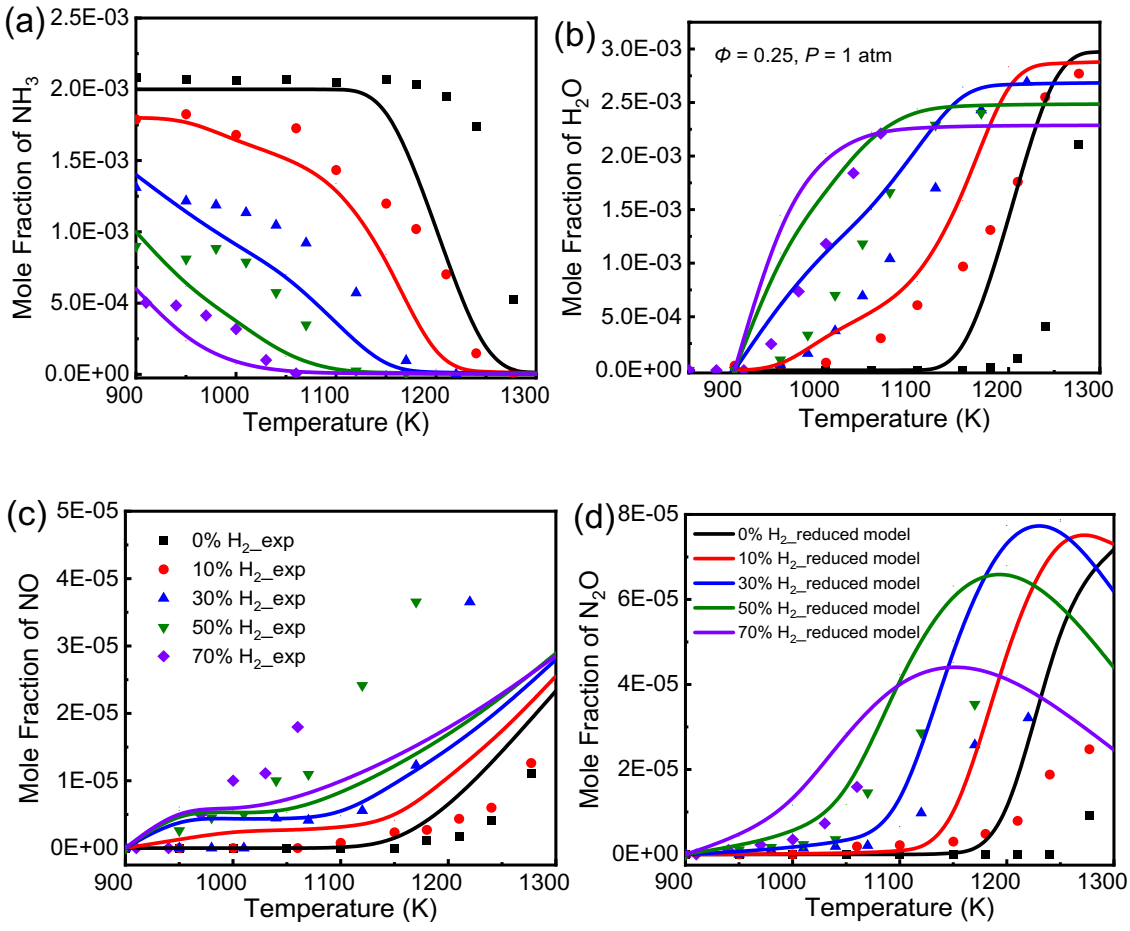

Figure 4.13 Comparison of modeling and experimental results [319] for species concentration of NH_3/H_2 oxidation in JSR at Φ= 0.25, diluted by N_2. Other parameters are P = 1atm, τ = 1s.

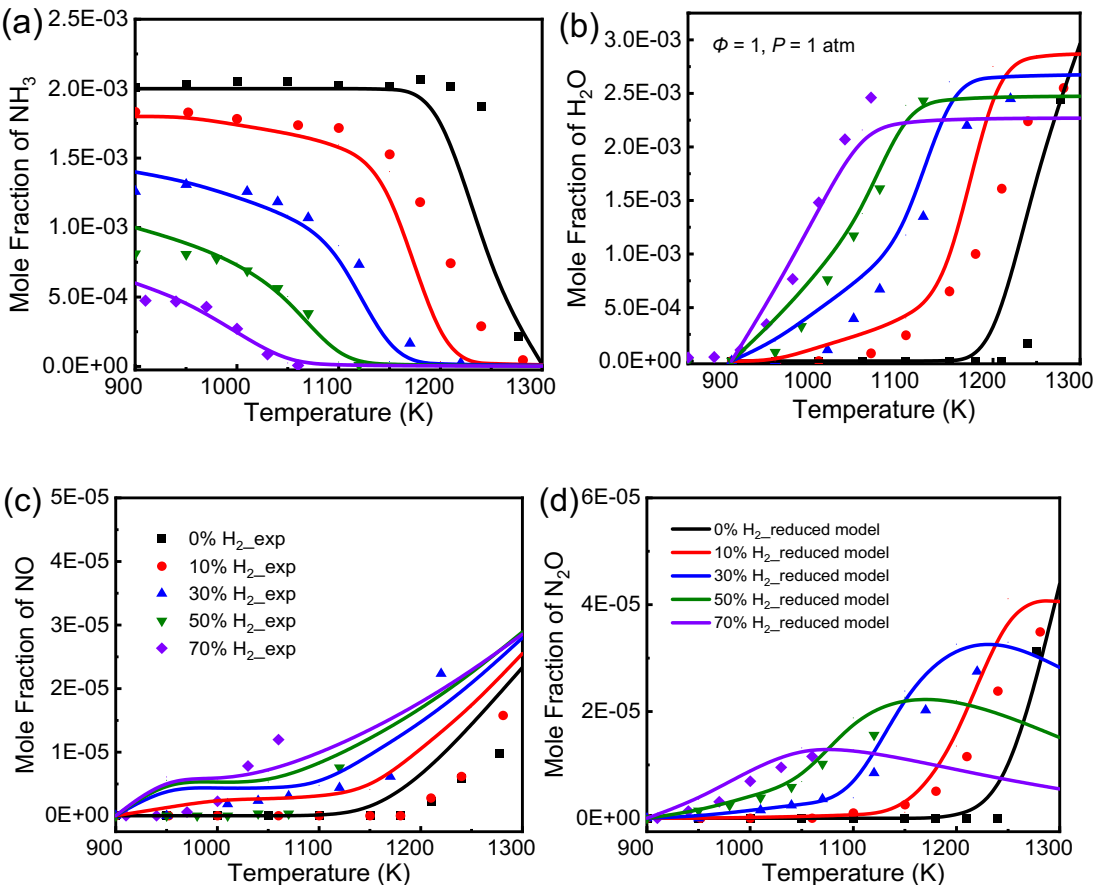

Figure 4.14 Comparison of modeling and experimental results [319] for species concentration of NH_3/H_2 oxidation in JSR at Φ = 1.0, diluted by N_2. Other parameters are P = 1atm, τ = 1s.

4.3.4. Validation for laminar flame speed

Premixed laminar flame is simulated employing the PREMIX module in the CHEMKIN-PRO software. The thermal diffusion (i.e., Soret effect) is considered in one-dimensional simulation, and the number of grid points is approximately 1000 with adaptive mesh parameters (GRAD 0.2, CURV 0.2). Figure 4.15 displays the comparison of simulated results and experimental data [320,7,6,321,8,322,323,126,127] for laminar flame speeds of NH_3/air at 1atm and 298K conditions. Due to the different measurement methods of ammonia laminar flame speed, the subtle differences among experimental values are reasonable. It is seen in Figure 4.15, that Shrestha's detailed mechanism shows good agreement with the measurements under lean

and stoichiometric conditions, while discrepancies appear at rich fuel side, which is in accordance with the study of Shrestha et al. [196]. In rich conditions, the curve of detailed model fits well with the measurements from Ronney (1998) [126] and Mei et al. (2019) [7]. As for the reduced mechanism based on Shrestha detailed mechanism, good agreement are observed compared with the experiment and calculated results of laminar flame speed for detailed model. Generally, the proposed reduced mechanism is able to reflect the experimental trends qualitatively. It shows that the laminar flame speed first increases with Φ rising to about 1.1, and then shows a decreasing trend at Φ > 1.1.

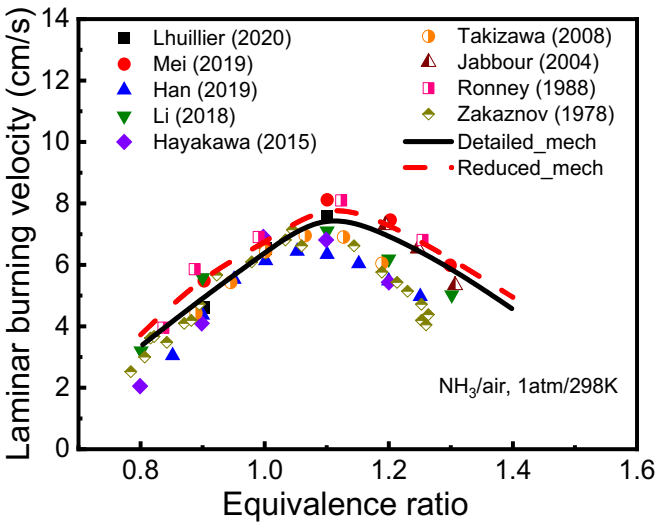

Figure 4.15 The variation of laminar burning velocities of NH3/air flames with Φ, measured in the works of Lhuillier et al. [320], Mei et al. [7], Han et al. [6], Li et al. [321], Hayakawa et al. [8], Takizawa et al. [322], Jabbour et al. [323], Ronney [126], Zakazno et al. [127], and predicted using the Shrestha's detailed mechanism and the present reduced mechanism.

Figure 4.16 presents the laminar flame speeds of NH_3/H_2/air blends under P = 1atm, T = 473K as a function of equivalence ratio with varying H_2 content (X_H_2%) in mixtures. The symbols represent experimental results reported by Shrestha et al. [196], and the solid and dash lines are simulation results using detailed as well as reduced mechanism correspondingly. It is

observed that the reduced model agrees well with experimental measurements especially under lean and stoichiometric conditions. In addition, the results of reduced model are slightly over-predicted compered to detailed model in general. However, the discrepancies of simulation results between the detailed and reduced model are considerably small, and the errors are around ±5%. In Figure 4.16, it also shows that the laminar flame speed increases with more content of hydrogen varying from zero to 30 vol%, which indicates that blending H_2 is an effective option to improve ammonia combustion. Besides, the tendencies of laminar flame speed in NH_3/H_2/air blends at 473K show the same pattern as that of oxidation in NH_3/air flame at 298K.

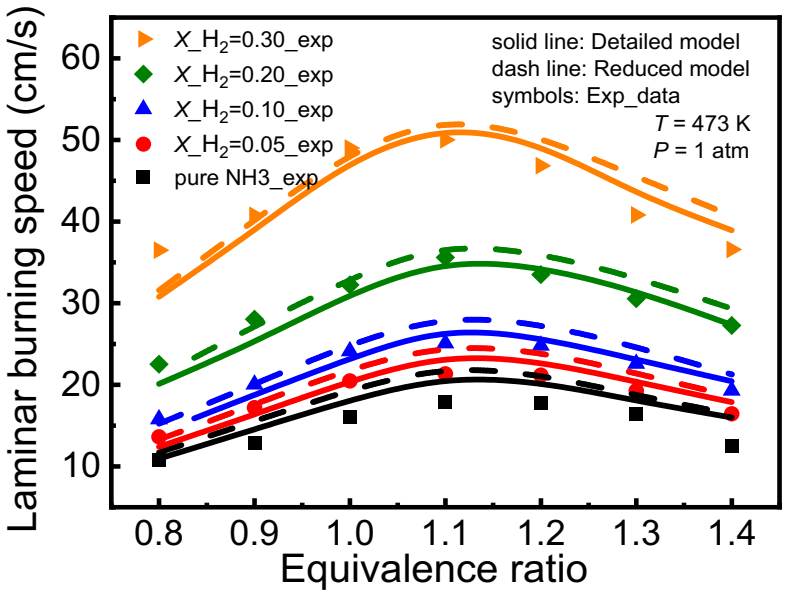

Figure 4.16 Comparison of reduced and detailed modeling with experimental results [196] for laminar burning velocity of NH_3/H_2/air blends oxidation at various equivalence ratios and H_2 content (P = 1atm, T = 473K).

The effect of H_2 content on the laminar flame speed is demonstrated in NH_3/H_2/air flame at P = 1 atm, T = 298K, and Φ = 1.0, shown in Figure 4.17. Experimental values (Symbols) were reported by Lee (2010) [107], Han (2019) [6] and Lhuillier (2020) [320] in recent years. It can

be illustrated that the laminar flame speed has a monotonic increase with H_2 content in NH_3/H_2/air flame. The curves of laminar flame speed for detailed and reduced model are almost overlapped for H_2 content in the blend below 30%. For H_2 content in the blend above 30%, the gap between two models begins to appear, but the error is still small, for example, the values of laminar flame speed in reduced as well as detailed model are around 33.90 and 31.28, respectively.

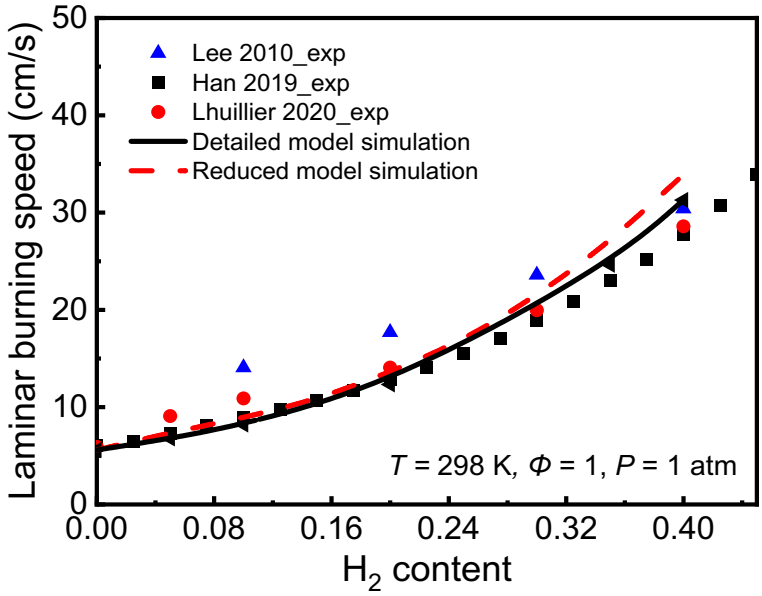

Figure 4.17 Comparison of reduced and detailed modelling with experimental results [6,107 ,320] for laminar burning velocity of NH_3/H_2/air blends oxidation at various H_2 content (P = 1atm, T = 298K, Φ=1.0).

Figure 4.18 shows measured laminar flame speeds [320] compared with the model predictions for NH_3/H_2/air blends at P = 3atm and T = 473K. Both detailed and reduced models over-predict the laminar burning velocity for pure NH_3 combustion. With blending 10% H_2 in the fuel, the accuracy of predictions is improved. Generally, the best agreement is found with measurements at rich-fuel conditions, while it is slightly overestimated under lean to stoichiometric conditions.

Figure 4.19 demonstrates the effect of pressure (1, 3, 5 atm) on the laminar flame speed in NH_3/H_2/air flame at T = 473K, Φ = 1.1, and various H_2 content. Basically, the reduced mechanism captures the experimental trends at different conditions very well. The laminar burning velocity rises with the increase of H_2 content in mixture and decrease of pressure. In addition, it can be observed that predictions of the reduced model are slightly higher than measurements and detailed model predictions but remain within the error margins of experiments. Besides, the laminar flame speed is reduced significantly when pressure varies from 1 to 3atm.

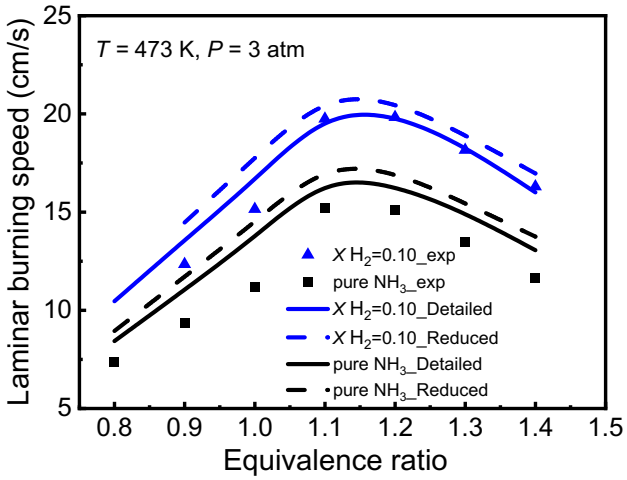

Figure 4.18 Comparison of reduced and detailed modeling with experimental results [320] for laminar burning velocity of NH_3/H_2/air blends oxidation at various equivalence ratios and H_2 content (P = 3atm, T = 473K).

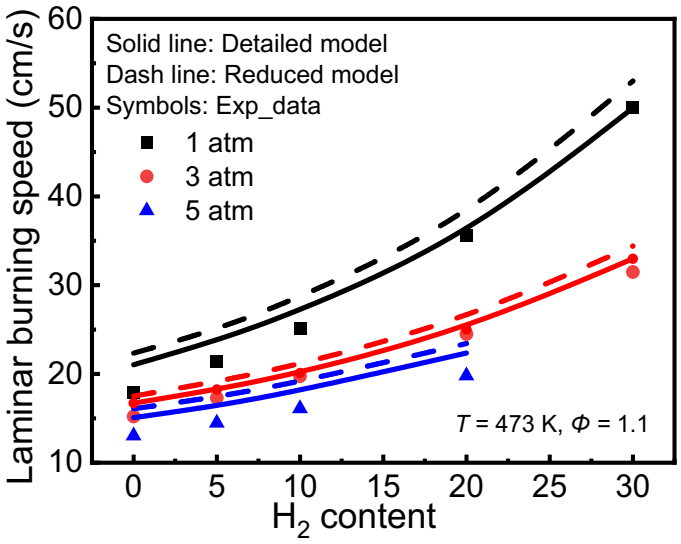

Figure 4.19 Comparison of reduced and detailed modelling with experimental results [196] for laminar burning velocity of NH_3/H_2/air blends oxidation at various pressures and H_2 content (T = 473K, Φ = 1.1).

Han et al. [6] measured laminar burning velocities of NH_3/CH_4/air flames at P = 1atm, T = 298K as a function of the equivalence ratio with varying CH_4 content (X_CH_4%) in mixtures. Figure 4.20 demonstrates the effect of CH_4 content from 0 to 40% on the laminar flame speed in NH_3/CH_4/air flame at various equivalence ratios. An excellent agreement is observed between results of reduced mechanism and experiments for various equivalence ratios, particularly in pure NH_3/air flame and blending with 20% CH_4 in mixtures. Moreover, slightly larger discrepancies are generally observed at equivalence ratio below 1.2 for around 40% CH_4 content in the blend. However, good agreement can be observed when the equivalence ratio is above 1.2. Similar prediction results were performed and analyzed in the study of Han et al. [6] by using GRI-3.0 mechanism [194]. Besides, they investigated the Okafor mechanism [11], showing the opposite results, in other words, the Okafor mechanism predicts the laminar burning velocities very well for Φ < 1.2 but the results are overestimated when the equivalence ratio increases. Although the reduced mechanism established in present work

under-predict the laminar burning velocities at lean conditions with blending of 40% CH_4 in fuel, it is able to capture the trend of laminar burning velocity varying with equivalence ratio. Moreover, improving the ammonia kinetics mechanism with CH_4 blending and extending experimental database are required.

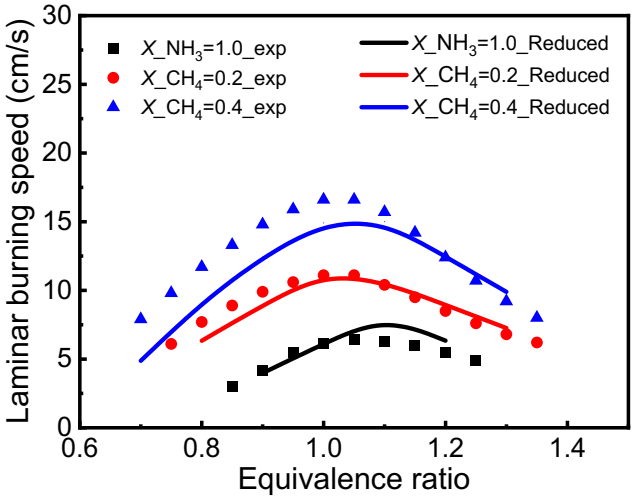

Figure 4.20 Comparison of reduced mechanism production and experimental results [11] for laminar burning velocity of NH_3/CH_4/air blends oxidation at various equivalence ratios and CH_4 content (P = 1atm, T = 298K).

4.3.5. Application of ammonia reduction mechanism

A great number of studies have reported the combustion of ammonia in gas turbines [302, 324, 325, 326], which gives insight of ammonia application for marine and power generation [151,168]. However, the high NOx emission is one of main challenges for ammonia combustion in gas turbines. Predictions of NO_X emission are numerically analyzed on the basis of the reduced model proposed in this work. Figure 4.21 shows the predictions of NO_X emission against the equivalence ratio in NH_3/air, 70%NH_3/30%H_2/air and 70%NH_3/30%CH_4/air flames by using CRN model at T = 1800K and P = 10atm. It can be seen that NO_X emission is higher at lean burning conditions (Φ = 0.6-0.9) than in rich conditions

(Φ = 1.0-1.4) for all flames. The main reason is that at lean fuel reaction regions, although the fuel NO_X emission is declined, the thermal NO_X emission is increased. When 30% H_2 is added into ammonia, the NO_X emission is increased compared to the pure ammonia combustion flame at lean-fuel conditions, and the same pattern is shown in 70%NH_3/30%CH_4/air flame. The values of NO_X emission in 70%NH_3/30%H_2/air flame are generally higher than those in 70%NH_3/30%CH_4/air flame at lean-fuel conditions. In addition, as value of the equivalence ratio beyond 0.9, the NO_X emission is decreased significantly for all three flames.

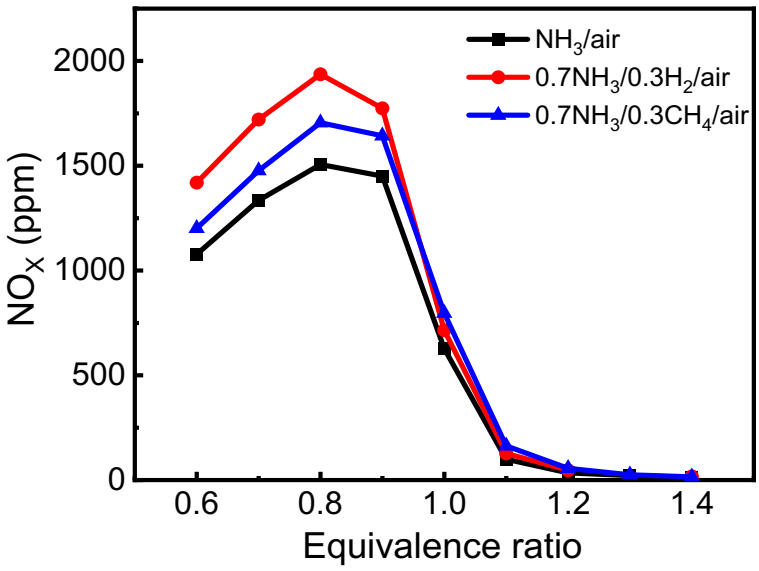

Figure 4.21 NO_X emission from the CRN predictions for NH_3/air, 70%NH_3/30%H_2/air and 70%NH_3/30%CH_4/air flames in a gas turbine based on the proposed reduced mechanism.

To further reveal the effect of H_2 and CH_4 in the combustion of ammonia on emission characteristics, Figure 4.22 shows the NO_X emission at various content of NH_3 in NH_3/H_2/air and NH_3/CH_4/air flames and Φ = 1.0. Generally, the NO_X emissions in both flames show an obvious decrease at the content of NH_3 above 20%. Similar trend was found by Somarathne et al. [327] in non-premixed CH_4/NH_3/air flames. Blending with H_2 and CH_4 is beneficial for enhancing ammonia combustion, leading to higher temperature of the flame that stimulates

NO_X production. Therefore, introducing additives reasonably plays a vital role in NO_X emission control and ammonia combustion promotion.

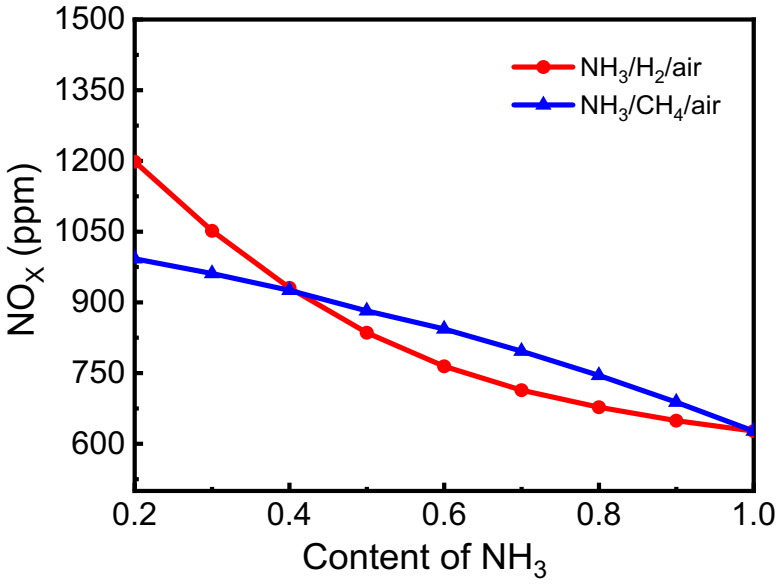

Figure 4.22 Predictions of NO_X emission with various NH_3 content in NH_3/H_2/air and NH_3/CH_4/air flames.

Figure 4.23 presents the temperature sensitivity coefficients of the top 10 important reactions in NH_3/air, 70%NH_3/30%H_2/air and 70%NH_3/30%CH_4/air flames at *P* = 10atm and stoichiometric conditions, respectively. The temperature sensitivity coefficients are calculated to analyse the reactions that have great effects on ignition delay time. It is seen from Figure 4.23(a) those reactions of NH_2 with NO (R125, R126), O_2 (R123), HO_2 (R162) or self-recombining (R133, R135) and reactions of NO production occupy the leading position in NH_3/air flame. Considering 30% H_2 added into ammonia, the reactions relating with H, OH and HO_2 radicals play a significant role in 70%NH_3/30%H_2/air flames, seen in Figure 4.23(b). The production of these reactive radicals promotes temperature rapidly in combustion system. When ammonia blends with 30% CH_4, the reactions of CH_3 oxidation are dominant in

70%NH_3/30%CH_4/air flame, resulting in high temperature. The reactions of CH_3 oxidation consume an amount of oxygen that promotes NO_X emission, however, the endothermic reaction $2CH_3$ (+M) = C_2H_6 (+M) (R55) becomes more significant with the increase of CH_4 content, which decreases the temperature and suppresses NO_X. The analysis above suggests that the two effects should be taken into careful considerations to minimize the NOx emissions in NH_3/CH_4/air flame.

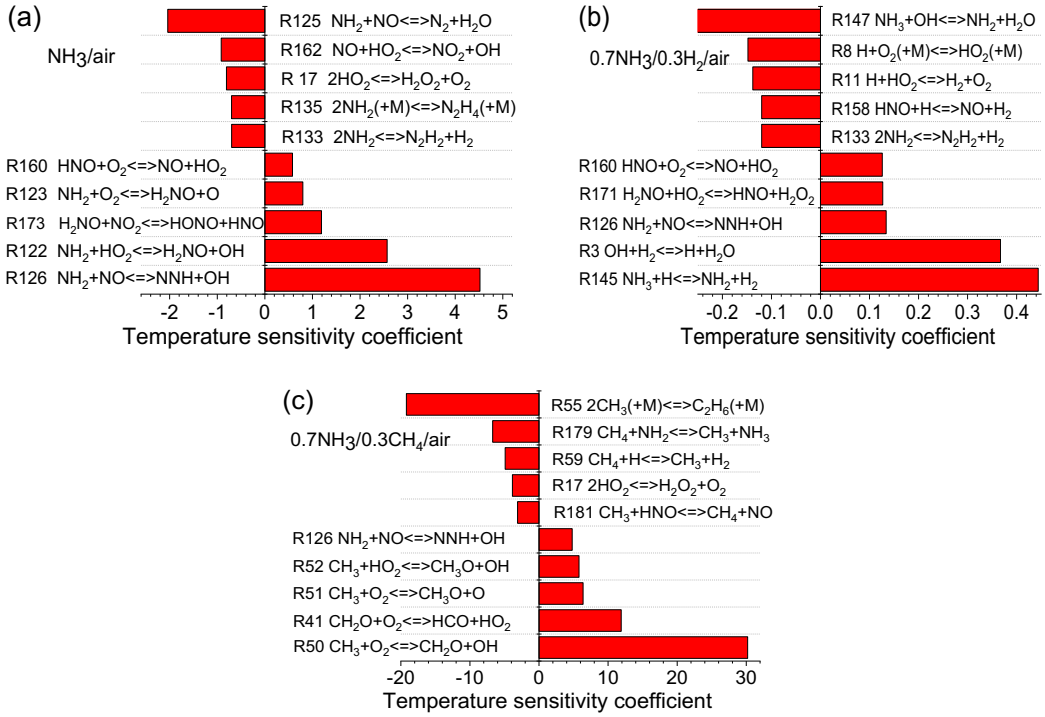

Figure 4.23 Temperature sensitivity analysis at the time of ignition for NH_3/air, 70%NH_3/30%H_2/air and 70%NH_3/30%CH_4/air combustion.

4.4. Conclusion

4.4.1. Summary of ethanol reduction mechanism

An ethanol reduced chemical kinetics mechanism is developed and validated at T = 850-1650K, P = 1-10atm and Φ = 0.5-2. The reduced ethanol mechanism (26 species and 105 reactions)

has lower average error and smaller size, and the final uncertainty is about 10.3%.

The reduced ethanol mechanism is validated with available experimental measurements of ignition delay time, species mole fraction in jet stirred reactor as well as laminar burning velocity over various conditions. It is shown that agreements remain generally good between reduced as well as detailed ethanol mechanism. Moreover, the reduced mechanism enables to well capture the ignition characteristics and concentrations of species at wide operation conditions.

4.4.2. Summary of ammonia reduction mechanism

A novel reduced chemical kinetics mechanism for $NH_3/H_2/CH_4$/air mixture is proposed for the first time by a two-stage reduction procedure, which combines both the IPFA method and the GEPA method. Specifically, in the first stage, the detailed mechanism (125 species and 1099 reactions) is reduced by the IPFA. A skeletal mechanism including 68 species as well as 687 reactions is obtained within the 5% tolerance on auto-ignition. In the second stage, the mechanism is further reduced by the GEPA. As a result, the final skeletal mechanism involving 59 species and 210 reactions is obtained within the 10% tolerance auto-ignition.

Extensive validations of the proposed reduced model are conducted by comparing to detailed mechanism and experimental measurements of ignition delay time in shock tube, species profiles in JSR and the laminar flame velocity in wide range of temperatures (T = 1300–2500K), pressures (P = 1–40bar), as well as equivalence ratios (Φ = 0.25–2.0). Results show that the reduced mechanism makes prediction for ignition delays of NH_3, NH_3/H_2 and NH_3/CH_4 mixtures very well. Additionally, predictions of laminar burning velocity using reduced model generally agree well with the results of measurements and detailed model. Although the

result of the reduced model is slightly over-predicted compared to the detailed mechanism for laminar burning velocity, the discrepancies are quite small within the error margins around 5%. It is noted that the reduced mechanism established in the present work under-predict the laminar burning velocities at lean conditions with blending of 40% CH_4 in fuel. Moreover, improving the ammonia kinetics mechanism with CH_4 blending and extending experimental database are required.

Furthermore, the NO_X emission characteristics of $NH_3/H_2/CH_4$ mixtures in a gas turbine are numerically analyzed through a chemical reactor network (CRN) model. The effects of H_2 and CH_4 in the combustion of ammonia and the equivalence ratio on emission characteristics are investigated. Moreover, the temperature sensitivity analysis is employed to explore the reactions that have great impact on the combustion in NH_3/air, 70%NH_3/30%H_2/air as well as 70%NH_3/30%CH_4/air flames. Results show that the NO_X emission is increased compared to pure ammonia combustion flame especially at lean-fuel (Φ = 0.6-0.9) conditions, when the ammonia blends with H_2 or CH_4. Also, generally, the NO_X emissions show an obvious decrease at the content of NH_3 above 20% in both NH_3/H_2/air and NH_3/CH_4/air flames. Therefore, introducing additives reasonably plays a vital role in NO_X emission control and ammonia combustion promotion.

5. Ammonia Combustion and Emission Characteristics in Gas Turbines

5.1. Introduction

This chapter is mainly studying combustion and emission characteristics of partially cracked ammonia in gas turbines. It is already known that chemical kinetic mechanisms are good for understanding the combustion process. Therefore, first of all, the kinetic modelling of ammonia is analysed. Then, a one-dimensional freely propagating laminar flame calculation model is validated for further study of partially cracked ammonia combustion characteristics. After that, in section 5.4, the effect of equivalence ratio, cracking ratio as well as initial pressure on the laminar flame velocity (LBV) are numerically discussed. In section 5.5-5.6, numerical investigations of the combustion and emission characteristics for partially cracked ammonia ($NH_3/H_2/N_2$/air mixtures) in single and 2-stage rich-lean combustor are performed, respectively. At the end of the chapter, to further explore the mechanism of partially cracked ammonia oxidation, a reaction pathways flux method is used to represent NO reaction pathways at various operating factors and cracking ratios. Also, the potential of controlling the important intermediate species and reactions on NO formation/reduction is demonstrated by identifying the major NO_X reaction pathways and analysing the NO rate of production (ROP).

5.2. Kinetic modelling

Better understanding the ammonia reaction mechanism is essential in analysing and designing ammonia combustion systems in a gas turbine. Mathieu and Petersen carried out Shock Tube experiments and developed a NH_3 oxidation mechanism [102]. By comparing their work

against nine other NH_3 containing mechanisms, large discrepancies between the ammonia mechanisms were clarified. Xiao and Valera-Medina compared 12 different NH_3-NO_X kinetic mechanisms; the majority of mechanisms could not show good performance between the measured laminar flame experimental data at various equivalence ratios [31]. As for representing comprehensive prediction of the LBV and ignition delay time of NH_3, Otomo et al. [32] proposed an ammonia oxidation mechanism (UT-LCS) according to the model developed by Song et al. [195], including 33 species and 222 reactions. This model was well validated of ignition delay time as well as laminar flame speed under wide ranges of conditions. It is also appropriately applied to investigate the NH_3/H_2/air combustion. Therefore, the UT-LCS mechanism is used in the present work to calculate LBV and NO_X emissions characteristic in partially cracked ammonia fuelled gas turbines.

In this work, the cracking ratio (γ) changes from 10% to 80%, which is defined as the mole fraction of cracked NH_3 ($[NH_3]_{cracked}$) in initial NH_3 ($[NH_3]_{init}$). The definition of γ is calculated according to the following equations Eq. (5.1), (5.2) and (5.3):

$$[NH_3]_{init}=\gamma[NH_3]_{cracked}+(1-\gamma)[NH_3]_{remained} \quad (5.1)$$

$$2NH_3=3H_2+1N_2 \quad (5.2)$$

$$\gamma=[NH_3]_{cracked}/[NH_3]_{init}=2[H_2]/(3[NH_3]_{remained}+2[H_2]) \quad (5.3)$$

When partially cracked NH_3 completely burn with air into H_2O and N_2, the equivalence ratio (Φ) used in the calculations is listed in the following equation (Eq. (5.4)).

$$X((1-\gamma)NH_3+\gamma(1.5H_2+0.5N_2))+astoi(O_2+3.76N_2)=\alpha H_2O+\beta N_2 \quad (5.4)$$

5.3. Validation of Laminar burning velocity

The laminar burning velocity in the present study is performed with a one-dimensional freely propagating laminar flame calculation model of the CHEMKIN-PRO. Thermal diffusion effects are considered and the values of both GRAD and CURV are set as 0.02. All simulations are converged to a grid-independent solution. Numerical simulation of LBV for ammonia premixed flame is validated against the previous experiment research at 298K temperature and atmospheric pressure conditions (P = 0.1 MPa), presented in Figure 5.1. The solid line represents calculated results with UT-LCS mechanism, the dots represent LBV values measured by experiments published in recent years [8,7,6,328]. Laminar burning velocities of the present model agree with experimental flame speeds very well over a broad range of equivalence ratios.

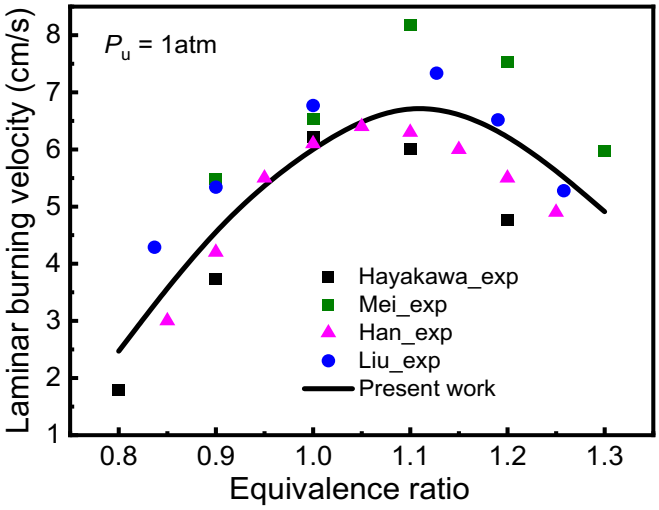

Figure 5.1 Laminar flame speed for NH_3/air at 1atm and 298K. Symbols: measurements published literature [6, 7, 8, 328]. Solid line: this work.

As for partially cracked ammonia combustion, the comparison of measured and simulated LBV of partially cracked NH_3/air mixtures ($NH_3/H_2/N_2$) is presented in Figure 5.2 at various

equivalence ratios and pressures when the cracking ratio of ammonia is fixed at 40%. Moreover, the validation for variations of the laminar burning velocity with changing ammonia cracking ratio is presented in Figure 5.3. The dots are the experimental measurements of LBVs [184], and solid lines are simulation results in current work. Generally good performance is presented on simulating measured LBVs at various equivalence ratios, pressures and ammonia cracking ratios.

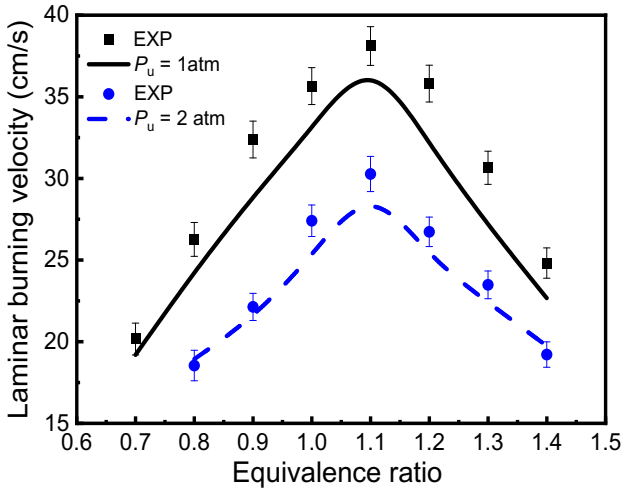

Figure 5.2 Laminar flame speed for partially cracked NH_3/air mixtures at 1, 2atm and 298K.

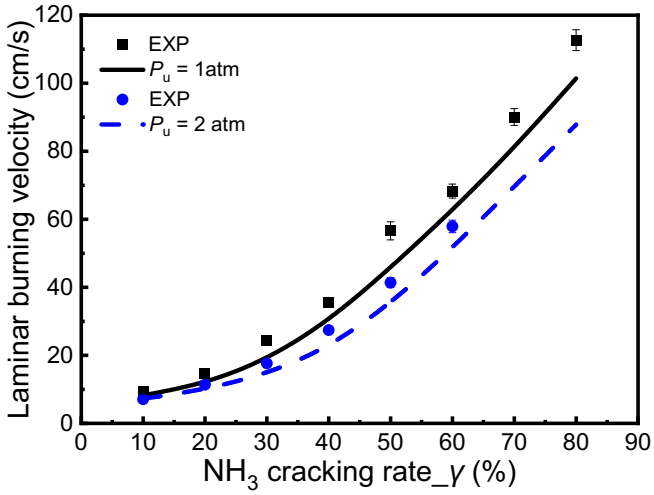

Figure 5.3 Variation of the laminar burning velocity with changing ammonia cracking ratio for partially cracked NH_3/air mixtures at 1, 2atm and 298K.

5.4. Factors influence on the laminar burning velocity

As one of the most siginificant parameters for premixed flames, many studies on laminar burning velocities of NH_3 containing premixed flame were investigated experimentally and numerically [7, 8, 11, 102, 113,186, 188, 197, 195, 196, 320].

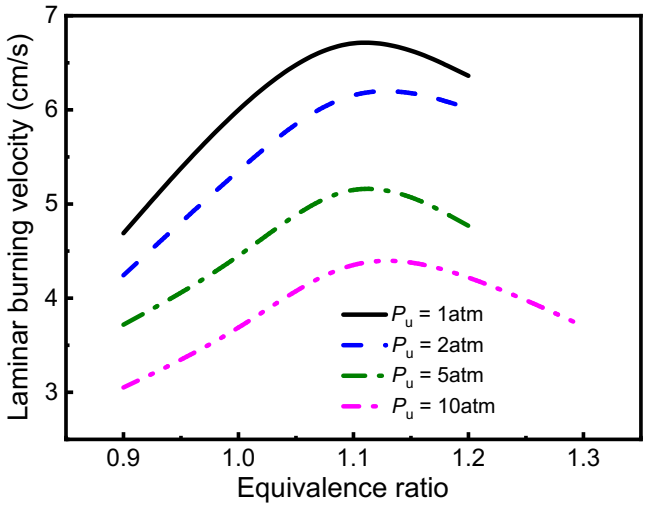

Figure 5.4 LBVs of pure NH_3/air flames against the equivalence ratio at *Tu* = 298K and *Pu* = 1, 2, 5 and 10atm.

Figure 5.4 shows the simulated LBVs of NH_3/air mixtures at various equivalence ratios and 40% ammonia cracking ratio. Similarly, single positive curves tendencies are captured as that of NH_3/air flames in Figure 5.1. The maximum values of laminar burning velocity are located around Φ = 1.1 for all calculated initial pressures. It can be observed that the peak value of LBV is close 37 cm/s at *Tu* = 298K and *Pu* = 1atm when ammonia is cracked to 40% (seen in Figure 5.2), which considerably improved LBV of $NH_3/O_2/N_2$ flame (around 7cm/s). When the initial mixture pressure is increased from 1atm to 10atm, the LBV is decreasing obviously in Figure 5.4, and the tendency is in concordance with experimental data of Hayakawa et al. [8] for ammonia/air premixed flames. However, when pressure increases to 10atm, the maximum

value is around 4.5cm/s, which could lead to unstable flame in this condition.

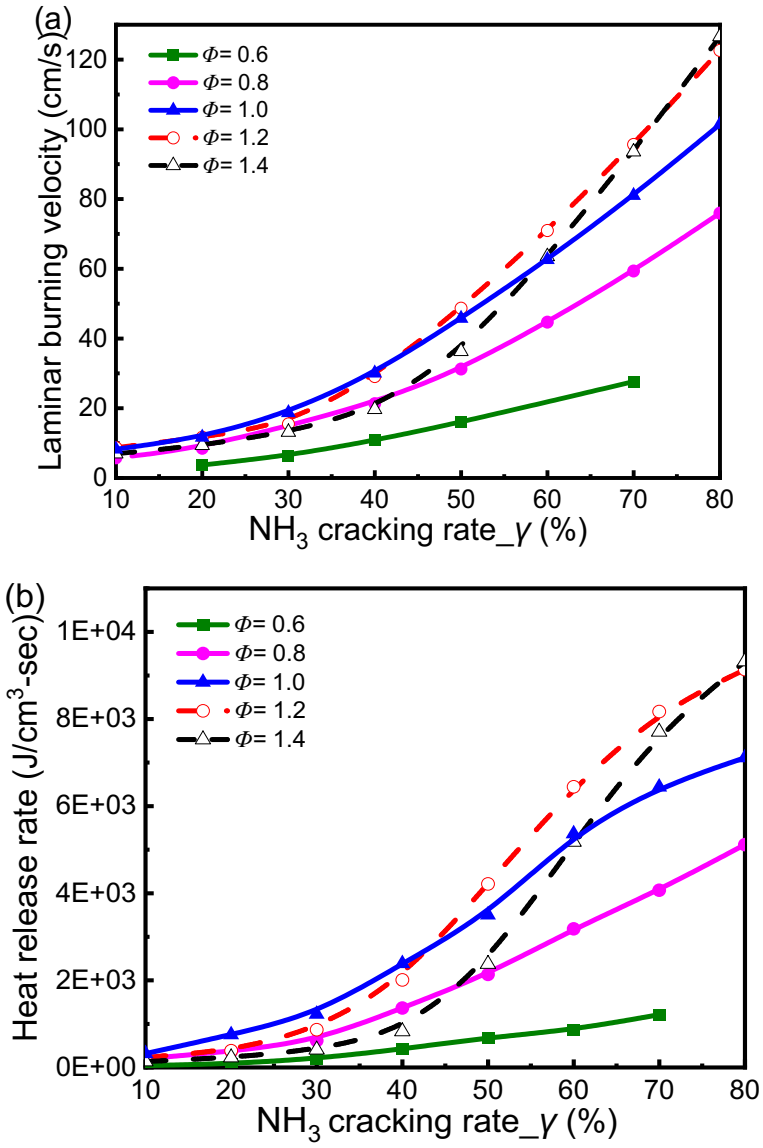

Figure 5.5 LBVs (a) and HRR (b) versus ammonia cracking ratio at various equivalence ratio.

Figure 5.5 (a) shows the effect of equivalence ratio and ammonia cracking ratio on laminar burning velocity of partially cracked NH_3/air mixtures premixed flames. The LBVs increases significantly when the cracking ratio increases from 10% to 80 %. The tendency indicates that the combustion intensity is remarkably enhanced as cracking ratio increases. Furthermore, comparison of performance among different ammonia cracking ratios reveals that the ammonia combustion performance can be improved by partially cracking. The heat release

rate versus different equivalence ratios and ammonia cracking ratios is also displayed in Figure 5.5(b). The trend of HRR variety is similar as that of the LBV in same conditions, while the increasing speed of heat release rate is slow down when ammonia cracking ratio increases to 80% at fuel rich region.

5.5. NO_X emission predictions in a single stage combustor

The effects of ammonia cracking ratio and equivalence ratio on NO_X emissions (consisting of NO, NO_2 and N_2O) of the partially cracked ammonia are investigated in single stage gas turbine combustor. To remove the influence of dilution in the gas measurement system, the concentration measured in experiments is corrected to the concentration in dry conditions as following equation 5.5.

$$[\mathrm{NO}]_{15\%\mathrm{O}_2} = \frac{[\mathrm{NO}]_{\mathrm{measured,dry}} \times (0.21-0.15)}{0.21-[\mathrm{O}_2]_{\mathrm{measured,dry}}} \quad (5.5)$$

Therefore, all NO_X emissions illustrated throughout this paper are corrected to 15% O_2 and dry condition unless otherwise specified. Analysis of the factors on NO_X emission characteristics is shown in Figure 5.6. It can be observed that the amount of NO_X emission firstly increases and then decreases sharply when the equivalence ratio is within 0.4-1.1. After that, a decreasing trend is shown with further equivalence ratio increasing. When the equivalence ratio exceeds 0.8, NO_X is reduced rapidly as the equivalence ratio of mixtures increases. The maximum value of NO_X emission can be reached when equivalence ratio is close to 0.8 for all ammonia cracking ratios.

Traditional lean burn combustion is used to reduce the generation of thermal NO_X emissions, because of the low flame temperature in the combustor. However, more NO_X emission seems

to be produced under lean burn conditions than that in rich conditions as shown in Figure 5.6(a). Because the fuel NO_X emissions will decrease at lean fuel reaction regions, while thermal NO_X would be increased due to high temperature. The temperature of 40% cracked ammonia flame is shown in Figure 5.6(b). It should be noted that the maximum NO_X formation is located at around Φ = 0.8, which does not match the peak temperatures. Similar result was found by Li et al. [175] and they demonstrated that the NO_X formation was not just controlled by the Zeldovich thermal NO_X mechanism [329]. Seen from Figure 5.6, it shows that high NO_X emission zone is located at high ammonia cracking ratio and 0.6-1.0 ranges of equivalence ratio. Generally, the content of H_2 increases with cracking of ammonia, which can improve the combustion intensity conspicuously. In addition, the NO_X emission is promoted with increasing NH_3 cracking ratio from 10% to 80% at all equivalence ratio studied.

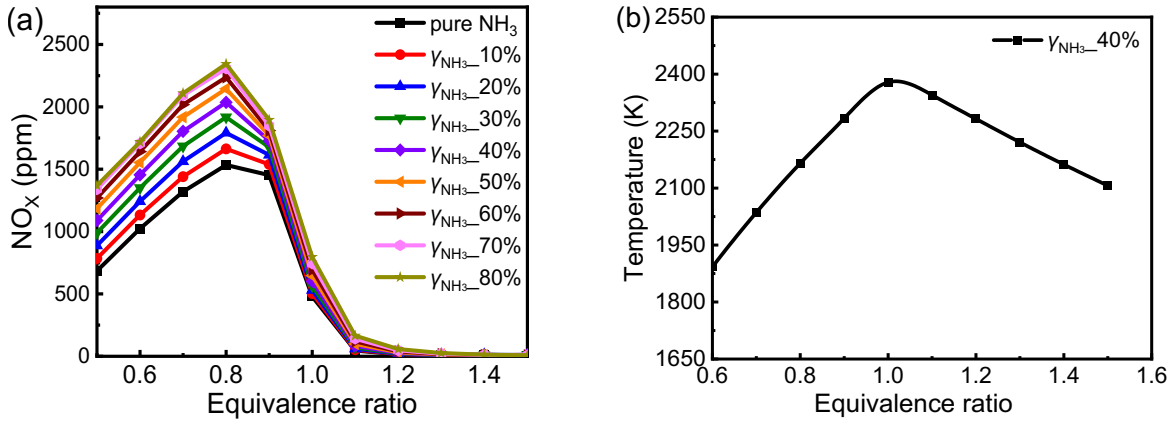

Figure 5.6 NO_X emission from the CRN predictions in single stage combustor at various equivalence ratio and cracking ratio.

To reveal emission characteristics of the partially cracked ammonia/air premixed swirl flame, the mole fraction of important intermediate components, such as NO, HNO, N_2O, NH_i, OH, O, H, are analysed at different equivalence ratios and fixed 40% NH_3 cracking ratio, as illustrated in Figure 5.7. It is directly seen that mole fractions of OH and HNO have similar trend

compared with that of NO and N_2O, which displays upward trend as the equivalence ratio rising to 0.9. The NH_i effect on the NO formation can be neglected in this area. As the equivalence ratio further increasing, the mole fraction of OH and HNO reduce and both of NO and N_2O decreased correspondingly, while the NH_i mole fraction increases significantly. It is shown that NH_i contributes more on NO reduction, and HNO radical can promote NO formation.

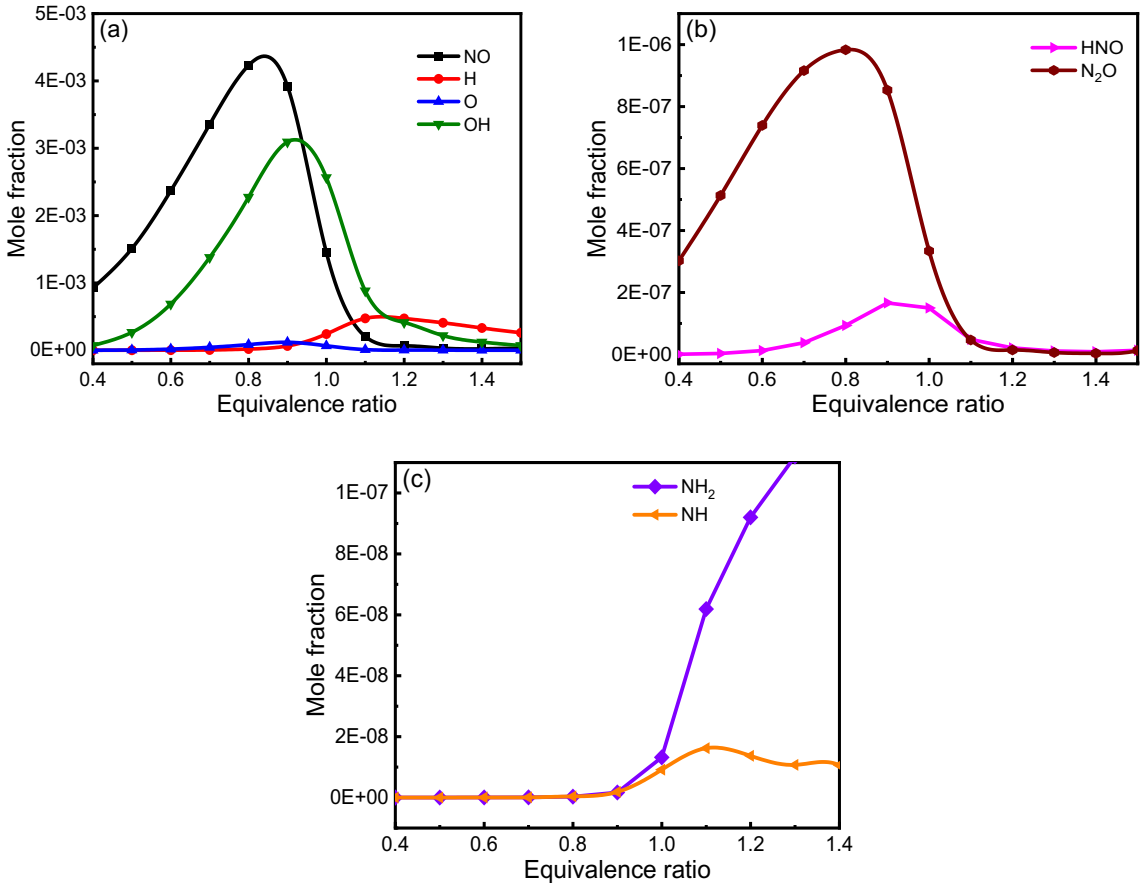

Figure 5.7 Mole fraction of NO, HNO, N_2O, NH_i, OH, O, H at different equivalence ratios and fixed 40% NH3 cracking ratio.

Further analysis on NO generation is performed based on calculate individual reaction related of NO rate of production, shown in Figure 5.8. Top 10 reaction pathways that have great contribution on NO generation are concluded in Table 5.1. Clearly relative NO rate of

production for each reaction shown in Table 5.1 at various equivalence ratios is calculated and demonstrated in Figure 5.8. A positive value represents prompting effect while a negative value represents inhibitive effect on NO production.

Table 5.1 Top 10 reaction pathways on NO generation contribution rate in partially cracked NH_3/Air.

Number	Reaction	A	B	Ea
R49	$NH_2+NO=N_2+H_2O$	1.30×10^{16}	-1.2	0.0
R50	$NH_2+NO=N_2+H_2O$	-3.10×10^{13}	-0.5	1180.0
R51	$NH_2+NO=NNH+OH$	4.290×10^{10}	0.3	-870.0
R60	$NH+O_2=NO+OH$	1.30×10^{6}	1.5	100.0
R63	$NH+NO=N_2O+H$	5.00×10^{14}	-0.4	0.0
R117	NO+H(+M)=HNO(+M)	1.50×10^{15}	-0.4	0.0
R120	$HNO+OH=NO+H_2O$	3.60×10^{13}	0.0	0.0
R121	$HNO+O_2=HO_2+NO$	2.00×10^{13}	0.0	16000.0
R124	$NO+HO_2=NO_2+OH$	2.10×10^{12}	0.0	-497.0
R127	$NO_2+H=NO+OH$	1.30×10^{14}	0.0	362.0

It can be seen from Figure 5.8, the ROPs of two reactions R120 and R117 are in positive values (Φ < 0.85), meanwhile, the NO mole fraction is increasing in Figure 5.7. Therefore, HNO + OH = NO + H2O (R120) and NO + H (+ M) = HNO (+ M) (R117) make major contribution on NO production. The decrease of NO formation when Φ > 0.8 is mainly because of the decreased ROP of R120. Furthermore, as equivalence ratio increases, R117, R121 and R60 have slight encouraging effect on NO production, but the NH_i pathways, such as $NH_2+NO=N_2+H_2O$ (R49), $NH_2+NO=NNH+OH$ (R51), and $NH+NO=N_2O+H$ (R63), still dominate NO reduction.

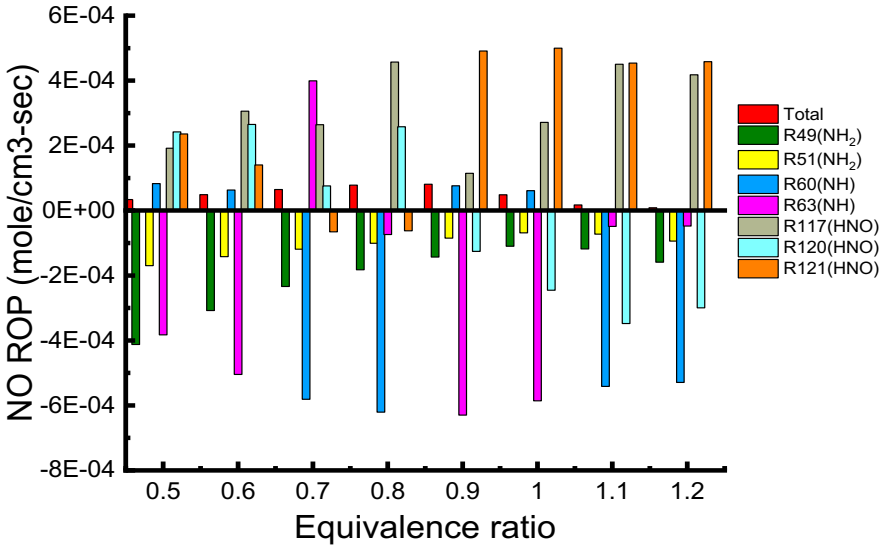

Figure 5.8 NO Rate of productions of major reaction pathways.

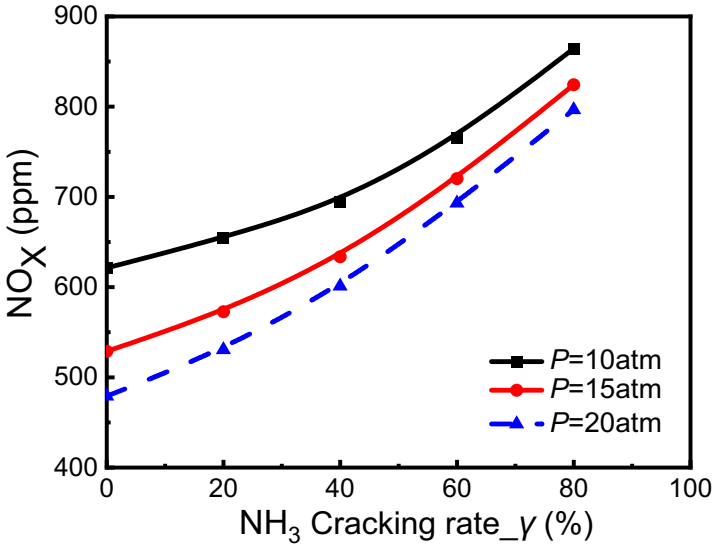

Figure 5.9 NO_X emission as a function of pressure.

Figure 5.9 explores the effect of initial pressure on NO_X emission throughout all NH_3 cracking ratios. It should be noted that the NO_X emission goes to a lower value at each cracking ratio when the pressure rises from 10 to 20atm. The growth of pressure will generate more flame reaction regions and increase the high temperature local points where thermal NO_X emissions would be promoted. Therefore, the thermal NO_X will increase with the rising pressure owing

to the increase of the intensity of the reaction zone. Nevertheless, the fuel NO_X emission will a decrease, which have a significant effect on total NO_X emissions.

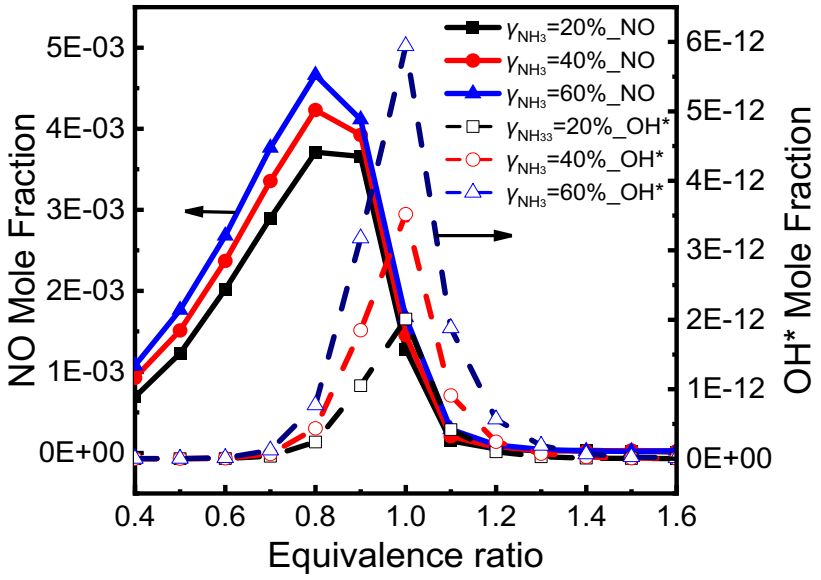

Figure 5.10 The mole fraction of NO and OH* at different equivalence ratio and NH_3 cracking ratio.

It is known that chemiluminescence intensity is an excellent signature to detect the kinetics of the reaction system. Many studies were concentrated on identifying flame structure by capturing the OH* chemiluminescence [330, 331]. Zhu et al. [332] indicates that OH* chemiluminescence intensity can be used as the surrogate of NO mole fraction under certain conditions. This makes it possible to detect emissions-free flame combustion of partially cracked ammonia mixtures by employing a low-cost OH* chemiluminescence technology. Therefore, the mole fraction of NO and OH* are shown in Figure 5.10 at various equivalence ratios and three different NH_3 cracking ratios (γ = 0.2, 0.4, and 0.6). The intensity of chemiluminescence is proportional to the product of the excited reactants concentration, and is capable of identifying the position of flame [333]. Thus, it can be demonstrated that peak OH* chemiluminescence intensity located at the position of large NO mole fraction gradients.

Seen from Figure 5.10, both mole fraction of NO and OH* are increased with increasing NH_3 cracking ratio, which is expectable, since higher OH radical generated from higher ammonia cracking ratio results in rise of NO formation. Besides, considerably higher intensities of OH* for all cracking ratios are located at Φ = 1.0 followed by a decaying trend due to lower oxygen, suggesting that the flame position hardly changes with NH_3 cracking ratios.

5.6. NO_X emission predictions in a rich-lean burn combustor

According to the results of research in section 5.5, NO_X emissions decreased obviously at slightly rich equivalence ratios. Therefore, stratified-charged strategy is adopted to discuss the NO_X emissions. Figure 5.11 shows the predictions of NO_X emission in rich-lean burn combustor at fixed 40% NH_3 cracking ratio. The overall equivalence ratio ($\Phi_{overall}$) is controlled within 0.4-0.8, which is calculated by volume flow rate of intake partially cracked NH_3 mixtures and total combustion air in two stages. $\Phi_{primary}$ is the equivalence ratio in primary stage. The residence times of PSRs are shown at Table 3.1 and PFR residence times in primary and secondary stage are fixed at 18ms and 2ms separately.

As the primary equivalence ratio increases, NO_X emissions show almost the same performance as U-shaped curves, and the turning points are almost located at 1.3 and 1.4. The primary equivalence ratio ranges of low NO_X emissions (below 50ppm) are observed at around from 1.2 to 1.5 when the $\Phi_{overall}$ = 0.4-0.6, as shown in Figure 5.11. However, it is increased significantly with overall equivalence ratio rising to 0.7 and 0.8. As primary equivalence ratio increases, NO_X emissions decrease with the increase of $\Phi_{primary}$ observed from 1.0 to around 1.3 firstly, and the NO_X prediction values at $\Phi_{primary}$ = 1.0 for all $\Phi_{overall}$

are very small (less than 1000ppm), which are considerably lower than those in single stage. Because secondary air is added after the main flame zone to form a reducing atmosphere where NO can be reduced in air classification. Therefore, using a second combustion stage burning is promising to reduce NO_X emission and solving the unburned NH_3 mixtures problem. Then, the gap is enlarged, after that the discrepancy among NO_X emissions shrinks, but the values are growing up at high $\Phi_{primary}$. It should be influenced remarkably by unburned cracked NH_3 mixtures.

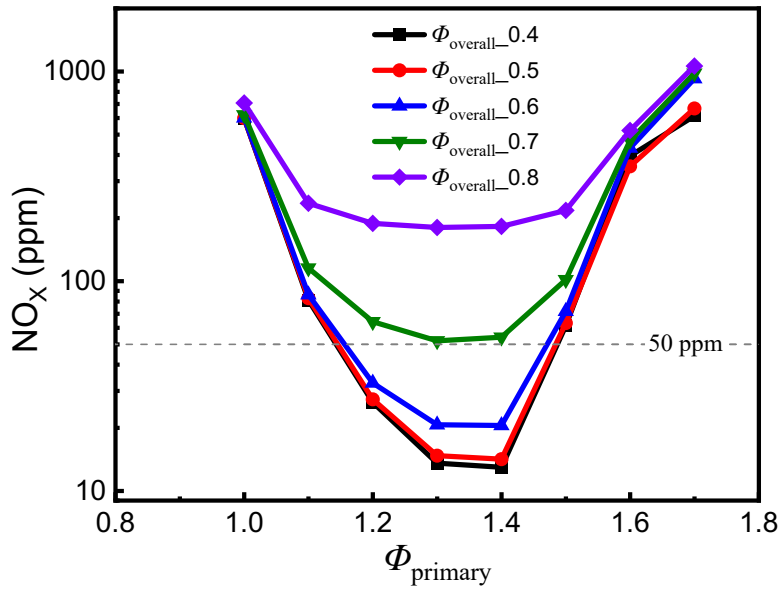

Figure 5.11 NO_X emission predictions versus $\Phi_{primary}$ in rich-lean burn combustor at NH_3 cracking ratio γ =40%.

The explanation of high NO_X emission that disappeared at high $\Phi_{primary}$ ($\Phi_{primary}$ > 1.4) is presented in Figure 5.12. The solid dot lines represent NO_X emissions in primary stage (rich burn stage), while the dash dot lines are in lean burn stage. The NO_X formation lines are overlapped and decreased in primary stage, but clearly differences of NO_X emissions with increasing $\Phi_{primary}$ are shown in lean stage. It is expected because the unburned cracked

NH_3 mixtures content takes a dominant place on NO_X formation in the lean stage. Therefore, the initial decrease of overall NO_X is owing to reduced NO_X in rich stage, while the increase of overall NO_X at high $\Phi_{primary}$ should be influenced by NO_X formation in lean stage. It is worth noting that discrepancy among NO_X emissions is reduced with more unburned NH_3 cracking at higher $\Phi_{primary}$ ($\Phi_{primary}$ > 1.6), suggesting that the impact of unburned cracked NH_3 mixtures is reduced in this region. Therefore, NO_X formation is prompted by thermal NO_X instead of fuel NO_X in this region.

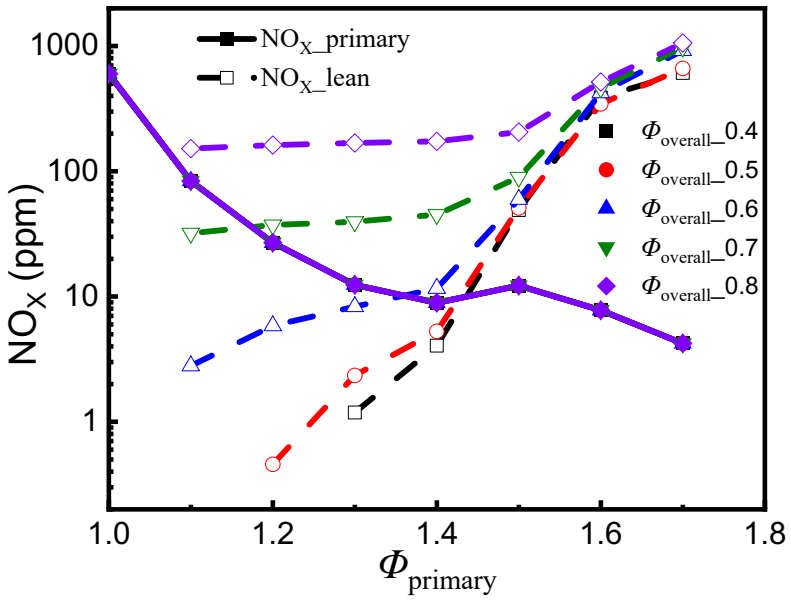

Figure 5.12 NO_X emissions in primary stage (solid lines) and the lean-burn stage (dash lines) at all overall equivalence ratios.

The effect of NH_3 cracking ratio is also explored, shown in Figure 5.13. NO_X emissions versus primary equivalence ratio are displayed at various cracking ratios and fixed $\Phi_{overall}$ =0.6, other conditions are the same as those in Figure 5.11. Similar tendency curves are captured at various cracking ratios, shown in Figure 5.13(a), but the position of turning points is right shifted with increasing cracking ratio. Interesting noting that the operating ranges of low NO

emissions (below 50ppm) are obviously widened with increasing cracking ratio, since more content of hydrogen produced from ammonia facilitates the reactivity of ammonia. In addition, NO_X formation is slightly increased with the growth of cracking ratio, whereas it shows gradually reducing trend at high primary equivalence ratio.

In order to better understanding overall NO_X emission, the dependences of NO_X emission on primary equivalence ratio is considered in the rich and burn stage separately. Figure 5.13(b) shows the rich and lean NO_X at various NH_3 cracking ratio. In primary stage, NO_X emissions show slightly increase at high cracking ratio, mainly because the proportion of H_2 content is high in the initial $NH_3/H_2/N_2$ mixture. An amount of H_2 and OH radical enhance NH_3 reactivity and increase the flame temperature, resulting in producing more NO_X [334]. Besides, the effect of cracking ratio on lean NO_X shows obviously different tendency at various primary equivalence ratios. The influence of H_2 content on enhancing NO formation is in predominant at low primary equivalence ratio, thus NO_X emission increases in lean stage firstly. Then, NO_X formation significantly drops with increasing cracking ratio at high primary equivalence ratio, which can be attributed to lower unburnt NH_3 in lean stage. Therefore, the overall NO_X emission is greatly dependent on NO_X formation in primary stage at low $\Phi_{primary}$, whereas the lean NO_X is more important for overall NO_X production at high $\Phi_{primary}$. In conclusion, cracking more NH_3 is beneficial for reducing NO_X emission and widening operation. Controlling cracking ratio (around at 40%) and primary equivalence ratio (i.e., controlling unburnt NH_3) in the range of 1.2-1.4 primary equivalence ratio enable to comprehensively widen operation range and reduce NO_X emissions.

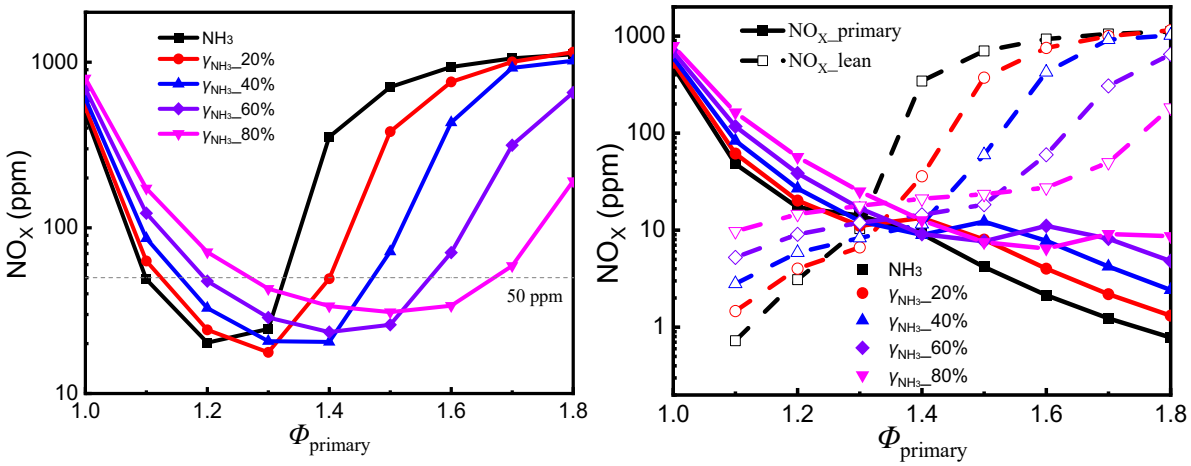

Figure 5.13 NO_X emission with different primary equivalence ratio and NH_3 cracking ratio at fixed $\Phi_{overall}$ =0.6. (a) Overall NO_X emission (b) NO_X emission in primary and lean stage.

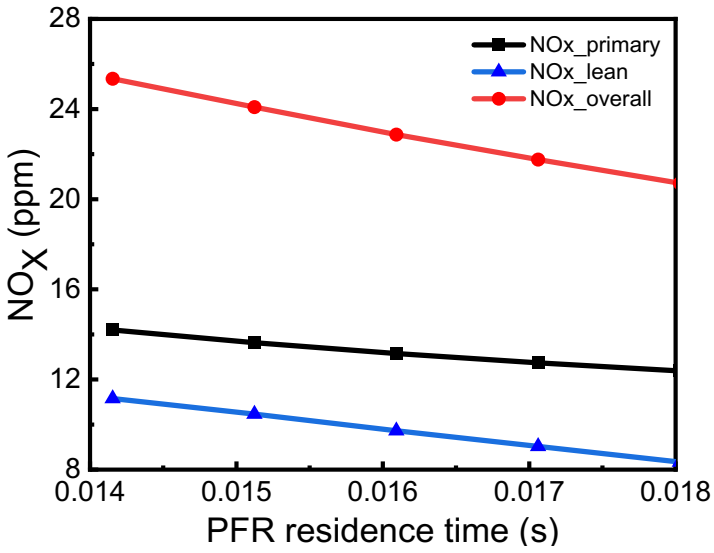

Figure 5.14 NO_X emission against PFR residence time in primary stage.

Figure 5.14 discussed the influence of PFR residence time in primary stage on NO_X emission. According to the description of residence time setting, the global residence time for two PFRs is kept as 20ms, the PFR1 residence time in primary stage was varied from 14 to 18ms. Cracking ratio is 40%, $\Phi_{overall}$ = 0.6 and $\Phi_{primary}$ = 1.3 based on the study in Figure 5.13, other conditions are the same as those in Figure 5.11. The NO_X in each stage shows monotonically decrease with the residence time in rich burn stage increasing. As the matter

of fact, in post-flame zone, NH_i plays an essential role in consuming NO formed, where OH radical has already been depleted, while $NH_2 + NO = N_2 + H_2O$ and $NH + NO = N_2O + H$ are key reactions impacting NO consumption [335,336]. Therefore, increasing residence time within reasonable context in primary stage has an advantage on NO_X reduction.

5.7. Reaction pathways analysis

Better understanding of NO_X production kinetics mechanism in combustion enables to develop effective controlling strategies to reduce NO_X emissions. Formation mechanisms for NO usually results from three main kinetic processes: thermal NO, prompt NO, as well as fuel NO [197].

The thermal mechanism (or Zeldovich mechanism [329]) that dominates in combustion systems is described by three chain reactions:

$$N_2+O=NO+N \quad (5.6)$$

$$N+OH=NO+H \quad (5.7)$$

$$N+O_2=NO+O \quad (5.8)$$

The prompt NO mechanism also has significant effect on NO formation, however, NO in prompt NO mechanism is mainly produced in hydrocarbon/air flames zones. In addition, the fuel NO mechanism is also a principal source of NO_X production, in which N_2O and NNH are main reaction paths of NO. Since the rate of NO formation in thermal NO_X mechanism is much slower compared to fuel combustion process, in general, thermal NO is formed in post-flame zone.

In order to analyse partially cracked ammonia combustion process, the formation and

consumption of NO are further discussed. The numbers shown in reaction pathways present the contribution rate of the main reaction path on the corresponding radicals' consumption.

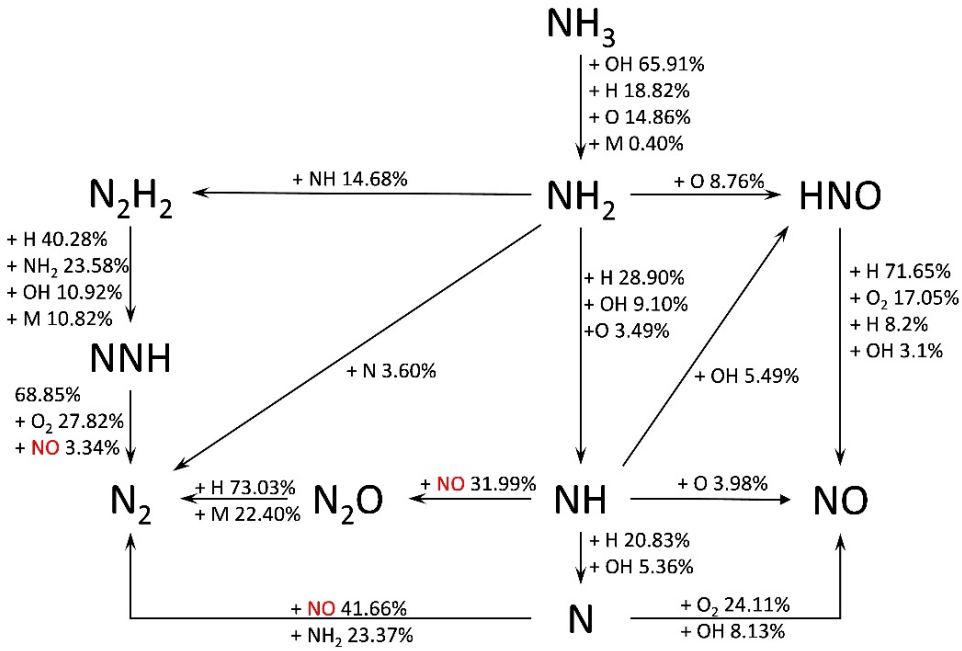

Figure 5.15 Reaction path diagram in pure NH_3 combustion progress at stoichiometric condition.

Figure 5.15 shows a reaction path diagram of pure NH_3 combustion progress under stoichiometric condition. Ammonia is primarily converted to NH_2 by H-atom abstraction reactions, specifically by reactive radicals (O, OH, H). Then, the NH_2 radical reacts with the radical pool and generates NH and N in the sequence. Also, part of NH_2 is oxidated by O to form HNO radical, and the reaction with NH as well as self-combination to produce N_2H_2. For N_2H_2, it is mainly consumed to form NNH, while NNH by oxidation, unimolecular decomposition reaction and reacting with NO to produce N_2 finally. It is readily seen that NH_i radicals are important to NO formation/consumption. In other words, controlling the reaction pathways of NH_i reacting with NO or with O, OH, O_2 radicals can effectively promote or Inhibit NO production. Furthermore, HNO radical obviously shows positive effect on the NO

production. As for NO consumption, it is mainly reacted with NH, N, and NNH scheme to generate N_2.

(a)

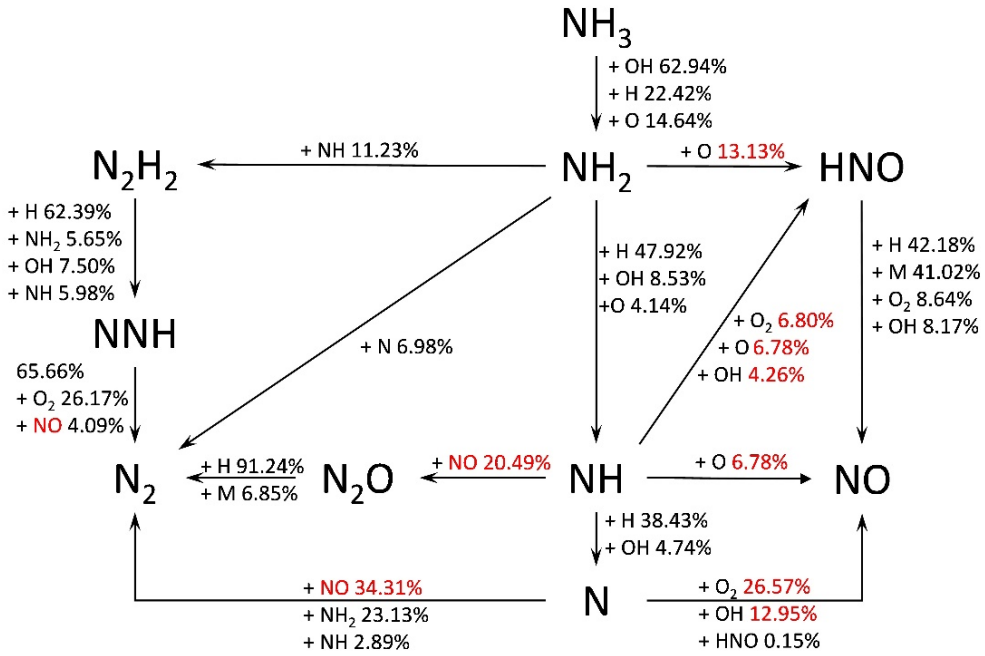

(b)

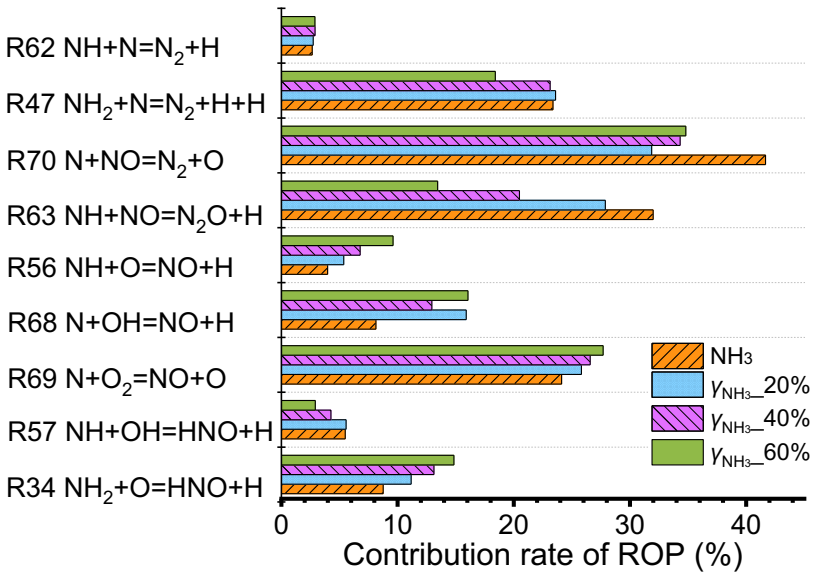

Figure 5.16 (a) Reaction path diagram in 40% cracking NH_3 mixtures combustion progress at stoichiometric condition. (b) ROP of different reactions related with NO formation and consumption of 20%-60% cracking NH_3 mixtures at stoichiometric condition.

Compared with pure NH_3 reaction pathways, the combustion reaction path diagram of cracking 40% NH_3 is shown in Figure 5.16(a) under stoichiometric condition. The contribution rate of reaction paths that have important influence on NO formation/consumption are signed to red for comparison with NH_3 reaction paths. The contribution of reactions that related with NO formation are obviously increased in 40% cracking ammonia mixtures combustion process, while the proportion of reactions with NO consumption decrease. More detailed rate of production of major reactions are identified in Figure 5.16(b). It is noted that the proportion of O radical reacting with NH_2 is increased from 8.76% to 13.13% (R34), and more N radical is reacting with O, OH, O_2 radicals to form NO. Nevertheless, less NO is consumed to convert to N_2. For example, there is 31.99% NH reacting with NO to form N_2O and then convert into N_2 in ammonia/air flame, but the number is decreased to 20.49% in reaction NH + NO = N_2O + H (R63). Seen from Figure 5.16(b), when ammonia cracking rate increases from 20% to 60%, the contribution rates of ROP of promoting NO formation reactions appear rising tendency (R34, R69, R68, R56), while the contribution rates for reactions relating with NO consumption is reduced. Therefore, more NO is generated when more ammonia is cracked.

The impact of equivalence ratio on NO formation is illustrated in Figure 5.17. Figure 5.17(a) and (b) show 40% cracking ammonia combustion reaction pathways at 0.8 and 1.2 equivalence ratio, respectively. Compared with Figure 5.15, the contribution rate of reactions related with NO formation are generally decreased with increasing equivalence ratio, while the proportion of reactions that react with NO are increasing. Therefore, the overall NO formation is reduced with growing equivalence ratio.

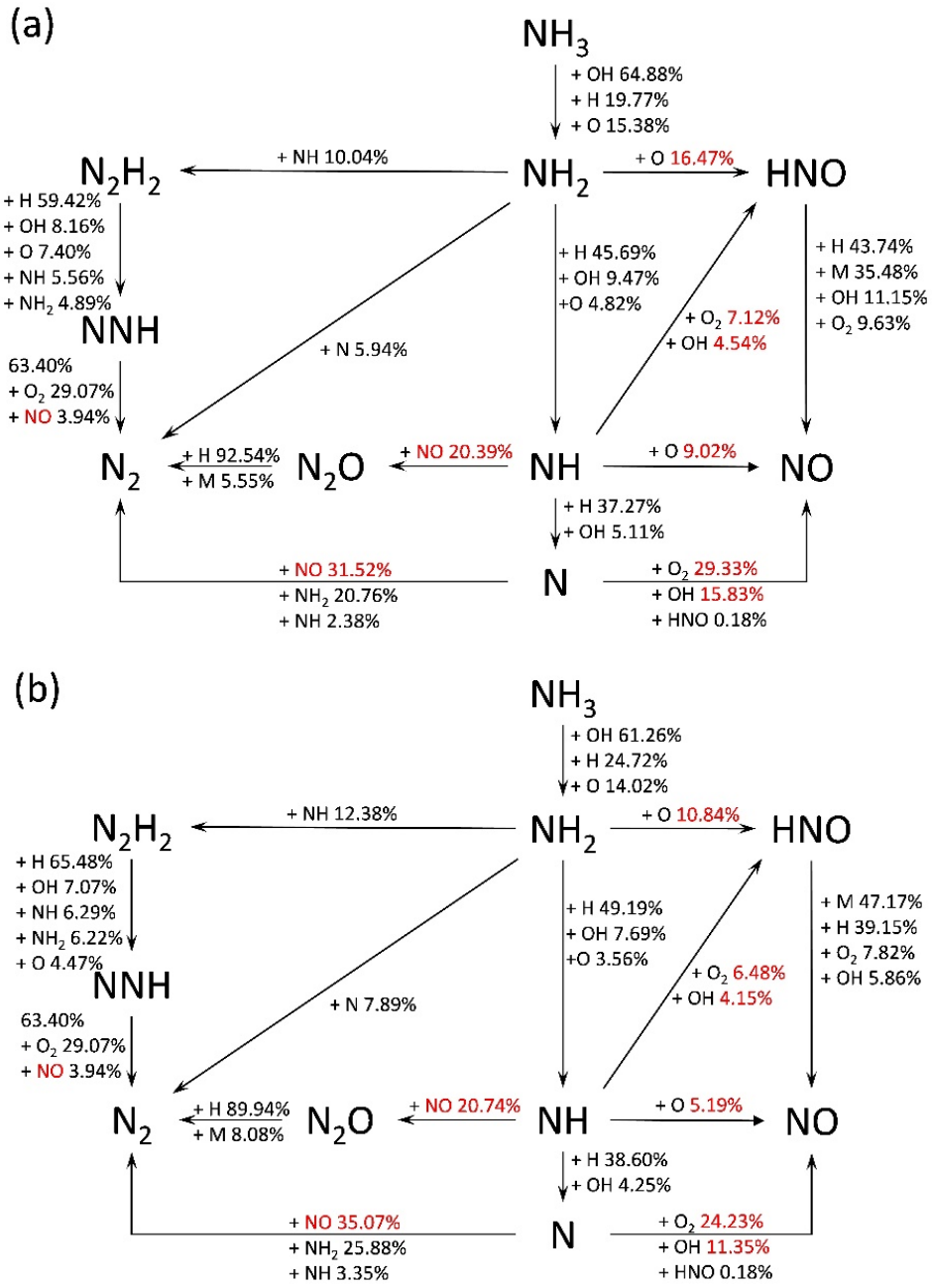

Figure 5.17 Reaction path diagram in 40% cracking NH_3 mixtures combustion progress at various equivalence ratio. (a) Φ = 0.8; (b) Φ = 1.2.

More specific, the ROP of reactions NH_2+O (R34), NH+O (R56), N+O_2 (R69) and N+OH (R68) that play essential role in NO formation are reduced when equivalence ratio rises from 0.8 to 1.2, demonstrated in Figure 5.18. Opposite tendency for NO consumption reactions (R63, R70, R47 and R62) is shown. In conclusion, the overall NO formation is decreasing when the

equivalence ratio rises from 0.8 to 1.2.

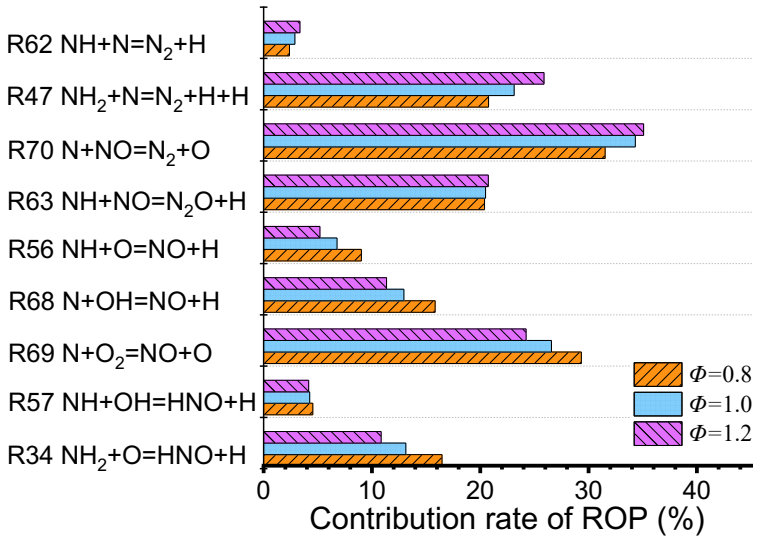

Figure 5.18 ROP of different reactions related with NO formation and consumption of in 40% cracking NH_3 mixtures at 0.8, 1.0 and 1.2 equivalence ratio.

5.8. Conclusion

Laminar flame propagation and NO_X emission characteristics of partial cracked ammonia ($NH_3/H_2/N_2$/air mixtures) in single and 2-stage rich-lean gas turbine combustor has been numerically investigated at various combustor operating parameters. The effects of ammonia cracking ratio, equivalence ratio, pressure, as well as residence time on NO_X emissions of the partially cracked ammonia are explored. In addition, modelling analysis of identifying the major NO_X reaction pathways and analysing the NO rate of production were conducted to give insight into the effects of NH_3 cracking ratio and equivalence ratio on NO formation/consumption. The major conclusions are summarized below.

(1) To conclude, the laminar burning speeds rise with increasing equivalence ratio initially, and then follows a decreasing tendency at Φ > 1.1. The maximum values of LBV are located around Φ = 1.1 for all calculated initial pressures. The peak value of LBV is

close to 37cm/s at *T*u = 298K and *P*u = 1atm, which considerably improve LBV of $NH_3/O_2/N_2$ flame (around 7cm/s). Additional, LBV is decreased obviously when the initial mixture pressure is increased from 1atm to 10atm.

(2) The LBVs increases significantly when the cracking ratio increases from 10% to 80 %. The tendency indicates that the combustion intensity is remarkably enhanced as cracking ratio increases.

(3) In single stage gas turbine combustor, the amount of NO_X emission firstly increases and then decreases sharply when the equivalence ratio is within 0.4-1.1. The location of maximum value of NO_X emission is close to 0.8 for all ammonia cracking ratios. After that, a decreasing trend is shown with further equivalence ratio increasing. Therefore, rich burn conditions can be employed to reduce total NO_X emissions in gas turbines. By identifying important intermediate components and reactions, the HNO radical, HNO + OH = NO + H_2O (R120) and NO + H (+ M) = HNO (+ M) (R117) play important role in NO production, while pathways of NH_i contribute more on NO reduction. More specifically, high NO_X emission zone is located at high ammonia cracking ratio and 0.6-1.0 ranges of equivalence ratio. In addition, the NO_X emission is promoted with increasing NH_3 cracking ratio from 10% to 80% at all equivalence ratio studied. As for the effect of initial pressure on NO_X emission throughout all NH_3 cracking ratios, it is noted that the NO_X emission goes to a lower value at each cracking ratio when the pressure increases from 10atm to 20atm.

(4) Both mole fraction of NO and OH* are increased as NH_3 cracking ratio increases in single stage gas turbine combustor. The peak OH* chemiluminescence intensity

located at the position of large NO mole fraction gradients. Besides, considerably higher intensities of OH* for all cracking ratios are located at Φ = 1.0 followed by a decaying trend due to lower oxygen, suggesting the flame position hardly changes with NH_3 cracking ratios.

(5) In rich-lean burn stage gas turbine combustor, as the primary equivalence ratio increases, NO_X emissions show almost the same performance as U-shaped curves, and the turning points are almost located at 1.3 and 1.4. The ranges of primary equivalence ratio for low NO emissions (below 50ppm) are around at 1.2-1.5 when the $\Phi_{overall}$ = 0.4 - 0.6. The NO_X prediction values at $\Phi_{primary}$ = 1.0 for all $\Phi_{overall}$ are very small (less than 1000 ppm), which are considerably lower than that in single stage. Therefore, using a second combustion stage burning is promising to reduce NO_X emission and solving the unburned NH_3 mixtures problem.

(6) The effect of NH_3 cracking ratio on NO_X emission is also explored in rich-lean burn stage gas turbine combustor. Similar tendency curves are captured at various cracking ratio, but the position of turning points is right shifted with rising cracking ratio. Interesting noting that the operating ranges of low NO emissions (below 50ppm) are obviously widen with increasing cracking ratio. In addition, NO_X formation is slightly increased with the increase of cracking ratio, whereas it shows gradually reducing trend at high primary equivalence ratio. In conclusion, cracking more NH_3 is beneficial for reducing NO_X emission and widening operation. Controlling cracking ratio (around at 40%) and primary equivalence ratio (i.e., controlling unburnt NH_3) in the range of 1.2-1.4 primary equivalence ratio enable to comprehensively widen operation range and reduce NO_X

emissions.

(7) The NO_X in each stage shows monotonically decrease with the increasing residence time in rich burn stage. Therefore, increasing residence time within reasonable context in primary stage has an advantage on NO_X reduction.

(8) When ammonia cracking rate increases from 20% to 60%, the ROP of promoting NO formation reactions rises (R34, R69, R68, R56), while the ROP of reactions related with NO consumption decreases. Therefore, more NO is generated with higher ammonia cracking rate.

(9) The contribution rate of reactions related with NO formation are generally decreased with increasing equivalence ratio, while the proportion of reactions that react with NO are increased. Therefore, the overall NO formation is reduced with equivalence ratio increasing from 0.8 to 1.2.

6. Chemiluminescent Emission as A Combustion Diagnostic Tool and Their Numerical Investigation

6.1. Introduction

The flame self-light emission can be readily imaged with modern digital cameras and analyzed with the ever-increasing computing and processing power. Therefore, chemiluminescence, as a promising optical diagnostic tool, is an area worth of further investigation. In section 6.2, numerical analysis on the heat release rate as well as equivalence ratio determination by applying excited state species (OH*, CH* and C_2*) chemiluminescence profiles is performed in a one-dimensional laminar premixed ethanol flame. The ability of flame chemiluminescence as a sensor of heat release rate at various equivalence ratios is discussed by combining rate of production analysis with sensitivity analysis. In section 6.3, the correlations between the chemiluminescence intensity ratio of C_2*/CH* as well as the equivalence ratio are investigated in hydrocarbon premixed flames based on chemical reaction kinetics mechanisms. Also, the phenomenon that the peak chemiluminescence intensity ratio of C_2*/CH* increases almost linearly following by a descending trend with local equivalence ratio is demonstrated from the chemical mechanisms' aspect for the first time.

6.2. Chemiluminescence intensity in ethanol flame

6.2.1. Signals of heat release rate with chemiluminescent emission

Heat release rate (HRR) is one of fundamental flame characteristics for identifying intensive reactive flame zone and predicting the unsteady combustion [337,338]. Owing to impractical measurement of HRR in flames, chemiluminescence has been employed as a marker of HRR

in premixed hydrocarbon flames [338,339]. Therefore, numerical analysis of the correlation between OH*, CH* and C_2* chemiluminescence profile and heat release rate is carried out in one-dimensional laminar premixed ethanol flame via PRE-MIX code of CHEMKIN-PRO package. The thermal diffusion effects are considered, and all simulations are converged to a grid-independent solution.

The mole fraction of excited state species and HRR profile are presented in Figure 6.1. OH* mole fraction increases earlier than others, and has a broader distribution than the others, consistent with the experimental results of Kojima et al. [226]. Nevertheless, discrepancy of breadth for CH* and C_2* is not obvious. It is interesting noted that the trend of excited species mole fraction coincides with the profile of heat release rate. The location of peak value of HRR matches that of large OH*, CH* and C_2* mole fraction gradients. The results suggest that the concentration of excited species can be a signal of heat release rate.

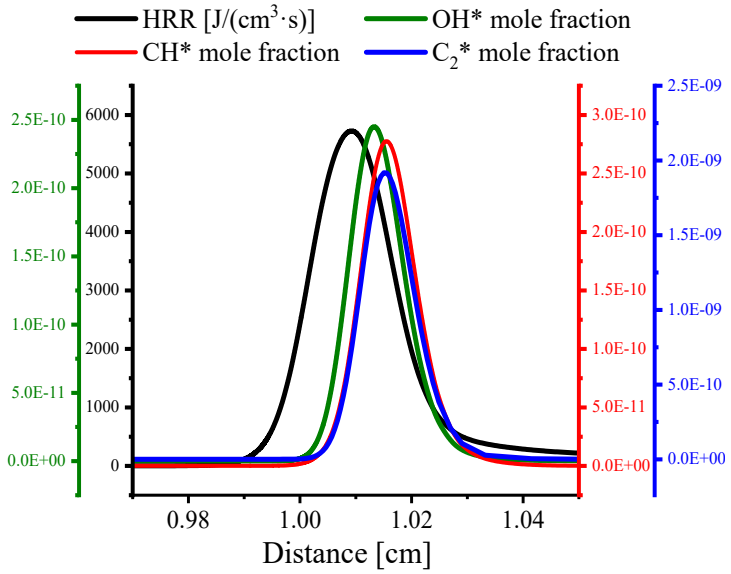

Figure 6.1 Mole fraction profiles and heat release rate at atmosphere pressure and Φ = 1.

In order to investigate the relationship between chemiluminescent intensity and heat release

rate in an ethanol flame, OH*, CH* and C_2* concentrations are calculated. Figure 6.2 (a) presents correlations of local heat release rate and mole concentration for excited state species in an ethanol/air premixed flame. The local heat release shows a multi-valued characteristic of local concentration for all excited state species. The concentrations have two profiles with the same value at different distances away from burner port, which shows a similar tendency of the heat release rate that can be seen in Figure 6.1. However, the looping behaviour indicates that the concentration profile is not able to express a specific monotonous correlation with chemiluminescent intensity.

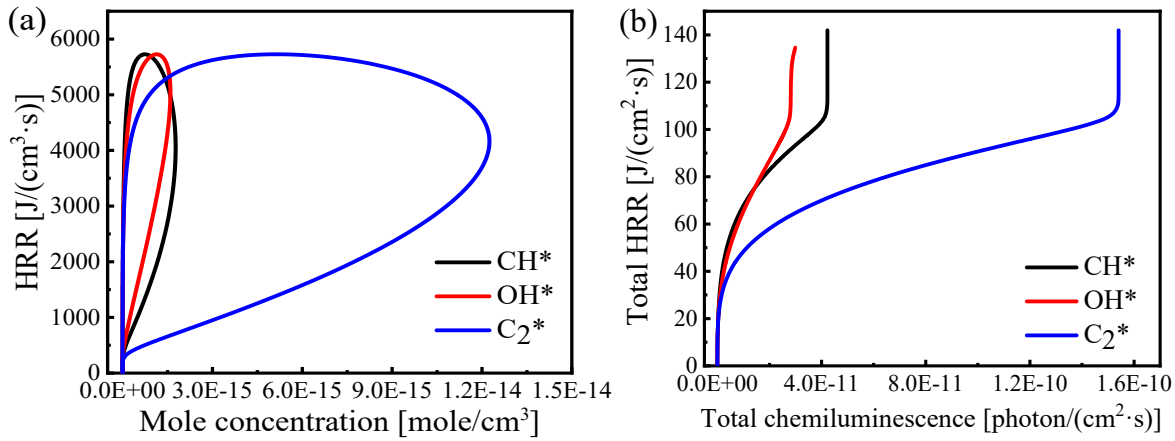

Figure 6.2 The correlation between chemiluminescent intensity and heat release rate at atmosphere pressure and Φ = 1.

To find the one-to-one relation between chemical markers and HRR in detail, the total chemiluminescent intensity is calculated to diagnose total HRR that is obtained by integrating the HRR profile over the calculating distance. The computational relationship of total heat release rate as well as total chemiluminescent emission is presented in Figure 6.2(b). It appears that the total heat release rate rises almost linearly with the total chemiluminescence. However, it shows a sudden rise at the end of curves followed by a linear relationship because the chemical reaction continues when the excited state radicals are consumed totally. This

process is going very fast. Additionally, the basic gradient of the corresponding correlation for OH*, CH* and C_2* decreases gradually. Consequently, the total chemiluminescent intensity is more than acceptable as a reliable signal to character the heat release rate.

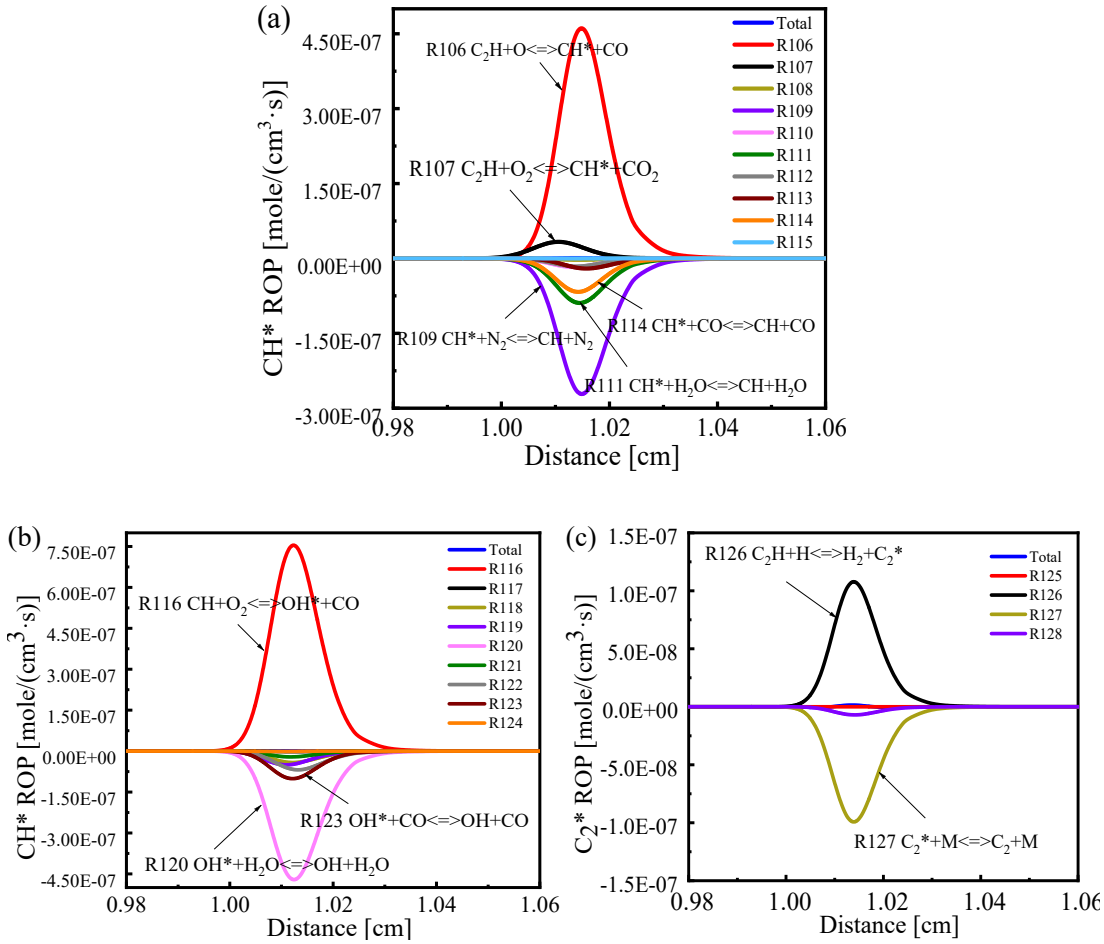

Figure 6.3 The major reactions for excited state species at atmosphere pressure and Φ = 1.

Rate of production is an effective method to identify contribution of each elementary reaction on production and consumption rate of species. In Figure 6.3, it demonstrates the contribution rate of each reaction related with excited state species on its rate of production at the atmosphere pressure and Φ = 1. Clearly appearing that CH* is generated mainly via oxidation reaction of R106 and R107. C_2H reacted with O atom and O_2 molecule are predominant reactions for CH* production, which agree with results reported by Nori et al.

[228] and Panoutsos et al. [311]. Moreover, CH* is deactivated via collision reactions with N_2(R109), CO(R114) and H_2O(R111) radicals. Moreover, it is found that the CH oxidation by O_2 plays a major role in producing OH*, which is more important than other reactions of the OH* formation. Actually, R116 is a primary exothermic reaction as proposed by Gaydon et al. [248]. Similarly, OH* reacting with CO and H_2O are main channels to consume OH* radical, according to Figure 6.3(b), and this conclusion agrees with the results of the model proposed by Kathrotia [340]. In addition, seen from Figure 6.3(c), abstracting H from C_2H contributes more on C_2* formation in ethanol flame.

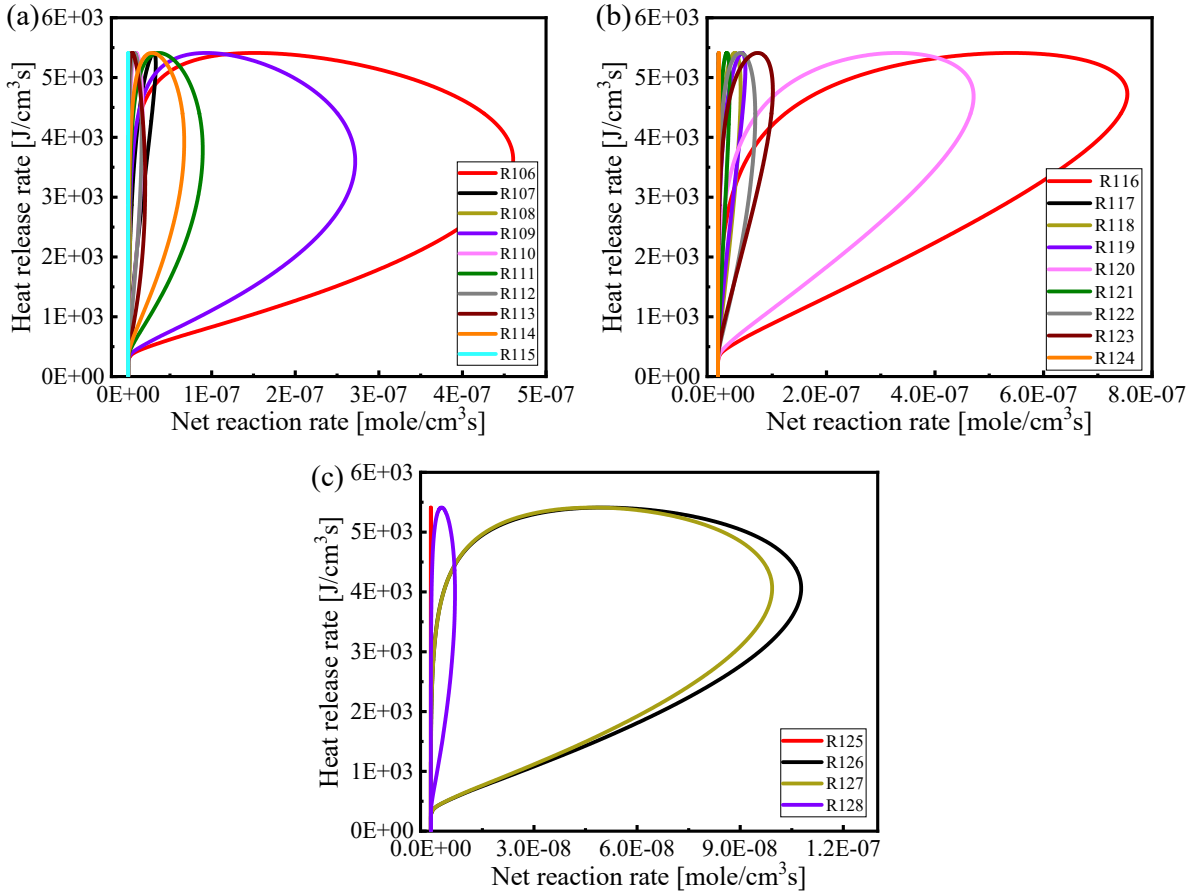

Figure 6.4 The correlation between net reaction rate of elementary reaction for OH*(a), CH*(b), C_2*(c) and heat release rate at atmosphere pressure and Φ = 1.

It is interestingly noted that those important reactions involving excited state species also

have a great influence on heat release rate, consistent with results presenting in Figure 6.1. The net reaction rate of each elementary for excited state species and heat release rate are simulated and displayed in Figure 6.4. Each reaction has individual effect on the heat release rate, which depends on its contribution to the major carbon flow. More importantly, reactions with a large contribution rate on the formation as well as consumption of the excited state species also have a great influence on the heat release rate.

6.2.2. Flame structure at various equivalence ratio

Traditionally, accurate control of flame stoichiometry is essential to maintain low levels of pollutant emissions while ensuring high efficiency and stable combustion. Usually, The NO_X production would increase as the fuel-air ratio increases. However, when the flame equivalence ratio is in a lean region, there is a serious risk of producing high CO emissions, triggering pressure fluctuations and even flame extinction. Therefore, it is of great significance to monitor and optimize the fuel-air ratio to improve premixed combustion. Thus, the effect of equivalence ratio on the chemiluminescent emissions of OH*, CH* and C_2* are analysed.

Figure 6.5 shows the concentration profile of OH*, CH* and C_2* radicals over the range of distance at atmosphere pressure, and equivalence ratio varying from 0.6 to 1.5. It can be found that the trend of concentration of each excited state species is basically uniform for all equivalence ratios, showing single and positive peak curves. In addition, it can be observed that the broadness of concentration emissions increases first and then reduces as the equivalent ratio rises. The width is narrowest when the peak value of concentration reaches the largest. However, the peak values of concentration profiles for different species are located at various distances under various equivalence ratios.

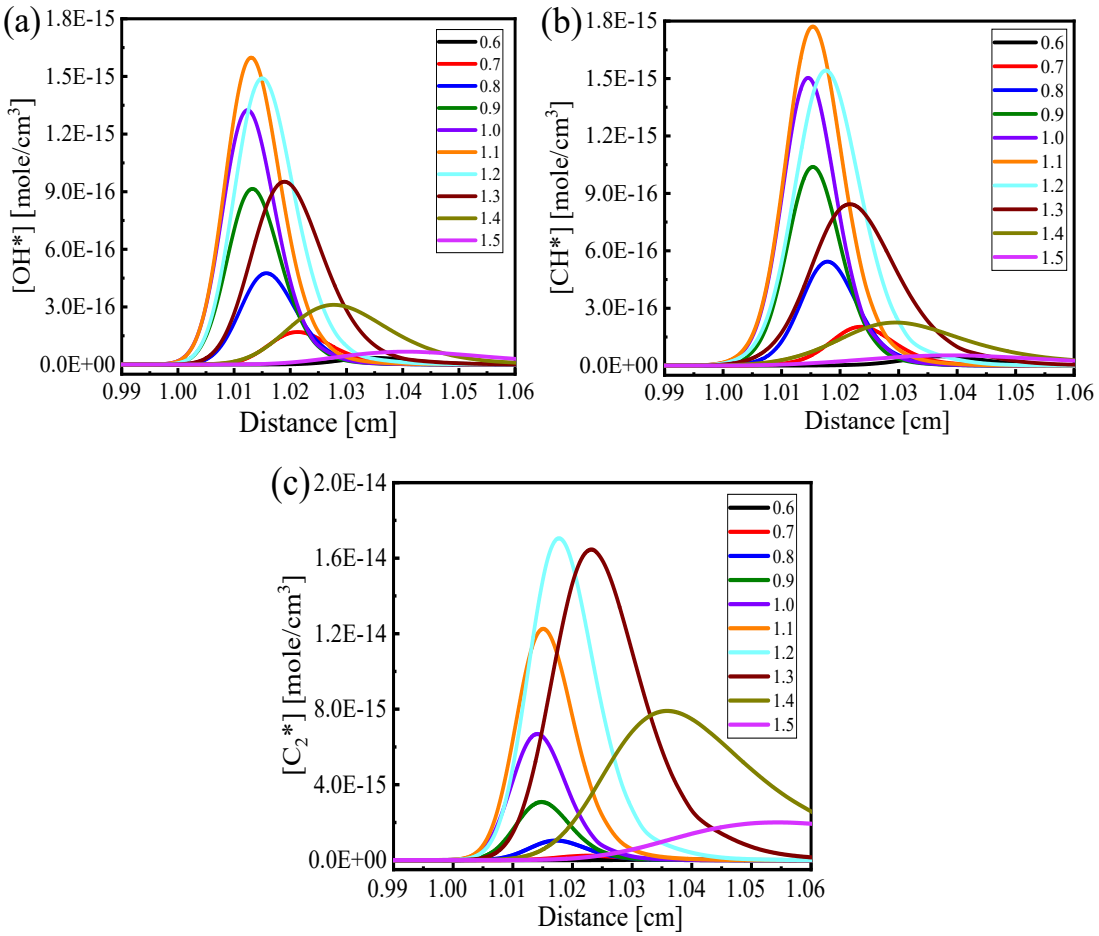

Figure 6.5 Concentration profiles of OH*, CH* and C_2* radicals at atmosphere pressure and various equivalence ratio.

The total heat release rate is also calculated at various equivalence ratios, displayed in Figure 6.6. It increases at the first time and reduces monotonically with equivalence ratio going up thereafter. The peak values of chemiluminescent intensity at different equivalence ratios for OH*, CH* and C_2* are compared in Figure 6.7. All peak intensity variations are scaled from 0 to 1 by its maximum value among all the equivalence ratios for each species. Similar trend curves are captured as that of total heat release rate, the peaks of normalized chemiluminescence for the three excited state species increase firstly, followed by a decreasing trend with the increasing equivalent ratio. The results also shows that chemiluminescent intensity is able to characterize the total heat release rate. However, the

locations of maximum peak intensities are different. The trends observed the chemiluminescent intensity for CH* and C_2* are same as that of OH*. The maximum value of OH* and CH* intensities is located at Φ = 1.1, while it appears at around 1.35 for the C_2* maximum intensity. The deviation should be affected by the specific reaction paths.

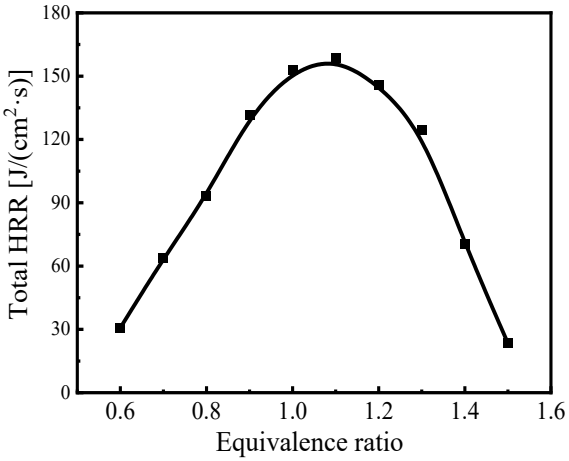

Figure 6.6 The total heat release rate at various equivalence ratio.

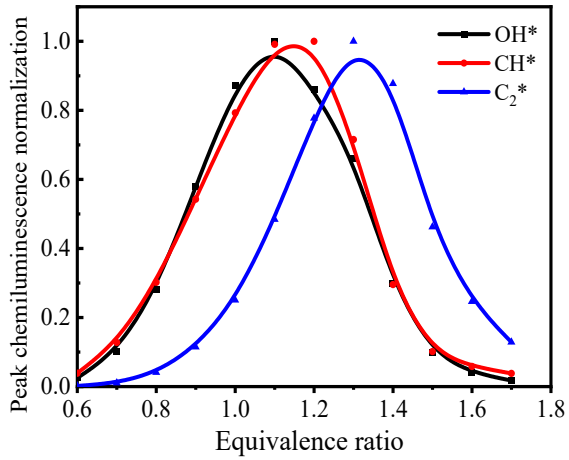

Figure 6.7 Normalized OH*, CH* and C_2* radicals' chemiluminescent intensity as a function of equivalence ratio for premixed ethanol flames.

Taking into account the non-monotonicity of the chemiluminescent intensity with the change of equivalence ratio, the sensitivity analysis is performed to detect the influence of important

reactions on the peak of chemiluminescent intensity at different equivalence ratios. Three equivalence ratios are chosen to explore important producing and consuming reactions of each excited state species at lean and rich fuel conditions under atmosphere situation. Sensitivity coefficients of important reactions for OH*, CH* and C_2* are plotted in Figure 6.8. It points out that R116: CH reacts with O_2 generating OH* and R120: OH* is deactivated by H_2O are dominating reactions on OH* concentration, which is consistent with the analysis of Figure 6.3. Similarly, reactions R106, R107 and R109 make a significant contribution to CH* concentration around all equivalence ratios. Moreover, although the contributions of other parts of reactions are different, abstracting H from C_2H_5OH, and other reactions related intermediate species like CH_3CHOH, CO, OH, CH_2O, C_2H_4 and CH_3 play a crucial role in all of excited state species concentration. However, seen from Figure 6.8(a), the sensitivity coefficient of reactions CO + OH <=> CO_2 + H and H + O_2 + M <=> HO_2 + M are large for OH* at Φ = 0.8, while the sensitivity coefficients of them are small when the equivalence ratio increases to 1.4. On the other hand, except for these two reactions, others do not show obvious difference. The contribution of O_2 + H <=> O + OH on CH* and C_2* sensitivity coefficient decreases with the reducing equivalence ratio. Besides, the discrepancies of sensitivity coefficient of reactions C_2H_4 + OH <=> C_2H_3+ H_2O and CH_3 + HO_2 <=> CH_3O + OH are also distinct for CH* and C_2* in lean and rich fuel mixtures, shown in Figure 6.8(b) and (c) accordingly.

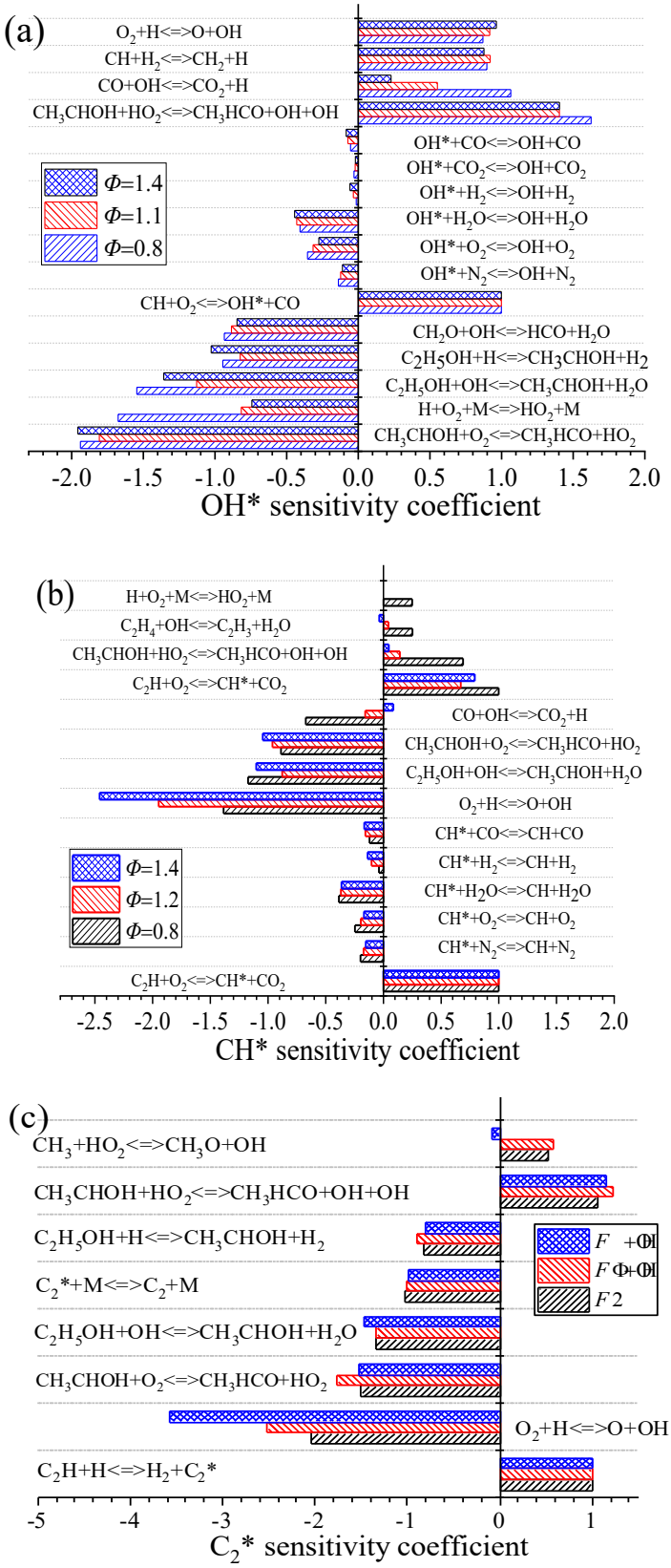

Figure 6.8 Sensitivity coefficients for OH*(a), CH*(b)and C_2*(c) at 298K, atmosphere pressure and different equivalence ratio.

6.2.3. Reaction path analysis of ethanol flame

A further step is to investigate the major mole flux of ethanol oxidation flame with excited species at 1atm, Φ = 1 and 1100K, shown in Figure 6.9.

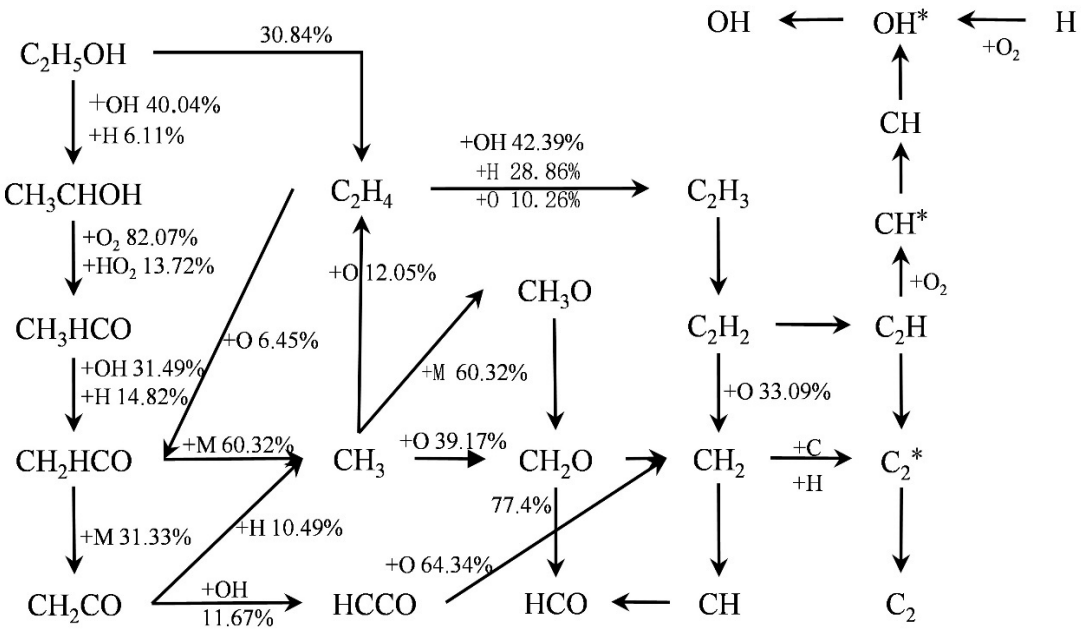

Figure 6.9 The mole flux analyses of ethanol oxidation with excited species.

The most important intermediates are identified during the ethanol mechanism reduction process. The mole fraction of the target radicals is calculated by integrating the production rate of the principal reaction paths during the ignition time. Starting from the C_2H_5OH, which is mainly consumed by OH radicals to generate CH_3CHOH (around 40.04%) and C_2H_4 (around 30.84%). The number indicates the mass fraction of the reactants consumed in the ethanol reaction pathway. It can be used to analyze the contribution percentages of the main reaction paths to production of the excited state radicals. Reaction $C_2H_5OH + M <=> CH_3 + CH_2OH + M$ and H-atom abstraction reactions $C_2H_5OH + HO_2 <=> CH_3CHOH + H_2O_2$ from ethanol dominate the consumption of ethanol. After that, the CH_3CHOH isomer decomposes with oxygen forming CH_3HCO, which is an important intermediate radical to impact the generation of CH_3

radical. Reactions of ethanol consumption and $CH_3CHOH + HO_2 <=> CH_3HCO + OH + OH$ are the main channels of carbon flow, and CH_3, CH_2, C_2H_2 and HO_2 radicals show the great influence on significant intermediate species in Figure 6.9.

Besides, it is clearly noted that excited species (OH*, CH* and C_2*) are dominated by C_2H, CH_2 and CH_2O radicals, however, these radicals are affected greatly by CH_3 radicals. As shown in Figure 6.9, CH_2HCO (60.32%), C_2H_4 (12.05%) and part of CH_2CO react with reactive species to form CH_3, so the conclusion is that CH_3 radical is more likely a precursor of excited species in ethanol flames.

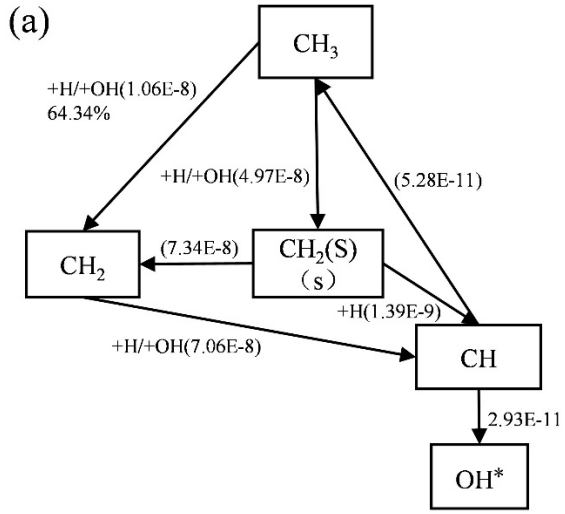

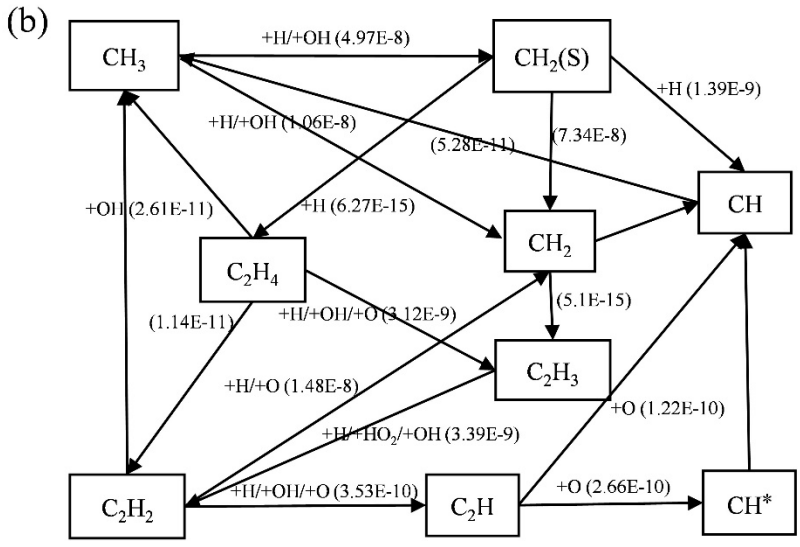

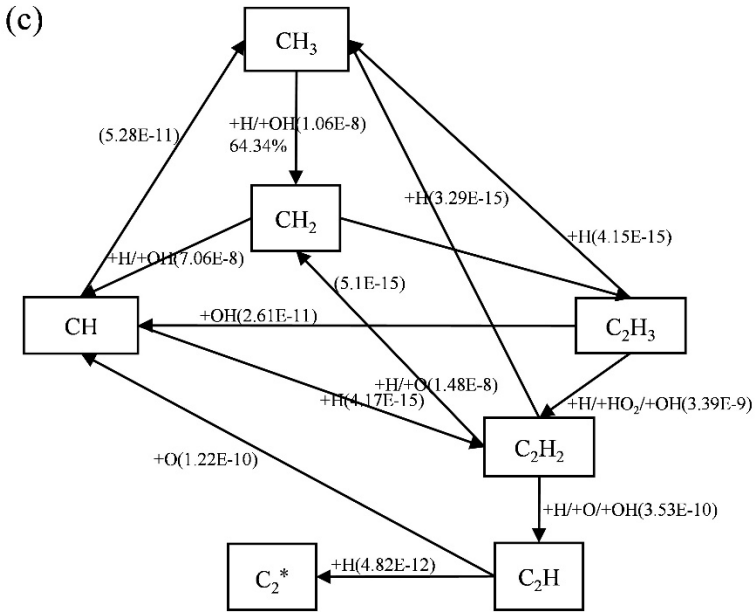

Figure 6.10 Reaction scheme of OH*(a), CH*(b) and C_2*(c) in ethanol combustion.

Figure 6.10 presents the reaction scheme that is preferred by the CH_3 radical to identify the predominant reaction paths for excited species formation and consumption. The number represents rate of production for each elementary reaction between two species, which is calculated in a closed chamber with constant volume. Only the most important reaction paths are kept. According to the reaction scheme, the CH_3 radical is the precursor for CH_2 formation via reaction with H and OH radicals. The CH_2 radical is responsible for excited species formation, especially for OH* radical production (Figure 6.10a). Except for CH_3 and CH_2 radicals, C_2H_3, C_2H_2 and C_2H also have significant effects on the chain production reactions of CH* and C_2*, but these species do not show great influence on the OH* formation. In conclusion, the most important formation reactions of excited state species involve CH_3, CH_2, C_2H_2 and HO_2 radicals in ethanol combustion. It gives a sight that the variation of the precursor reaction parameters would significantly affect the chemiluminescence profiles.

6.3. Chemiluminescence intensity ratio in hydrocarbon flames

6.3.1. Chemiluminescence intensity ratio versus local flame stoichiometry

Investigating the relation between the chemiluminescence intensity ratio of C_2*/CH* and the equivalence ratio in hydrocarbon premixed flames is very important and desirable. The experimental results reported by Kojima et al. [341] indicate that there is linear relationship of C_2*/CH* to the equivalence ratio from Φ = 0.9 to 1.35. Measurement of chemiluminescent emissions of C_2* and CH* is much easier than that of OH*. Kojima et al. [341] measured the distributions of OH*, CH*, and C_2* chemiluminescent intensities at equivalence ratios of 0.9-1.5 in a premixed methane/air flame. They analyzed the correlations between the peak intensity ratios of the excited state radicals and the equivalence ratio, suggesting that the intensity ratio of C_2*/CH* is a function of the equivalence ratio. The experimental records are applied to compare with the simulation results of methane kinetics mechanism that is extended with sub-models of excited state species. Figure 6.11 presents the comparison between experimental (dot dash line) [341] and simulated (dot solid line) chemiluminescent profiles of the chemiluminescence intensity ratio at different equivalence ratios. Generally, the predictions of the intensity ratios of C_2*/CH*, C_2*/OH*, and OH*/CH* agree well with experimental results. The reason for the experimental data of C_2*/CH* become higher than predictions at an equivalence ratio of 0.9 is that C_2* chemiluminescent intensity is low, and the experimental data become less reliable, but a high proportion is produced in the rich flames, which was also interpreted by Kojima et al. [341]. In any case, the calculated results still can well predict experimental data and the little differences that can be tolerated in the current study. Therefore, the sub-models of excited state species used in this

work are able to be added into other fuel mechanisms for further studying the chemiluminescence and flame structure.

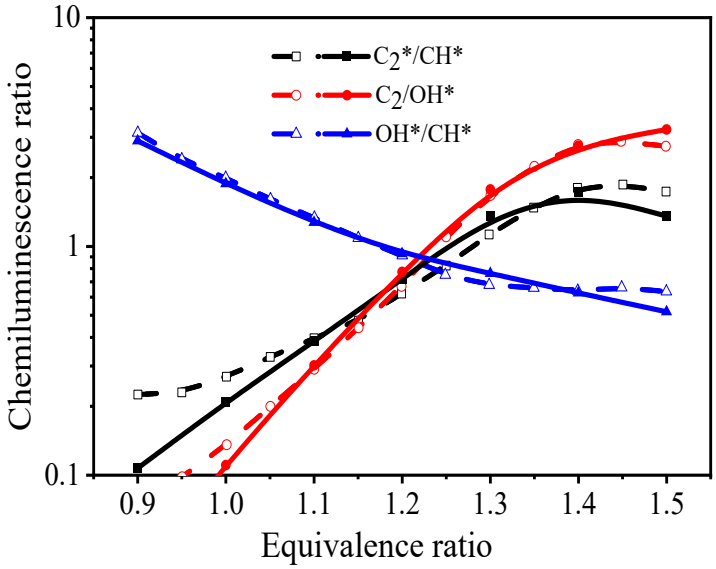

Figure 6.11 The comparison between experimental (dot dash line) and simulated (dot solid line) chemiluminescent profiles of the chemiluminescence intensity ratio at various of the equivalence ratio.

The dependence of the peak chemiluminescence intensity ratio of C_2*/CH* on equivalence ratios is also simulated in the ethanol and propane flames. Figure 6.12 presents that the peak chemiluminescence intensity ratios of C_2*/CH* against the equivalence ratio from 0.9 to 1.6 in ethanol and propane reaction zone. It is interestingly noted that the trend of peak intensity ratio of ethanol flame coincides with that of propane. In both, the peak chemiluminescence intensity ratio of C_2*/CH* increased almost linearly as the equivalence ratio increases to around 1.5. After that, similar to the methane curve, the peak intensity ratios present a slowly descending tendency. Consequently, the peak intensity ratio of C_2*/CH* is formed as a function of the equivalence ratio in certain local regions, however, it is insensitive with the flame stoichiometry when the equivalence ratio exceeds a specific value. Therefore, it is of

interest to analyse the mechanism around the inflection point.

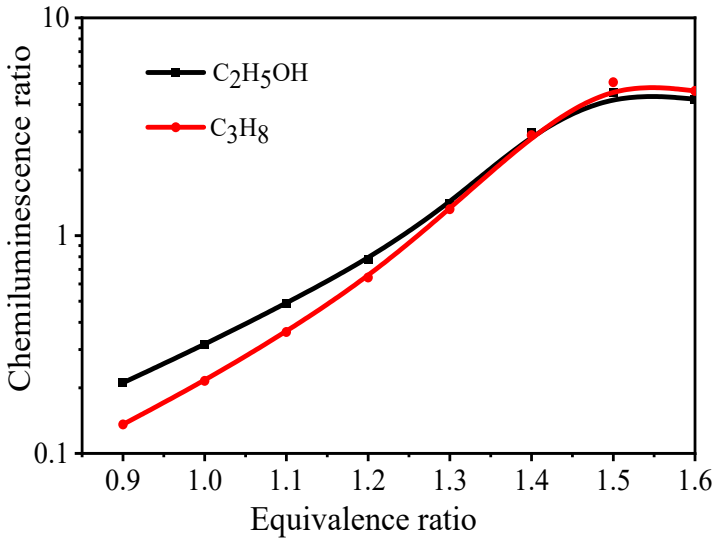

Figure 6.12 The peak chemiluminescence intensity ratios of C_2*/CH* against the equivalence ratio in ethanol and propane premixed laminar flames.

6.3.2. ROP analysis of the inflection point

The concentration of excited state species can indicate the chemiluminescence intensity, because the life of electron excitation is low, and it can be quickly removed by collision quenching. So, the reactions of excited species are usually of interest in the quasi-steady state assumption. In this case, the production and removal rate of the excited state species can be analysed to interpret the chemiluminescence intensity.

Figure 6.13 presents the normalized peak chemiluminescence profiles of OH*, CH* and C_2* radicals for three fuels over the range of equivalence ratio from 0.6 to 1.6. All peak intensity variations were scaled from 0 to 1 by its maximum value among all the equivalence ratios for each species. The OH*, CH* and C_2* peak chemiluminescent intensities increase monotonically with equivalence ratio for all lines initially and then reduces monotonically with equivalence ratio going up in the three flames before reaching a maximum. However, the locations of the maximum peak intensities are different. In addition, for all of three fuel flames,

C_2* peak chemiluminescence intensity is relatively higher than that of the CH*, so the production and consumption reactions of C_2* contributes more than CH* in the peak chemiluminescence intensity ratio of C_2*/CH*.

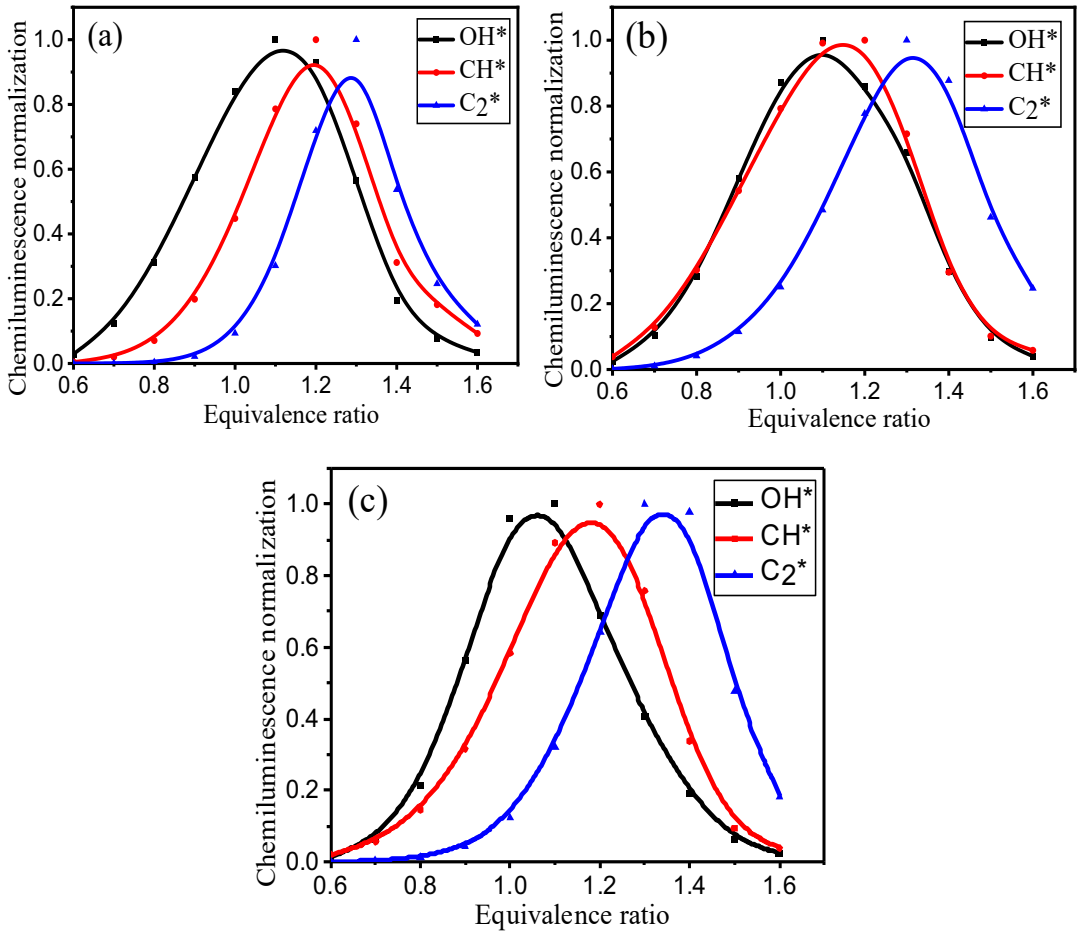

Figure 6.13 Normalized chemiluminescent intensity of OH*, CH* and C_2* radicals as a function of equivalence ratio for (a) methane, (b) ethanol and (c) propane flames.

Rate of production (ROP) is an effective method to identify the contribution of each elementary reaction on production and consumption rate of species. To explain the peak chemiluminescence intensity ratio of C_2*/CH* around the inflection point, major producing and consuming reactions related to CH* and C_2* in methane, ethanol, and propane fuel premixed flames are presented separately in Figure 6.14-6.16. It is clear that the CH* is generated mainly through oxidation reactions of $C_2H + O <=> CH^* + CO$ (red line) and $C_2H + O_2$

<=> CH* + CO_2 (blue line), and C_2* is generated mainly via CH_2 + C <=> H_2 + C_2*(red line) and C_2H + H <=> H_2 + C_2* (blue line).

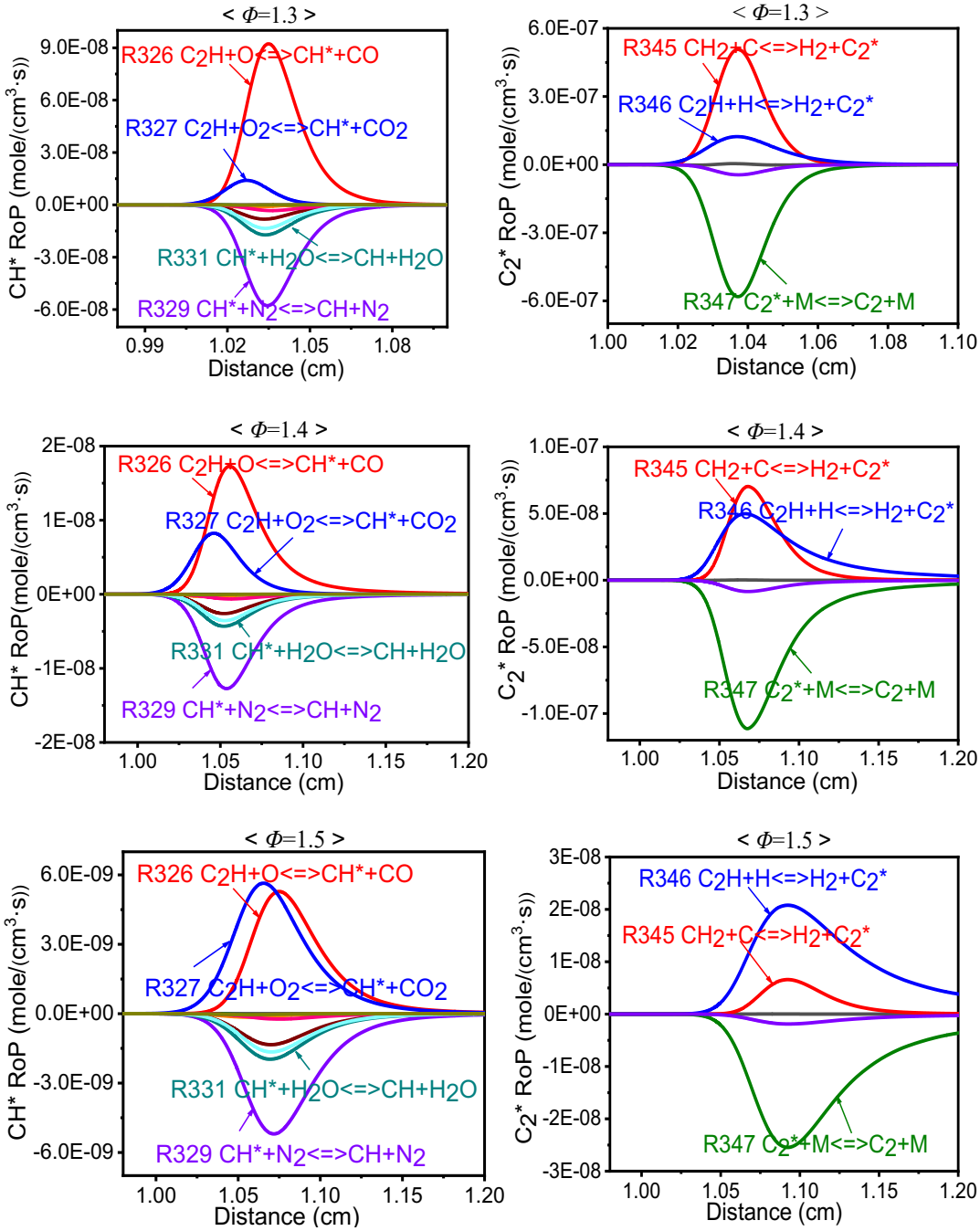

Figure 6.14 The major reactions for CH* and C_2* at Φ = 1.3, 1.4 and 1.5 in methanol flame.

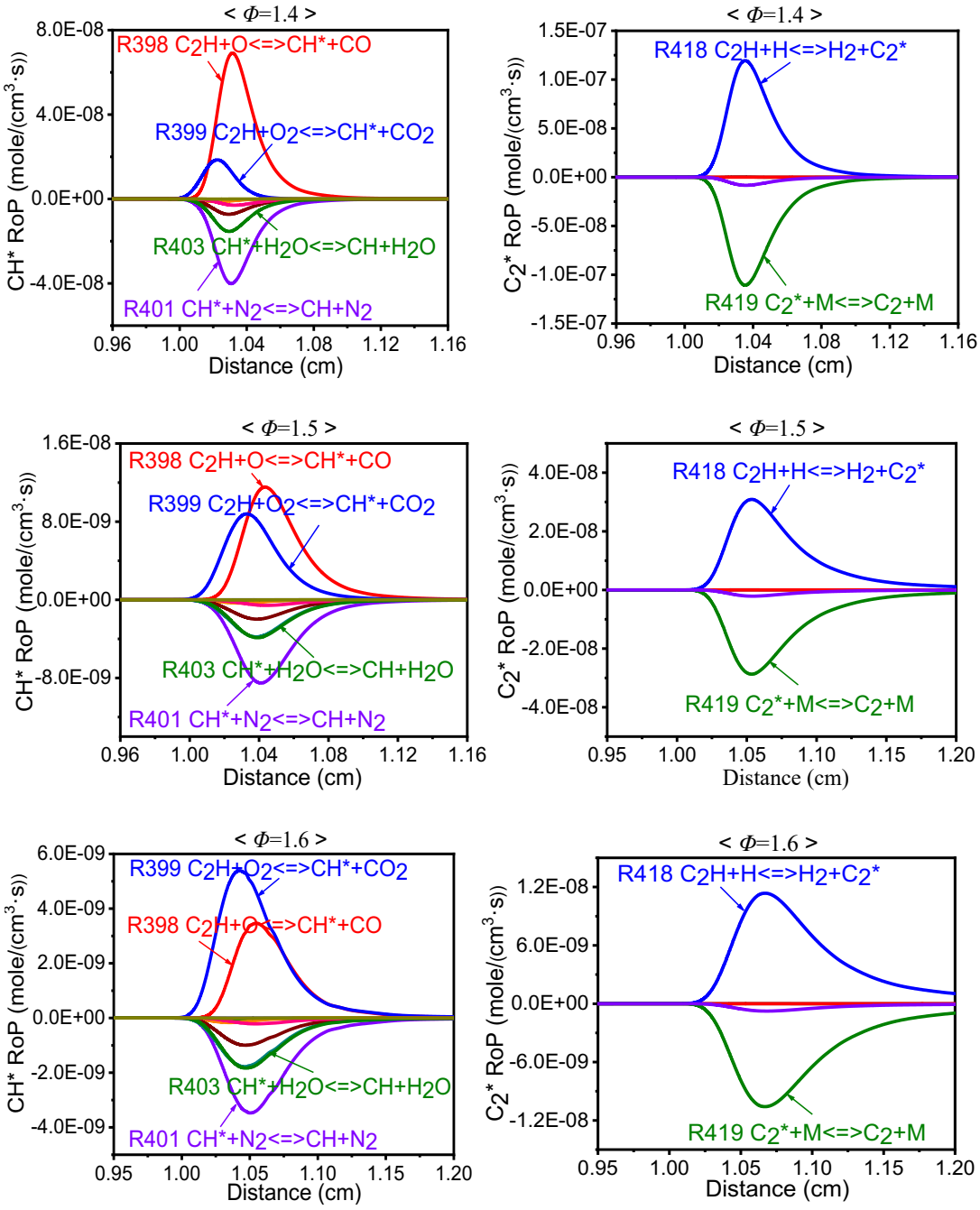

Figure 6.15 The major reactions for CH* and C_2* at Φ = 1.4, 1.5 and 1.6 in ethanol flame.

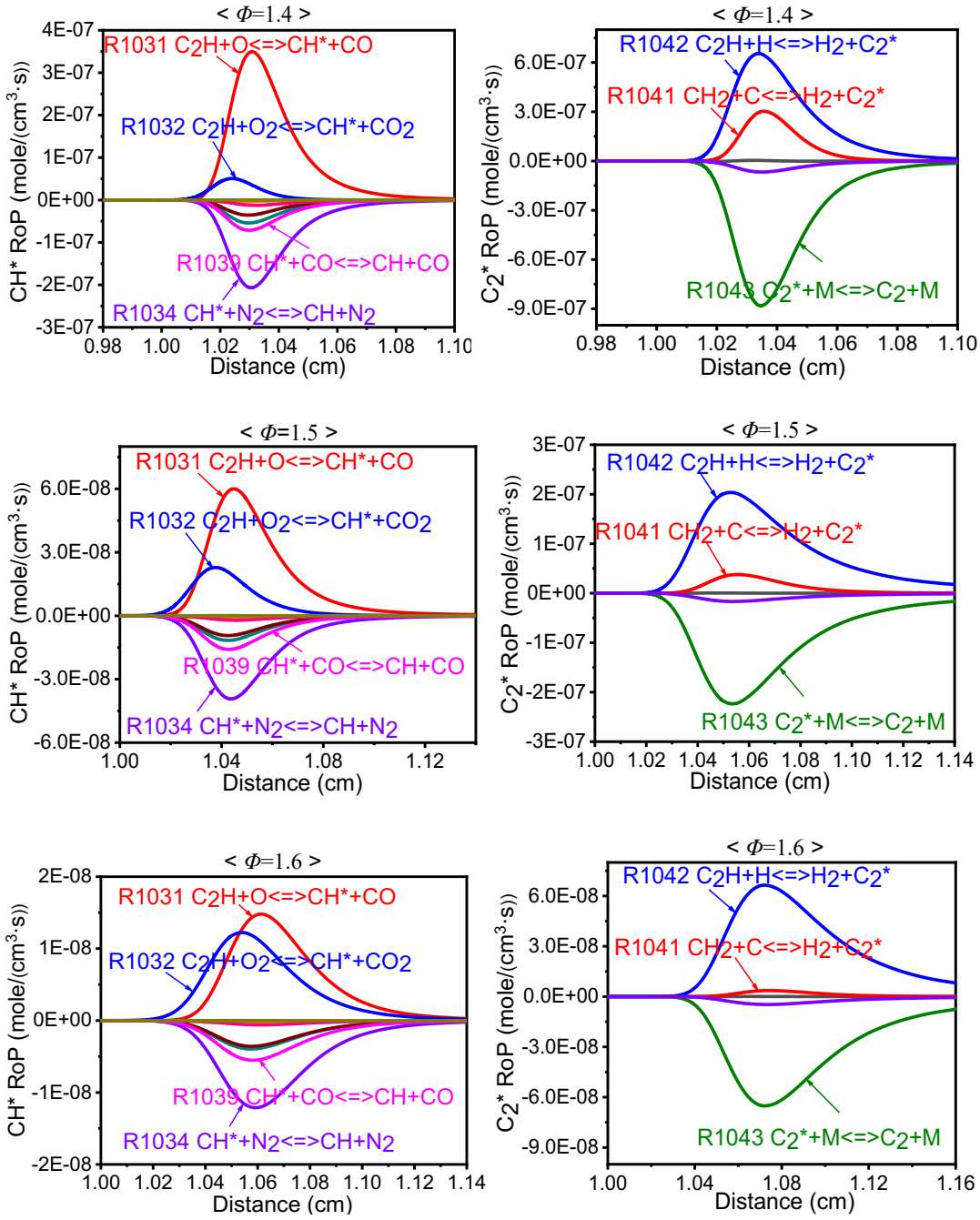

Figure 6.16 The major reactions for CH* and C_2* at Φ = 1.4, 1.5 and 1.6 in propane flame.

In the case of CH*, it is notable that the contribution rate of reaction $C_2H + O <=> CH^* + CO$ decreases when the equivalence ratio increases for all the three fuel flames, while the reaction $C_2H + O_2 <=> CH^* + CO_2$ becomes more important. As a result, the contribution rate of reaction $C_2H + O_2 <=> CH^* + CO_2$ is even higher than the reaction $C_2H + O <=> CH^* + CO$

when the equivalence ratio is beyond the inflection point. It is not the same as methane and ethanol, the CH* rate of production of the blue line for propane stays lower than that of the red line at Φ = 1.6, but the tendency of the blue line keeps raising with the growing equivalence ratio. On the other hand, for C_2*, the reaction $CH_2 + C <=> H_2 + C_2$* is more important than $C_2H + H <=> H_2 + C_2$* at Φ = 1.3, 1.4 in methane flame, but its contribution rate becomes lower than that of the reaction $C_2H + H <=> H_2 + C_2$* when Φ > 1.4. Different from the methane flame, the reaction $C_2H + H <=> H_2 + C_2$* is dominant in all cases in both ethanol and propane flames. In addition, the relative consumption contribution rate of each reaction for CH* and C_2* does not show great difference in the three fuel premixed flames. Therefore, it is concluded that reactions $C_2H + O_2 <=> CH^* + CO_2$ and $C_2H + H <=> H_2 + C_2$* are of great significance to invert the monotonicity of the chemiluminescence intensity ratio of C_2*/CH* with the equivalence ratio.

6.3.3. SA analysis of the inflection point

The sensitivity coefficient can be used to indicate the effect of the small perturbation of each reaction rate constant on a target value, such as species concentration, temperature and reaction rate, based on the Arrhenius equation. In this study, the sensitivity analysis is employed to identify the influence of important reactions related to CH* and C_2* on the peak of chemiluminescence intensity at different equivalence ratios. Three equivalence ratios were chosen based on Figures 6.14-6.16 corresponding to the three chosen fuels to explore the important reactions under lean and rich fuel conditions in atmosphere circumstance. Sensitivity coefficients of CH*and C_2* in different fuel flames are plotted in Figure 6.17. A positive sensitivity coefficient indicates that the generation of radicals can be promoted, and

vice versa.

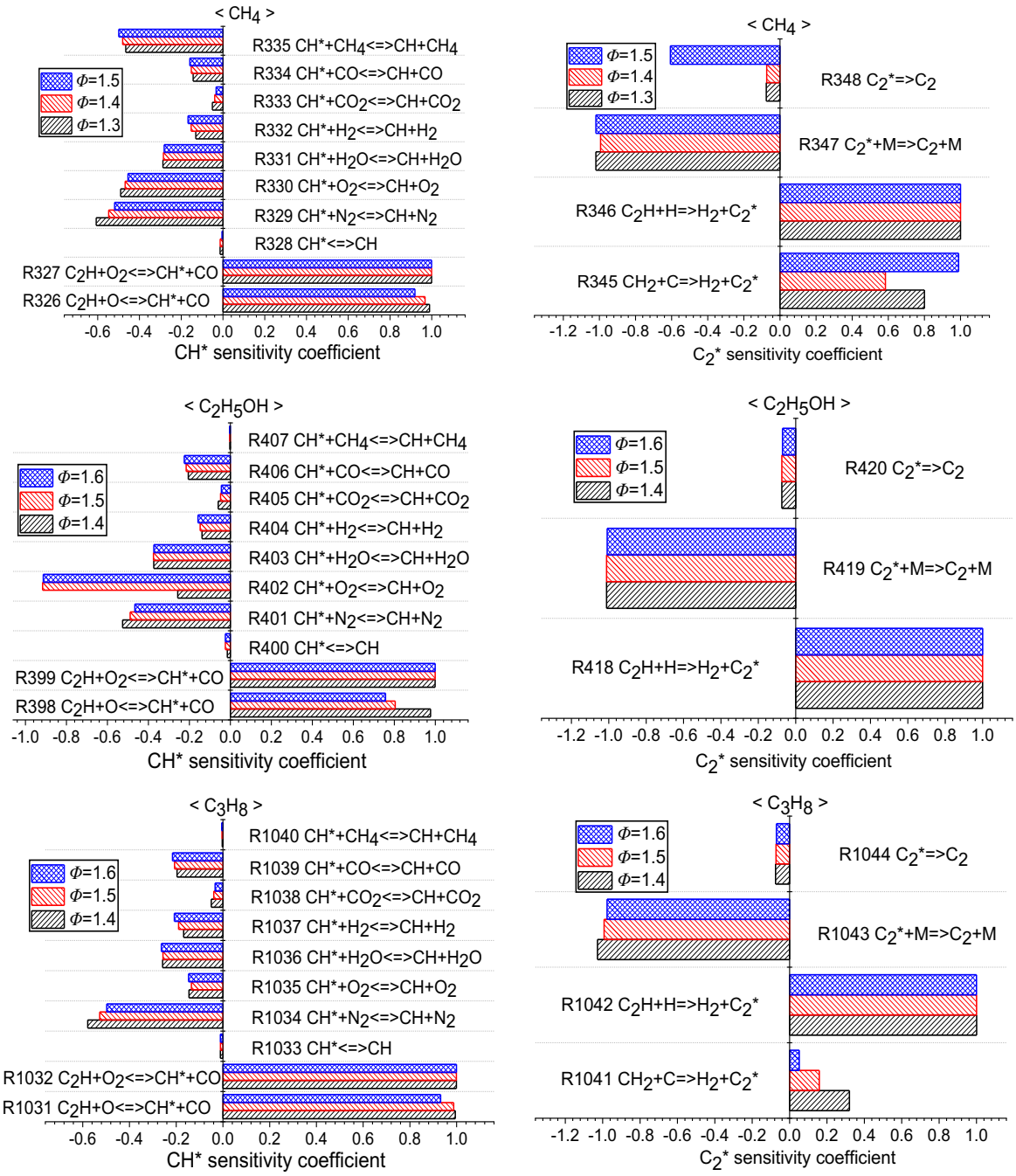

Figure 6.17 Sensitivity coefficients for CH* and C_2* at atmosphere pressure and different equivalence ratio in methane, ethanol and propane flames.

Seen from Figure 6.17, it points out that C_2H reacting with O_2 and oxygen atoms generating CH* are dominating reactions on CH* concentration in the three flames, which is consistent with the analysis of Figures 6.14-6.16. Furthermore, the sensitivity coefficient of production

reactions of CH* and C_2* is greater than that of consumption reactions. More interestingly, the contribution rate of the reaction that C_2H reacts with O_2 on the CH* generation stays at a high level and keeps almost unchanged, but it is on the decline for the reaction that C_2H reacts with oxygen atoms with increasing equivalence ratio. Similar results are found in C_2* production reactions. The reaction of C_2H and H atom is dominant in the generation of C_2*, and the effect of the reaction $CH_2 + C <=> H_2 + C_2$* on the sensitivity coefficient can be even neglected in ethanol and propane flames. This demonstrates that the chemical reactions $C_2H + O <=> CH^* + CO$ and $CH_2 + C <=> H_2 + C_2$* are not the principal causes of the change of the chemiluminescence intensity ratio of C_2*/CH*. According to the sensitivity analysis of CH* and C_2* for the three fuels, it can be concluded that the influence of reactions $C_2H + O_2 <=> CH^* + CO_2$ and $CH_2 + C <=> H_2 + C_2$* on the sensitivity is more obvious at all ranges of the equivalence ratio.

6.4. Conclusions

A comprehensive mechanism that is combined with ethanol chemical kinetics mechanism and excited species sub-model is successfully validated. It is applied to numerically simulate the chemiluminescent emission intensities of OH*, CH* and C_2* in one-dimensional ethanol premixed flames. The results are concluded in the following points:

A) For the chemiluminescence Intensity in Ethanol Flame:

- Chemiluminescence as a signal of heat release rate is discussed. The results show that the local heat release presents a multi-valued characteristic of local concentration for all excited state species. However, the total heat release rate rised almost linearly with

increasing total chemiluminescence. Consequently, total chemiluminescence is more acceptable as a reliable signal to character the heat release rate. Besides, it is also presented that the reactions with a large contribution rate on formation and consumption of the excited state species also have significant effects on the heat release rate.

- In addition, effects of equivalence ratios on chemiluminescent emissions of OH*, CH* as well as C_2* are analyzed. All peaks of chemiluminescent intensity for the three excited states increase at the first time, following that a decreasing trend with the increasing equivalent ratio is displayed. The total heat release rate also appears to have the same tendency at different equivalence ratios. Moreover, results indicate that the maximum value of OH* and CH* chemiluminescence intensities appears at Φ = 1.1, while the maximum intensity for C_2* appears at around Φ = 1.35. The deviation should be affected by the specific reaction paths.
- During the process of the formation and decay reactions of the excited radicals, CH_3 radical is more likely a precursor of excited species in ethanol flames. Analyzing the reaction paths can conclude that the variation of the precursor reaction parameters would significantly affect the chemiluminescence profiles. As a result, the present numerical simulation provides a guidance for employing much easier chemiluminescence experiments setup to detect flame characteristics using imaging-based techniques.

B) For the chemiluminescence intensity ratio versus local flame stoichiometry:

- Extended mechanisms including OH*, CH* and C_2* sub-models for methane, ethanol and propane are developed and successfully validated, which are used to examine the reliance

of the chemiluminescence intensity ratio of C_2*/CH* on the equivalence ratio in three premixed laminar flames.

- In agreement with the experimental observation, the peak chemiluminescence intensity ratio of C_2*/CH* increases almost linearly as the local equivalence ratio grows from 0.9 for all of three fuel flames at first. After that, the intensity ratios present a slowly descending tendency when Φ > 1.35, 1.5, 1.5 for methane, ethanol and propane flames respectively.
- the most important reactions that invert the monotonicity of the chemiluminescence intensity ratio of C_2*/CH* with increasing equivalence ratio are analysed numerically for the first time in three fuel flames. The reactions $C_2H + O_2 <=> CH^* + CO_2$ and $C_2H + H <=> H_2 + C_2^*$ are identified to be the most important reactions that invert the monotonicity of the chemiluminescence intensity ratio of C_2*/CH* with equivalence ratio in all the three fuel flames.

7. Conclusions and Future work

The main objective of the thesis is to study combustion and emission characteristics of partially cracked ammonia ($NH_3/H_2/N_2$/air mixtures) and chemiluminescent emission for hydrocarbon fuel based on the chemical kinetic mechanism. Various methodologies of establishing compact reduced kinetics mechanisms for ethanol and $NH_3/H_2/CH_4$ mixtures have been developed, including the DRGEP combined with GEPA method and IPFA integrating with GEPA method. The two means of 2-stage reducing mechanism methods have been well validated with available experimental data of ignition delay time, species profiles and laminar flame speed over a broad range of operating conditions. To study the combustion and emission characteristics of partially cracked ammonia in gas turbines, the CRN model is proposed to explore the potential of partially cracked ammonia ($NH_3/H_2/N_2$/air mixtures) in controlling NO_X emission and widening operation range in a single and two-staged combustion system. In details, the main contributions in current work are summarised as below together with suggestions for the future work.

7.1. Conclusions of the thesis

7.1.1. Developed reduced mechanisms

In this part, the DRGEP combined with GEPA method are integrated to establish the ethanol reduced kinetic mechanism. In addition, an integrating method of IPFA and GEPA are firstly employed to reduce $NH_3/H_2/CH_4$ mechanism. Besides, the proposed reduced models are well validated by comparing with the detailed mechanism as well as available experimental data of ignition delay time in shock tube, species profiles and laminar flame speed over various

temperatures, pressures, and equivalence ratios. Results shows that the methods in present work can accurately reduce mechanisms, and the reduced ethanol mechanism and ammonia mechanism can be applied for further study. In detail, the contributions can be concluded as:

- An ethanol reduced chemical kinetics mechanism is developed and validated at T = 850-1650K, P = 1-10atm and Φ = 0.5-2. The reduced ethanol mechanism (26 species and 105 reactions) has lower average error and smaller size, and the final uncertainty is about 10.3%.
- The reduced ethanol mechanism is validated with available experimental data of ignition delay time, species mole fraction in jet stirred reactor and laminar burning velocity over numerous conditions. Results show that agreements remain generally good between reduced and detailed ethanol mechanism. Moreover, the reduced mechanism can well capture the ignition characteristics and concentrations of species at wide operation conditions.
- A novel reduced chemical kinetics mechanism for $NH_3/H_2/CH_4$/air mixture is proposed for the first time by a two-stage reduction procedure, which combines both the IPFA method and the GEPA method. Specifically, in the first stage, the detailed mechanism (125 species and 1099 reactions) is reduced by the IPFA. A skeletal mechanism including 68 species and 687 reactions is obtained within the 5% tolerance on auto-ignition. In the second stage, the mechanism is further reduced by the GEPA. As a result, the final skeletal mechanism involving 59 species and 210 reactions is obtained within the 10% tolerance auto-ignition.
- Extensive validations of the proposed reduced model are conducted by comparing

with the detailed mechanism and experimental measurements of ignition delay time in shock tube, species profiles in JSR and the laminar flame speed in wide range of temperatures (T = 1300–2500K), pressures (P = 1–40bar), and equivalence ratios (Φ = 0.25–2.0). Results show that the reduced mechanism can predict ignition delays of NH_3, NH_3/H_2 and NH_3/CH_4 mixtures very well. Additionally, predictions of laminar burning velocity using reduced model generally agree well with the results of measurements and detailed model. Although the result of reduced model is slightly over-predicted compared with the detailed mechanism for laminar burning velocity, the discrepancies are quite small within the error margins around 5%. It should be noted that the reduced mechanism established in the present study under-predict the laminar burning velocities at lean conditions with blending of 40% CH_4 in fuel. Moreover, improving the ammonia kinetics mechanism with CH_4 blending and extending experimental database are required.

- The NO_X emission characteristics of $NH_3/H_2/CH_4$ mixtures in a gas turbine are numerically analysed through a chemical reactor network (CRN) model. The effects of H_2 and CH_4 in the combustion of ammonia and the equivalence ratio on emission characteristics are investigated. Moreover, the temperature sensitivity analysis is employed to explore the reactions that have great impact on the combustion in NH_3/air, 70%NH_3/30%H_2/air and 70%NH_3/30%CH_4/air flames. Results show that the NO_X emission is increased compared to pure ammonia combustion flame especially at lean-fuel (Φ = 0.6-0.9) conditions, when the ammonia blends with H_2 or CH_4. Also, generally, the NO_X emissions show an obvious decrease at the content of NH_3 above

20% in both NH_3/H_2/air and NH_3/CH_4/air flames. Therefore, introducing additives reasonably plays a vital role in NO_X emission control and ammonia combustion promotion.

7.1.2. Combustion and emission characteristics of partially cracked ammonia in gas turbines

Based on the chemical kinetics mechanism of partially cracked ammonia, the potential of partially cracked ammonia ($NH_3/H_2/N_2$/air mixtures) in controlling NO_X emission and widening operation range in a single and two-staged combustion system is investigated for the first time. The effect of cracking ratio, equivalence ratio and initial pressure on the NO_X emissions and laminar flame velocity (LBV) are numerically discussed. Moreover, a reaction pathways flux method is performed to present NO reaction pathways of practically cracked ammonia at virous operating parameters. In addition, important species and reactions of NO formation/reduction are analysed for getting low levels of NO_X emissions. The current study provides a deep insight in improving combustion and controlling emission characteristics of partially cracked ammonia in both single and 2-stage rich-lean gas turbine combustor. In detail, the main contributions can be summarised as below:

- To conclude, the laminar burning velocities rise with increasing equivalence ratio first, and then appears decreasing tendency at Φ > 1.1. The maximum values of LBV are located around Φ = 1.1 for all calculated initial pressures. The peak value of LBV is close to 37cm/s at *T*u = 298K and *P*u = 1atm, which considerably improve LBV of $NH_3/O_2/N_2$ flame (around 7cm/s). Additional, LBV is decreased obviously when the initial mixture pressure is increased from 1atm to 10atm.

- The LBVs increases significantly when the cracking ratio increases from 10% to 80 %. The tendency indicates that the combustion intensity is remarkably enhanced as cracking ratio increases.
- In a single stage gas turbine combustor, the amount of NO_X emission firstly increases and then decreases sharply when the equivalence ratio is within 0.4-1.1. The location of maximum value of NO_X emission is close to 0.8 for all ammonia cracking ratios. After that, a decreasing trend is shown with further equivalence ratio increasing. Therefore, rich burn conditions can be employed to reduce total NO_X emissions in gas turbines. By identifying important intermediate components and reactions, the HNO radical, HNO + OH = NO + H_2O (R120) and NO + H (+ M) = HNO (+ M) (R117) play important role in NO production, while pathways of NH_i contribute more on NO reduction. More specifically, high NO_X emission zone is located at high ammonia cracking ratio and 0.6-1.0 ranges of equivalence ratio. In addition, the NO_X emission is promoted with increasing NH_3 cracking ratio from 10% to 80% at all equivalence ratio studied. As for the effect of initial pressure on NO_X emission throughout all NH_3 cracking ratios, it is noted that the NO_X emission goes to a lower value at each cracking ratio when the pressure increases from 10atm to 20atm.
- Both mole fraction of NO and OH* are increased as NH_3 cracking ratio increases in single stage gas turbine combustor. The peak OH* chemiluminescence intensity located at the position of large NO mole fraction gradients. Besides, considerably higher intensities of OH* for all cracking ratios are located at Φ = 1.0 followed by a decaying trend due to lower oxygen, suggesting the flame position hardly changes with

NH_3 cracking ratios.

- In rich-lean burn stage gas turbine combustor, as the primary equivalence ratio increases, NO_X emissions show almost the same performance as U-shaped curves, and the turning points are almost located at 1.3 and 1.4. The ranges of primary equivalence ratio for low NO emissions (below 50ppm) are around at 1.2-1.5 when the $\Phi_{overall}$ = 0.4 - 0.6. The NO_X prediction values at $\Phi_{primary}$ = 1.0 for all $\Phi_{overall}$ are very small (less than 1000 ppm), which are considerably lower than that in single stage. Therefore, using a second combustion stage burning is promising to reduce NO_X emission and solving the unburned NH_3 mixtures problem.
- The effect of NH_3 cracking ratio on NO_X emission is also explored in rich-lean burn stage gas turbine combustor. Similar tendency curves are captured at various cracking ratio, but the position of turning points is right shifted with rising cracking ratio. Interesting noting that the operating ranges of low NO emissions (below 50ppm) are obviously widen with increasing cracking ratio. In addition, NO_X formation is slightly increased with the increase of cracking ratio, whereas it shows gradually reducing trend at high primary equivalence ratio. In conclusion, cracking more NH_3 is beneficial for reducing NO_X emission and widening operation. Controlling cracking ratio (around at 40%) and primary equivalence ratio (i.e., controlling unburnt NH_3) in the range of 1.2-1.4 primary equivalence ratio enable to comprehensively widen operation range and reduce NO_X emissions.
- The NO_X in each stage monotonically decrease with the increasing residence time in the rich burn stage. Therefore, increasing residence time within reasonable context in

the primary stage has an advantage on NO_X reduction.

- When ammonia cracking rate increases from 20% to 60%, the ROP of promoting NO formation reactions rises (R34, R69, R68, R56), while the ROP of reactions related with NO consumption decreases. Therefore, more NO is generated with higher ammonia cracking rate.
- The contribution rate of reactions related with NO formation are generally decreased with increasing equivalence ratio, while the proportion of reactions that react with NO are increased. Therefore, the overall NO formation is reduced with equivalence ratio increasing from 0.8 to 1.2.

7.1.3. The study of the chemiluminescent emission

Chemiluminescence, as a promising optical diagnostic tool, is an area worth of further investigation. In this part, numerically analysing on the heat release rate as well as equivalence ratio determination by applying excited state species (OH*, CH* and C_2*) chemiluminescence profiles is investigated in one-dimensional laminar premixed ethanol flame. The ability of flame chemiluminescence as a sensor of heat release rate at various equivalence ratios is discussed by combining rate of production analysis with sensitivity analysis. Also, correlations between the chemiluminescence intensity ratio of C_2*/CH* and the equivalence ratio are investigated in hydrocarbon premixed flames based on chemical reaction kinetics mechanisms. Results show that the peak chemiluminescence intensity ratio of C_2*/CH* increases almost linearly following by a descend trend with the local equivalence ratio, which is demonstrated from the chemical mechanisms' aspect for the first time. The contributions of this study are listed as below:

- Chemiluminescence as a signal of heat release rate is discussed. The results show that the local heat release presents a multi-valued characteristic of local concentration for all excited state species. However, the total heat release rate rises almost linearly with the increasing total chemiluminescence. Consequently, the total chemiluminescence is more acceptable as a reliable signal to character the heat release rate. Besides, it is also presented that the reactions with a large contribution rate on formation and consumption of the excited state species also have a significant effect on the heat release rate.
- In addition, effects of equivalence ratios on the chemiluminescent emissions of OH*, CH* and C_2* are analyzed. All peaks of chemiluminescent intensity for the three excited states increase at the first time, following that a decreasing trend with the increasing equivalent ratio is displayed. The total heat release rate also appears same tendency at various equivalence ratios. Moreover, results show that the maximum value of OH* and CH* chemiluminescence intensities appears at Φ = 1.1, while the maximum intensity for C_2* appears at around Φ = 1.35. The deviation should be affected by the specific reaction paths.
- During the process of the formation and decay reactions of the excited radicals, CH_3 radical is more likely a precursor of excited species in ethanol flames. Analyzing the reaction paths can conclude that the variation of the precursor reaction parameters would significantly affect the chemiluminescence profiles. As a result, the present numerical simulation provides a guidance for employing much easier chemiluminescence experiments setup to detect flame characteristics using imaging-based techniques.

- Extended mechanisms including OH*, CH* and C_2* sub-models for methane, ethanol and propane are developed and successfully validated, which can be applied to examine the reliance of the chemiluminescence intensity ratio of C_2*/CH* on the equivalence ratio in three premixed laminar flames.
- In agreement with the experimental observation, the peak chemiluminescence intensity ratio of C_2*/CH* increases almost linearly as the local equivalence ratio grows from 0.9 for all of three fuel flames at first. After that, the intensity ratios present a slowly descending tendency when Φ > 1.35, 1.5, 1.5 for methane, ethanol and propane flames respectively.
- The most important reactions that invert the monotonicity of the chemiluminescence intensity ratio of C_2*/CH* with the increasing equivalence ratio are analysed numerically for the first time in three fuel flames. The reactions $C_2H + O_2 <=> CH^* + CO_2$ and $C_2H + H <=> H_2 + C_2^*$ are identified to be the most important reactions that invert the monotonicity of the chemiluminescence intensity ratio of C_2*/CH* with equivalence ratio in all the three fuel flames.

7.2. Suggested future work in this field

The suggestions for future work in this field are summarized as follows:

For the methods of reducing chemical kinetic mechanism:

- For the current methods of reducing chemical kinetic mechanism, the total calculation times for both of DRGEP combining with GEPA and IPFA combining with GEPA are dependent on the target species selection. In this study, the reactants and products are selected as the target species. However, the target species are flexible. In theory,

the more species are selected, the higher the accuracy would be for the reduced mechanism. But choosing more target species extends the calculation time, and more unimportant reactions will remain. Therefore, the two effects must be carefully considered and analysed quantitatively in future work to reduce mechanism.

- For the present reduction methods, due to their dependence on path flow, if the detailed mechanisms contain a large number of paths, the computing efficiency will be affected. In most of cases for fuel mixtures, the mechanisms are so complicated that include many paths, which leads to the rise of computing time of the present method. Considering this, the present reduction methods need to be optimized with several path-searching methods.

For the study of practically cracked ammonia combustion and emission characteristics in gas turbines:

- This work numerically investigates the potential of partially cracked ammonia ($NH_3/H_2/N_2$/air mixtures) in controlling NO_X emission and widening operation range in a single and two-staged combustion system. Experimental measurements are beneficial to better understand combustion and emission performance of practically cracked ammonia in gas turbines.
- The combustion in gas turbines is related with turbulence. Although the CRN model is regarded as an effective numerical method to predict NO_X emissions via calibrated and validated in previously research [304,305,306], it is difficult to reflect the flow field structure and temperature field distribution in real combustors. Develop turbulent

model can predict NO_X emission of ammonia combustion more accuracy in gas turbines.

For the study of the chemiluminescent emission:

- This work numerically analysing the ability of flame chemiluminescence as a sensor of heat release rate at various equivalence ratio. As a promising optical diagnostic tool, chemiluminescence can be readily imaged with modern digital cameras and analysed with the ever-increasing computing and processing power. Experiments of chemiluminescence can be conducted to measure the chemiluminescence intensity in ethanol and hydrocarbon fuel flame.
- Then the chemiluminescence can be further employed to monitor the comprehensive combustion performance in engines, for example, studying the correlations between chemiluminescence and ignition and other indeterminate mixtures in HCCI engine.

References

[1] Mansoori, G. A., Agyarko, L. B., Estevez, L. A., Fallahi, B., Gladyshev, G., Santos, R. G. D., Niaki, S., Perišić, O., Sillanpää, M., Tumba, K. and Yen, J., 2021. Fuels of the future for renewable energy sources (ammonia, biofuels, hydrogen). *arXiv preprint arXiv:2102.00439*.

[2] Issayev, G., Giri, B. R., Elbaz, A. M., Shrestha, K. P., Mauss, F., Roberts, W. L. and Farooq, A., 2021. Combustion behavior of ammonia blended with diethyl ether. *Proceedings of the Combustion Institute*, 38(1), pp.499-506.

[3] Hayakawa, A., Hirano, Y., Okafor, E. C., Yamashita, H., Kudo, T. and Kobayashi, H., 2021. Experimental and numerical study of product gas characteristics of ammonia/air premixed laminar flames stabilized in a stagnation flow. *Proceedings of the Combustion Institute*, 38(2), pp.2409-2417.

[4] Lhuillier, C., Brequigny, P., Contino, F. and Rousselle, C., 2019. Performance and emissions of an ammonia-fueled SI engine with hydrogen enrichment. *SAE Technical Paper*.

[5] Dimitriou, P. and Javaid, R., 2020. A review of ammonia as a compression ignition engine fuel. *International Journal of Hydrogen Energy*, 45(11), pp.7098-7118.

[6] Han, X., Wang, Z., Costa, M., Sun, Z., He, Y. and Cen, K., 2019. Experimental and kinetic modeling study of laminar burning velocities of NH_3/air, NH_3/H_2/air, NH_3/CO/air and NH_3/CH_4/air premixed flames. *Combustion and Flame*, 206, pp.214-226.

[7] Mei, B., Zhang, X., Ma, S., Cui, M., Guo, H., Cao, Z. and Li, Y., 2019. Experimental and kinetic modeling investigation on the laminar flame propagation of ammonia under oxygen enrichment and elevated pressure conditions. *Combustion and Flame*, 210, pp.236-246.

[8] Hayakawa, A., Goto, T., Mimoto, R., Arakawa, Y., Kudo, T. and Kobayashi, H., 2015. Laminar burning velocity and Markstein length of ammonia/air premixed flames at various pressures. *Fuel*, 159, pp.98-106.

[9] Takizawa, K., Takahashi, A., Tokuhashi, K., Kondo, S. and Sekiya, A., 2008. Burning velocity measurements of nitrogen-containing compounds. *Journal of Hazardous Materials*, 155(1-2), pp.144-152.

[10] Ichikawa, A., Naito, Y., Hayakawa, A., Kudo, T. and Kobayashi, H., 2019. Burning velocity and flame structure of CH_4/NH_3/air turbulent premixed flames at high pressure. *International Journal of Hydrogen Energy*, 44(13), pp.6991-6999.

[11] Okafor, E. C., Naito, Y., Colson, S., Ichikawa, A., Kudo, T., Hayakawa, A. and Kobayashi, H., 2018. Experimental and numerical study of the laminar burning velocity of CH_4-NH_3-air premixed flames. *Combustion and Flame*, 187, pp.185-198.

[12] Kobayashi, H., Hayakawa, A., Somarathne, K. K. A. and Okafor, E. C., 2019. Science and technology of ammonia combustion. *Proceedings of the Combustion Institute*, 37(1), pp.109-133.

[13] Lan, R., Irvine, J. T. and Tao, S., 2012. Ammonia and related chemicals as potential indirect hydrogen storage materials. *International Journal of Hydrogen Energy*, 37(2), pp.1482-1494.

[14] Hayakawa, A., Arakawa, Y., Mimoto, R., Somarathne, K. K. A., Kudo, T. and Kobayashi, H., 2017. Experimental investigation of stabilization and emission characteristics of

ammonia/air premixed flames in a swirl combustor. *International Journal of Hydrogen Energy*, 42(19), pp.14010-14018.

[15] Nozari, H., Karaca, G., Tuncer, O. and Karabeyoglu, A., 2017. Porous medium based burner for efficient and clean combustion of ammonia-hydrogen-air systems. *International Journal of Hydrogen Energy*, 42(21), pp.14775-14785.

[16] Valera-Medina, A., Marsh, R., Runyon, J., Pugh, D., Beasley, P., Hughes, T. and Bowen, P., 2017. Ammonia-methane combustion in tangential swirl burners for gas turbine power generation. *Applied Energy*, 185, pp.1362-1371.

[17] Somarathne, K. D. K. A., Hatakeyama, S., Hayakawa, A. and Kobayashi, H., 2017. Numerical study of a low emission gas turbine like combustor for turbulent ammonia/air premixed swirl flames with a secondary air injection at high pressure. *International Journal of Hydrogen Energy*, 42(44), pp.27388-27399.

[18] Okafor, E. C., Somarathne, K. K. A., Hayakawa, A., Kudo, T., Kurata, O., Iki, N. and Kobayashi, H., 2019. Towards the development of an efficient low-NOx ammonia combustor for a micro gas turbine. *Proceedings of the combustion institute*, 37(4), pp.4597-4606.

[19] Somarathne, K. D. K. A., Colson, S., Hayakawa, A. and Kobayashi, H., 2018. Modelling of ammonia/air non-premixed turbulent swirling flames in a gas turbine-like combustor at various pressures. *Combustion Theory and Modelling*, 22(5), pp.973-997.

[20] Pilling, M. J., 2009. From elementary reactions to evaluated chemical mechanisms for combustion models. *Proceedings of the Combustion Institute*, 32(1), pp.27-44.

[21] Barraza-Botet, C. L. and Wooldridge, M. S., 2018. Combustion chemistry of iso-octane/ethanol blends: Effects on ignition and reaction pathways. *Combustion and Flame*, 188, pp.324-336.

[22] Chen, R. and Nishida, K., 2014. Spray evaporation of ethanol-gasoline-like blend and combustion of ethanol-gasoline blend injected by hole-type nozzle for direct-injection spark ignition engines. *Fuel*, 134, pp.263-273.

[23] García, A., Monsalve-Serrano, J., Sari, R.L. and Martinez-Boggio, S., 2021. An optical investigation of thermal runway phenomenon under thermal abuse conditions. *Energy Conversion and Management*, 246, pp.114663.

[24] Park, H., Lee, J., Jamsran, N., Oh, S., Kim, C., Lee, Y. and Kang, K., 2021. Comparative assessment of stoichiometric and lean combustion modes in boosted spark-ignition engine fueled with syngas. *Energy Conversion and Management*, 239, pp.114224.

[25] Charalambides, A. G., Sahu, S., Hardalupas, Y., Taylor, A. M. and Urata, Y., 2018. Evaluation of homogeneous charge compression ignition (HCCI) autoignition development through chemiluminescence imaging and proper orthogonal decomposition. *Applied Energy*, 210, pp.288-302.

[26] Guethe, F., Guyot, D., Singla, G., Noiray, N. and Schuermans, B., 2012. Chemiluminescence as diagnostic tool in the development of gas turbines. *Applied Physics B*, 107(3), pp.619-636.

[27] Persson, H., Hultqvist, A., Johansson, B. and Remón, A., 2007. Investigation of the early flame development in spark assisted HCCI combustion using high speed chemiluminescence imaging. *SAE Technical Paper*.

[28] Mollahoseini, Z., Heydarlaki, R., Kostka, P., Aitchison, W. and Kheirkhah, S., 2021. Flame development characteristics inside a reverse-flow combustor at early stages of combustion. *Experimental Thermal and Fluid Science*, 121, pp.110254.

[29] Chemkin-Pro, ANSYS, 2017. 18.0. ANSYS Reaction Design: San Diego.

[30] Zhang, Y., Fu, J., Xie, M. and Liu, J., 2021. Improvement of H_2/O_2 chemical kinetic mechanism for high pressure combustion. *International Journal of Hydrogen Energy*, 46(7), pp.5799-5811.

[31] Xiao, H. and Valera-Medina, A., 2017. Chemical kinetic mechanism study on premixed combustion of ammonia/hydrogen fuels for gas turbine use. *Journal of Engineering for Gas Turbines and Power*, 139(8).

[32] Otomo, J., Koshi, M., Mitsumori, T., Iwasaki, H. and Yamada, K., 2018. Chemical kinetic modeling of ammonia oxidation with improved reaction mechanism for ammonia/air and ammonia/hydrogen/air combustion. *International Journal of Hydrogen Energy*, 43(5), pp.3004-3014.

[33] da Rocha, R. C., Costa, M. and Bai, X. S., 2019. Chemical kinetic modelling of ammonia/hydrogen/air ignition, premixed flame propagation and NO emission. *Fuel*, 246, pp.24-33.

[34] Shrestha, K. P., Seidel, L., Zeuch, T. and Mauss, F., 2018. Detailed kinetic mechanism for the oxidation of ammonia including the formation and reduction of nitrogen oxides. *Energy & Fuels*, 32(10), pp.10202-10217.

[35] Nakamura, H., Hasegawa, S. and Tezuka, T., 2017. Kinetic modeling of ammonia/air weak flames in a micro flow reactor with a controlled temperature profile. *Combustion and Flame*, 185, pp.16-27.

[36] He, X., Shu, B., Nascimento, D., Moshammer, K., Costa, M. and Fernandes, R. X., 2019. Auto-ignition kinetics of ammonia and ammonia/hydrogen mixtures at intermediate temperatures and high pressures. *Combustion and Flame*, 206, pp.189-200.

[37] Curran, H. J., 2019. Developing detailed chemical kinetic mechanisms for fuel combustion. *Proceedings of the Combustion Institute*, 37(1), pp.57-81.

[38] Shimizu, K., Hibi, A., Koshi, M., Morii, Y. and Tsuboi, N., 2011. Updated kinetic mechanism for high-pressure hydrogen combustion. *Journal of Propulsion and Power*, 27(2), pp.383-395.

[39] Ju, Y. and Niioka, T., 1994. Reduced kinetic mechanism of ignition for nonpremixed hydrogen/air in a supersonic mixing layer. Combustion and Flame, 99(2), pp.240-246.

[40] Arrhenius, S., 1889. On the reaction rate of the inversion of non-refined sugar upon souring. *Zeitschrift für Physikalische Chemie*, 4, pp.226-248.

[41] Berthelot, M., 1862. Essai d'une theorie sur la formation des ethers. *Annales de Chimie et de Physique*, 66, pp.110-128.

[42] Kooshkbaghi, M., Frouzakis, C. E., Boulouchos, K. and Karlin, I. V., 2014. Entropy production analysis for mechanism reduction. *Combustion and Flame*, 161(6), pp.1507-1515.

[43] Lu, T. and Law, C. K., 2009. Toward accommodating realistic fuel chemistry in large-scale computations. Progress in Energy and Combustion Science, 35(2), pp.192-215.

[44] Okafor, E. C., Naito, Y., Colson, S., Ichikawa, A., Kudo, T., Hayakawa, A. and Kobayashi, H., 2019. Measurement and modelling of the laminar burning velocity of methane-ammonia-air flames at high pressures using a reduced reaction mechanism. *Combustion and Flame*, 204, pp.162-175.

[45] Cazères, Q., Pepiot, P., Riber, E. and Cuenot, B., 2021. A fully automatic procedure for the analytical reduction of chemical kinetics mechanisms for computational fluid dynamics applications. *Fuel*, 303, pp.121247.

[46] Tian, Z., Yan, Y. and Li, J., 2019. A simplified 1-butene mechanism with combined reduction method. *Fuel*, 241, pp.826-835.

[47] Lin, S., Sun, W., Guo, L., Cheng, P., Sun, Y. and Zhang, H., 2021. Development of a reduced mechanism of a three components surrogate fuel for the coal-to-liquid and diesel combustion simulation. *Fuel*, 294, p.120370.

[48] Pope, S. B., 2013. Small scales, many species and the manifold challenges of turbulent combustion. *Proceedings of the Combustion Institute*, 34(1), pp.1-31.

[49] Pekař, M., 2005. Thermodynamics and foundations of mass-action kinetics. *Progress in Reaction Kinetics and Mechanism*, 30(1-2), pp.3-113.

[50] Turanyi, T., 1994. Parameterization of reaction mechanisms using orthonormal polynomials. *Computers & Chemistry*, 18(1), pp.45-54.

[51] Tonse, S. R., Moriarty, N. W., Frenklach, M. and Brown, N. J., 2003. Computational economy improvements in PRISM. *International Journal of Chemical Kinetics*, 35(9), pp.438-452.

[52] Pope, S. B., 1997. Computationally efficient implementation of combustion chemistry using in situ adaptive tabulation.

[53] Yang, B. and Pope, S. B., 1998. Treating chemistry in combustion with detailed mechanisms-in situ adaptive tabulation in principal directions-premixed combustion. *Combustion and Flame*, 112(1-2), pp.85-112.

[54] Zhang, Y., 2005. Acceleration of detailed chemistry calculation in multidimensional engine modeling using DOLFA. *In International Multidimensional Engine Modeling User's Group Meeting*, Detroit, MI.

[55] Maas, U. and Tomlin, A. S., 2013. Time-scale splitting-based mechanism reduction. In Cleaner Combustion, Springer, London, pp. 467-484.

[56] Williams, F. A., 1985. Combustion Theory Addison-Wesley. Redwood City.

[57] Tomlin, A. S., Pilling, M. J., Turányi, T., Merkin, J. H. and Brindley, J., 1992. Mechanism reduction for the oscillatory oxidation of hydrogen: sensitivity and quasi-steady-state analyses. *Combustion and Flame*, 91(2), pp.107-130.

[58] Hughes, K. J., Fairweather, M., Griffiths, J. F., Porter, R. and Tomlin, A. S., 2009. The application of the QSSA via reaction lumping for the reduction of complex hydrocarbon oxidation mechanisms. *Proceedings of the Combustion Institute*, 32(1), pp.543-551.

[59] Maas, U. and Pope, S. B., 1992. Simplifying chemical kinetics: intrinsic low-dimensional manifolds in composition space. *Combustion and Flame*, 88(3-4), pp.239-264.

[60] Lam, S. H., 1993. Using CSP to understand complex chemical kinetics. *Combustion Science and Technology*, 89(5-6), pp.375-404.

[61] Massias, A., Diamantis, D., Mastorakos, E. and Goussis, D. A., 1999. An algorithm for the construction of global reduced mechanisms with CSP data. *Combustion and Flame*, 117(4), pp.685-708.

[62] Lu, T., Ju, Y. and Law, C. K., 2001. Complex CSP for chemistry reduction and analysis. *Combustion and Flame*, 126(1-2), pp.1445-1455.

[63] Valorani, M., Creta, F., Goussis, D. A., Lee, J. C. and Najm, H. N., 2006. An automatic procedure for the simplification of chemical kinetic mechanisms based on CSP. *Combustion and Flame*, 146(1-2), pp.29-51.

[64] Li, G., Rabitz, H. and Tóth, J., 1994. A general analysis of exact nonlinear lumping in chemical kinetics. *Chemical Engineering Science*, 49(3), pp.343-361.

[65] Li, G., Tomlin, A. S., Rabitz, H. and Tóth, J., 1994. A general analysis of approximate nonlinear lumping in chemical kinetics. I. Unconstrained lumping. *The Journal of Chemical Physics, 101(2), pp.1172-1187.*

[66] Tomlin, A. S., Li, G., Rabitz, H. and Toth, J., 1994. A general analysis of approximate nonlinear lumping in chemical kinetics. II. Constrained lumping. *The Journal of chemical physics*, 101(2), pp.1188-1201.

[67] Dodge, M. C., 2000. Chemical oxidant mechanisms for air quality modeling: critical review. *Atmospheric Environment*, 34(12-14), pp.2103-2130.

[68] Karadeniz, H., Soyhan, H. S. and Sorusbay, C., 2012. Reduction of large kinetic mechanisms with a new approach to the necessity analysis method. *Combustion and Flame*, 159(4), pp.1467-1480.

[69] Turanyi, T., 1990. Reduction of large reaction mechanisms. *New Journal of Chemistry*, 14(11), pp.795-803.

[70] Nagy, T. and Turányi, T., 2009. Reduction of very large reaction mechanisms using methods based on simulation error minimization. *Combustion and Flame*, 156(2), pp.417-428.

[71] Lu, T. and Law, C. K., 2005. A directed relation graph method for mechanism reduction. *Proceedings of the Combustion Institute*, 30(1), pp.1333-1341.

[72] Lu, T. and Law, C.K., 2006. On the applicability of directed relation graphs to the reduction of reaction mechanisms. *Combustion and Flame*, 146(3), pp.472-483.

[73] Lu, T. and Law, C. K., 2006. Linear time reduction of large kinetic mechanisms with directed relation graph: n-Heptane and iso-octane. *Combustion and Flame*, 144(1-2), pp.24-36.

[74] Lu, T. and Law, C. K., 2008. Strategies for mechanism reduction for large hydrocarbons: n-heptane. *Combustion and Flame*, 154(1-2), pp.153-163.

[75] Luo, Z., Lu, T. and Liu, J., 2011. A reduced mechanism for ethylene/methane mixtures with excessive NO enrichment. *Combustion and Flame*, 158(7), pp.1245-1254.

[76] Zheng, X. L., Lu, T. F. and Law, C. K., 2007. Experimental counterflow ignition temperatures and reaction mechanisms of 1, 3-butadiene. *Proceedings of the Combustion Institute*, 31(1), pp.367-375.

[77] Pepiot-Desjardins, P. and Pitsch, H., 2008. An efficient error-propagation-based reduction method for large chemical kinetic mechanisms. *Combustion and Flame*, 154(1-2), pp.67-81.

[78] Niemeyer, K. E. and Sung, C. J., 2011. On the importance of graph search algorithms for DRGEP-based mechanism reduction methods. *Combustion and Flame*, 158(8), pp.1439-1443.

[79] Niemeyer, K. E., Sung, C. J. and Raju, M. P., 2010. Skeletal mechanism generation for surrogate fuels using directed relation graph with error propagation and sensitivity analysis. *Combustion and Flame*, 157(9), pp.1760-1770.

[80] Sun, W., Chen, Z., Gou, X. and Ju, Y., 2010. A path flux analysis method for the reduction of detailed chemical kinetic mechanisms. *Combustion and Flame*, 157(7), pp.1298-1307.

[81] Wang, W. and Gou, X., 2016. An improved path flux analysis with multi generations method for mechanism reduction. *Combustion Theory and Modelling*, 20(2), pp.203-220.

[82] Vajda, S., Valko, P. and Turanyi, T., 1985. Principal component analysis of kinetic models. *International Journal of Chemical Kinetics*, 17(1), pp.55-81.

[83] Vajda, S. and Turányi, T., 1986. Principal component analysis for reducing the Edelson-Field-Noyes model of the Belousov-Zhabotinskii reaction. *The Journal of Physical Chemistry*, 90(8), pp.1664-1670.

[84] Gokulakrishnan, P., Lawrence, A. D., McLellan, P. J. and Grandmaison, E. W., 2006. A functional-PCA approach for analyzing and reducing complex chemical mechanisms. *Computers & Chemical Engineering*, 30(6-7), pp.1093-1101.

[85] Turanyi, T., Berces, T. and Vajda, S., 1989. Reaction rate analysis of complex kinetic systems. *International Journal of Chemical Kinetics*, 21(2), pp.83-99.

[86] Rabitz, H., Kramer, M. and Dacol, D., 1983. Sensitivity analysis in chemical kinetics. *Annual Review of Physical Chemistry*, 34(1), pp.419-461.

[87] Turányi, T., 1990. Sensitivity analysis of complex kinetic systems. Tools and applications. *Journal of Mathematical Chemistry*, 5(3), pp.203-248.

[88] Tomlin, A. S., Pilling, M. J., Merkin, J. H., Brindley, J., Burgess, N. and Gough, A., 1995. Reduced mechanisms for propane pyrolysis. *Industrial & Engineering Chemistry Research*, 34(11), pp.3749-3760.

[89] Wang, H. and Frenklach, M., 1991. Detailed reduction of reaction mechanisms for flame modeling. *Combustion and Flame*, 87(3-4), pp.365-370.

[90] Acampora, L., Kooshkbaghi, M., Frouzakis, C. E. and Marra, F. S., 2019. Generalized entropy production analysis for mechanism reduction. *Combustion Theory and Modelling*, 23(2), pp.197-209.

[91] Xiao, H., Lai, S., Valera-Medina, A., Li, J., Liu, J. and Fu, H., 2020. Experimental and modeling study on ignition delay of ammonia/methane fuels. *International Journal of Energy Research*, 44(8), pp.6939-6949.

[92] Yu, L., Zhou, W., Feng, Y., Wang, W., Zhu, J., Qian, Y. and Lu, X., 2020. The effect of ammonia addition on the low-temperature autoignition of n-heptane: An experimental and modeling study. *Combustion and Flame*, 217, pp.4-11.

[93] Drummond, L. J., 1972. High temperature oxidation of ammonia. *Combustion Science and Technology*, 5(1), pp.175-182.

[94] Wooldridge, S. T., Mertens, J. D., Hanson, R. K. and Bowman, C. T., 1994. A shock tube study of the reactions of CN and NCO with NO_2. *In Symposium (International) on Combustion*, 25(1), pp.983-991.

[95] Salimian, S., Hanson, R. K. and Kruger, C. H., 1984. Ammonia oxidation in shock-heated NH_3/N_2O/Ar mixtures. *Combustion and Flame*, 56(1), pp.83-95.

[96] Bull, D. C., 1968. A shock tube study of the oxidation of ammonia. *Combustion and Flame*, 12(6), pp.603-610.

[97] Soloukhin, R. I., 1971. High-temperature oxidation of ammonia, carbon monoxide, and methane by nitrous oxide in shock waves. *In Symposium (International) on Combustion*, 13(1) pp.121-128.

[98] Takeyama, T. and Miyama, H., 1967. A shock-tube study of the ammonia-oxygen reaction. *In Symposium (International) on Combustion*, 11(1), pp.845-852.

[99] Shu, B., He, X., Ramos, C. F., Fernandes, R. X. and Costa, M., 2021. Experimental and modeling study on the auto-ignition properties of ammonia/methane mixtures at elevated pressures. *Proceedings of the Combustion Institute*, 38(1), pp.261-268.

[100] Pochet, M., Dias, V., Moreau, B., Foucher, F., Jeanmart, H. and Contino, F., 2019. Experimental and numerical study, under LTC conditions, of ammonia ignition delay with and without hydrogen addition. *Proceedings of the Combustion Institute*, 37(1), pp.621-629.

[101] Shu, B., Vallabhuni, S. K., He, X., Issayev, G., Moshammer, K., Farooq, A. and Fernandes, R. X., 2019. A shock tube and modeling study on the autoignition properties of ammonia at intermediate temperatures. *Proceedings of the Combustion Institute*, 37(1), pp.205-211.

[102] Mathieu, O. and Petersen, E. L., 2015. Experimental and modeling study on the high-temperature oxidation of Ammonia and related NO_X chemistry. *Combustion and Flame*, 162(3), pp.554-570.

[103] Feng, Y., Zhu, J., Mao, Y., Raza, M., Qian, Y., Yu, L. and Lu, X., 2020. Low-temperature auto-ignition characteristics of NH_3/diesel binary fuel: Ignition delay time measurement and kinetic analysis. *Fuel*, 281, pp.118761.

[104] Dai, L., Gersen, S., Glarborg, P., Mokhov, A. and Levinsky, H., 2020. Autoignition studies of NH_3/CH_4 mixtures at high pressure. *Combustion and Flame*, 218, pp.19-26.

[105] Dai, L., Gersen, S., Glarborg, P., Levinsky, H. and Mokhov, A., 2020. Experimental and numerical analysis of the autoignition behavior of NH_3 and NH_3/H_2 mixtures at high pressure. *Combustion and Flame*, 215, pp.134-144.

[106] Ichikawa, A., Hayakawa, A., Kitagawa, Y., Somarathne, K. K. A., Kudo, T. and Kobayashi, H., 2015. Laminar burning velocity and Markstein length of ammonia/hydrogen/air premixed flames at elevated pressures. *International Journal of Hydrogen Energy*, 40(30), pp.9570-9578.

[107] Lee, J. H., Kim, J. H., Park, J. H. and Kwon, O. C., 2010. Studies on properties of laminar premixed hydrogen-added ammonia/air flames for hydrogen production. *International Journal of Hydrogen Energy*, 35(3), pp.1054-1064.

[108] Maclean, D. I. and Wagner, H. G., 1967. The structure of the reaction zones of ammonia-oxygen and hydrazine-decomposition flames. *In Symposium (International) on Combustion*, 11(1), pp.871-878.

[109] Manna, M. V., Sabia, P., Ragucci, R. and de Joannon, M., 2020. Oxidation and pyrolysis of ammonia mixtures in model reactors. *Fuel*, 264, pp.116768.

[110] Okafor, E. C., Somarathne, K. K. A., Ratthanan, R., Hayakawa, A., Kudo, T., Kurata, O., Iki, N., Tsujimura, T., Furutani, H. and Kobayashi, H., 2020. Control of NO_X and other emissions in micro gas turbine combustors fuelled with mixtures of methane and ammonia. *Combustion and Flame*, 211, pp.406-416.

[111] Sabia, P., Manna, M. V., Cavaliere, A., Ragucci, R. and de Joannon, M., 2020. Ammonia oxidation features in a jet stirred flow reactor. The role of NH2 chemistry. *Fuel*, 276, pp.118054.

[112] Stagni, A., Cavallotti, C., Arunthanayothin, S., Song, Y., Herbinet, O., Battin-Leclerc, F. and Faravelli, T., 2020. An experimental, theoretical and kinetic-modeling study of the gas-phase oxidation of ammonia. *Reaction Chemistry & Engineering*, 5(4), pp.696-711.

[113] Tian, Z., Li, Y., Zhang, L., Glarborg, P. and Qi, F., 2009. An experimental and kinetic modeling study of premixed $NH_3/CH_4/O_2$/Ar flames at low pressure. *Combustion and Flame*, 156(7), pp.1413-1426.

[114] Blint, R. J. and Dasch, C. J., 1983. Formation of NO and N_2 from NH_3 in flames.

[115] Dagaut, P., 2019. On the oxidation of ammonia and mutual sensitization of the oxidation of NO and ammonia: experimental and kinetic modeling. *Combustion Science and Technology*, pp.1-13.

[116] Dasch, C. J. and Blint, R. J., 1984. A mechanistic and experimental study of ammonia flames. *Combustion Science and Technology*, 41(5-6), pp.223-244.

[117] Dean, A. M., Chou, M. S. and Stern, D., 1984. Kinetics of rich ammonia flames. *International Journal of Chemical Kinetics*, 16(6), pp.633-653.

[118] Dean, A. M., Hardy, J. E. and Lyon, R. K., 1982. Kinetics and mechanism of NH_3 oxidation. *In Symposium (International) on Combustion*, 19(1), pp.97-105.

[119] Dean, A. M., Chou, M. S. and Stern, D., 1983. Nitrogen chemistry in flames: observations and detailed kinetic modeling. [J]. ACS Symposium Series, pp.71-86.

[120] Duynslaegher, C., Contino, F., Vandooren, J. and Jeanmart, H., 2012. Modeling of ammonia combustion at low pressure. Combustion and Flame, 159(9), pp.2799-2805.

[121] Xiao, H., Howard, M., Valera-Medina, A., Dooley, S. and Bowen, P. J., 2016. Study on reduced chemical mechanisms of ammonia/methane combustion under gas turbine conditions. *Energy & Fuels*, 30(10), pp.8701-8710.

[122] Murray, R. C. and Hall, A. R., 1951. Flame speeds in hydrazine vapour and in mixtures of hydrazine and ammonia with oxygen. *Transactions of the Faraday Society*, 47, pp.743-751.

[123] Buckley, W. L. and Husa, H. W., 1962. Combustion properties of ammonia. *Chemical Engineering Progress*, 58(2), pp.81-84.

[124] Andrews, D. G. R. and Gray, P., 1964. Combustion of ammonia supported by oxygen, nitrous oxide or nitric oxide: laminar flame propagation at low pressures in binary mixtures. *Combustion and Flame*, 8(2), pp.113-126.

[125] Gray, P., Mackinven, R. and Smith, D. B., 1967. Combustion of hydrogen and oxygen with ammonia and nitrous oxide-laminar flame speeds and flammability limits at low pressure for ternary mixtures. *Combustion and Flame*, 11(2), pp.109-119.

[126] Ronney, P. D., 1988. Effect of chemistry and transport properties on near-limit flames at microgravity. *Combustion Science and Technology*, 59(1-3), pp.123-141.

[127] Zakaznov, V. F., Kursheva, L. A. and Fedina, Z. I., 1978. Determination of normal flame velocity and critical diameter of flame extinction in ammonia-air mixture. *Combustion, Explosion and Shock Waves*, 14(6), pp.710-713.

[128] Li, R., Konnov, A. A., He, G., Qin, F. and Zhang, D., 2019. Chemical mechanism development and reduction for combustion of $NH_3/H_2/CH_4$ mixtures. *Fuel*, 257, pp.116059.

[129] Luo, Z., Lu, T., Maciaszek, M. J., Som, S. and Longman, D. E., 2010. A reduced mechanism for high-temperature oxidation of biodiesel surrogates. *Energy & Fuels*, 24(12), pp.6283-6293.

[130] Xi, S., Xue, J., Wang, F. and Li, X., 2020. Reduction of large-size combustion mechanisms of n-decane and n-dodecane with an improved sensitivity analysis method. *Combustion and Flame*, 222, pp.326-335.

[131] Han, W. and Gou, X., 2020. Improved path flux analysis mechanism reduction method for high and low temperature oxidation of hydrocarbon fuels. *Combustion Theory and Modelling*, 24(6), pp.1090-1107.

[132] Perini, F., Brakora, J. L., Reitz, R. D. and Cantore, G., 2012. Development of reduced and optimized reaction mechanisms based on genetic algorithms and element flux analysis. *Combustion and Flame*, 159(1), pp.103-119.

[133] Posada, J. O. G., Abdalla, A. H., Oseghale, C. I. and Hall, P. J., 2016. Multiple regression analysis in the development of NiFe cells as energy storage solutions for intermittent power sources such as wind or solar. *International Journal of Hydrogen Energy*, 41(37), pp.16330-16337.

[134] Ordoñez, J., Gago, E. J. and Girard, A., 2016. Processes and technologies for the recycling and recovery of spent lithium-ion batteries. *Renewable and Sustainable Energy Reviews*, 60, pp.195-205.

[135] Lefebvre, D. and Tezel, F.H., 2017. A review of energy storage technologies with a focus on adsorption thermal energy storage processes for heating applications. *Renewable and Sustainable Energy Reviews*, 67, pp.116-125.

[136] Jradi, M., Veje, C. and Jørgensen, B. N., 2017. Performance analysis of a soil-based thermal energy storage system using solar-driven air-source heat pump for Danish buildings sector. *Applied Thermal Engineering*, 114, pp.360-373.

[137] Alva, G., Liu, L., Huang, X. and Fang, G., 2017. Thermal energy storage materials and systems for solar energy applications. *Renewable and Sustainable Energy Reviews*, 68, pp.693-706.

[138] Das, L. M., 1990. Fuel induction techniques for a hydrogen operated engine. *International Journal of Hydrogen Energy*, 15(11), pp.833-842.

[139] Aydin, K. and Kenanoğlu, R., 2018. Effects of hydrogenation of fossil fuels with hydrogen and hydroxy gas on performance and emissions of internal combustion engines. *International Journal of Hydrogen Energy*, 43(30), pp.14047-14058.

[140] Kahraman, E., Ozcanlı, S. C. and Ozerdem, B., 2007. An experimental study on performance and emission characteristics of a hydrogen fuelled spark ignition engine. *International Journal of Hydrogen Energy*, 32(12), pp.2066-2072.

[141] Serin, H. and Yildizhan, Ş., 2017. Influence of the compression ratio on the performance and emission characteristics of a vcr diesel engine fuelled with alcohol blended fuels. *European Mechanical Science*, 1(2), pp.39-46.

[142] Baltacioglu, M. K., Kenanoglu, R. and Aydın, K., 2019. HHO enrichment of bio-diesohol fuel blends in a single cylinder diesel engine. *International Journal of Hydrogen Energy*, 44(34), pp.18993-19004.

[143] Kenanoğlu, R., Baltacıoğlu, M. K., Demir, M. H. and Özdemir, M. E., 2020. Performance & emission analysis of HHO enriched dual-fuelled diesel engine with artificial neural network prediction approaches. *International Journal of Hydrogen Energy*, 45(49), pp.26357-26369.

[144] Khalil, A. E. and Gupta, A. K., 2013. Hydrogen addition effects on high intensity distributed combustion. *Applied Energy*, 104, pp.71-78.

[145] Lovegrove, K. M., 1996. High pressure ammonia dissociation experiments for solar energy transport and storage. *International journal of energy research*, 20(11), pp.965-978.

[146] Lovegrove, K., Luzzi, A., Soldiani, I. and Kreetz, H., 2004. Developing ammonia based thermochemical energy storage for dish power plants. Solar energy, 76(1-3), pp.331-337.

[147] Lovegrove, K., Luzzi, A., Soldiani, I. and Kreetz, H., 2004. Developing ammonia based thermochemical energy storage for dish power plants. *Solar Energy*, 76(1-3), pp.331-337.

[148] Morgan, E., Manwell, J. and McGowan, J., 2014. Wind-powered ammonia fuel production for remote islands: A case study. *Renewable Energy*, 72, pp.51-61.

[149] Zamfirescu, C. and Dincer, I., 2009. Ammonia as a green fuel and hydrogen source for vehicular applications. *Fuel Processing Technology*, 90(5), pp.729-737.

[150] Zamfirescu, C. and Dincer, I., 2008. Using ammonia as a sustainable fuel. *Journal of Power Sources*, 185(1), pp.459-465.

[151] Valera-Medina, A., Xiao, H., Owen-Jones, M., David, W. I. and Bowen, P. J., 2018. Ammonia for power. *Progress in Energy and Combustion Science*, 69, pp.63-102.

[152] Avery, W. H., 1988. A role for ammonia in the hydrogen economy. *International Journal of Hydrogen Energy*, 13(12), pp.761-773.

[153] Dunn, R. and Lovegrove, K., Ammonia–the other hydrogen.

[154] Kojima, Y., Miyaoka, H. and Ichikawa, T., 2015. Ammonia-Based Hydrogen Storage Materials. *Advanced Materials for Clean Energy*, pp.497.

[155] Zacharakis-Jutz, G. E., 2013. Performance characteristics of ammonia engines using direct injection strategies. Doctoral dissertation, Iowa State University.

[156] Garabedian, C. G. and Johnson, J. H., 1966. The theory of operation of an ammonia burning internal combustion engine. *Army Tank-Automotive Center Warren Mi*.

[157] Starkman, E. S., James, G. E. and Newhall, H. K., 1968. Ammonia as a diesel engine fuel: theory and application. *SAE Transactions*, pp.3193-3212.

[158] Rehbein, M. C., Meier, C., Eilts, P. and Scholl, S., 2019. Mixtures of ammonia and organic solvents as alternative fuel for internal combustion engines. *Energy & Fuels*, 33(10), pp.10331-10342.

[159] Comotti, M. and Frigo, S., 2015. Hydrogen generation system for ammonia-hydrogen fuelled internal combustion engines. *International Journal of Hydrogen Energy*, 40(33), pp.10673-10686.

[160] Haputhanthri, S. O., Maxwell, T. T., Fleming, J. and Austin, C., 2015. Ammonia and gasoline fuel blends for spark ignited internal combustion engines. *Journal of Energy Resources Technology*, 137(6).

[161] Lesmana, H., Zhang, Z., Li, X., Zhu, M., Xu, W. and Zhang, D., 2019. NH_3 as a transport fuel in internal combustion engines: A technical review. *Journal of Energy Resources Technology*, 141(7), p.070703.

[162] Frigo, S. and Gentili, R., 2013. Analysis of the behaviour of a 4-stroke Si engine fuelled with ammonia and hydrogen. *International Journal of Hydrogen Energy*, 38(3), pp.1607-1615.

[163] Ryu, K., Zacharakis-Jutz, G. E. and Kong, S. C., 2014. Effects of gaseous ammonia direct injection on performance characteristics of a spark-ignition engine. *Applied Energy*, 116, pp.206-215.

[164] Cornelius, W., Huellmantel, L. W. and Mitchell, H. R., 1966. Ammonia as an engine fuel. *SAE Transactions*, pp.300-326.

[165] Koike, M., Miyagawa, H., Suzuoki, T. and Ogasawara, K., 2012. Ammonia as a hydrogen energy carrier and its application to internal combustion engines. *Sustainable Vehicle Technologies: Driving the Green Agenda*, pp.61-70.

[166] Cooper, J. R., Crookes, R. J., Rose, J. W. and Mozafari, A., 1991. Ammonia as a Fuel for the IC Engine.

[167] Dissanayake, K., 2017. Ammonia as an alternative for fuel internal combustion engines. *IOSR Journal of Medical and Civil Engineering*, 14(1), pp.46-9.

[168] Yapicioglu, A. and Dincer, I., 2019. A review on clean ammonia as a potential fuel for power generators. *Renewable and Sustainable Energy Reviews*, 103, pp.96-108.

[169] Brohi, E., 2014. Ammonia as fuel for internal combustion engines? Master thesis.

[170] Li, J., Huang, H., Kobayashi, N., He, Z. and Nagai, Y., 2014. Study on using hydrogen and ammonia as fuels: Combustion characteristics and NOx formation. *International Journal of Energy Research*, 38(9), pp.1214-1223.

[171] Xiao, H., Valera-Medina, A., Bowen, P. and Dooley, S., 2017. 3D simulation of ammonia combustion in a lean premixed swirl burner. *Energy Procedia*, 142, pp.1294-1299.

[172] Meyer, T., Kumar, P., Li, M., Redfern, K. and Diaz, D., 2011. Ammonia combustion with near-zero pollutant emissions. *In NH3 Congress*, Iowa, USA.

[173] Hayakawa, A., Goto, T., Mimoto, R., Kudo, T. and Kobayashi, H., 2015. NO formation/reduction mechanisms of ammonia/air premixed flames at various equivalence ratios and pressures. *Mechanical Engineering Journal*, pp.14-00402.

[174] Iki, N., Kurata, O., Matsunuma, T., Inoue, T., Tsujimura, T., Furutani, H., Kobayashi, H., Hayakawa, A. and Okafor, E., 2018, June. NOx reduction in a swirl combustor firing ammonia for a micro gas turbine. *In Turbo Expo: Power for Land, Sea, and Air*, 51173, pp. V008T26A009.

[175] Li, S., Zhang, S., Zhou, H. and Ren, Z., 2019. Analysis of air-staged combustion of NH_3/CH_4 mixture with low NO_X emission at gas turbine conditions in model combustors. *Fuel*, 237, pp.50-59.

[176] Somarathne, K. D. K. A., Hayakawa, A. and Kobayashi, H., 2016. Numerical investigation on the combustion characteristics of turbulent premixed ammonia/air flames stabilized by a swirl burner. *Journal of Fluid Science and Technology*, 11(4), pp.JFST0026.

[177] Gill, S. S., Chatha, G. S., Tsolakis, A., Golunski, S. E. and York, A. P. E., 2012. Assessing the effects of partially decarbonising a diesel engine by co-fuelling with dissociated ammonia. *International journal of hydrogen energy*, 37(7), pp.6074-6083.

[178] Frigo, S. and Gentili, R., 2013. A hybrid vehicle powered by ammonia and hydrogen. *In Proceedings of the 10th NH_3 Fuel Conference*, Sacramento, CA, USA, pp.22-25.

[179] Frigo, S. and Gentili, R., 2014. Further evolution of an ammonia fuelled range extender for hybrid vehicles. *Proceedings of the NH_3 Fuel Association*, pp.21-24.

[180] Pratt D. T., 1967. Performance of ammonia-fired gas-turbine combustors. Report TS-67-5, 1967; pp.35.

[181] Verkamp, F. J., Hardin, M. C. and Williams, J. R., 1967. Ammonia combustion properties and performance in gas-turbine burners. *In Symposium (International) on Combustion*, 11(1), pp.985-992.

[182] Ni, M., Leung, M. K. and Leung, D. Y., 2009. Ammonia-fed solid oxide fuel cells for power generation-a review. *International Journal of Energy Research*, 33(11), pp.943-959.

[183] García-Bordejé, E., Armenise, S. and Roldán, L., 2014. Toward practical application of H_2 generation from ammonia decomposition guided by rational catalyst design. *Catalysis Reviews*, 56(2), pp.220-237.

[184] Mei, B., Zhang, J., Shi, X., Xi, Z. and Li, Y., 2021. Enhancement of ammonia combustion with partial fuel cracking strategy: Laminar flame propagation and kinetic modeling investigation of $NH_3/H_2/N_2$/air mixtures up to 10 atm. *Combustion and Flame*, 231, pp.111472.

[185] Alboshmina, N., 2019. Ammonia cracking with heat transfer improvement technology. Doctoral dissertation. Cardiiff University.

[186] Kumar, P. and Meyer, T. R., 2013. Experimental and modeling study of chemical-kinetics mechanisms for H_2-NH_3-air mixtures in laminar premixed jet flames. *Fuel*, 108, pp.166-176.

[187] Konnov, A. A., 2009. Implementation of the NCN pathway of prompt-NO formation in the detailed reaction mechanism. *Combustion and Flame*, 156(11), pp.2093-2105.

[188] Mendiara, T. and Glarborg, P., 2009. Ammonia chemistry in oxy-fuel combustion of methane. *Combustion and Flame*, 156(10), pp.1937-1949.

[189] Klippenstein, S. J., Harding, L. B., Glarborg, P. and Miller, J. A., 2011. The role of NNH in NO formation and control. *Combustion and Flame*, 158(4), pp.774-789.

[190] Shmakov, A. G., Korobeinichev, O. P., Rybitskaya, I. V., Chernov, A. A., Knyazkov, D. A., Bolshova, T. A. and Konnov, A. A., 2010. Formation and consumption of NO in H_2+O_2+N_2 flames doped with NO or NH_3 at atmospheric pressure. *Combustion and Flame*, 157(3), pp.556-565.

[191] Xiao, H., Valera-Medina, A., Marsh, R. and Bowen, P. J., 2017. Numerical study assessing various ammonia/methane reaction models for use under gas turbine conditions. *Fuel*, 196, pp.344-351.

[192] Dias, V., Duynslaegher, C., Contino, F., Vandooren, J. and Jeanmart, H., 2012. Experimental and modeling study of formaldehyde combustion in flames. *Combustion and Flame*, 159(5), pp.1814-1820.

[193] Nozari, H. and Karabeyoğlu, A., 2015. Numerical study of combustion characteristics of ammonia as a renewable fuel and establishment of reduced reaction mechanisms. *Fuel*, 159, pp.223-233.

[194] Smith, G. P., Golden, D. M., Frenklach, M., Moriarty, N. W., Eiteneer, B., Goldenberg, M., Bowman, C. T., Hanson, R. K., Song, S., Gardiner, W. C. and Lissianski, V. V., 2016. What's New in GRI-Mech 3.0. *GRI-Mech*. 22, pp.2017.

[195] Song, Y., Hashemi, H., Christensen, J. M., Zou, C., Marshall, P. and Glarborg, P., 2016. Ammonia oxidation at high pressure and intermediate temperatures. *Fuel*, 181, pp.358-365.

[196] Shrestha, K. P., Lhuillier, C., Barbosa, A. A., Brequigny, P., Contino, F., Mounaïm-Rousselle, C., Seidel, L. and Mauss, F., 2021. An experimental and modeling study of ammonia with enriched oxygen content and ammonia/hydrogen laminar flame speed at elevated pressure and temperature. *Proceedings of the Combustion Institute*, 38(2), pp.2163-2174.

[197] Glarborg, P., Miller, J. A., Ruscic, B. and Klippenstein, S. J., 2018. Modeling nitrogen chemistry in combustion. *Progress in Energy and Combustion Science*, 67, pp.31-68.

[198] Abdel-Rahman, A. A., 1998. On the emissions from internal-combustion engines: a review. *International Journal of Energy Research*, 22(6), pp.483-513.

[199] Auer, M. P., Gebauer, C., Mösl, K. G., Hirsch, C. and Sattelmayer, T., 2005. Active instability control: feedback of combustion instabilities on the injection of gaseous fuel.

[200] Saxena, S. and Bedoya, I. D., 2013. Fundamental phenomena affecting low temperature combustion and HCCI engines, high load limits and strategies for extending these limits. *Progress in Energy and Combustion Science*, 39(5), pp.457-488.

[201] Nemitallah, M. A., Rashwan, S. S., Mansir, I. B., Abdelhafez, A. A. and Habib, M. A., 2018. Review of novel combustion techniques for clean power production in gas turbines. *Energy & Fuels*, 32(2), pp.979-1004.

[202] Okojie, R., Danehy, P., Grinstead, J., Watkins, A. and Mielke, A., 2009. An overview of NASA hypersonic experimental diagnostic and instrumentation technologies for ground and flight testing. *In 16th AIAA/DLR/DGLR International Space Planes and Hypersonic Systems and Technologies Conference.* pp.7279.

[203] Hoffman, D., Münch, K. U. and Leipertz, A., 1996. Two-dimensional temperature determination in sooting flames by filtered Rayleigh scattering. *Optics Letters*, 21(7), pp.525-527.

[204] Jiang, L. Y. and Sislian, J. P., 2002. Rayleigh scattering in supersonic high-temperature exhaust plumes. *Experiments in Fluids*, 32(4), pp.487-493.

[205] Meier, U. E., Wolff-Gaßmann, D. and Stricker, W., 2000. LIF imaging and 2D temperature mapping in a model combustor at elevated pressure. *Aerospace Science and Technology*, 4(6), pp.403-414.

[206] Noren, C., Truman, C. R., Vorobieff, P., Madden, T. and Hager, G., 2006. PLIF visualization and quantitative mixing measurements of a supersonic injection nozzle. *In 37th AIAA Plasmadynamics and Lasers Conference.* pp.2895.

[207] Liu, T., Campbell, B. T., Burns, S. P. and Sullivan, J. P., 1997. Temperature-and pressure-sensitive luminescent paints in aerodynamics.

[208] Allison, S., Beshears, D., Bencic, T., Hollerman, W. and Boudreaux, P., 2001. Development of temperature-sensitive paints for high-temperature aeropropulsion applications. *In 37th Joint Propulsion Conference and Exhibit.* pp.3528.

[209] Zhao, H., 2012. Laser diagnostics and optical measurement techniques in internal combustion engines. *SAE*. pp.i-xii.

[210] Zhao, H. and Ladommatos, N., 2001. Engine combustion instrumentation and diagnostics. Warrendale, *PA: Society of Automotive Engineers*. 842.

[211] Schulz, C. and Sick, V., 2005. Tracer-LIF diagnostics: quantitative measurement of fuel

concentration, temperature and fuel/air ratio in practical combustion systems. *Progress in Energy and Combustion Science*, 31(1), pp.75-121.

[212] Settles, G. S., 2001. Schlieren and shadowgraph techniques: visualizing phenomena in transparent media. Springer Science & Business Media.

[213] Pastor, J. V., Payri, R., Garcia-Oliver, J. M. and Nerva, J. G., 2012. Schlieren measurements of the ECN-spray a penetration under inert and reacting conditions. *SAE Technical Paper*.

[214] Desantes, J. M., Payri, R., Salvador, F. J. and De la Morena, J., 2010. Influence of cavitation phenomenon on primary break-up and spray behavior at stationary conditions. *Fuel*, 89(10), pp.3033-3041.

[215] Manin, J., Bardi, M., Pickett, L. M., Dahms, R. N. and Oefelein, J. C., 2014. Microscopic investigation of the atomization and mixing processes of diesel sprays injected into high pressure and temperature environments. *Fuel*, 134, pp.531-543.

[216] Aldén, M., Bood, J., Li, Z. and Richter, M., 2011. Visualization and understanding of combustion processes using spatially and temporally resolved laser diagnostic techniques. *Proceedings of the Combustion Institute*, 33(1), pp.69-97.

[217] Harrington, J.E. and Smyth, K.C., 1993. Laser-induced fluorescence measurements of formaldehyde in a methane/air diffusion flame. *Chemical Physics Letters*, 202(3-4), pp.196-202.

[218] Paul, P. H. and Najm, H. N., 1998. Planar laser-induced fluorescence imaging of flame heat release rate. *In Symposium (International) on Combustion*. 27(1), pp. 43-50.

[219] Liu, Y., 2018. Chemiluminescence and CO pollutant formation in premixed counterflow flames.

[220] Karnani, S. V., 2011. Electric field-driven flame dynamics. University of California, Irvine.

[221] Kinsey, J. L., 1977. Laser-induced fluorescence. *Annual Review of Physical Chemistry*, 28(1), pp.349-372.

[222] Aleiferis, P. G., Hardalupas, Y., Taylor, A. M. K. P., Ishii, K. and Urata, Y., 2004. Flame chemiluminescence studies of cyclic combustion variations and air-to-fuel ratio of the reacting mixture in a lean-burn stratified-charge spark-ignition engine. *Combustion and Flame*, 136(1-2), pp.72-90.

[223] Hardalupas, Y. L. and Orain, M., 2004. Local measurements of the time-dependent heat release rate and equivalence ratio using chemiluminescent emission from a flame. *Combustion and Flame*, 139(3), pp.188-207.

[224] Tinaut, F. V., Reyes, M., Giménez, B. and Pastor, J. V., 2011. Measurements of OH* and CH* chemiluminescence in premixed flames in a constant volume combustion bomb under autoignition conditions. *Energy & Fuels*, 25(1), pp.119-129.

[225] Glassman, I., Yetter, R. A. and Glumac, N. G., 2014. Combustion. Academic press.

[226] Kojima, J., Ikeda, Y. and Nakajima, T., 2005. Basic aspects of OH(A), CH(A), and C_2(d) chemiluminescence in the reaction zone of laminar methane-air premixed flames. *Combustion and Flame*, 140(1-2), pp.34-45.

[227] Asaba, T., Gardiner Jr, W. C. and Stubbeman, R. F., 1965. Shock-tube study of the hydrogen-oxygen reaction. *In Symposium (International) on Combustion*. 10(1), pp. 295-302.

[228] Nori, V. and Seitzman, J., 2008. Evaluation of chemiluminescence as a combustion diagnostic under varying operating conditions. *In 46th AIAA Aerospace Sciences Meeting and Exhibit*. pp. 953.

[229] Carrington, T., 1959. Electronic quenching of OH (2+) in flames and its significance in the interpretation of rotational relaxation. *The Journal of Chemical Physics*, 30(4), pp.1087-1095.

[230] Belles, F. E. and Lauver, M. R., 1964. Origin of OH chemiluminescence during the induction period of the H_2-O_2 reaction behind shock waves. *The Journal of Chemical Physics*, 40(2), pp.415-422.

[231] Hidaka, Y., Takahashi, S., Kawano, H., Suga, M. and Gardiner Jr, W. C., 1982. Shock-tube measurement of the rate constant for excited OH (A/sup2/. sigma./sup+/) formation in the hydrogen-oxygen reaction. *The Journal of Physical Chemistry*. 86(8).

[232] Petersen, E., Kalitan, D. and Rickard, M., 2003. Calibration and chemical kinetics modeling of an oh chemiluminesence diagnostic. *In 39th AIAA/ASME/SAE/ASEE Joint Propulsion Conference and Exhibit*. pp.4493.

[233] Kaskan, W. E., 1959. Abnormal excitation of OH in $H_2/O_2/N_2$ flames. *The Journal of Chemical Physics*, 31(4), pp.944-956.

[234] Dandy, D. S. and Vosen, S. R., 1992. Numerical and experimental studies of hydroxyl radical chemiluminescence in methane-air flames. *Combustion Science and Technology*, 82(1-6), pp.131-150.

[235] Krishnamachari, S. L. N. G. and Broida, H. P., 1961. Effect of Molecular Oxygen on the Emission Spectra of Atomic Oxygen-Acetylene Flames. *The Journal of Chemical Physics*, 34(5), pp.1709-1711.

[236] Gutman, D., Lutz, R. W., Jacobs, N. F., Hardwidge, E. A. and Schott, G. L., 1968. Shock-Tube Study of OH Chemiluminescence in the Hydrogen-Oxygen Reaction. *The Journal of Chemical Physics*, 48(12), pp.5689-5694.

[237] Yoo, S. W., Law, C. K. and Tse, S. D., 2002. Chemiluminescent OH* and CH* flame structure and aerodynamic scaling of weakly buoyant, nearly spherical diffusion flames. *Proceedings of the Combustion Institute*, 29(2), pp.1663-1670.

[238] Ticktin, S., Spindler, G. and Schiff, H. I., 1967. Production of excited OH (A^2+) molecules by the association of ground-state oxygen and hydrogen atoms. *Discussions of the Faraday Society*, 44, pp.218-225.

[239] Smith, G. P., Luque, J., Park, C., Jeffries, J. B. and Crosley, D. R., 2002. Low pressure flame determinations of rate constants for OH (A) and CH (A) chemiluminescence. *Combustion and Flame*, 131(1-2), pp.59-69.

[240] Carl, S. A., Van Poppel, M. and Peeters, J., 2003. Identification of the $CH+O_2 \rightarrow OH\ (A)+$ CO reaction as the source of OH (A−X) chemiluminescence in $C_2H_2/O/H/O_2$ atomic

flames and determination of its absolute rate constant over the range *T* = 296 to 511K. *The Journal of Physical Chemistry A*, 107(50), pp.11001-11007.

[241] Hall, J. M. and Petersen, E. L., 2006. An optimized kinetics model for OH chemiluminescence at high temperatures and atmospheric pressures. *International Journal of Chemical Kinetics*, 38(12), pp.714-724.

[242] Bailey, A. E., Heard, D. E., Paul, P. H. and Pilling, M. J., 1997. Collisional quenching of OH ($A^2 + v' = 0$) by N_2, O_2 and CO_2 between 204 and 294K. Implications for atmospheric measurements of OH by laser-induced fluorescence. *Journal of the Chemical Society, Faraday Transactions*, 93(16), pp.2915-2920.

[243] Hemming, B. L., Crosley, D. R., Harrington, J. E. and Sick, V., 2001. Collisional quenching of high rotational levels in A^2+OH. *The Journal of Chemical Physics*, 115(7), pp.3099-3104.

[244] Hemming, B. L. and Crosley, D. R., 2002. Rotational-level dependence of OH A^2+ quenching at 242 and 196K. *The Journal of Physical Chemistry A*, 106(39), pp.8992-8995.

[245] Dempsey, L. P., Murray, C. and Lester, M. I., 2007. Product branching between reactive and nonreactive pathways in the collisional quenching of OH A^2 radicals by H_2. *The Journal of Chemical Physics*, 127(15), p.151101.

[246] Davidson, D. F., Roehrig, M., Petersen, E. L., Di Rosa, M. D. and Hanson, R. K., 1996. Measurements of the OH AX (0, 0) 306nm Absorption Bandhead at 60atm and 1735K. *Journal of Quantitative Spectroscopy and Radiative Transfer*, 55(6), pp.755-762.

[247] Schulz, C., Jeffries, J. B., Davidson, D. F., Koch, J. D., Wolfrum, J. and Hanson, R. K., 2002. Impact of UV absorption by CO_2 and H_2O on no lif inhigh-pressure combustion applications. *Proceedings of the Combustion Institute*, 29(2), pp.2735-2742.

[248] Gaydon, A., 2012. The spectroscopy of flames. springer science & business media.

[249] Bowman, C. T. and Seery, D. J., 1968. Chemiluminescence in the high-temperature oxidation of methane. *Combustion and Flame*, 12(6), pp.611-614.

[250] Brenig, H. H., Ph.D. Thesis, Wuppertal, 1981.

[251] Smith, W. H., Liszt, L. S. and Lutz, B. L., 1973. A reevaluation of the diatomic processes leading to CH and CH+ formation in the interstellar medium. *The Astrophysical Journal*, 183, pp.69-80.

[252] Glass, G. P., Kistiakowsky, G. B., Michael, J. V. and Niki, H., 1965. Mechanism of the acetylene—oxygen reaction in shock waves. *The Journal of Chemical Physics*, 42(2), pp.608-621.

[253] Grebe, J. and Homann, K.H., 1982. Kinetics of the Species OH (A^2+), OH (X^2 and CH (X^2) in the System C_2H_2/O/H. *Berichte der Bunsengesellschaft für physikalische Chemie*, 86(7), pp.581-587.

[254] Hand, C. W. and Kistiakowsky, G. B., 1962. Ionization accompanying the acetylene-oxygen reaction in shock waves. *The Journal of Chemical Physics*, 37(6), pp.1239-1245.

[255] Hall, J., De Vries, J., Amadio, A. and Petersen, E., 2005. Towards a kinetics model of CH chemiluminescence. *In 43rd AIAA Aerospace Sciences Meeting and Exhibit*. pp.1318.

[256] Devriendt, K. and Peeters, J., 1997. Direct identification of the C_2H (X^2+)+ O (3P)→CH (A^2)+ CO reaction as the source of the CH (A^2→X^2) chemiluminescence in C_2H_2/O/H atomic flames. *The Journal of Physical Chemistry A*, 101(14), pp.2546-2551.

[257] Renlund, A. M., et al. "Gas-phase reactions of C_2H ($\tilde{X}^2\Sigma$+) with O_2, H_2, and CH_4 studied via time-resolved product emissions." *Chemical Physics Letters* 84.2 (1981): 293-298.

[258] Joklik, R. G., Daily, J. W. and Pitz, W. J., 1988, January. Measurements of CH radical concentrations in an acetylene/oxygen flame and comparisons to modeling calculations*. In Symposium (International) on Combustion*. 21(1), pp. 895-904.

[259] Devriendt, K., Van Look, H., Ceursters, B. and Peeters, J., 1996. Kinetics of formation of chemiluminescent CH (A^2) by the elementary reactions of C_2H (X^2+) with O (3P) and O_2 (X^3g−): A pulse laser photolysis study. *Chemical Physics Letters*, 261(4-5), pp.450-456.

[260] Hwang, S. M., Gardiner Jr, W. C., Frenklach, M. and Hidaka, Y., 1987. Induction zone exothermicity of acetylene ignition. *Combustion and Flame*, 67(1), pp.65-75.

[261] Elsamra, R. M., Vranckx, S. and Carl, S. A., 2005. CH (A^2) formation in hydrocarbon combustion: The temperature dependence of the rate constant of the reaction C_2H+ O2→CH (A^2)+ CO_2. *The Journal of Physical Chemistry A*, 109(45), pp.10287-10293.

[262] Kathrotia, T., Fikri, M., Bozkurt, M., Hartmann, M., Riedel, U. and Schulz, C., 2010. Study of the H+O+M reaction forming OH*: Kinetics of OH* chemiluminescence in hydrogen combustion systems. *Combustion and Flame*, 157(7), pp.1261-1273.

[263] Eraslan, A. N. and Brown, R. C., 1988. Chemiionization and ion-molecule reactions in fuel-rich acetylene flames. *Combustion and Flame*, 74(1), pp.19-37.

[264] Kathrotia, T., Riedel, U., Seipel, A., Moshammer, K. and Brockhinke, A., 2012. Experimental and numerical study of chemiluminescent species in low-pressure flames. *Applied Physics B*, 107(3), pp.571-584.

[265] Tamura, M., Berg, P. A., Harrington, J. E., Luque, J., Jeffries, J. B., Smith, G. P. and Crosley, D. R., 1998. Collisional quenching of CH (A), OH (A), and NO (A) in low pressure hydrocarbon flames. *Combustion and Flame*, 114(3-4), pp.502-514.

[266] Smith, W. H., 1971. Absolute Oscillator Strengths for the CH+, CD+, and BH A 1–X 1+ transition. *The Journal of Chemical Physics*, 54(3), pp.1384-1386.

[267] Erman, P., Brzozowski, J. and Sigfridsson, B., 1973. Gas excitations using high frequency deflected electron beams: a convenient method for determinations of atomic and molecular lifetimes. *Nuclear Instruments and Methods*, 110, pp.471-476.

[268] Hartfuss, H. J., Neumann, J. and Schneider, H. D., 1976. Intensity ratios within the balmer lines H_α and H_β after dissociative excitation of C_6H_6 and H_2. *Zeitschrift fur Naturforschung A*, 31(11), pp.1292-1297.

[269] SW, J., 1975. Rgensen and G. S rensen. *The Journal of Chemical Physics*, 62, p.2550.

[270] Brzozowski, J., Bunker, P., Elander, N. and Erman, P., 1976. Predissociation effects in the A, B, and C states of CH and the interstellar formation rate of CH via inverse predissociation. *The Astrophysical Journal*, 207, pp.414-424.

[271] Carozza, J. and Anderson, R., 1977. Radiative lifetime of the A^2 state of CH. *Journal of the Optical Society of America*, 67(1), pp.118-119.

[272] Cvejanovic, D., Adams, A. and King, G. C., 1978. Radiative lifetime measurements of NH

and CH using the electron-photon delayed coincidence method. *Journal of Physics B: Atomic and Molecular Physics*, 11(9), p.1653.

[273] Becker, K. H. and Wiesen, P., 1989. Measurements on the CH* ($A^2 \rightarrow X^2$) chemiluminescence in the C^2H^2+ O Flame and quenching rate constants for different reactants at 297 K. *Zeitschrift fur Physikalische Chemie*, 161(1-2), pp.131-144.

[274] Ferguson, R. E., 1955. On the origin of the electronically excited C_2* radical in hydrocarbon flames. *The Journal of Chemical Physics*, 23(11), pp.2085-2089.

[275] Grebe, J. and Homann, K. H., 1982. Blue-green chemiluminescence in the system C_2H_2/O/H. Formation of the Emitters CH(A^2), C_2(d^3g) and C_2H. *Berichte der Bunsengesellschaft fur physikalische Chemie*, 86(7), pp.587-597.

[276] Bleekrode, R. and Nieuwpoort, W. C., 1965. Absorption and emission measurements of C_2 and CH electronic bands in low-pressure oxyacetylene flames. *The Journal of Chemical Physics*, 43(10), pp.3680-3687.

[277] Bulewicz, E. M., Padley, P. J. and Smith, R. E., 1970. Spectroscopic studies of C_2, CH and OH radicals in low pressure acetylene+ oxygen flames. *Proceedings of the Royal Society of London. A. Mathematical and Physical Sciences*, 315(1520), pp.129-147.

[278] Marques, C. S., Benvenutti, L. H. and Bertran, C. A., 2001. Experimental study of OH*, CHO*, CH*, and C_2* radicals in $C_2H_2/0_2$ and C_2H_2/O_2/Ar flames in a closed chamber. *Combustion Science and Technology*, 167(1), pp.113-129.

[279] Savadatti, M. I. and Broida, H. P., 1966. Spectral study of flames of carbon vapor at low pressure. *The Journal of Chemical Physics*, 45(7), pp.2390-2396.

[280] Irvin G. and Yetter, R. A., 2008. Combustion, Fourth Edition.

[281] Glassman, I. and Yetter, R. A., 2008. Flame phenomena in premixed combustible gases. Combustion, 4th ed. Academic Press, pp.153-162.

[282] Sataloff R. T., Johns M. M., and Kost K. M., Combustion, 2006. 4th ed.

[283] Andersson, B., Andersson, R., Håkansson, L., Mortensen, M., Sudiyo, R. and Van Wachem, B., 2011. Computational fluid dynamics for engineers. Cambridge university press.

[284] Winterbone, D. and Turan, A., 2015. Advanced thermodynamics for engineers. Butterworth-Heinemann.

[285] Botha, J. P. and Spalding, D. B., 1954. The laminar flame speed of propane/air mixtures with heat extraction from the flame. *Proceedings of the Royal Society of London. Series A. Mathematical and Physical Sciences*, 225(1160), pp.71-96.

[286] Khudhair, O. and Shahad, H. A., 2017. A review of laminar burning velocity and flame speed of gases and liquid fuels. *International Journal of Current Engineering and Technology*, 7(1), pp.183-197.

[287] Benim, A. C. and Syed, K. J., 2014. Flashback mechanisms in lean premixed gas turbine combustion. Academic press.

[288] Frank-Kamenetskii, D. A., 2015. Diffusion and heat exchange in chemical kinetics. Princeton University Press.

[289] Turns, S. R., 1996. Introduction to combustion (Vol. 287, p. 569). New York, NY, USA: McGraw-Hill Companies.

[290] Wang, W. and Gou, X., 2017. A mechanism reduction method integrating path flux analysis with multi generations and sensitivity analysis. *Combustion Science and Technology*, 189(1), pp.24-42.

[291] Bykov, V. I., Yablonskii, G. S., Akramov, T. A. and Slin'ko, M. G., 1977. The rate of the free energy decrease in the course of the complex chemical reaction. *In Dokl. Akad. Nauk USSR*, 234(3), pp. 621-634.

[292] Gorban, A. N. and Karlin, I. V., 2005. Invariant manifolds for physical and chemical kinetics. Berlin: Springer.

[293] Beretta, G. P., Keck, J. C., Janbozorgi, M. and Metghalchi, H., 2012. The rate-controlled constrained-equilibrium approach to far-from-local-equilibrium thermodynamics. *Entropy*, 14(2), pp.92-130.

[294] De Donder, T. and Van Rysselberghe, P., 1936. Thermodynamic theory of affinity. Stanford university press.

[295] Kuo, K. K., 1986. Principles of combustion. Wiley.

[296] Gyftopoulos, E. P. and Beretta, G. P., 2005. Thermodynamics: foundations and applications. Courier Corporation.

[297] McBride, B. J., 1993. Coefficients for calculating thermodynamic and transport properties of individual species. NASA Langley Research Center.

[298] Chaos, M. and Dryer, F. L., 2010. Chemical-kinetic modeling of ignition delay: Considerations in interpreting shock tube data. *International Journal of Chemical Kinetics*, 42(3), pp.143-150.

[299] Design, R., 2015. ANSYS Chemkin Theory Manual 17.0.

[300] Fichet, V., Kanniche, M., Plion, P. and Gicquel, O., 2010. A reactor network model for predicting NOx emissions in gas turbines. *Fuel*, 89(9), pp.2202-2210.

[301] Božo, M. G., Vigueras-Zuniga, M. O., Buffi, M., Seljak, T. and Valera-Medina, A., 2019. Fuel rich ammonia-hydrogen injection for humidified gas turbines. *Applied Energy*, 251, p.113334.

[302] Valera-Medina, A., Gutesa, M., Xiao, H., Pugh, D., Giles, A., Goktepe, B., Marsh, R. and Bowen, P., 2019. Premixed ammonia/hydrogen swirl combustion under rich fuel conditions for gas turbines operation. *International Journal of Hydrogen Energy*, 44(16), pp.8615-8626.

[303] Rocha, R. C., Costa, M. and Bai, X. S., 2021. Combustion and emission characteristics of ammonia under conditions relevant to modern gas turbines. *Combustion Science and Technology*, 193(14), pp.2514-2533.

[304] Goh, E., Sirignano, M., Li, J., Nair, V., Emerson, B., Lieuwen, T. and Seitzman, J., 2019. Prediction of minimum achievable NOx levels for fuel-staged combustors. *Combustion and Flame*, 200, pp.276-285.

[305] Goh, E., Sirignano, M., Nair, V., Emerson, B., Lieuwen, T. and Seitzman, J., 2017. Modeling of minimum NOx in staged-combustion architectures at elevated temperatures. *In Turbo Expo: Power for Land, Sea, and Air*. American Society of Mechanical Engineers.

[306] Hoferichter, V., Ahrens, D., Kolb, M. and Sattelmayer, T., 2014. A reactor model for the NOx formation in a reacting jet in hot cross flow under atmospheric and high pressure conditions. *In Turbo Expo: Power for Land, Sea, and Air*. American Society of Mechanical Engineers.

[307] Zhang, M., An, Z., Wei, X., Wang, J., Huang, Z. and Tan, H., 2021. Emission analysis of the CH_4/NH_3/air co-firing fuels in a model combustor. *Fuel*, 291, p.120135.

[308] Yuri, M., Masada, J., Tsukagoshi, K. U. and Hada, S., 2013. Development of 1600 C-class high-efficiency gas turbine for power generation applying J-Type technology. *Mitsubishi Heavy Industries Technical Review*, 50(3), pp.1-10.

[309] Kee, R. J., Grcar, J. F., Smooke, M. D. and Miller, J. A., 1985. A FORTRAN program for modeling steady laminar one-dimensional premixed flames, Report No. SAND85-8240, Sandia National Laboratories, p.72.

[310] Higgins, B., McQuay, M. Q., Lacas, F. and Candel, S., 2001. An experimental study on the effect of pressure and strain rate on CH chemiluminescence of premixed fuel-lean methane/air flames. *Fuel*, 80(11), pp.1583-1591.

[311] Panoutsos, C. S., Hardalupas, Y. and Taylor, A. M. K. P., 2009. Numerical evaluation of equivalence ratio measurement using OH* and CH* chemiluminescence in premixed and non-premixed methane-air flames. *Combustion and Flame*, 156(2), pp.273-291.

[312] Leplat, N., Dagaut, P., Togbé, C. and Vandooren, J., 2011. Numerical and experimental study of ethanol combustion and oxidation in laminar premixed flames and in jet-stirred reactor. *Combustion and Flame*, 158(4), pp.705-725.

[313] Le Bourlot, J., Roueff, E. and Viala, Y., 1987. Rotational equilibrium of C_2 in diffuse interstellar clouds. I-Static model: the case of Zeta Ophiuchi. *Astronomy and Astrophysics*, 188, pp.137-144.

[314] Benvenutti, L. H., Marques, C. S. and Bertran, C. A., 2004. Chemiluminescent emission data for kinetic modeling of ethanol combustion. *Combustion Science and Technology*, 177(1), pp.1-26.

[315] Dagaut, P. and Togbé, C., 2008. Experimental and modeling study of the kinetics of oxidation of ethanol-gasoline surrogate mixtures (E85 surrogate) in a jet-stirred reactor. *Energy & Fuels*, 22(5), pp.3499-3505.

[316] Feng, H., Zhang, J., Liu, D., An, M., Zhang, W. and Zhang, X., 2017. Development of a reduced *n*-butanol mechanism with combined reduction methods. *Fuel*, 187, pp.403-416.

[317] Natarajan, K. and Bhaskaran, K. A., 1981. An experimental and analytical investigation of high temperature ignition of ethanol. Indian Inst of Tech Madras Dept of Mechanical Engineering, pp.834-542.

[318] Dunphy, M. P. and Simmie, J. M., 1991. High-temperature oxidation of ethanol. Part 1.-Ignition delays in shock waves. *Journal of the Chemical Society*, 87(11), pp.1691-1696.

[319] Zhang, X., Moosakutty, S. P., Rajan, R. P., Younes, M. and Sarathy, S. M., 2021. Combustion chemistry of ammonia/hydrogen mixtures: Jet-stirred reactor measurements and comprehensive kinetic modeling. *Combustion and Flame*, 234, p.111653.

[320] Lhuillier, C., Brequigny, P., Lamoureux, N., Contino, F. and Mounaïm-Rousselle, C., 2020. Experimental investigation on laminar burning velocities of ammonia/hydrogen/air mixtures at elevated temperatures. *Fuel*, 263, p.116653.

[321] Li, Y., Bi, M., Li, B. and Gao, W., 2018. Explosion behaviors of ammonia-air mixtures. *Combustion Science and Technology*, 190(10), pp.1804-1816.

[322] Kondo, S., Takizawa, K., Takahashi, A., Tokuhashi, K. and Sekiya, A., 2008. A study on flammability limits of fuel mixtures. *Journal of hazardous Materials*, 155(3), pp.440-448.

[323] Jabbour, T. and Clodic, D. F., 2004. Burning velocity and refrigerant flammability classification/discussion. *ASHRAE Transactions*, 110, p.522.

[324] Pratt, D. T. and Starkman, E. S., 1968. Gas turbine combustion of ammonia. *SAE Transactions*, pp.3160-3168.

[325] Reiter, A. J. and Kong, S. C., 2008. Demonstration of compression-ignition engine combustion using ammonia in reducing greenhouse gas emissions. *Energy & Fuels*, 22(5), pp.2963-2971.

[326] Ilbas, M., Kumuk, O. and Karyeyen, S., 2021. Numerical study of a swirl gas turbine combustor for turbulent air and oxy-combustion of ammonia/kerosene fuels. *Fuel*, 304, p.121359.

[327] Somarathne, K. D. K. A., Okafor, E. C., Sugawara, D., Hayakawa, A. and Kobayashi, H., 2021. Effects of OH concentration and temperature on NO emission characteristics of turbulent non-premixed CH_4/NH_3/air flames in a two-stage gas turbine like combustor at high pressure. *Proceedings of the Combustion Institute*, 38(4), pp.5163-5170.

[328] Liu, Q., Chen, X., Huang, J., Shen, Y., Zhang, Y. and Liu, Z., 2019. The characteristics of flame propagation in ammonia/oxygen mixtures. Journal of Hazardous Materials, 363, pp.187-196.

[329] Zeldovich, Y. B., 2014. 26. Oxidation of Nitrogen in Combustion and Explosions. *In Selected Works of Yakov Borisovich Zeldovich*. Princeton University Press.

[330] Pugh, D., Runyon, J., Bowen, P., Giles, A., Valera-Medina, A., Marsh, R., Goktepe, B. and Hewlett, S., 2021. An investigation of ammonia primary flame combustor concepts for emissions reduction with OH*, NH_2* and NH* chemiluminescence at elevated conditions. *Proceedings of the Combustion Institute*, 38(4), pp.6451-6459.

[331] Turner, M. A., Paschal, T. T., Parajuli, P., Kulatilaka, W. D. and Petersen, E. L., 2021. Resolving flame thickness using high-speed chemiluminescence imaging of OH* and CH* in spherically expanding methane-air flames. *Proceedings of the Combustion Institute*, 38(2), pp.2101-2108.

[332] Zhu, X., Khateeb, A. A., Guiberti, T. F. and Roberts, W. L., 2021. NO and OH* emission characteristics of very-lean to stoichiometric ammonia-hydrogen-air swirl flames. *Proceedings of the Combustion Institute*, 38(4), pp.5155-5162.

[333] Ayoola, B. O., Balachandran, R., Frank, J. H., Mastorakos, E. and Kaminski, C. F., 2006. Spatially resolved heat release rate measurements in turbulent premixed flames. *Combustion and Flame*, 144(1-2), pp.1-16.

[334] Tsukada, N., Kinoshita, N., Kabuki, Y., Taguchi, Y., Takashima, Y., Tsumura, T. and Taniguchi, M., 2020. Role of OH radical in fuel-NOx formation during cocombustion of

ammonia with hydrogen, methane, coal, and biomass. *Energy & Fuels*, 34(4), pp.4777-4787.

[335] Li, Z. and Li, S., 2021. Kinetics modeling of NOx emissions characteristics of a NH_3/H_2 fueled gas turbine combustor. *International Journal of Hydrogen Energy*, 46(5), pp.4526-4537.

[336] Hussein, N. A., Valera-Medina, A. and Alsaegh, A. S., 2019. Ammonia-hydrogen combustion in a swirl burner with reduction of NOx emissions. *Energy Procedia*, 158, pp.2305-2310.

[337] Lauer, M. and Sattelmayer, T., 2010. On the adequacy of chemiluminescence as a measure for heat release in turbulent flames with mixture gradients. *Journal of Engineering for Gas Turbines and Power*, 132(6).

[338] Li, J., Richecoeur, F. and Schuller, T., 2012. Determination of heat release rate disturbances in unconfined flames based on fluctuations in the travel time of ultrasonic waves. *Combustion Science and Technology*, 184(4), pp.533-555.

[339] Röder, M., Dreier, T. and Schulz, C., 2013. Simultaneous measurement of localized heat-release with OH/CH_2O-LIF imaging and spatially integrated OH* chemiluminescence in turbulent swirl flames. *Proceedings of the Combustion Institute*, 34(2), pp.3549-3556.

[340] Kathrotia, T., Riedel, U. and Warnatz, J., 2009, April. A numerical study on the relation of OH*, CH*, and C_2* chemiluminescence and heat release in premixed methane flames. *In Proceedings of the European Combustion Meeting*.

[341] Kojima, J., Ikeda, Y. and Nakajima, T., 2000. Spatially resolved measurement of OH*, CH*, and C_2* chemiluminescence in the reaction zone of laminar methane/air premixed flames. *Proceedings of the Combustion Institute*, 28(2), pp.1757-1764.